POLITECNICO
MILANO 1863

A Parametric Framework for Adaptive Façade Design:

Transition from Manual Optioneering to Multi-Objective Optimization Based on Energy Performance Analysis

Authors: Mina Ahmadsamei, Mahdi Jazini, Nazanin Nobakht

Supervisor: Prof. Graziano Salvalai

MASTER'S DEGREE THESIS IN BUILDING AND ARCHITECTURAL ENGINEERING

AY 2025-2026

ACKNOWLEDGE

We are truly grateful for the opportunity to have studied in an environment enriched by very brilliant, committed, and inspiring individuals. During this trip, we have developed both intellectually and personally, emerging as more resilient and self-aware individuals. The experiences and memories acquired over these years will persist, influencing our perspectives and objectives moving forward. We wish to express our profound appreciation to our supervisor, Professor Graziano Salvalai, for his outstanding instruction, and assistance. His mentorship has enhanced this study and shaped our growth as designers and researchers. We are deeply grateful for the support of our wonderful family and friends. Their support, faith, and unwavering affection have sustained us along this journey. We extend our deepest appreciation to our parents, whose unwavering support and confidence have facilitated our self-discovery and personal development.

With Endurance, We Conquer…

Mina, Mahdi, Nazanin

Lecco, Italy

March 2026

ABSTRACT

This thesis investigates the application of parametric design and optimization for a more sustainable façade design by analyzing energy performance, daylight factors, and glare reduction. This research applies computational methods to systematically analyze and compare diverse façade design alternatives, rather than relying on experiential decision-making or trial-and-error approaches.

A computational design methodology is established through the integration of parametric design, environmental simulation, and multi-objective optimization. Automated energy, daylight, and glare simulations are used to test how effectively a building will function, and parametric design is used to make the façade designs. An evolutionary optimization algorithm based on the NSGA-II method is used to look for façade designs that meet several conflicting building performance criteria.

This study focuses on the external shading devices that are built into the building's facade. To make the environment better, the most important design parameters, such as the size, orientation, and shape of the shading devices, are set as variables. To validate the design methodology and examine the effects of diverse geometric shading device configurations on building performance in a real climate, a mixed-use building has been chosen as a test case.

The results demonstrate that the proposed computational design method looks into the façade design space and allows us to understand the trade-offs between energy efficiency, glare reduction, and daylighting. The method helps people make decisions in the early stages of design by giving them a set of optimized design options instead of just one perfect solution. This study shows that parametric optimization can be a useful and effective way to design performance-driven facades in modern architecture.

Keywords: Parametric Design; Façade Optimization; Multi-Objective Optimization; NSGA-II; Building Performance Simulation; External Shading Systems; Daylighting and Glare; Sustainable Architecture.

ABSTRACT (ITALIAN)

La presente tesi indaga l'applicazione della progettazione parametrica e dell'ottimizzazione per lo sviluppo di soluzioni di facciata più sostenibili, attraverso l'analisi delle prestazioni energetiche, dei fattori di illuminazione naturale e della riduzione dell'abbagliamento. La ricerca adotta metodi computazionali per analizzare e confrontare in modo sistematico diverse alternative progettuali di facciata, superando approcci basati esclusivamente sull'esperienza o su processi di tipo trial-and-error.

La metodologia proposta si fonda sull'integrazione tra progettazione parametrica, simulazione ambientale e ottimizzazione multi-obiettivo. Simulazioni automatizzate delle prestazioni energetiche, dell'illuminazione naturale e dell'abbagliamento vengono impiegate per valutare l'efficacia funzionale dell'edificio, mentre la progettazione parametrica consente la generazione e la modifica delle configurazioni di facciata. L'esplorazione dello spazio progettuale è condotta mediante un algoritmo evolutivo di ottimizzazione basato sul metodo NSGA-II, finalizzato all'individuazione di soluzioni in grado di soddisfare criteri prestazionali tra loro potenzialmente conflittuali.

Lo studio si concentra in particolare sui dispositivi di schermatura solare esterni integrati nell'involucro edilizio. I principali parametri progettuali — quali dimensioni, orientamento e configurazione geometrica delle schermature — sono definiti come variabili di ottimizzazione al fine di migliorare le prestazioni ambientali complessive. Per validare la metodologia proposta e analizzare l'impatto di differenti configurazioni geometriche delle schermature sulle prestazioni dell'edificio in condizioni climatiche reali, è stato selezionato come caso studio un edificio a uso misto.

I risultati dimostrano che il metodo computazionale sviluppato consente un'esplorazione sistematica dello spazio progettuale della facciata e permette di comprendere i compromessi tra efficienza energetica, controllo dell'abbagliamento e disponibilità di luce naturale. L'approccio supporta il processo decisionale nelle fasi preliminari della progettazione, offrendo un insieme di soluzioni ottimizzate anziché un'unica soluzione ideale. La ricerca evidenzia come l'ottimizzazione parametrica rappresenti uno strumento efficace per la progettazione di facciate orientate alle prestazioni nell'architettura contemporanea.

Parole chiave: Progettazione parametrica; Ottimizzazione della facciata; Ottimizzazione multi-obiettivo; NSGA-II; Simulazione delle prestazioni edilizie; Sistemi di schermatura solare esterni; Illuminazione naturale e abbagliamento; Architettura sostenibile.

Table of content

1 Introduction 1

1.1 Problem Definition: Façade Performance as a Multi-Criteria Design Challenge 2

1.1.1 Adaptive Façade Innovation in Contemporary Practice 2

1.2 Limitations of Conventional Façade Design Approaches 4

1.3 Necessity of a performance-driven Multi-Objective Optimization 4

1.4 Research Focus and Scope of the Thesis 5

1.5 Overview of Methodology 6

1.6 Objectives and Contributions 6

2 Background knowledge 8

2.1 Optimization theory: 9

2.1.1 (NSGA-II) Suitable Optimization Algorithms for Architectural Design Problems: 16

2.1.2 NSGA-II optimization overall process: 17

2.1.3 Optimization concepts and terminologies: 20

2.1.4 After optimization; visualization, graphs and interpretations: 25

2.2 Energy and daylight analysis theory 33

2.3 Tool Selection and Rationale 34

3 Article review 39

3.1 Article 1: 40

3.1.1 Introduction 40

3.1.2 Methodology 40

3.1.3 Results 45

3.1.4 Conclusions: 45

3.2 Article 2: 47
3.2.1 Introduction 47
3.2.2 Methodology 48
3.2.3 Result 53
3.2.4 Conclusions 55
3.3 Article 3: 57
3.3.1 Introduction 57
3.3.2 Methodology: 57
3.3.3 Objectives: 61
3.3.4 Results 61
3.3.5 Conclusion: 62
4 Framework of Algorithm 64
4.1 Simulation Tools: 67
4.1.1 Ladybug 67
4.1.2 Honeybee 69
4.1.3 Honeybee Energy 79
4.1.4 Honeybee Radiance 91
4.2 Optimization Tool (Wallacei) 103
5 Results on an existing case study 123
5.1 Parametric Zones Modeling 142
5.2 Parametric shader modeling 145
5.3 Baseline analysis before shading application 152
5.3.1 Zonal program & setpoint assignment 152
5.3.2 Definition of Material Properties for Baseline Simulation 156
5.3.3 Energy results 158
5.3.4 Daylight Analysis 171

5.4 Optimization results on the representative spaces 185
5.5 Optioneering (Solution selection) 199
5.6 Analysis for the whole building based on selected solutions: 204
6 Conclusion 220
7 References 224

01

INTRODUCTION

1.1 Problem Definition: Façade Performance as a Multi-Criteria Design Challenge

The building façade is the primary connection between the internal and external environments, and it plays an important role in building energy performance and indoor environmental quality, particularly in modern commercial and mixed-use buildings with high glazing ratios and complex functional needs. A lot of research has shown that façade design variables have a direct effect on building energy consumption, daylight supply, glare, and thermal comfort, therefore influencing both building efficiency and occupant comfort.(Yao et al., 2024; Zhang et al., 2025). However, façade design remains a fundamentally multifunctional and sensitive topic. Façade design solutions that improve daylighting may result in greater glare and cooling loads, whereas solar control methods that reduce overheating can affect daylight quality and demand more artificial lighting consumption. Because of these conflicting requirements, the façade is a system in which energy efficiency, visual comfort, and temperature management are inseparable and contradictory rather than complementary (Wu et al., 2025; Zhang et al., 2025).

1.1.1 Adaptive Façade Innovation in Contemporary Practice

Figure 1-1 Adaptive ETFE façade system of the Media-TIC Building.

In recent decades, numerous completed projects have proven the capability of adaptive façade solutions to effectively balance environmental performance requirements with architectural aesthetics. These projects exemplify the growing aim to seamlessly incorporate solar protection, daylight accessibility, and thermal comfort. The Media-TIC Building includes an ETFE façade technology with pneumatic characteristics that adjust its opacity in response to solar radiation. The façade system actively regulates solar gains to reduce cooling requirements while maintaining access to daylight. This adaptive design demonstrates how the shape and material characteristics of façades can directly influence energy performance and visual comfort in actual environmental circumstances (Loonen et al., 2013; Attia, 2018).

Figure 1-2 Kinetic shading façade of the Kiefer Technic Showroom.

Similarly, the Kiefer Technic Showroom employs motorized aluminum shade panels that adjust according to sun radiation. The adaptive façade mitigates warming while preserving daylight access and sightlines. The system illustrates the trade-offs of sun protection, visual comfort, and energy performance, which are essential considerations in façade design (Loonen et al., 2015).While these examples effectively demonstrate environmentally sensitive façade systems, their design processes have relied on simulation testing and engineering optimization instead of systematic multi-objective computational analysis. Although adaptive technology might enhance façade

performance, the framework for dynamically evaluating competing performance criteria and supplying architectural knowledge to inform design decisions remains insufficiently developed.

1.2 Limitations of Conventional Façade Design Approaches

Typical conventional façade design methods would generally involve intuition-driven decision-making, rule-of-thumb analysis, or isolated parameter adjustments for variables such as window-to-wall ratio, glazing properties, or shading depth. Although these methods may provide acceptable results for simplified design tasks, they are not adequate for dealing with the non-linear relationships involved in façade performance under real-world climatic conditions (Tian et al., 2025). Typical conventional façade design methods would generally involve manual optioneering, intuition-driven design exploration, or isolated adjustment of a few design parameters. Although these methods may be tolerable for early conceptual design tasks or low-dimensional design problems, they become increasingly less effective as the number of variable design parameters increases. With each additional design parameter, the façade design problem space grows combinatorially, leading to many possible design alternatives that cannot be systematically explored using manual or experience-driven design approaches.

This is particularly problematic for façade design, where important performance objectives such as energy demand, daylight availability, and glare control are not only interdependent but also often conflicting. Modifications made to improve one performance measure are likely to adversely affect another, making it challenging to predict design outcomes using sequential or intuition-driven decision-making. Consequently, manual design exploration becomes ineffective for identifying high-performing designs, let alone optimal or near-optimal designs, when confronted with complex multi-objective performance relationships. This leads to a mismatch between the growing complexity of façade design problems and the ability of manual, intuition-driven design exploration to effectively address multi-objective performance relationships.

1.3 Necessity of a performance-driven Multi-Objective Optimization

Single-objective optimization is not suitable for façade design because key performance criteria such as energy consumption, daylight availability, and glare

control are strongly interrelated and often conflict with each other. In many cases, improving one performance aspect leads to deterioration in another, which makes optimizing objectives independently both misleading and ineffective (Wu et al., 2025; Zhang et al., 2025).

As the number of façade design parameters increases, the number of possible design combinations grows rapidly. Under these conditions, manual trial-and-error design exploration becomes impractical, as designers can only test a limited number of options based on intuition and incremental adjustments. This approach explores only a small portion of the available design space and remains subjective and time-consuming, making it insufficient for identifying high-performing solutions in complex design problems (Tian et al., 2025).

For these reasons, façade optimization requires a multi-objective approach that can evaluate competing performance criteria simultaneously and systematically explore the design space. Multi-objective optimization methods enable designers to identify and compare different trade-offs between energy performance, daylight provision, and glare control, supporting more informed and transparent design decision-making (Alsukkar et al., 2025).

1.4 Research Focus and Scope of the Thesis

The purpose of this thesis is to explore a workflow for performance-driven, multi-objective optimization in façade design related to architectural decision support under competing performance criteria. In this regard, the proposed workflow combines parametric façade modeling, climate-driven energy and daylight simulation within an evolutionary multi-objective optimization algorithm in a single computational framework. Subsequently, a commercial building is used as a case study to test the applicability and robustness of the proposed methodology; however, the case study is merely a test bed for the validation of the proposed methodology and not the aim itself. The focus is on the methodological aspects of the proposed approach to make the proposed approach general and applicable to different building types, climatic conditions, and façade configurations. The thesis asserts that the main benefit of façade optimization is not in finding individual optimal solutions but in organizing knowledge about performance in a way that facilitates architectural decision support based on multi-dimensionally optimal and rated solutions.

1.5 Overview of Methodology

In a unified platform of Grasshopper of Rhino software for all parts, an algorithm for multi-objective optimization is designed, in which the workflow begins with the parametric definition of façade design variables, enabling systematic and transparent manipulation of geometric and shading parameters. Environmental performance is evaluated using climate-based energy, daylight, and glare simulations to ensure that façade behavior is assessed under realistic operating conditions. Finally, it explores the design space and generates sets of Pareto-optimal solutions and after clustering them based on density, it represents alternative performance compromises.

To be more cost-effective, some representative spaces will be optimized on behalf of the whole building, then after clustering the pareto-optimal solutions, those façade design options will be analyzed on the whole building model in the post-optimization part. It interprets outcomes through comparative analysis and visualization of performance metrics to enables designers to understand how variations in façade configuration influence energy demand, daylight availability, and glare risk.

In Grasshopper, the methodology is implemented using Wallacei plugin for NSGA-II–based optimization and Ladybug & Honeybee for environmental simulation. It is of paramount importance that the contribution lies in the structure and logic of the workflow rather than in the specific software tools employed.

1.6 Objectives and Contributions

The aims of this thesis are to fill the gap between the computational optimization of façades and architectural decision-making with competing criteria. This research aims to:

1. Investigate the relationships between façade design variables and key performance indicators for energy use, daylight access, and glare mitigation in real climatic conditions.
2. Develop a clear multi-objective optimization approach to facilitate the exploration of façade performance trade-offs instead of finding a single optimal solution.

3. Develop an analysis and interpretation approach to facilitate the interpretation of optimization outcomes into decision-making information for architectural designers.
4. Validate the applicability and effectiveness of the proposed approach by applying it to a real-world building case study.

The contribution of this research is an optimization approach that facilitates façade design decisions. The approach enables designers to understand trade-offs in performance rather than finding a single optimized solution. The contribution is methodological and can be generalized to other buildings and façades.

02

BACKGROUND KNOWLEDGE

2.1 Optimization theory:

Optimization is the computational process of identifying the best-performing solution from an extremely large, or even effectively infinite, set of possible design options by automatically evaluating, comparing, and improving alternatives according to defined goals and constraints.

It is useful because

- choosing the best value for each parameter independently does not ensure a globally optimal solution, because the performance of the overall system depends on interactions among variables
- and as the number of input parameters increases, it becomes impractical to test different combinations through trial and error.

Optimization becomes meaningful when objectives (at least one of them) are in conflict, creating trade-offs that require algorithms to identify optimal solutions.

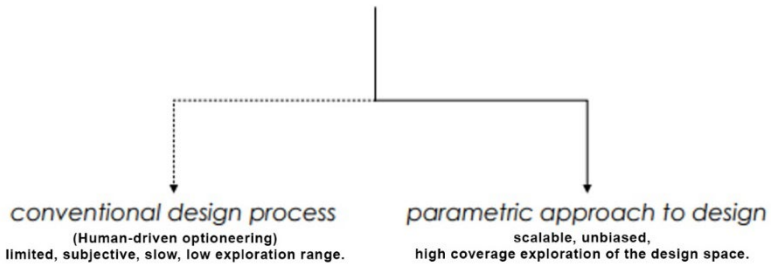

In a conventional (human-driven) design approach, improvements are made through repeated cycles of modeling and evaluation. It explores only a very small portion of the possible solution space because each iteration depends on the designer's intuition and limited manual adjustments, so the method remains subjective, slow, and unable to guarantee that the outcome is truly optimal. As the number of design parameters increases, the search space expands rapidly, making trial-and-error exploration impractical and often insufficient for finding high-performance solutions.

In other words, this conventional approach limits the capacity to capture dynamic interactions between energy demand, daylight availability, and visual comfort. As design complexity increases, human-driven decisions become less reliable, particularly when façade performance must be assessed across annual climatic conditions rather than under static or peak scenarios (Attia et al., 2013).

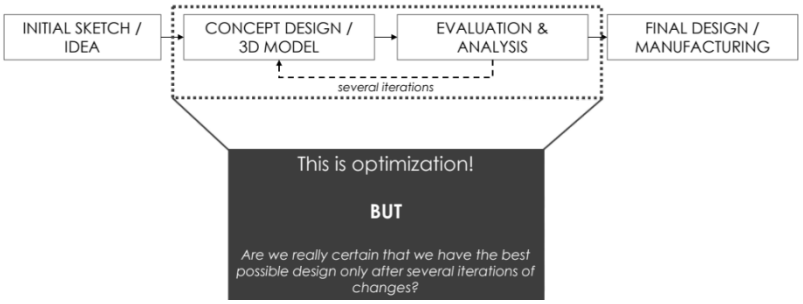

Figure 2-1 Diagram for a conventional (human-driven) design approach

So, there is necessity of parametric modeling for optimization as a modern approach because optimization requires the ability to systematically explore a wide range of design alternatives. A parametric model provides this capability by defining the design through adjustable parameters rather than fixed geometry. When inputs such as dimensions, angles, material properties, or performance criteria are encoded as variables, the model becomes responsive and computationally searchable.

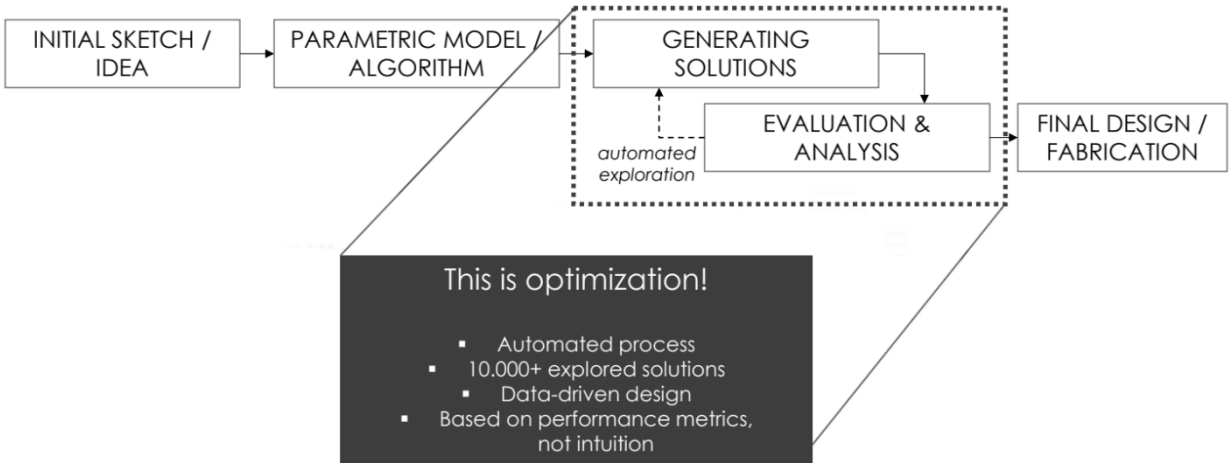

Figure 2-2 Diagram for parametric design approach to optimization

such a parametric model should have:

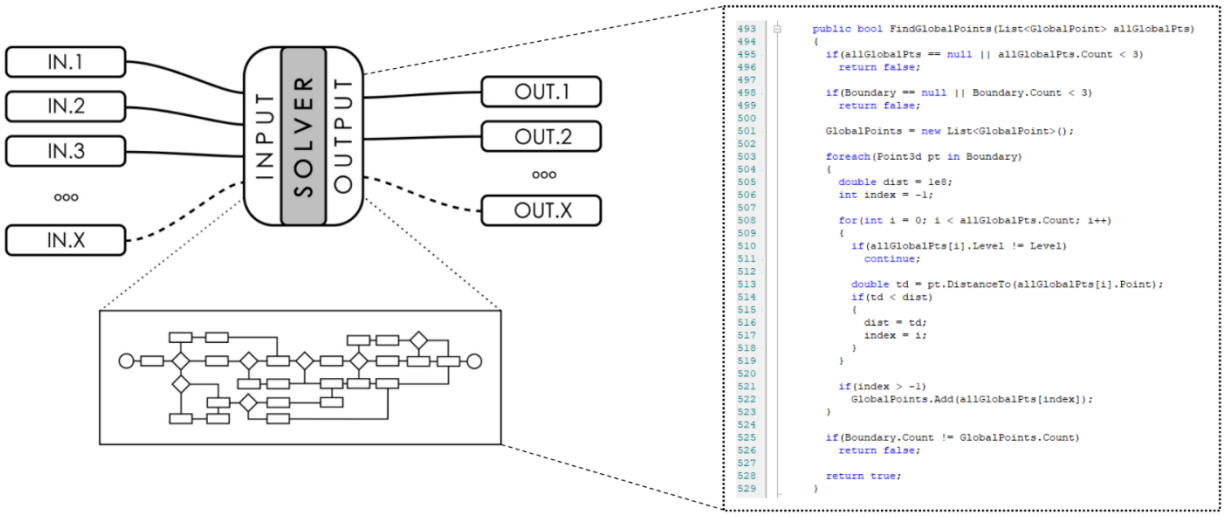

Figure 2-3 Schematic diagram of a parametric algorithm;visual programming . Screenshot from Grasshopper optimization online workshop, Source: (HowToRhino, 2026)

- Digital dynamic model = Design elements are defined by parameters, relationships and rules rather than fixed values.
- Series of geometric operations & mathematical function= instructions for a machine to automatically create a specific form
- Order of geometric operations is crucial
- End goal is the same => 3D digital model
- DNA of a building = different solution, but they still belong to the same “design family”
- Designing the whole spectrum of design possibilities, rather than a single 3D model
- Usually, there are endless possibilities – millions and even trillions

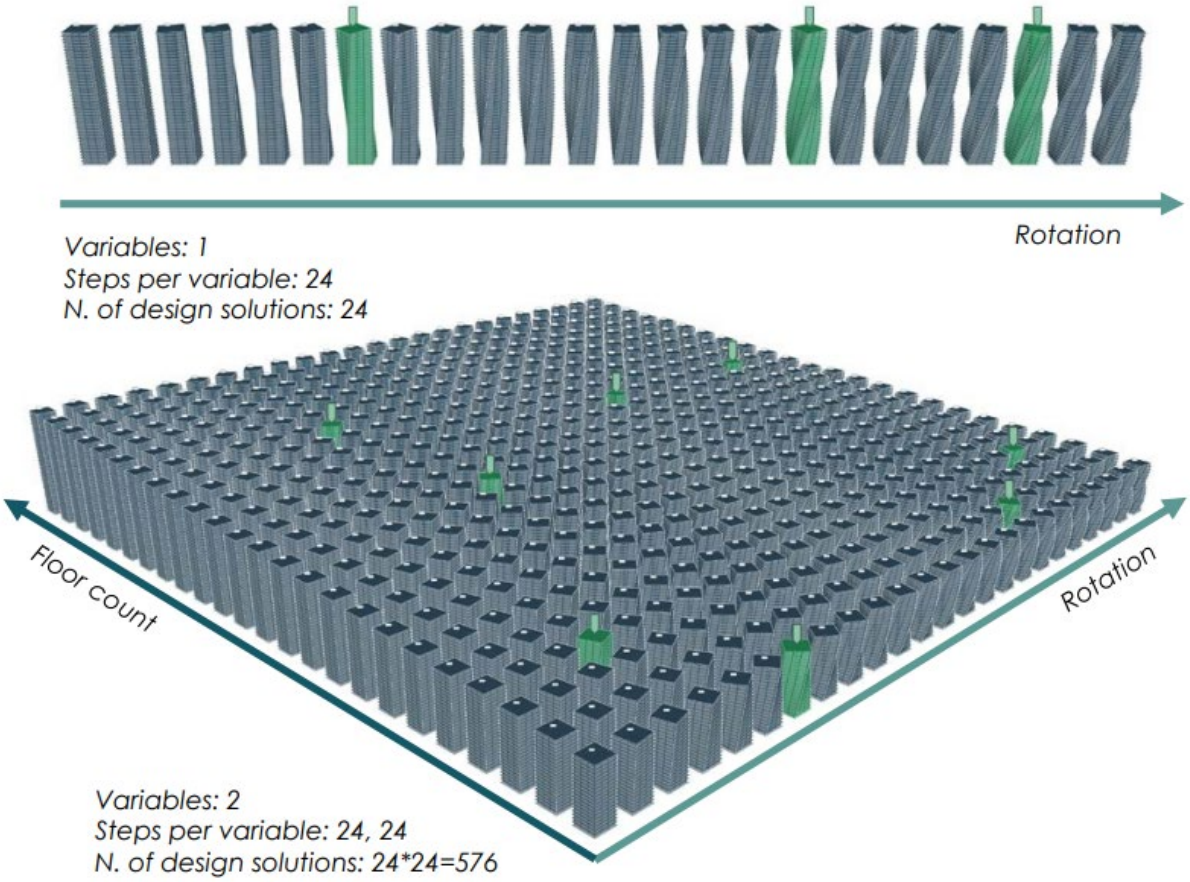

Figure 2-4 Example for design search space. Screenshot from Grasshopper optimization online workshop, Source: (HowToRhino, 2026)

Benefits of parametric optimization approach are

- Solving high-dimensional design problems
- Interactive design exploration
- Faster reaction time to design changes
- Making informed, more reliable decisions

And its disadvantages are

- It depends on diversity of solutions produced by parametric models
- Not able to produce anything “new”
- Requires more time and resources upfront
- Higher technical knowledge

When it comes to action, there are a lot of algorithms to choose from:

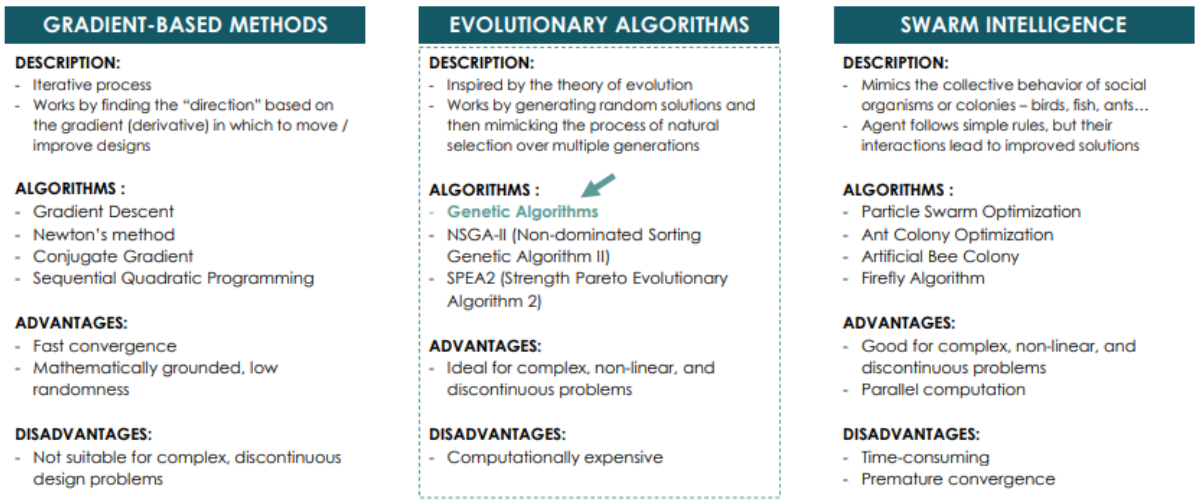

Figure 2-5 Optimization methods classification. Screenshot from Grasshopper optimization online workshop, Source: (HowToRhino, 2026)

A) Gradient-Based Optimization Methods:

Definition

Gradient-based optimization methods improve a solution by using derivative information of the objective function. At each iteration, the algorithm computes the gradient (and sometimes the Hessian) and moves the design variables in the direction that most rapidly decreases or increases the objective. Therefore, the objective function must be continuous, smooth and differentiable, so that its gradient can be evaluated and used to guide the search toward an optimum (Nocedal and Wright, 2006; Boyd and Vandenberghe, 2004).

It is suitable when:

- Smooth, continuous, differentiable problems
- Convex or Near Convex Optimization
- Problems where gradient information is available or can be computed
- Analytical or engineering systems with explicit mathematical formulations (Fletcher, 2013)

Advantages:

- Fast convergence in smooth and convex problems
- Low computational cost per iteration
- High reproducibility and strong theoretical background

Disadvantages:

- Not suitable for discontinuous, noisy, or Blackbox (simulation-based) objectives
- Prone to being trapped in local minimum in non-convex landscapes
- Requires explicit gradient information
- Sensitive to step-size and other algorithmic parameters

B) Evolutionary Algorithms (EAs)

Definition:

Evolutionary algorithms are population-based, stochastic optimization methods inspired by natural selection. A population of candidate solutions evolves over successive generations through selection, crossover and mutation, enabling robust exploration of complex, nonlinear and multi-modal search spaces without the need for gradient information (Deb, 2001; Bäck, Fogel and Michalewicz, 1997).

It is suitable when:

- Multi-objective optimization with conflicting objectives
- Nonlinear, non-differentiable or simulation-based problems
- Design spaces including both discrete and continuous variables
- Situations where global search and a Pareto front of trade-offs are required (Deb et al., 2002; Coello Coello, 2006)

Advantages:

- Do not require gradients or smooth objective functions
- Capable of handling discontinuities, noise and complex constraints
- Strong global search ability
- Naturally suited for multi-objective optimization and Pareto-front generation

Disadvantages:

- Computationally expensive due to many functions evaluations

- Slower convergence than gradient-based methods in smooth problems
- Performance depends on parameter choices (population size, mutation and crossover rates)
- Stochastic nature leads to variability between runs

C)Swarm Intelligence Methods:

Definition:

Swarm intelligence methods are population-based metaheuristics inspired by the collective behavior of social organisms such as bird flocks, fish schools and ant colonies. Individual agents update their positions according to simple rules that combine their own experience with information from neighbors, allowing the swarm to search the design space without gradient information (Kennedy and Eberhart, 1995; Dorigo and Stützle, 2004).

It is suitable when:

- Real-valued, continuous optimization problems
- Complex, nonlinear landscapes requiring global exploration
- Problems where gradients are unavailable or unreliable
- Applications where approximate global solutions are acceptable (Poli, Kennedy and Blackwell, 2007)

Advantages:

- Simple algorithmic structure and relatively few parameters
- Good global search capability
- Effective for medium- to high-dimensional continuous problems
- Straightforward to parallelize

Disadvantages:

- Risk of premature convergence to sub-optimal regions
- Sensitive to parameter tuning

- Less effective for highly constrained or purely discrete problems
- No formal guarantee of global optimality

2.1.1 (NSGA-II) Suitable Optimization Algorithms for Architectural Design Problems:

In multi-objective architectural optimization—particularly for problems involving energy use, daylight availability, glare mitigation, and thermal or visual comfort—the literature consistently indicates that multi-objective evolutionary algorithms (MOEAs) represent the most appropriate and widely validated class of optimization methods. Systematic reviews of building-performance optimization demonstrate that genetic-algorithm-based MOEAs, especially NSGA-II, appear far more frequently and deliver more reliable results compared to other metaheuristics, due to their ability to explore non-linear, simulation-based design spaces and to construct well-distributed Pareto fronts for conflicting objectives (Li et al., 2025; Izadi et al., 2023; Costa-Carrapiço et al., 2020). Their dominance is further supported by numerous architectural applications in façade and shading design, where NSGA-II has been successfully used to balance daylight, glare, energy consumption, and occupant comfort (Tang & Wang, 2025; Nazari et al., 2023). In contrast, gradient-based optimization is rarely applied in architectural contexts because performance metrics derived from simulation engines such as Radiance or EnergyPlus are typically non-differentiable, discontinuous, and nonlinear, preventing the computation of gradients and limiting these methods to analytical problems with smooth objective functions (Izadi et al., 2023). Swarm-intelligence algorithms, particularly multi-objective particle swarm optimization (MOPSO), have also been applied in building optimization and can achieve competitive results; however, reviews indicate that they remain less prevalent and are more sensitive to premature convergence and parameter tuning compared to MOEAs (Delgarm et al., 2016; Harshalatha et al., 2024). Overall, the current state of research demonstrates that MOEAs—especially NSGA-II and its variants—constitute the most robust, flexible, and empirically validated approach for multi-objective architectural optimization, while gradient-based methods are generally unsuitable and swarm-based approaches serve as secondary alternatives.

NSGA-II is an elitist, multi-objective evolutionary algorithm widely used for problems involving conflicting performance criteria. It improves earlier multi-objective genetic algorithms by introducing three key mechanisms: fast nondominated sorting, elitism, and crowding-distance-based diversity preservation. These features allow the algorithm to efficiently approximate a well-distributed and convergent Pareto front within a single optimization run. Also, it finds a better “spread” of solutions being well distributed along the Pareto front. You get more variety, more diverse trade-offs, and no big gaps between solutions while other algorithms often struggle to cover the whole Pareto curve evenly.

In multi-objective optimization, diversity of solutions is extremely important because you want a complete and evenly spaced Pareto front, not solutions clustered in a small part of it.

Deb is basically proving that NSGA-II:

- gives more diverse solutions
- gives higher-quality solutions
- gets closer to the true optimum
- works better than other top algorithms available at that time (Deb et al., 2002)

This is the main reason NSGA-II became the dominant MOEA in architecture, engineering, and simulation-based design.

2.1.2 NSGA-II optimization overall process:

A) Initialization

The algorithm begins with an initial population of size *N*, typically generated randomly within the defined design variable bounds. Each individual represents a candidate solution and is evaluated with respect to all objective functions.

B) Fast Nondominated Sorting

The population is sorted into multiple Pareto fronts according to the dominance relation:

- Front 1 consists of solutions that are not dominated by any other solution.
- Front 2 contains solutions dominated only by those in Front 1.
- This continues until all individuals are assigned to a front.

This sorting creates a hierarchical structure that reflects the quality of solutions across objectives.

C) Crowding Distance Calculation

Within each front, NSGA-II computes a crowding distance for every solution. Crowding distance measures how isolated a solution is in the objective space and is used to preserve diversity along the Pareto front.

Solutions with larger crowding distances are preferred because they help maintain a well-distributed set of trade-offs.

D) Selection (Binary Tournament):

Parents for reproduction are chosen using a crowded binary tournament selection:

1. A solution is preferred if it belongs to a better (lower-rank) Pareto front.
2. If both candidates are in the same front, the one with the larger crowding distance is selected.

This ensures that selection promotes both convergence (via nondominated rank) and diversity (via crowding distance).

E) Variation Operators:

Selected parents undergo genetic operators:

- **Crossover**: combines parent solutions to generate offspring.
- **Mutation**: introduces small random perturbations to maintain variation.

These operators produce a new offspring population of size *N*.

F) Elitist Population Update:

Elitism is the defining strength of NSGA-II. Parents and offspring are combined into a pool of size *2N*. Nondominated sorting is applied to the combined pool, producing Pareto fronts that include:

- high-quality solutions from the previous generation
- newly discovered solutions from offspring

Then the next generation is filled as follows:

- Entire fronts are added until adding the next full front would exceed size N.
- The remaining slots are filled by selecting individuals from the partially fitting front based on descending crowding distance.

This ensures:

- the best nondominated solutions are preserved
- diversity is maintained
- the population size remains fixed

G) Iteration and Termination

Steps B to F are repeated for a predetermined number of generations or until a convergence criterion is met. The final output approximates the Pareto-optimal front, representing diverse and high-quality trade-off solutions.

2.1.3 Optimization concepts and terminologies:

Generation:

One of many iterations where the old design variants are replaced by new solutions

Population:

Multiple design variations in a given iteration, that will evolve over time

Fitness and Fitness Objectives:

In optimization theory, the fitness of a solution represents a numerical evaluation of its quality with respect to one or more predefined objective functions. Each objective quantifies a specific performance criterion (e.g., energy consumption, daylight availability, thermal comfort), and the fitness value expresses how well a candidate solution satisfies these criteria. Because different objectives often conflict, solutions cannot be ranked with a single metric. Instead, their fitness vectors are compared through Pareto dominance, which is the basis for nondominated sorting and the construction of the Pareto front.

In evolutionary algorithms, the fitness values determine:

- How solutions are ranked
- which solutions are selected for reproduction
- how the algorithm moves through the search space
- How the Pareto front evolves generation by generation

Fitness Landscape:

The concept of a fitness landscape provides an abstract framework for understanding how the quality of solutions varies across the search space of an optimization problem. Each point in the search space corresponds to a particular configuration of decision variables, and the associated fitness value expresses how well that configuration satisfies the defined objective(s) (Deb, 2001). The landscape metaphor originates from evolutionary biology and complex systems theory, where it is used to describe how populations evolve across environments composed of peaks, valleys, and ridges (Kauffman, 1993).

Landscape Topologies:

The topology of a fitness landscape describes how fitness values change across the search domain. Certain topological features make optimization easier or harder, and thus strongly influence the performance of optimization algorithms.

Smooth Landscapes: Smooth landscapes exhibit gradual, predictable changes in fitness; small variations in design variables lead to correspondingly small changes in objective values. These landscapes are typical of convex or near-convex problems and are well-suited to gradient-based methods, which rely on local derivative information to navigate toward optimal regions (Deb, 2001).

Rugged Landscapes: Rugged landscapes contain many local optima, steep gradients, and irregular topological features (Kauffman, 1993). Such landscapes arise frequently in nonlinear, simulation-based architectural performance problems, where interactions between geometry, material properties, and environmental context produce highly complex relationships. Ruggedness complicates the optimization process because local search algorithms can become trapped in suboptimal regions (Jones, 1995).

Multimodal Landscapes: A multimodal landscape contains multiple peaks (local maxima or minima), each representing different high-quality solutions. This topology increases problem difficulty, requiring algorithms that can explore several regions simultaneously. Population-based algorithms such as evolutionary algorithms and swarm methods are more effective in these contexts because they maintain diversity and can escape local optima (Jones, 1995; Coello Coello et al., 2007).

Nondominated Sorting (Conceptual Explanation):

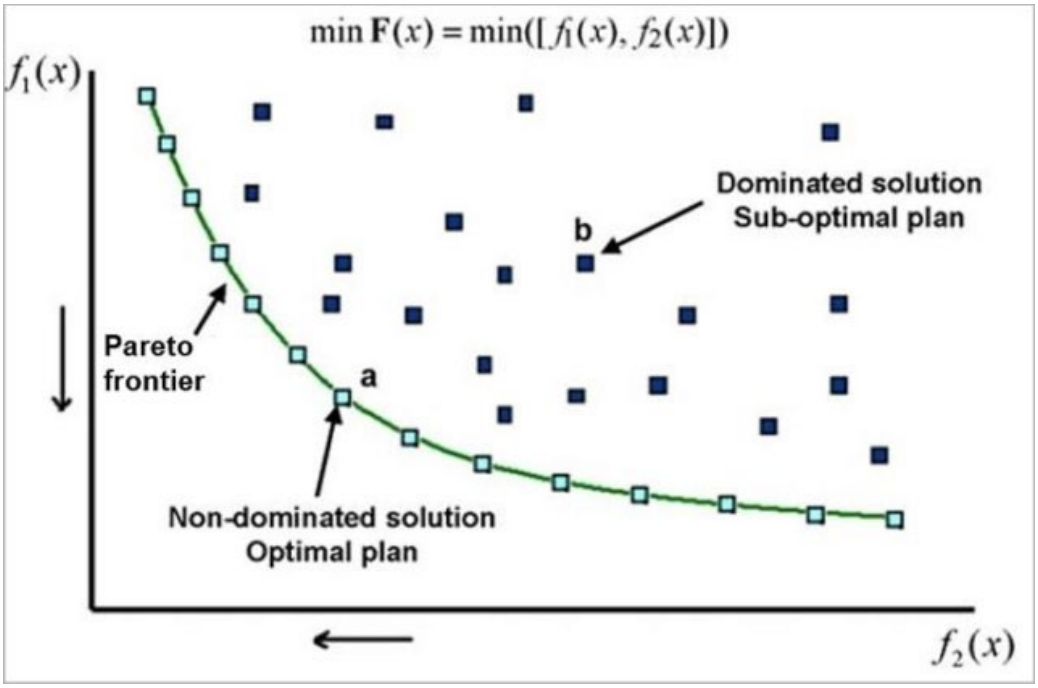

Figure 2-6 Example of a Pareto frontier for a multi-objective optimization problem with two objective functions. Source: (D. Somma, 2016).

In multi-objective optimization, a solution is evaluated on multiple (some of which conflicting) objectives (e.g., maximize daylight, minimize glare and minimize energy). There is no single best solution, because improving one objective can worsen another. So instead of ranking solutions with one score, we compare them using Pareto dominance. Using this rule, the population can be grouped into layers:

- Pareto Front 1 = solutions not dominated by any other
- Pareto Front 2 = dominated only by front 1 solutions
- Pareto Front 3, etc.

This layering process is called nondominated sorting. The Pareto front is the set of the best trade-off solutions in a multi-objective problem. No solution on this front is strictly better than another — each represents a different compromise.

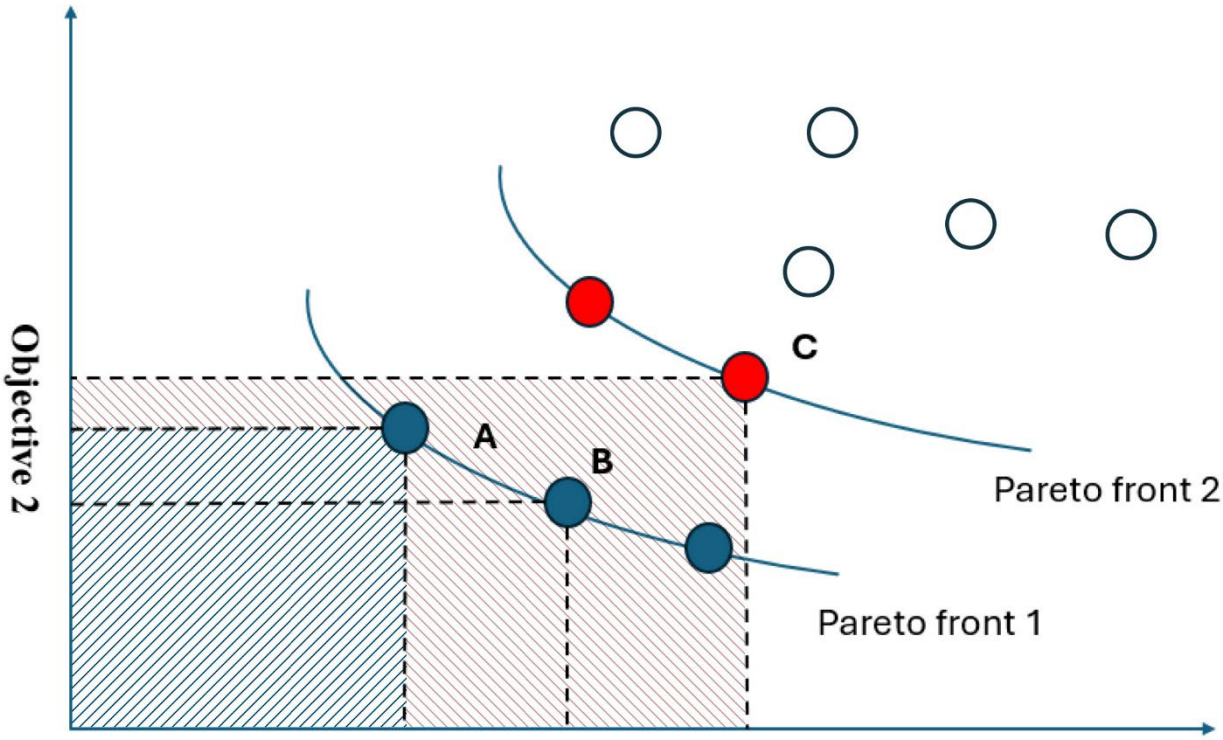

Figure 2-7 Set of objective space solutions for objective functions $f1$, $f2$ along with A, B, and C solutions. Source: Kesireddy and Medrano (2024).

in the example shown in figure 2-8 a solution **X dominates Y** if:

1. X is **no worse** in all objectives, **AND**
2. X is **better** with at least one objective.

So, in such example with only 2 goals (which demand only a 2D visualization graph), we need to look at the relative positions:

- **Downward & leftward** = *better in both objectives* (if both are minimization)
- **Upward & rightward** = *worse in both*

✓ Pareto Front 1 (blue points):

These points (A, B, etc.) are the best and non-dominated by anyone. If we draw downward and leftward lines, no other solution exists in the region (blue slanted hatch). And in reverse, if we draw upward and rightward lines in there, the solutions existing in the region are dominated and cannot be a member of the pareto front.

Also point C, for example, is not a pareto front because in its drawn region (red slanted hatch) some other solutions exist.

✓ Pareto Front 2 (red points):

We exclude the solutions in ParetoFront1 and do the sorting again to find Pareto 2. These are only dominated by some points in Front 1.

Now specifically B and C:

Point B (blue, Front 1):

→ belongs to the non-dominated (Pareto optimal) set
→ It is not dominated by any point, including C.

Point C (red, Front 2):

→ is dominated by some point(s) on Front 1
→ including possibly B or others

Therefore, the correct terminology is B is NON-dominating (nondominated)

Because B is on Pareto Front 1, meaning no one dominates it, and C is dominated.

2.1.4 After optimization; visualization, graphs and interpretations:

The standard deviation (SD) of fitness values:

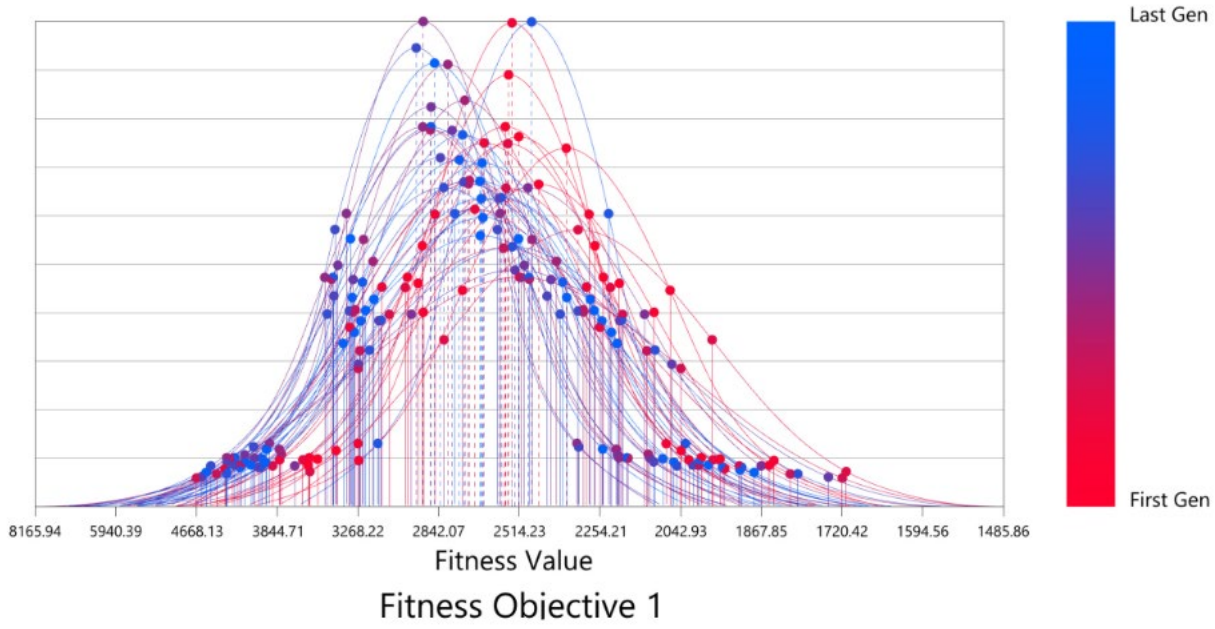

Figure 2-8 SD graph example. Source: Showkatbakhsh et al. (2018).

Description: In a NSGA-II based such as wallacei in grasshopper, the Standard Deviation (SD) (calculated using the equation below) chart calculates the SD for each generation in the population and plots each generation to 3 SD values on either side of the mean. In this example the generations are colored from red (first generation) to blue (last generation).

Aim: The standard deviation represents the distribution of a set of values from the mean. SD measures spread in fitness, not the fitness value itself. A low standard deviation factor indicates that most values are clustered around the mean (less variation within the population), while a high standard deviation factor indicates that the values are spread farther from the mean (more variation within the population). The aim of the chart is to present and analyze the levels of variation/convergence for each generation in the population, as well as whether the generations are getting fitter throughout the simulation. Increased variation is represented through a 'flat' curve, while increased convergence is represented through a 'narrow' curve. A shift in the curve to the left indicates better mean performance.

In population-based optimization methods—such as evolutionary algorithms or swarm Intelligence, the SD value trend line graph refers to a plot that tracks the standard deviation (SD) of the population's fitness values across generations. The standard deviation represents the spread, diversity, or variance of solutions in the population at each iteration of the algorithm (Showkatbakhsh et al., 2018).

Monitoring SD over time provides insight into:

- how broadly the algorithm is exploring the search space,
- whether the population is converging toward optima, and
- how stable or unstable the search dynamics are.

The SD trend reflects how the population spreads or contracts across the search space. During the early and middle generations, a bell-shaped SD curve is often desirable, as it indicates initial exploration followed by expansion of diversity and subsequent controlled convergence. In later generations, the SD is expected to decline gradually as the population becomes more homogeneous and increasingly concentrated around high-fitness regions. This gradual reduction may eventually form a narrow (sharp) SD profile, reflecting stable convergence rather than premature collapse (Deb, 2001; Jones, 1995; Coello Coello et al., 2007).

So as optimization progresses, a left shift means that fitness variability decreases from both sides — the "worst" solutions get better, and the "best" solutions become dominant. A leftward movement of the SD curve means that both ends of the SD distribution (minimum SD and maximum SD values) shift toward lower SD values as the optimization proceeds. This is interpreted as Convergence toward high-fitness regions of the search space. (Deb, 2001; Jones, 1995; Coello Coello et al., 2007).

At each generation t, the standard deviation of the fitness values across all individuals is computed as:

$$SD(t) = \sqrt{\frac{1}{N}\sum_{i=1}^{N}\left(f_i(t) - \bar{f}(t)\right)^2}$$

Where:

- N = population size,
- $fi\ (t)$ = fitness of the $i\text{-}th$ individual at generation t,
- $\bar{f}\ (t)$ = mean fitness at generation t.

Plotting SD(t)SD(t) against iteration number produces a trend line that reveals how the population's dispersion in the fitness landscape evolves over the course of optimization.

A sharp decline in SD indicates rapid convergence toward a narrow region of the fitness landscape, whereas persistent high SD suggests continued exploration of diverse regions, characteristic of problems with rugged or multimodal fitness landscapes.

This graph is frequently used to diagnose algorithmic behavior, detect premature convergence, and assess the balance between exploration and exploitation in evolutionary processes (Deb, 2001; Coello Coello et al., 2007; Jones, 1995).

SD mean-value trendline:

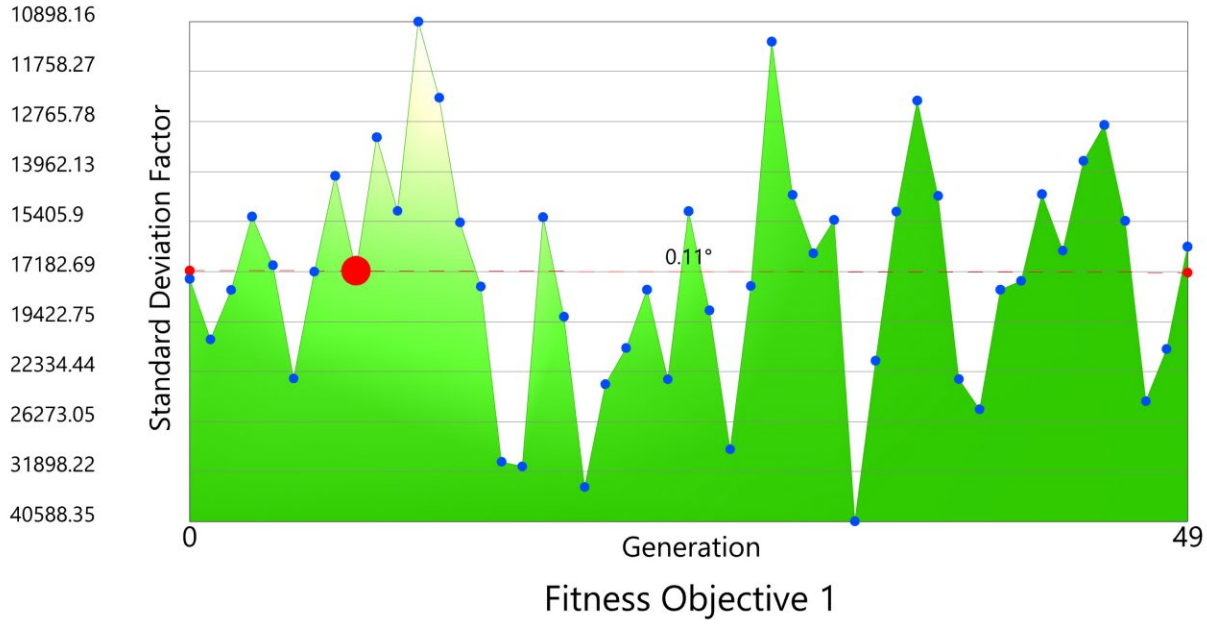

Figure 2-9 SD mean-value trendline chart example. Source: Showkatbakhsh et al. (2018).

Description: The standard deviation (SD) trendline chart calculates the SD value for each generation in the population and displays each value as a point from left (first generation) to right (last generation). A surface is created from the plotted points to better visualize the results.

Aim: The Standard Deviation Trendline Chart presents the standard deviation value, for each fitness objective independently, for each generation across the entire simulation from start to finish. The aim is to highlight specific trends in the variation and/or convergence of each generation across the population (Showkatbakhsh et al., 2018).

It is used to evaluate the evolutionary behavior of the population during the optimization process. Specifically, it helps to interpret:

- Population diversity within each generation and summarizes fitness dispersion across multiple objectives.
- Higher SD mean → strong exploration across competing objectives.
- Lower SD mean → the population converges toward the Pareto front.
- Convergence behavior of the algorithm over time
- The balance between exploration (diverse solutions) and exploitation (refinement of fit solutions)

A moderate SD mean is typically desirable in NSGA-II, showing a balance between exploration and exploitation (Deb, 2001). High SD values indicate a wide dispersion of solutions, meaning the algorithm is still exploring the search space. Decreasing and stabilizing SD values indicate convergence, where solutions cluster around similar fitness values.

When interpreted together with mean fitness trendlines, the SD trendline allows verification that improvements in fitness are accompanied by stable and controlled convergence, rather than premature collapse or random behavior.

Formally, if *SD(t)SD*(*t*) is the standard deviation of fitness values at generation *t*, then the SD mean over T generations is:

$$\overline{SD} = \frac{1}{T}\sum_{t=1}^{T} SD(t)$$

Mean fitness trendline:

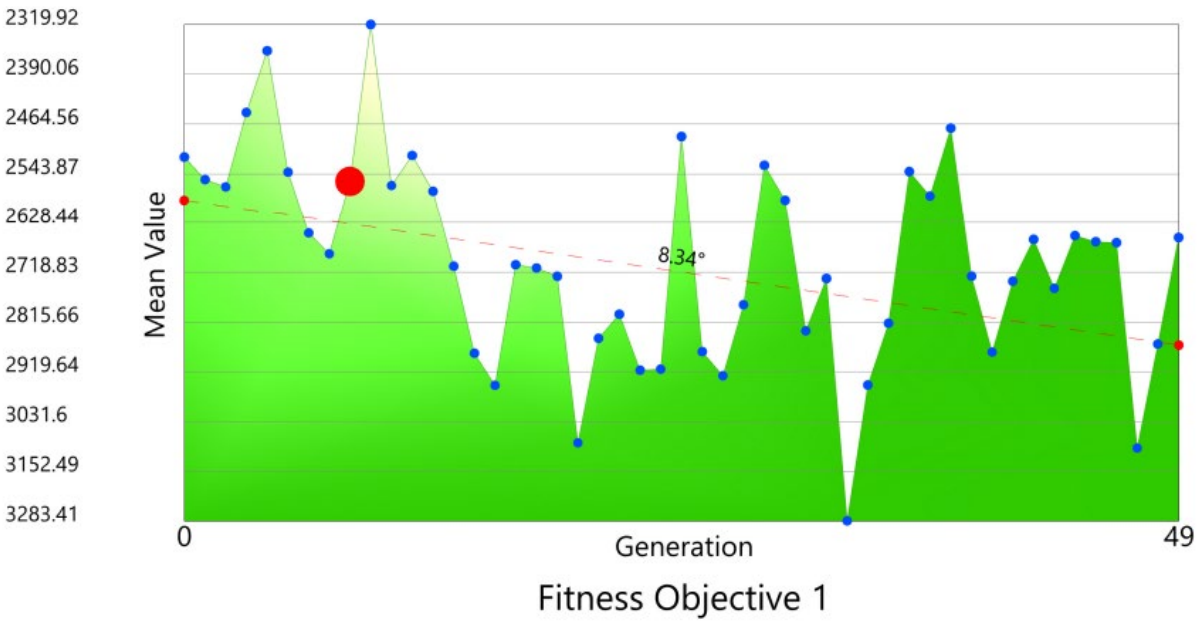

Figure 2-10 Mean Fitness trendline chart example. Source: Showkatbakhsh et al. (2018).

Description: The mean fitness trendline chart calculates the mean fitness value for each generation in the population and displays each value as a point from left (first generation) to right (last generation). A surface is created from the plotted points to better visualize the results.

Aim: The Mean Fitness Trendline Chart presents the mean fitness value, for each fitness objective independently, for each generation across the entire simulation from start to finish. The aim is to highlight specific trends in the mean fitness value of each generation across the population (Showkatbakhsh et al., 2018).

Fitness value:

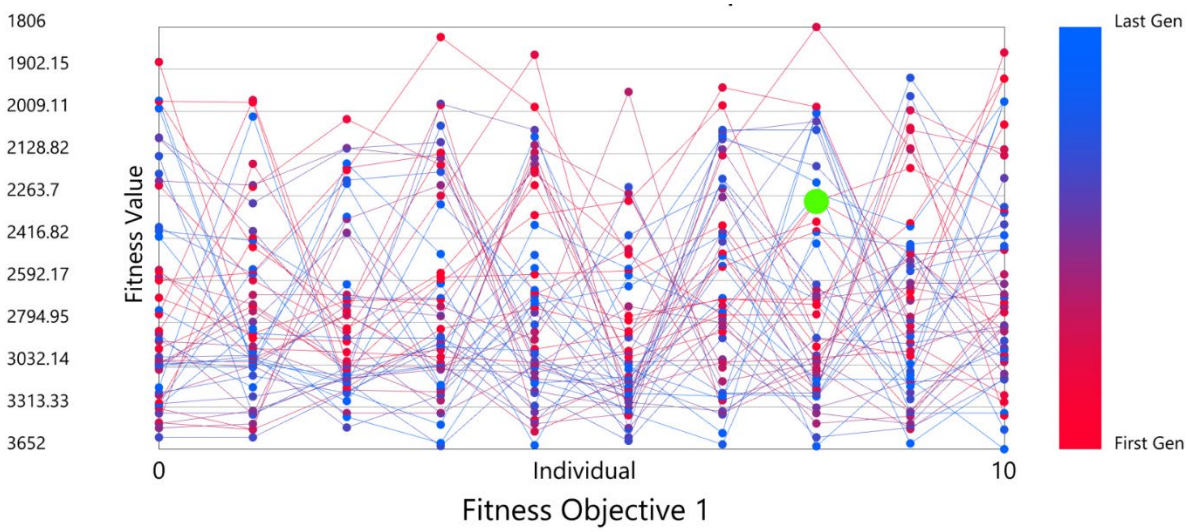

Figure 2-11 Fitness Value chart example. Source: Showkatbakhsh et al. (2018).

Description: The FV Chart (Fitness Values Chart) displays the fitness values for each solution in the population for each fitness objective independently. The solutions are displayed per generation from left to right (first point on the y-axis is the first solution in a generation, and the last point on the y-axis is the last solution in the same generation). Each generation relates to a polyline, and the generations are colored from first (red) to last (blue).

Aim: The Fitness Values chart analyses the fitness values for each fitness objective independently across the entire population. The aim is to visualize how the solutions are performing in relation to one another, both within each generation and across the population (Showkatbakhsh et al., 2018).

Parallel Coordinate plot:

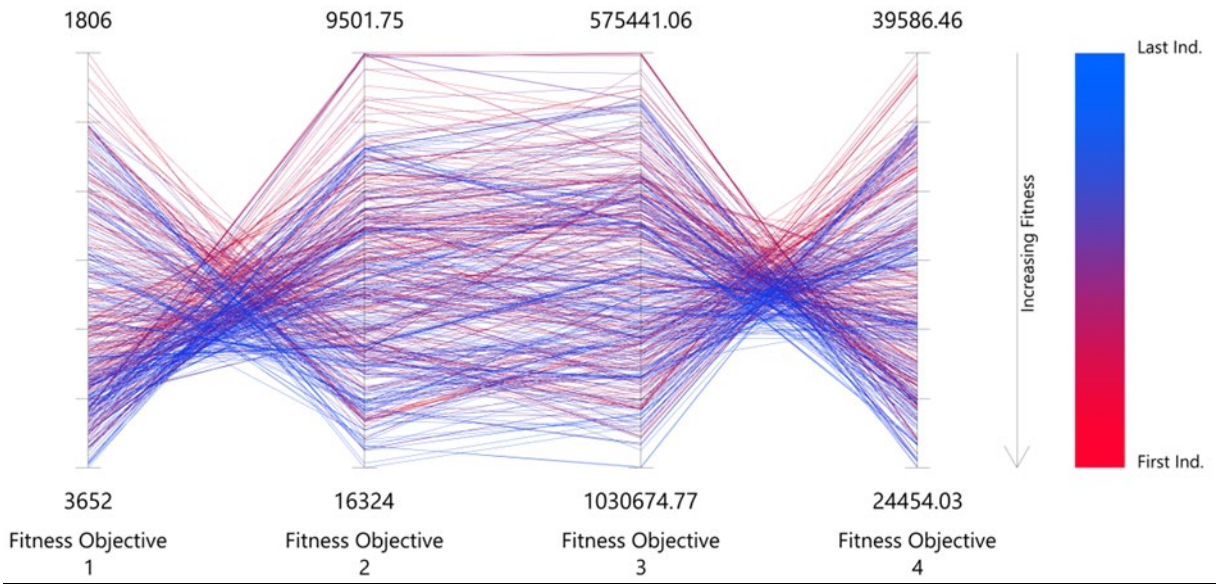

Figure 2-12 Parallel coordinate plot example. Source: Showkatbakhsh et al. (2018).

Description: In the PCP, each fitness objective is attributed to a y-axis, in which the first objective is the left most y-axis, and the last objective is the right most y-axis. However, users can manually control which axis displays which objective through the 'order fitness criteria' input.

Aim: The parallel coordinate plot (PCP) analyses all the solutions in the population through comparing the fitness values for each solution across all fitness objectives. The aim is to extract emergent behaviour exhibited by the simulation and better understand how the solutions are optimising throughout the simulation. The Parallel coordinate plot analysis component (PCP-A) provides the user with 4 methods of analysis of all solutions in the population (Showkatbakhsh et al., 2018).

Diamond fitness chart:

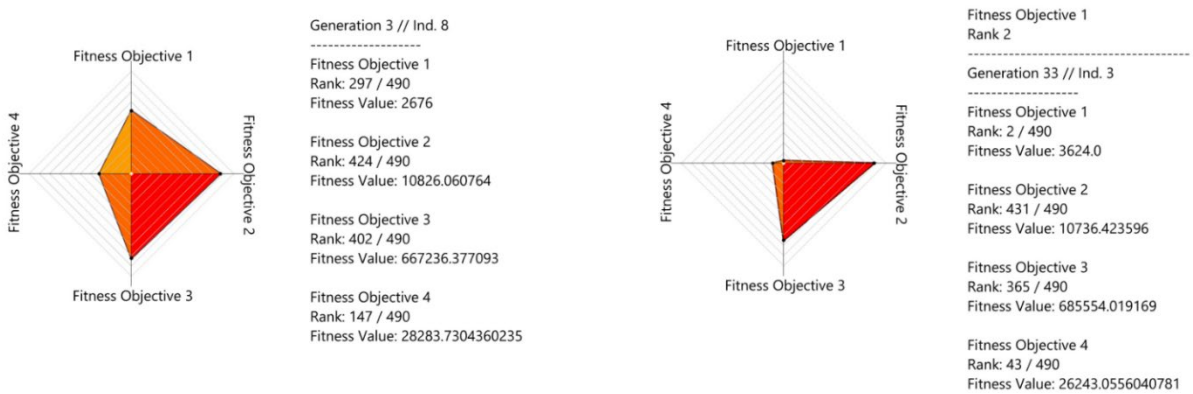

Figure 2-13 The Diamond fitness Chart Example. Source: Showkatbakhsh et al. (2018).

Aim: The Diamond fitness Chart (sometimes referred to as the ‘star coordinate method’) analyses the fitness values of a single solution (as opposed to the population wide analysis conducted in previous components). The aim is for the user to better understand how a single solution performs by comparing the fitness values and ranking for each of its fitness objectives.

Description: The diamond fitness chart can be used through two distinct methods:

1) Selection by generation and solution number.

2) Selection by fitness objective and rank

Objective Space:

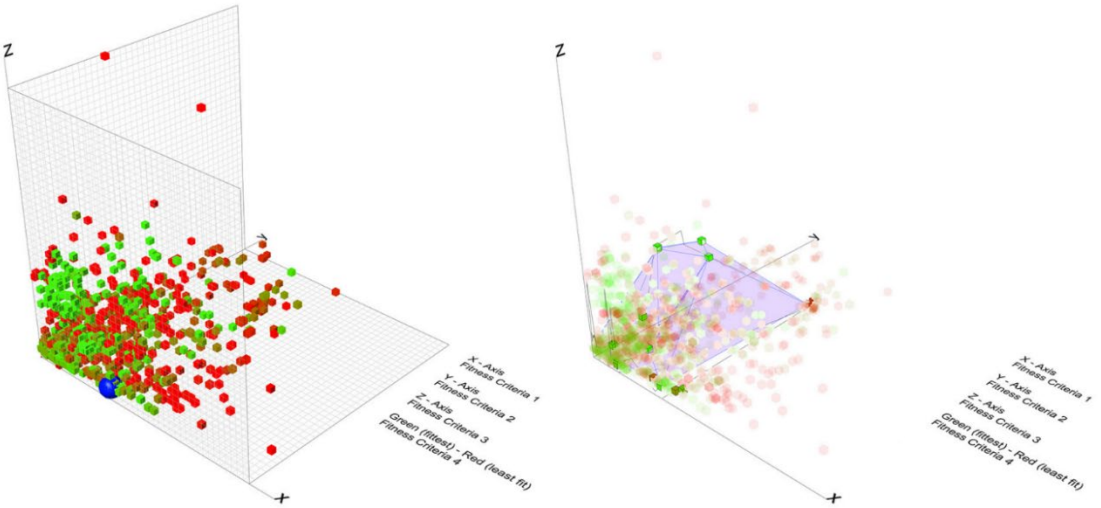

Figure 2-14 example of demonstration of an objective space with 3 objectives. Source: Showkatbakhsh et al. (2018).

Aim: The ‘Objective Space’ (OS) and ‘Pareto Front’ (PF) components go hand in hand and are recommended to be used together. Although the OS component can be used on its own, the PF component will require the output values from the OS component to function. The OS component displays the objective space for all the solutions in the population (as opposed to only one generation in the population). The PF component calculates the pareto front for any generation in the population.

Description: The Objective space component remaps the fitness values output by the simulation and assigns a distinct axis for each objective. Fitness objectives 1, 2 and 3 are displayed on the X, Y and Z axes respectively. Fitness objective 4 is displayed through color (Green (fittest) to Red (least fit)), while fitness objective 5 is represented through the scale of the cubes in the objective space (large (fittest) to small (least fit)).

2.2 Energy and daylight analysis theory

In contemporary building design, façade performance is understood as a multi-dimensional system rather than a passive envelope. Through its geometry, material properties, and shading configuration, the facade mediates energy exchange, daylight penetration, and visual comfort, regulating the interaction between outdoor climatic conditions and indoor environmental quality.

Energy performance is a fundamental aspect of façade design, as the building envelope directly controls heat transfer, solar gains, and operational energy demand. In facade-oriented studies, energy efficiency is commonly evaluated using indicators such as Energy Use Intensity (EUI), heating and cooling demand, and facade-related thermal loads, which together reflect the impact of envelope design decisions on overall building performance (Crawley et al., 2008). While EUI enables comparison between design scenarios, façade-focused analyses typically disaggregate energy use into heating, cooling, and solar gains to better capture the mechanisms through which façade parameters influence energy demand (Crawley et al., 2001). Key design variables, including window-to-wall ratio, glazing properties, and shading geometry, have been shown to significantly affect energy performance in a climate- and orientation-dependent manner (Tzempelikos and Athienitis, 2007; Carroll et al., 2020). In retrofit contexts, where design flexibility is limited, targeted façade interventions such as glazing upgrades and shading systems can still deliver meaningful energy savings (Pomponi et al., 2016). Collectively, these findings demonstrate that façade energy performance cannot be represented by a single indicator, but instead requires a multi-metric, simulation-based assessment approach.

Beyond energy, the facade plays a central role in regulating daylight availability by controlling both the quantity and spatial distribution of natural light. Although increased façade transparency can enhance daylight penetration, the relationship between glazing area and useful daylight is non-linear and highly climate-dependent, making climate-based evaluation essential (Ochoa et al., 2012). Façade design also strongly influences visual comfort, as excessive solar penetration and high luminance contrasts can lead to discomfort glare even in spaces with adequate daylight levels. Accordingly, daylight availability and glare must be assessed concurrently, since improvements in daylight do not necessarily mitigate glare risk (Reinhart and Wienold, 2011).

Energy performance, daylight availability, and visual comfort are therefore characterized by inherent trade-offs. Strategies that maximize daylight may increase cooling demand and glare risk, while measures aimed at limiting solar gains can reduce daylight quality and increase reliance on artificial lighting (Tzempelikos and Athienitis, 2007; Ochoa et al., 2012). These interactions position the facade as a multi-objective system that necessitates integrated, performance-driven assessment approaches.

In response to this complexity, daylight evaluation has increasingly shifted toward climate-based metrics that capture temporal and spatial variability under real sky conditions. Metrics such as Daylight Autonomy (DA) and spatial Daylight Autonomy (sDA) enable annual assessment of daylight sufficiency, while Useful Daylight Illuminance (UDI) further distinguishes between insufficient, useful, and excessive daylight levels by introducing upper illuminance thresholds relevant to occupant comfort (Reinhart et al., 2006; Nabil and Mardaljevic, 2005). However, daylight sufficiency alone does not guarantee visual comfort.To address this limitation, glare is commonly evaluated using metrics such as Daylight Glare Probability (DGP), Daylight Glare Index (DGI), and Unified Glare Rating (UGR). Among these, DGP is particularly suitable for daylight analysis, as it accounts for eye-level illuminance and luminance distribution and has been shown to provide more reliable predictions of perceived glare under dynamic daylight conditions (Wienold and Christoffersen, 2006). The persistent conflict between daylight sufficiency and glare risk reinforces the need for integrated assessment frameworks that jointly evaluate daylight availability and visual comfort.

2.3 **Tool Selection and Rationale**

A wide range of simulation tools are available for evaluating building energy performance, daylight availability, and visual comfort. These tools vary in terms of physical accuracy, level of abstraction, and integration with design workflows. In performance-driven architectural research, they are commonly classified into core simulation engines, graphical user interfaces, and parametric design plugins.

Core simulation engines constitute the computational backbone of environmental performance analysis, offering high physical accuracy but limited direct accessibility for design exploration.

Among these, Energy Plus is the most widely adopted dynamic engine for whole-building energy and thermal simulation and is regarded as a reference standard due to its rigorous physical formulation and extensive validation (Crawley et al., 2001; Crawley et al., 2008). However, its lack of native daylight and glare modelling restricts its ability to represent façade performance holistically.

Other research-oriented engines such as TRNSYS and ESP-r provide high modelling flexibility at the system level but are characterized by increased complexity and reduced usability within design-driven workflows (Clarke, 2001; Klein et al., 2017). DOE-2, while historically influential, is now largely considered a legacy engine with limited relevance to contemporary performance analysis (DOE, 1980).

For daylight and visual comfort assessment, Radiance represents the benchmark physically based lighting simulation engine, enabling accurate computation of illuminance and luminance distributions while accounting for complex geometry and material properties (Ward, 1994). Despite its accuracy, Radiance operates independently of thermal simulation engines, limiting its use in integrated energy–daylight studies without external coupling frameworks.

Graphical user interfaces provide more accessible access to core engines by simplifying model setup and result interpretation. Open Studio and Design Builder facilitate structured interaction with Energy Plus but often abstract underlying modelling assumptions, reducing transparency for research-oriented applications (NREL, 2023; Design Builder Software Ltd., 2023). IES VE and IDA ICE offer integrated environments for energy and thermal analysis, yet their closed or semi-closed ecosystems constrain parametric and optimization-based investigations (IES Ltd., 2023; Equa Simulation AB, 2023).

For early-stage design, tools such as eQUEST, Sefaira, and Cove. tool prioritize rapid feedback and usability through simplified modelling approaches, making them suitable for preliminary decision-making but inadequate for detailed, performance-driven research (Hirsch, 2016; Sefaira Inc., 2023; Cove.tool Inc., 2023). In the domain of daylight analysis, Radiance-based interfaces such as Climate Studio and DIVA for Rhino improve accessibility while retaining physical accuracy, with DIVA offering

greater transparency and control for academic research (Jakubiec and Reinhart, 2011; Solemma LLC, 2023).

Simplified tools such as VELUX Daylight Visualizer and DIALux evo are commonly used in professional practice but lack the analytical depth required for advanced façade performance studies (Velux Group, 2023; Dial GmbH, 2023).

The built-in grasshopper component named Galapagos is designed for single-objective purposes and adding all the fitness objects to give it to the only fitness input of Galapagos suppresses many information and we will not be able to distinguish the results in its output to get acceptable feedback by the graphs. Because in single-objective optimization by prioritizing a single criterion—such as minimizing energy consumption—these approaches fail to reflect the multi-dimensional character of façade performance and often produce biased solutions that overlook critical trade-offs between energy efficiency and indoor environmental quality (Nguyen et al., 2014).

Octopus plugin is based on SPEA-2 and HypE algorithms and is best for quickly identifying the best possible combinations of performance across several metrics.

Wallacei is another plugin based on the NSGA-2 algorithm (Deb et. al., 2001) as the primary evolutionary algorithm and is best for Gaining insights, seeing trends, and understanding the 'why' behind the optimization so was used in this thesis for our multi-objective optimization.

Tool	Advantages	Limitations
Energy Plus	High physical accuracy; dynamic whole-building energy and thermal simulation; extensively validated and widely accepted as a reference standard in research and practice.	No native daylight or glare modelling; limited ability to represent façade performance holistically without coupling to external tools.
TRNSYS	High flexibility for system-level and research-oriented energy modelling.	High complexity and reduced usability within design-driven workflows.
ESP-r	Detailed modelling of thermal, energy, and airflow interactions with strong research foundations.	Steep learning curve and limited accessibility for iterative design exploration.

DOE-2	Historically influential; foundational to many later energy analysis tools.	Considered a legacy engine with limited relevance to contemporary performance analysis.
Radiance	Benchmark engine for physically based daylight and glare simulation; high accuracy in luminance and illuminance calculations.	Operates independently of thermal simulation engines; limited support for integrated energy–daylight analysis without coupling frameworks.
Open Studio	Structured access to Energy Plus supports automation and parametric studies.	Primarily energy-focused; abstraction of modelling assumptions reduces transparency for research.
Design Builder	User-friendly interface for geometry, constructions, and HVAC modelling; widely used in academia and practice.	Reduced control over underlying assumptions; limited flexibility for advanced parametric exploration.
IES VE	Integrated analysis of energy, daylight, airflow, and compliance within a single environment.	Closed ecosystem limits transparency and optimization-oriented research workflows.
IDA ICE	High-fidelity dynamic thermal and HVAC simulation.	Weak integration with parametric and optimization-based design workflows.
eQUEST	Rapid feedback and ease of use for early-stage design decisions.	Simplified modelling assumptions; inadequate for detailed, performance-driven research.
Sefaira	Fast, usability-oriented feedback for conceptual design stages.	Limited control over assumptions and insufficient accuracy for advanced research applications.
Cove.tool	Efficient exploration of early-stage energy scenarios.	Unsuitable for detailed and transparent performance analysis.
Climate Studio	Streamlined access to Radiance; fast evaluation of climate-based daylight and glare metrics.	Less transparent and configurable than direct Radiance-based research workflows.
DIVA for Rhino	Greater transparency and control over Radiance simulations; widely adopted in academic research.	More complex and time-consuming workflows compared to simplified GUIs.

VELUX Daylight Visualizer	Simple and fast daylight visualization for professional practice.	Lacks analytical depth for performance-driven daylight research.
DIA Lux evo	Effective for electric lighting design in professional contexts.	Not suitable for advanced daylight or façade performance analysis.
Galapagos	Simple implementation of single-objective evolutionary optimization within Grasshopper.	Aggregation of multiple objectives suppresses information and obscures trade-offs; unsuitable for multi-dimensional façade optimization.
Octopus	SPEA-2 and HypE-based; effective for rapid identification of high-performing solution sets across multiple criteria.	Primarily exploratory; limited support for in-depth post-analysis and interpretability.
Wallacei	NSGA-II-based; strong support for understanding trends, trade-offs, and optimization behavior; well suited to research-driven multi-objective studies	Higher computational cost and analysis overhead compared to simpler optimization solvers.

Table 2-1 Comparative overview of simulation and optimization tools used in building performance

Based on the comparative evaluation of available tools and their respective advantages and limitations, this research adopts a transparent parametric workflow that enables integrated performance assessment and multi-objective optimization of the building façade. Grasshopper is used as the primary parametric modelling platform, with Ladybug and Honeybee providing direct links between the geometric model and validated simulation engines. Building energy performance is simulated using EnergyPlus, while daylight availability and glare are assessed through Honeybee's Radiance-based simulation workflow, without reliance on simplified or closed graphical interfaces. OpenStudio is employed as the standard execution framework for EnergyPlus simulations. To support multi-objective optimization and explicitly capture trade-offs between energy efficiency and indoor environmental quality, the NSGA-II evolutionary algorithm is implemented via Wallacei. This integrated tool chain ensures physical accuracy, methodological transparency, and reproducibility, which are essential for performance-driven academic research.

03

ARTICLE REVIEW

3.1 Article 1:

“Parametric Design and Comfort Optimization of Dynamic Shading Structures”

(Doris A. Chi *, Edwin González M. *, Renato Valdivia and Eduardo Gutiérrez J.)

Location | Malecón Cancún Tajamar, Mexico

Published | May 2021

3.1.1 Introduction

This case study investigates the optimization of dynamic, adaptive urban shading structures designed for open public spaces, with a specific focus on improving outdoor thermal comfort.

Outdoor thermal comfort is evaluated using the Universal Thermal Climate Index (UTCI), selected for its physiological accuracy and broad climatic validation. The optimization process, implemented through the NSGA-II algorithm in Wallacei X, simultaneously seeks to minimize thermal stress and maximize shaded area, producing a set of Pareto-optimal solutions.

3.1.2 Methodology

The proposed workflow includes four steps: (1) geometric modelling by parametric modelling tools; (2) simulation of environmental parameters by using BPS tools; (3) shape optimization by using an evolutionary algorithm; and (4) environmental verification of the results.

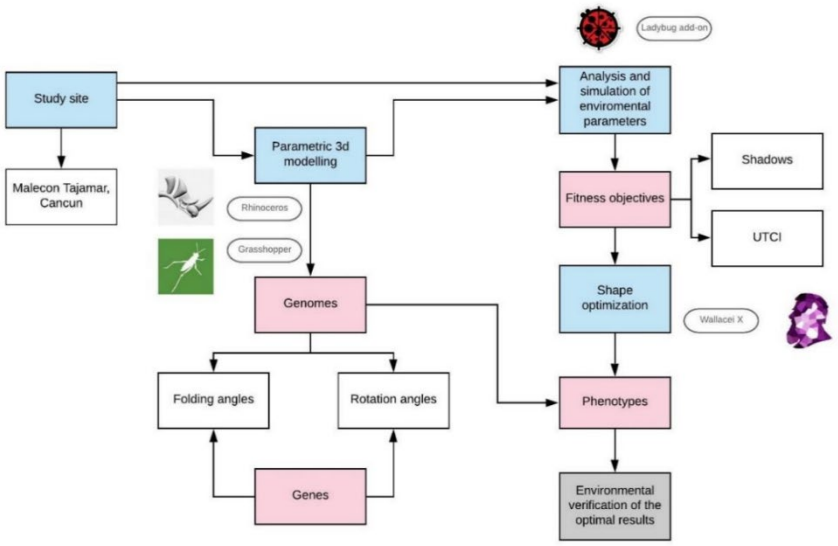

Figure 3-1 Workflow is used for optimization of dynamic shadings. Source: Chi et al. (2021)

Parametric Modelling of the Dynamic Shading Structures: (Figure 3-2)

Modeled using triangular folding modules and a central rotational axis, enabling adaptable geometric transformations that respond to changing sun positions throughout the year.

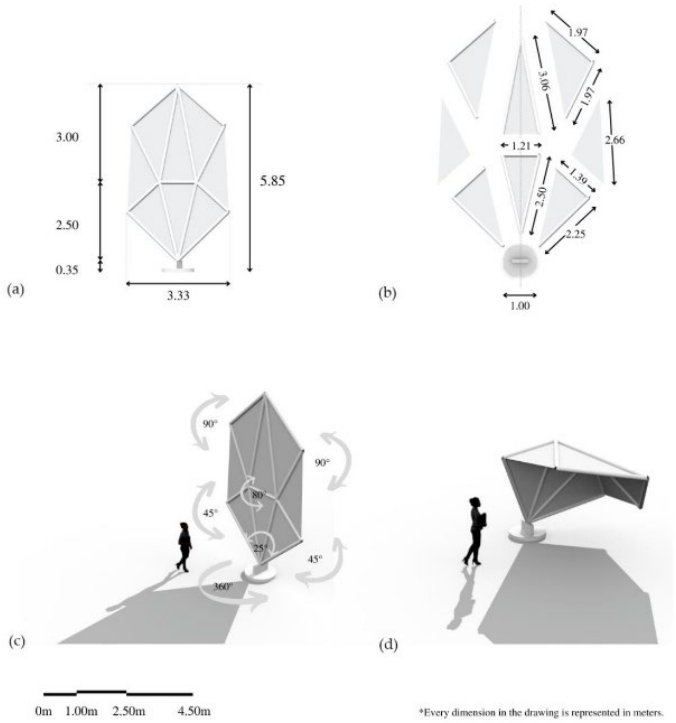

Figure 3-2 Dynamic shadings: (a) dimensions of the shading structure, (b) dimensions of the component units, (c) genes: folding and rotational axes, and (d) perspective view. Source: Chi et al. (2021)

Simulation of Environmental Parameters (Figure 3-3)

Representative days and hours (21 June and 21 December at 08:00, 12:00, and 16:00) are selected to capture seasonal and daily variations in solar exposure. Outdoor thermal comfort is evaluated using UTCI, with acceptable stress categories defined based on adaptive comfort considerations for warm–humid climates. UTCI calculations incorporate solar-adjusted mean radiant temperature, derived through Radiance-based simulations, while shaded areas are quantified at pedestrian using sun-path and shadow-projection analysis.

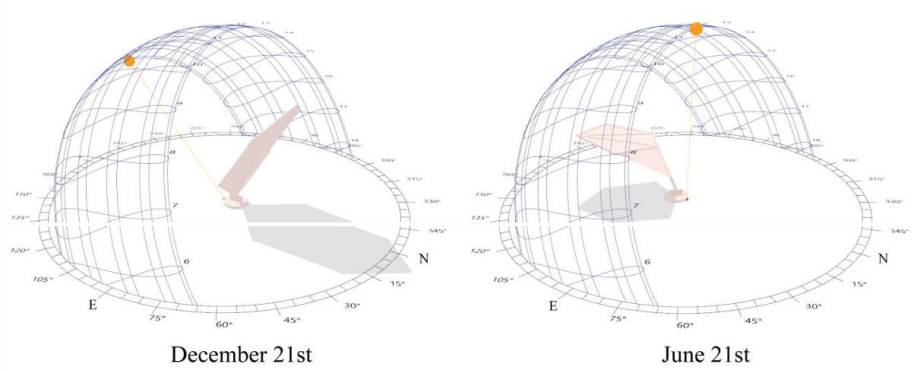

Figure 3-3 Example of shadings positions according to the sun trajectories in Cancun, Mexico, at 12 h Source: Chi et al. (2021)

Shape Optimization with Evolutionary Algorithms:

- A Multi objective evolutionary optimization is conducted using the NSGA-II algorithm through the Wallacei X plugin (Figure 3-4)
- Folding angles of the shading elements and rotational angles of the shading modules are the parameters that define the geometric behavior of each shading configuration
- Fitness objectives are maximizing the shaded area within a 144 m² ground area and minimizing the UTCI (°C) within the shaded area

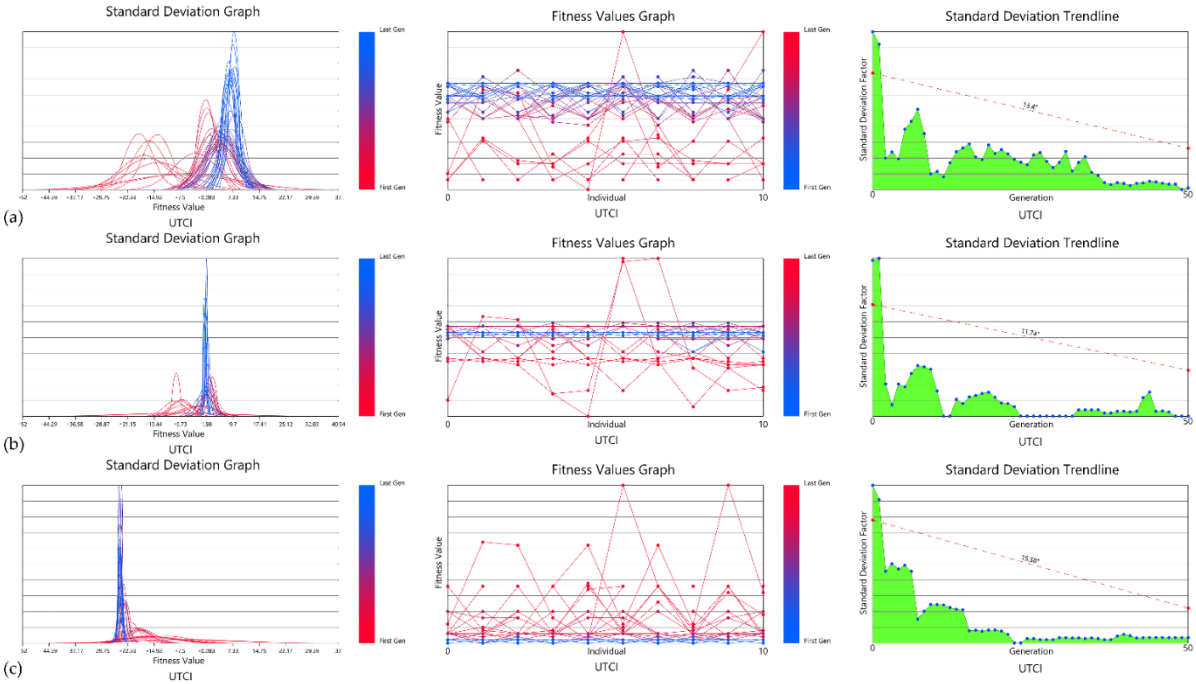

Figure 3-4 Second exercise with a population of 500 genomes. UTCI optimization graphs for 21 June: (a) 8 h, (b) 12 h, and (c) 16 h. Source: Chi et al. (2021)

Environmental Verification of Optimal Solutions: (Figure 3-5)

Following the optimization using Wallacei X, the best-ranked genomes according to each fitness objective (at the specific times studied) were chosen from the entire population of the Pareto Front solutions (phenotypes). Their specific genes were identified to test the shadings' performance, and 3D shading replications were modelled with the genes' information to further run environmental simulations with Ladybug as illustrated in Figure 3-6.The shadings were re-simulated using Ladybug Tools, with the aim of comparing the obtained results (shaded areas and UTCI values) (Figure 3-7) from the resultant phenotypes against the replicated shadings.

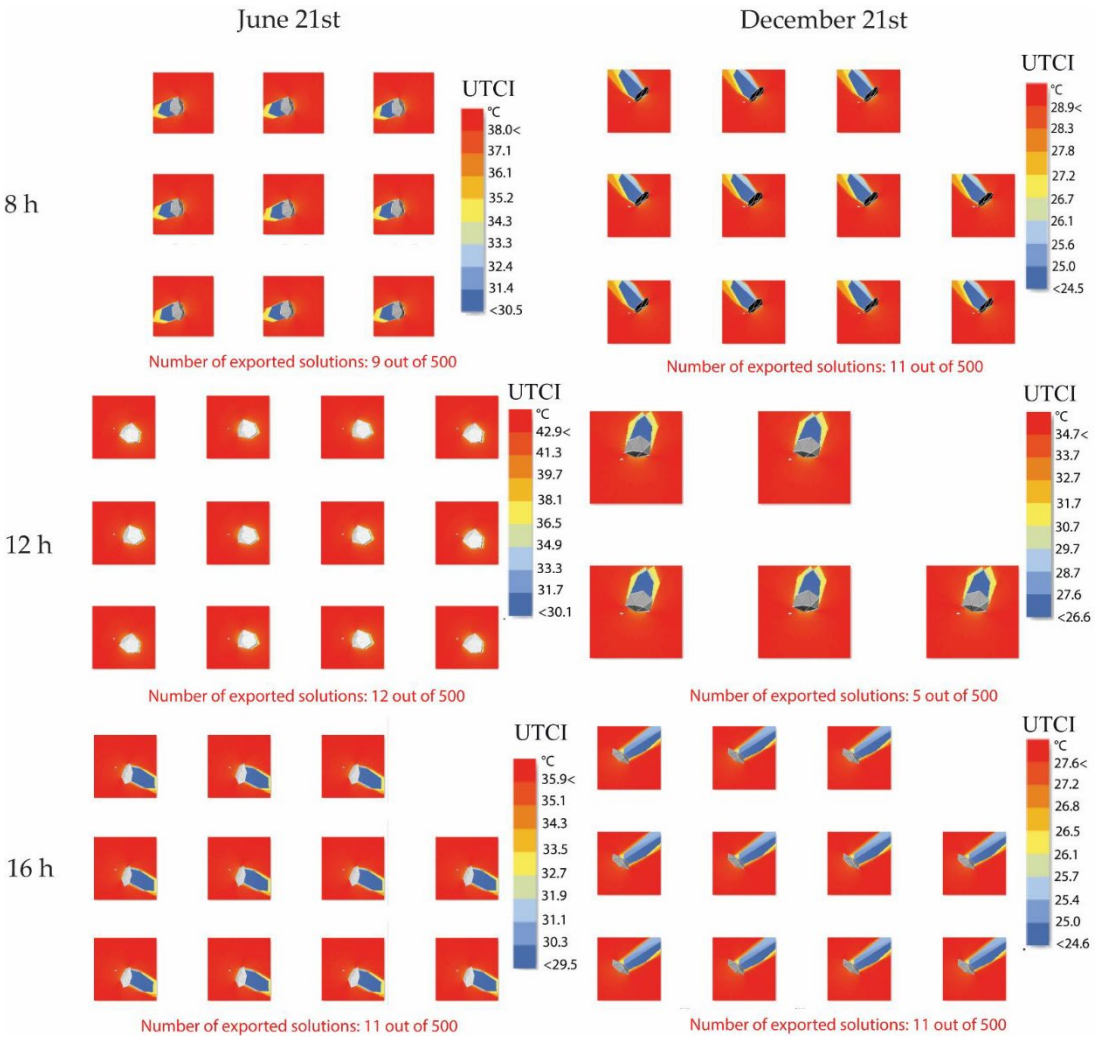

Figure 3-5 Pareto Front phenotypes: Solutions ranked as the best according to the two fitness

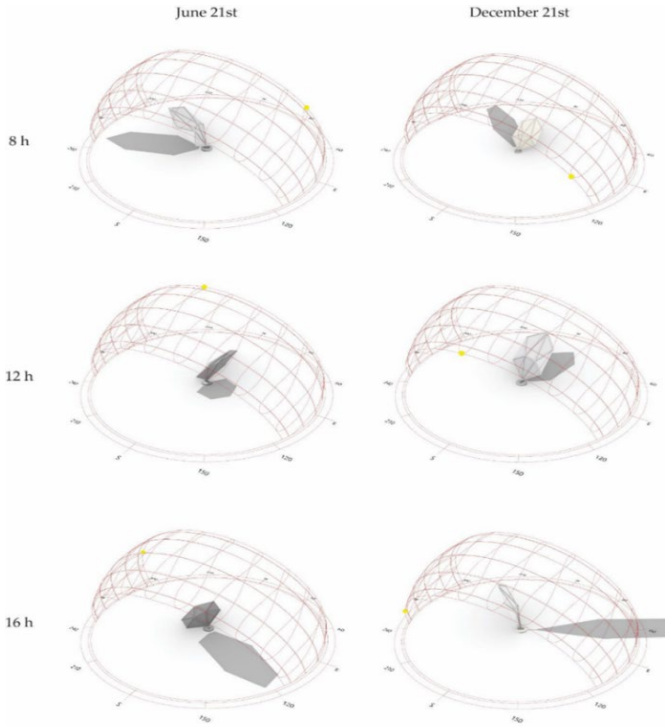

Figure 3-6 Comparison among the phenotypes during specific Source: Chi et al. (2021)

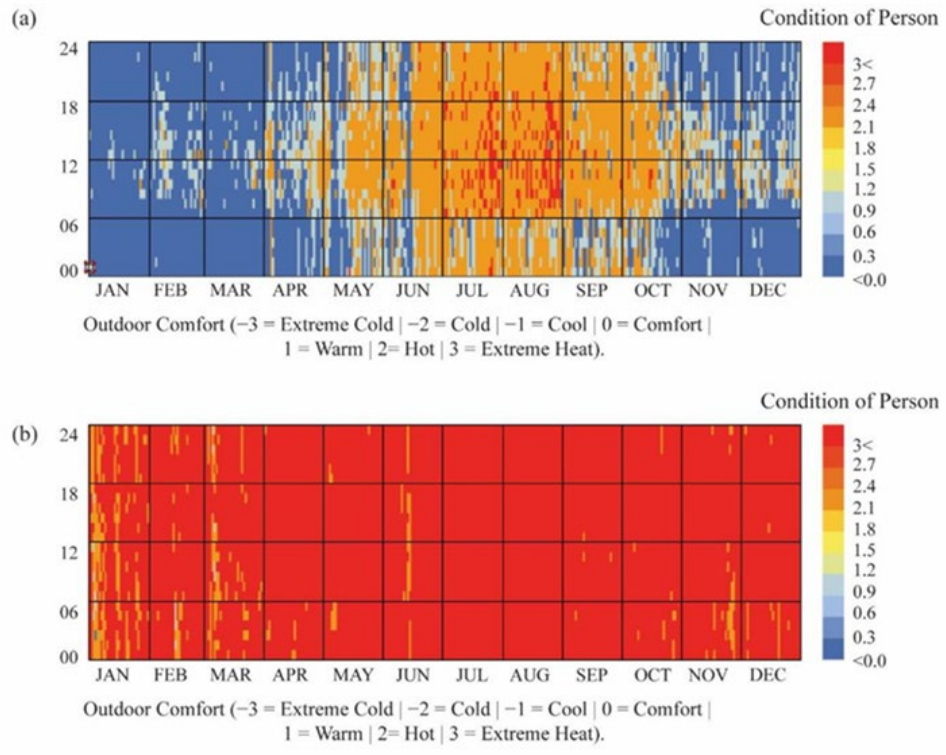

Figure 3-7 Comparative of the condition of a person throughout the year: (a) Shaded conditions vs. (b) unshaded conditions. Hourly data from the EPW file of Cancun, Mexico. Source: Chi et al. (2021)

3.1.3 Results

Performance was evaluated by comparing shaded and unshaded conditions over a 144 m² evaluation area, using average UTCI values and shaded area.

- During summer, shaded areas were mainly associated with moderate heat stress.
- During winter, shaded areas predominantly achieved no thermal stress or slight heat stress, with occasional moderate heat stress at midday.
- All optimal genomes achieved similar shaded areas and UTCI stress categories, demonstrating consistency across Pareto-optimal solutions.
- A significant improvement in outdoor thermal comfort was observed when comparing shaded and unshaded conditions:
- Summer: UTCI reductions up to 11.3 °C at midday.
- Winter: UTCI reductions up to 6.9 °C at midday.
- Visualizations of selected phenotypes show time-changing shading positions, with variations in folding and rotational angles across daily and seasonal cycles.

3.1.4 Conclusions:

This case study illustrates the power of adaptive shading systems as climate-responsive design strategies to enhance environmental performance and livability. The case study illustrates how the combination of environmental simulation and parametric optimization allows for a systematic connection between design intention and performance results, going beyond form-based parametric design.

One of the most important findings related to this thesis is the recognition of the existing gap between geometric parametric design (which is often driven by visual or formal variations) and performance-driven design methodologies. Although the case study illustrates the successful application of optimization to enhance thermal comfort conditions, its application is still limited to a specific set of performance criteria and environmental conditions. This is an important reminder of the need for more comprehensive and multi-objective frameworks that can address energy consumption, daylight availability, and visual comfort simultaneously.

From the point of view of this research, the case study illustrates that adaptive façade systems can only reach their full potential when assessed through integrated and

performance-driven optimization strategies rather than traditional design criteria. The case study illustrates the benefits of dynamic shading to improve user comfort, which is an important reminder of the need for adaptability and flexibility in façade design, but it does not investigate the trade-offs between the different performance criteria comprehensively.

Based on the above findings, this thesis continues to develop the approach by using a multi-objective optimization strategy that systematically assesses energy, daylight, and glare performance criteria within a single parametric design framework. This approach positions adaptive façade design not only as a climate-responsive formal strategy but also as a comprehensive and decision-support-driven process based on measurable environmental performance.

3.2 Article 2:

“Optimum external shading system for counterbalancing glare probability and daylight illuminance in Sydney's residential buildings”

(Ehsan Sorooshnia; Maria Rashidi; Payam Rahnamayiezekavat; Fatemeh Rezaei; Bijan Samali)

Published | Sep 2021

3.2.1 Introduction

Australia is characterized by frequent bright and cloudless skies, even during winter, which makes daylight glare a critical issue in residential buildings compared to European contexts with predominantly overcast skies. Useful daylight illuminance (UDI) plays a significant role in maintaining indoor visual comfort, particularly with the increased use of residential spaces as working environments following the COVID-19 pandemic. Windows are the primary source of discomfort glare due to direct sunlight penetration, especially in dwellings with high window-to-wall ratios. Most glare-related research focuses on office buildings, while Australian residential spaces remain insufficiently investigated. Existing building regulations address minimum illuminance levels but do not explicitly include glare alleviation strategies. Given the limitations of conventional glare indices developed for artificial lighting, this study adopts Daylight Glare Probability (DGP) as the primary glare metric and UDI as the daylight availability metric. The overall research framework and workflow are illustrated in Figure 3-8.

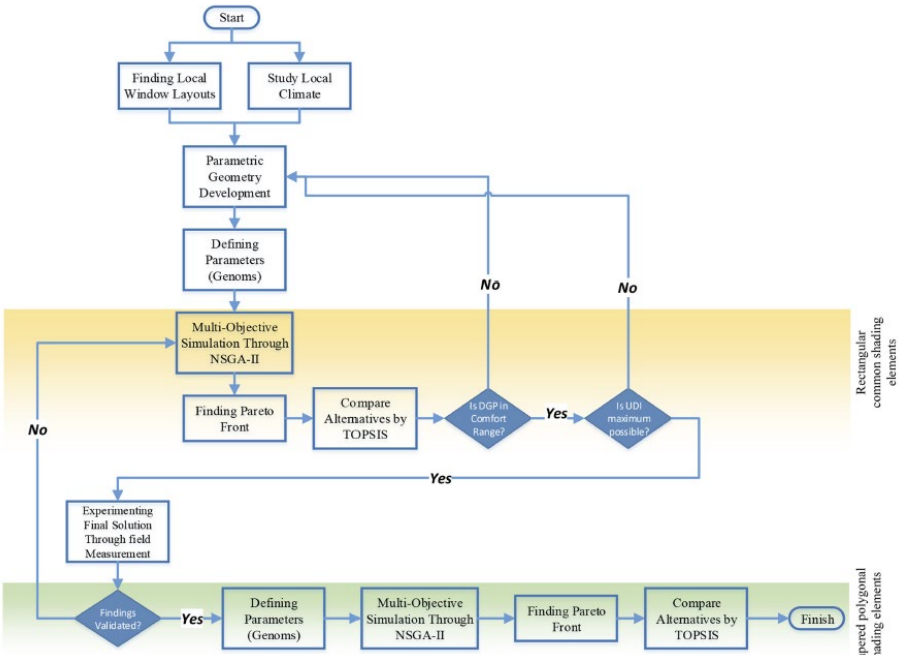

Figure 3-8 Block diagram of the research. Source: Sorooshnia et al. (2023)

3.2.2 Methodology

The study evaluates daylight glare probability (DGP) and useful daylight availability (UDI) in residential buildings in Sydney. The main objective is to identify an optimum external fixed shading system that:

- Improves indoor visual comfort
- Does not require occupant operation

Glare perception is assessed considering:

- Six occupant eye levels
  Seated: 1.1, 1.2, 1.3 m
  Standing: 1.5, 1.6, 1.7 m
- Eight view directions (cardinal and inter-cardinal)

A representative residential room is modelled with:

- Dimensions: 4 × 6 × 3 m
- Location: Sydney Olympic Park
- Orientation: north-facing window

The model is developed in Rhino3D and analyzed using DIVA (Radiance-based simulations), where multiple layout configurations are tested under local climatic conditions defined by EPW weather data, and fixed external shading elements are evaluated through multi-objective simulation by NSGA-II algorithm implemented in Wallacei X.

Experimental setup:

Annual glare and daylight illuminance are evaluated for seven north-facing window layouts within the same residential room, using opaque coverings to isolate each configuration. A 1×1 m sensor grid captures position-dependent glare and illuminance, highlighting the persistent glare risk of north-facing windows under clear-sky conditions.

Simulation parameters:

- The relationship between vertical eye illuminance and DGP is analyzed (Figure 3-10)

- Window–observer geometry and solid-angle formulation are illustrated in Figure 3-9.
- Independent parameters (Table 3-1) include:
  1) Window geometry
  2) Sun position and climate
  3) Observer position
  4) Shading geometry
  For each window case:
- Window-related parameters are kept constant
- Position- and shading-related parameters are treated as genomes in optimization.

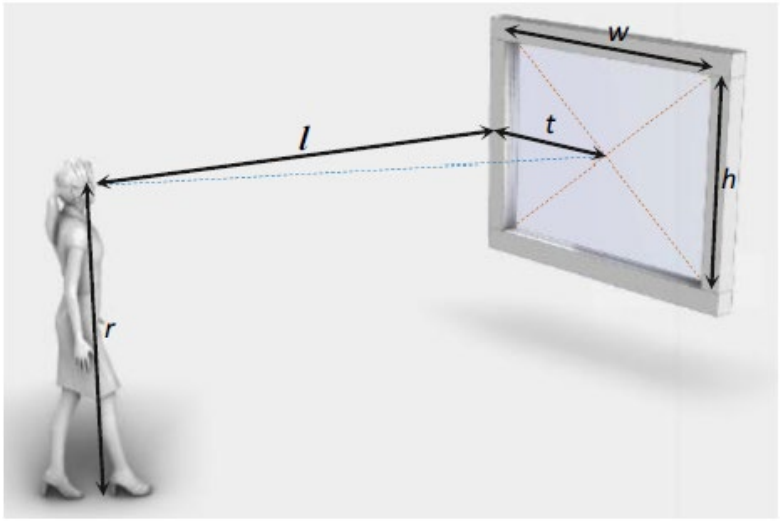

Figure 3-9 Parameters to calculate the configuration factor of a window. Sorooshnia et al. (2023)

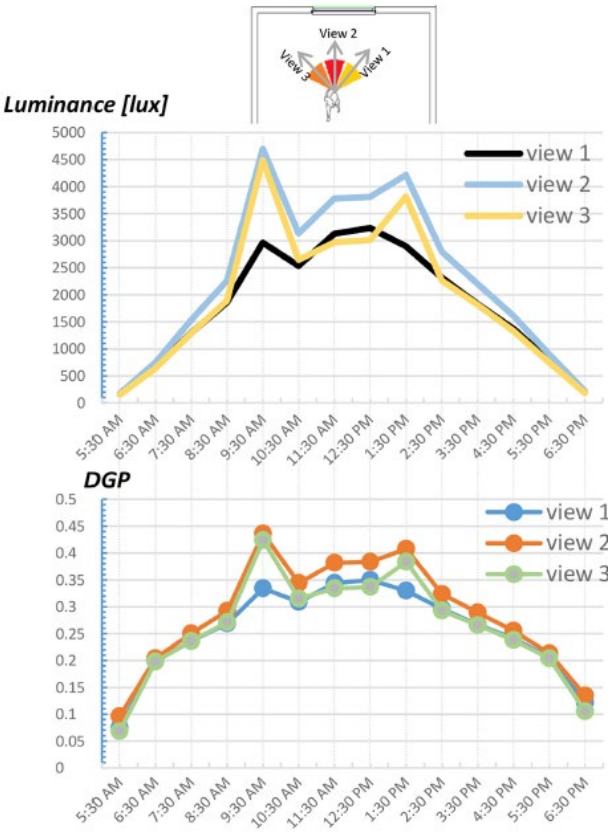

Figure 3-10 Vertical eye luminance [lux] at a level of 1.7 m on January 1st for a north-facing room at Sydney Olympic Park under clear sky condition with the sun (left); DGP for three views at the same position, location and time to left graph. Sorooshnia et al. (2023)

Two fitness objectives of optimization are defined as:

- Maximize Useful Daylight Illuminance (UDI)
- Minimize Daylight Glare Probability (DGP)

The optimization explores the parameter space defined in Table 3-1, and only north-facing window cases are reported due to their critical glare conditions.

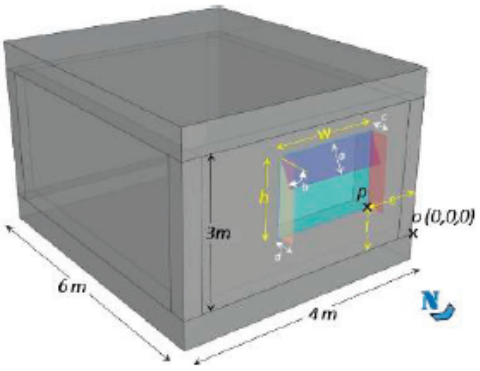

Category	Sub-category	Description	Symbol	Unit	Range
Window	window dimensions	window length	*w*	m	1≤ w ≤3.8
		window height	*h*	m	1≤ h ≤3
	window-to-wall relative position	horizontal relative coordinate	*e*	m	0.1≤ e ≤3.5
		vertical relative coordinate	*f*	m	0≤ f ≤2
Local climate	sun position	hour	*x*		5:30≤ x ≤18:30
		day	*y*		1≤ y ≤31
		month	*z*		1≤ z ≤12
Subject's position	solid angle	subject's eye relative distance perpendicular to the window	*l*	m	50≤ l ≤550
		subject's eye relative position to the centre of the window	*t*	m	0≤ t ≤300
		subject's eye height	*r*	m	110≤ r ≤190
Shading system	Horizontal shade element	horizontal element depth	*a*	m	0≤ a ≤2
		horizontal element inclination	*b*	degree	0≤ b ≤45
	Vertical shade element	vertical western-side shade element depth	*c*	m	0≤ c ≤1.5
		vertical eastern-side shade element depth	*d*	m	0≤ d ≤1.5

Table 3-1 Independent parameters breakdown.

Simulation results are validated through field measurements. Measurement methods include:

- Illuminance sensors
- Luminance meters
- HDR imaging for glare assessment

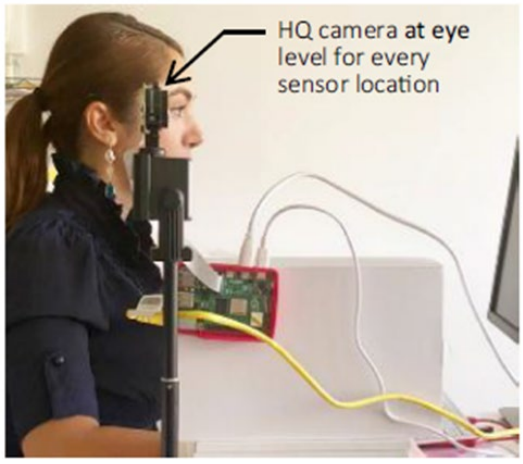

Figure 3-11 Validating DGP simulation data by taking HDR images of HQ cameras and human subjects' assessment. Every virtual sensor in simulation is replaced with a camera and human subject to assess data Gathered from simulation. Sorooshnia et al. (2023)

The experimental set-up and sensor positioning are shown in Figure 3-11, while measurement equipment specifications are provided in Table 3-2. Validation of simulated DGP values using HDR imaging and human-subject assessment is illustrated in Figure 3-12, demonstrating close agreement between measured and simulated results and confirming the robustness of the adopted workflow.

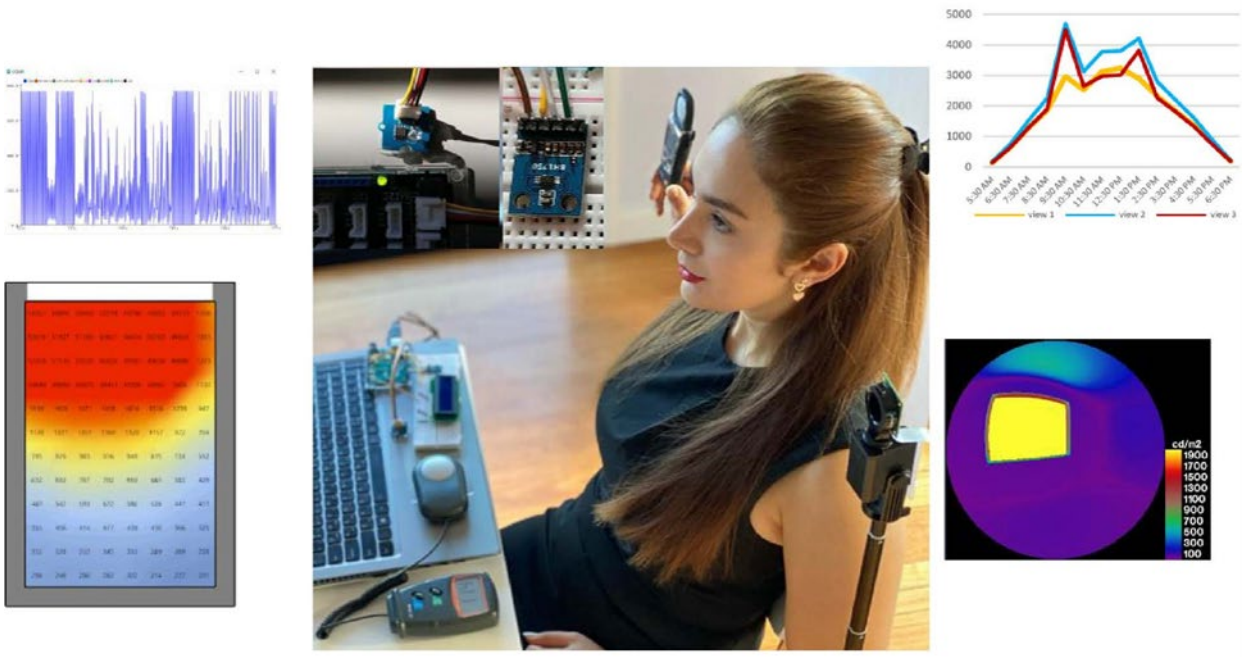

Figure 3-12 To validate data, light-dependent resistor sensor (Low dark current and low working lux) and ambient light sensors (Near human eye spectral response and very low IR sensitivity) positioned at the points that virtual sensors. Figure 3 11 To validate dat

Light Meter	*Range*	*Resolution*	*Accuracy*	*Specification*	*Experimental image*
Digital Lux Meter-LX10B	0-50,000[lux]	1/10/100[lux]	±(5%+2d)	Sampling time 0.4 seconds	
Testo 540 Pocket Lux Meter	0-99999[lux]	1[lux]	±3[lux] ±3% of mv		
Tenmars TM202 Light Meter	200,2000,20000,200000 [lux]	1/10/100[lux]	±3%		
Lutron LX 108 Lux Meter	0-19990[lux]	0.1[lux]	±(5%+2d)		
Light Intensity Sensor	*Range*	*Resolution*	*Accuracy*	*Specification*	
BH1750 digital ambient light sensor	1-65535[lux]		+/-20%	Minimal effect of IR radiation	
Light Sensor v1.2 is an analog module (a high-sensitive photodiode)			Light resistance: 20KΩ; Dark resistance: 1MΩ	Response time 20-30 milliseconds; Peak Wavelength	
HD Camera	*Quality*	*Sensor Resolution*	*Pixel Size*	*Field of view*	
Raspberry Pi NoIR Camera Module v2	8 megapixel (1080p30)	3280 × 2464 pixel static images	1.12μm×1.12μm	62.2° Horizontal & 48.8° Vertical	
Raspberry Pi HQ Camera	12.3 Megapixels (1080p30)	4056 × 3040 pixels	1.55μm×1.55μm		

Table 3-2 Equipment used to measure metrics. Sorooshnia et al. (2023)

3.2.3 Result

- Optimization based on DGP and UDI identifies effective fixed external shading solutions for north-facing residential windows (Table 3-3)
- **UDI improves by 2–57%** (average **+21.57%**), while **disturbing glare (sDG)** is reduced by up to **37.5%**; overall performance trends are shown in Figure 3-14.

Key geometric findings:

- Full-width windows require shading areas close to **90% of window area**
- No consistent relationship between **window-to-wall ratio** and shading area
- **Eastern vertical shading** is critical for glare control; western shading is often unnecessary

Effective shading proportions:

- **Horizontal shade ≥50% of window width**
- **Vertical shades ≈20–30% of window height**, without blocking useful daylight

A single consolidated shading configuration valid for all window types (N-01–N-07) is proposed (Figure 3-13), with re-simulation errors below 8.2%, confirming robustness.

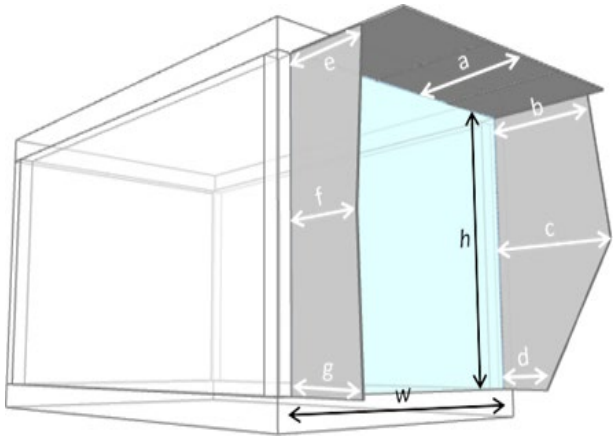

Figure 3-13 A single solution of shading system could be assumed to be installed on all layout north-facing windows in Sydney, alleviation DGP while keeping UDI at the highest possible level. Sorooshnia et al. (2023)

a: 0.53h or 0.43w which is greater.

b: 0.42h or 0.34w which is greater.

c: 0.50h or 0.14w which is greater.

d: 0.20h or 0.17w which is greater.

e: 0.34h or 0.29w which is greater.

f: 0.30h or 0.24w which is greater.

g: 0.32h or 0.25w which is greater.

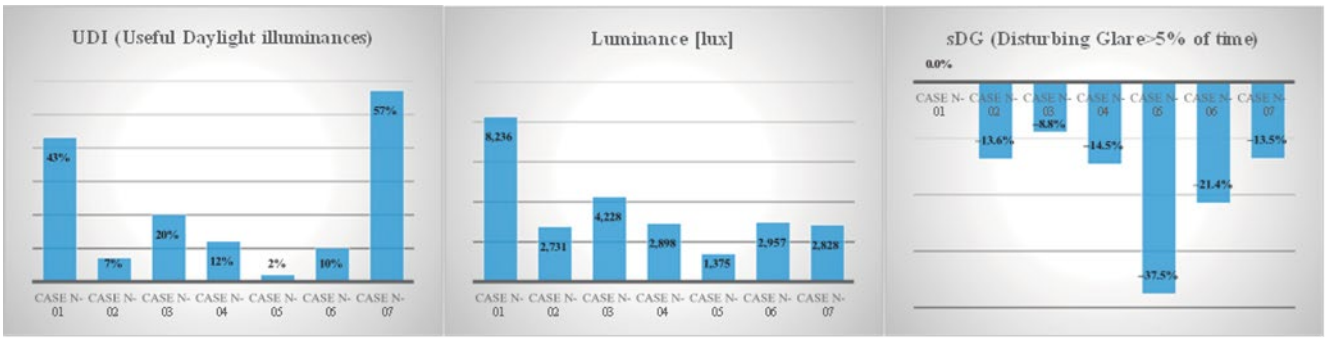

Figure 3-14 Changes optimum shading system brings to each case. Sorooshnia et al. (2023)

ladhausfbufblshksh

	Annual metrics for no shade				Shade features	Annual metrics for shade added				Result
Case N-01	Average Hourly DGP	59.5%	Imperceptible	13.59%	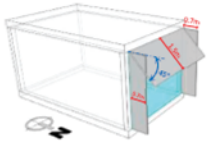	Average Hourly DGP	46.9%	Imperceptible	24.44%	79% Increase
			Perceptible	4.43%				Perceptible	10.06	127% Increase
	sDG[1]	100%	**Disturbing**	**9.51%**		sDG	100%	**Disturbing**	**14.69**	54% Increase
			Intolerable	**72.47%**				**Intolerable**	**50.80%**	30% Decrease
	Average UDI		**13.1%**			**Average UDI**		**18.8%**		43% Increase
	Average luminance		15,945 [lux]			Average luminance		8,236 [lux]		49% Decrease
Case N-02	Average Hourly DGP	27.1%	Imperceptible	73.99%	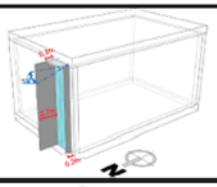	Average Hourly DGP	24.9%	Imperceptible	80.14%	8% Increase
			Perceptible	6.63%				Perceptible	5.52%	17% Decrease
	sDG	79.7%	**Disturbing**	**7.40%**		sDG	66.1%	**Disturbing**	**5.69%**	14% Decrease
			Intolerable	**11.97%**				**Intolerable**	**8.65%**	28% Decrease
	Average UDI		**70.1%**			**Average UDI**		**75.4%**		7% Increase
	Average luminance		3,343 [lux]			Average luminance		2,731 [lux]		19% Decrease
Case N-03	Average Hourly DGP	32.1%	Imperceptible	61.65%	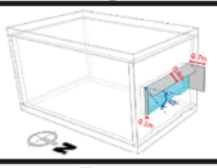	Average Hourly DGP	27.8%	Imperceptible	72.61%	17% Increase
			Perceptible	7.99%				Perceptible	6.91%	14% Decrease
	sDG	88.5%	**Disturbing**	**9.38%**		sDG	79.7%	**Disturbing**	**7.73%**	18% Decrease
			Intolerable	**20.99%**				**Intolerable**	**12.75%**	40% Decrease
	Average UDI		**55.5%**			**Average UDI**		**67.0%**		20% Increase
	Average luminance		6,069 [lux]			Average luminance		4,228 [lux]		31% Decrease
Case N-04	Average Hourly DGP	26.5%	Imperceptible	75.65%	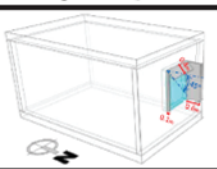	Average Hourly DGP	23.6%	Imperceptible	83.57%	10% Increase
			Perceptible	6.34%				Perceptible	5.06%	21% Decrease
	sDG	78.6%	**Disturbing**	**7.19%**		sDG	64.1%	**Disturbing**	**5.49%**	24% Decrease
			Intolerable	**10.81%**				**Intolerable**	**5.88%**	56% Decrease
	Average UDI		**68.9%**			**Average UDI**		**77.4%**		12% Increase
	Average luminance		4,136 [lux]			Average luminance		2,898 [lux]		30% Decrease
Case N-05	Average Hourly DGP	22.5%	Imperceptible	86.3%	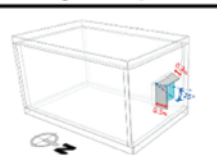	Average Hourly DGP	17.8%	Imperceptible	96.93%	12% Increase
			Perceptible	4.26%				Perceptible	1.25%	71% Decrease
	sDG	48.4%	**Disturbing**	**4.56%**		sDG	10.9%	**Disturbing**	**1.16%**	75% Decrease
			Intolerable	**4.88%**				**Intolerable**	**0.66%**	87% Decrease
	Average UDI		**79.5%**			**Average UDI**		**81.4%**		2% Increase
	Average luminance		2,780 [lux]			Average luminance		1,375 [lux]		51% Decrease
Case N-06	Average Hourly DGP	26.5%	Imperceptible	75.40%	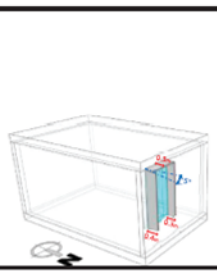	Average Hourly DGP	23.8%	Imperceptible	83.49%	10% Increase
			Perceptible	6.58%				Perceptible	4.92%	26% Decrease
	sDG	81.3%	**Disturbing**	**7.15%**		sDG	59.9%	**Disturbing**	**5.18%**	28% Decrease
			Intolerable	**10.87%**				**Intolerable**	**6.42%**	41% Decrease
	Average UDI		**67.2%**			**Average UDI**		**74.5%**		10% Increase
	Average luminance		3,976 [lux]			Average luminance		2,957 [lux]		26% Decrease
Case N-07	Average Hourly DGP	33.1%	Imperceptible	58.47%	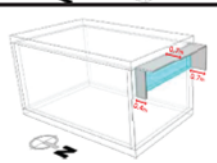	Average Hourly DGP	24.8%	Imperceptible	83.04%	42% Increase
			Perceptible	7.68%				Perceptible	5.11%	34% Decrease
	sDG	100%	**Disturbing**	**9.55%**		sDG	86.5%	**Disturbing**	**5.90%**	39% Decrease
			Intolerable	**24.29%**				**Intolerable**	**5.95%**	76% Decrease
	Average UDI		**47.0%**			**Average UDI**		**74.1%**		57% Increase
	Average luminance		5,741 [lux]			Average luminance		2,828 [lux]		51% Decrease

Note(s): [1]Percentage of views with discomfort glare (more than 5% of time)

Table 3-3 Found near-optimum solution for each case using DIVA simulation. Sorooshnia et al. (2023)

3.2.4 Conclusions

This case study illustrates the importance of performance-driven parametric optimization as a reliable method for assessing residential shading strategies,

especially regarding the trade-off between daylight access and glare mitigation. One of the most important transferable lessons from this article is the integration of computational optimization with strategic experimental verification of Pareto-optimal solutions. By verifying important simulation results through physical measurements, the authors show that verification beyond simulation can help improve confidence in optimization-driven design choices. While complete experimental verification is not possible within the framework of this thesis, this approach emphasizes the significance of critical performance indicator verification through cross-validation wherever possible.

Despite these advantages, case study has a narrow scope. The optimization process is performed at the level of a single room and is mainly based on visual comfort criteria, without considering explicit whole-building energy performance and the relationship between shading strategies and heating and cooling loads. Moreover, the analysis is limited to a particular residential scenario and environmental condition, which reduces the generalization of the results to more complex building types and operation conditions.

Based on these findings, this thesis will expand the optimization approach beyond the limitations of the case study by addressing façade performance at the whole-building level and incorporating energy consumption, daylight availability, and glare mitigation into a single multi-objective optimization procedure. By combining annual energy simulation with climate-based daylight and glare assessment, the developed approach describes the interrelationship between façade design optimization and visual and thermal performance. In this way, this thesis will move forward with performance-driven façade optimization towards a more general and applicable method for commercial and mixed-use buildings.

3.3 **Article 3:**

Homeostatic Generative Design Process: Adaptive Morphology for Extreme Solar Radiation (Showkatbakhsh & Kaviani, 2020)

3.3.1 Introduction

This article introduces a homeostatic generative design method inspired by biological self-regulation. Its goal is to test whether architectural forms can adapt automatically during optimization when exposed to extreme solar radiation. Using the Al-Bahr Towers as a reference, the study shows how environmental triggers can steer NSGA-II toward more resilient morphologies. Unlike conventional optimization that evaluates fixed geometry, the homeostatic approach responds dynamically to environmental thresholds, shifting the process from simple selection to incremental, biologically analogous morphogenesis. This 'self-regulatory' aspect of homeostatic processes will affect the final form and function of a system. This process occurs across the different levels of organisms and controls a wide range of parameters, one of which is heat. The homeostatic process that controls heat is called thermoregulation. Homeostasis is a responsive process by which the organism can sustain a steady-state through internal and external changes. In generative design, it means the geometry automatically adapts when environmental thresholds are exceeded. In this article, homeostasis is the ability of the system to self-regulate under changing conditions.

3.3.2 Methodology:

The objective of thermoregulation is to cancel the effects of an unfavourable change in the temperature of the system. This process comprises three main elements:

(1) **A setpoint**, (2) **Receptors** (3) **Effectors**. The form and skin will be generated through generative simulation with homeostatic feedback mechanisms. The form of Al-Bahr Towers was used to construct a primitive geometry algorithmically with added modifications to enable the changes necessary in the simulation, shown in Figure3-15. The selected group of generated solutions will be compared to the Al-Bahr Towers.

Two secondary feedback mechanisms are added to the generative simulation to drive it towards generating an extra set of formal attributes within the geometry. They are called homeostatic mechanism A and homeostatic mechanism B.

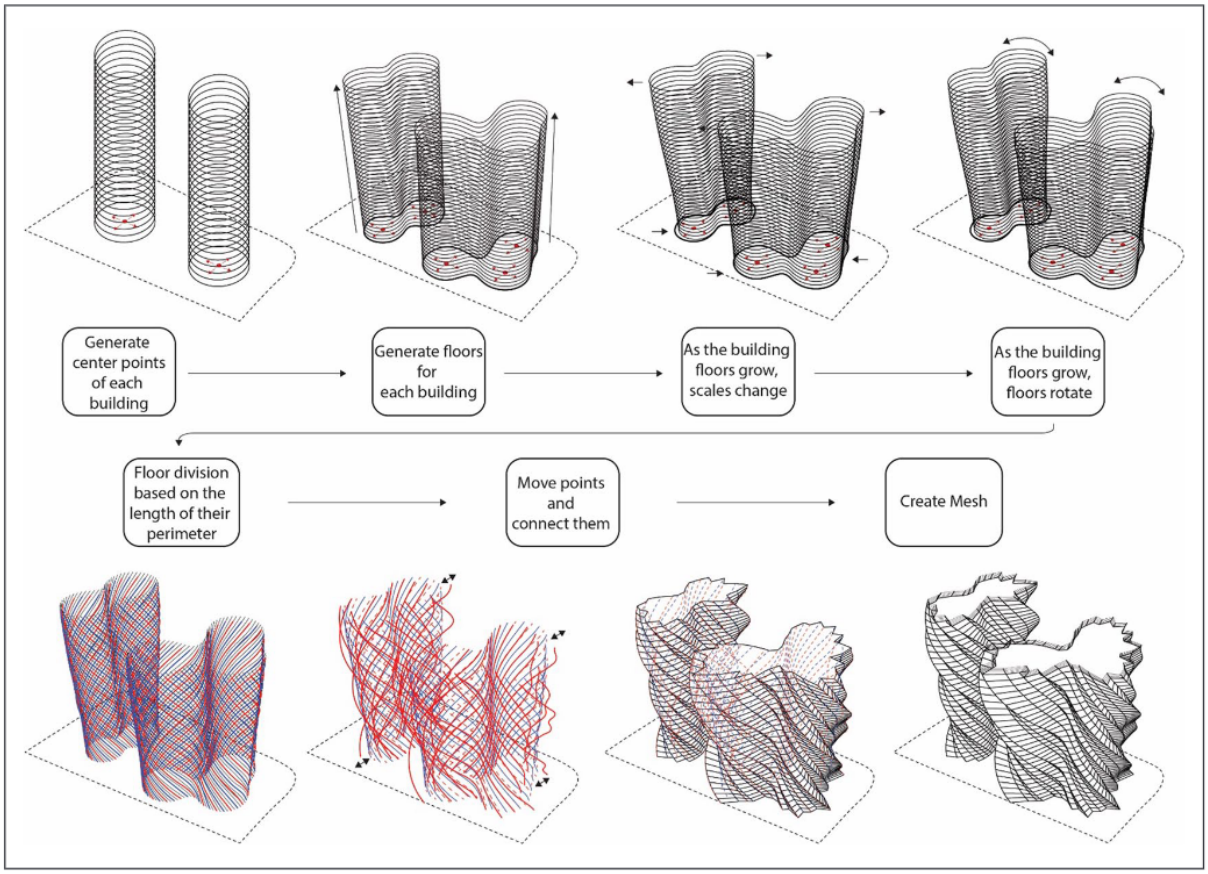

Figure 3-15 The algorithmic construction of the primitive geometry based on Al-Bahr towers geometry.

A) Homeostatic Mechanism A

Homeostatic Mechanism A directs the simulation to generate the skin system on the buildings should a specific condition be met. Its three main elements can be identified as follows: (Figure3-16)

Setpoint: 60% of solar radiation exposure on the building's form is the threshold after which a responsive feedback mechanism will be activated in order to counteract the deviation (the authors chose the figure 60% as a design input; this number can be modified accordingly in other scenarios).

Receptor: Building forms have been created algorithmically based on Figure 3-15, allowing for the evaluation of the solar radiation on the building surfaces.

Effector: If the amount of solar radiation exceeds 60%, a new morphological attribute, skin, will be activated on the exposed surfaces.

The effectiveness of the skin in terms of blocking the excessive solar radiation as well as providing a good view to outside relies on the elements that are considered as the

variable values of the shapes of building skin such as the number of modules, offset size, extrusion size.

By distinguishing the values of the building skin that are fixed and variable, during the early design exploration stage, geometrical adaptability of the skin can be tested to ensure the emergent skin, that may evolve throughout the simulation can be applied to any complex form. The process of setting up the variables and development is illustrated in 3-16. The hexagons are chosen as the skin system in this experiment as an example to show that even complex geometries can take advantage of homeostatic principles.

B) Homeostatic Mechanism B

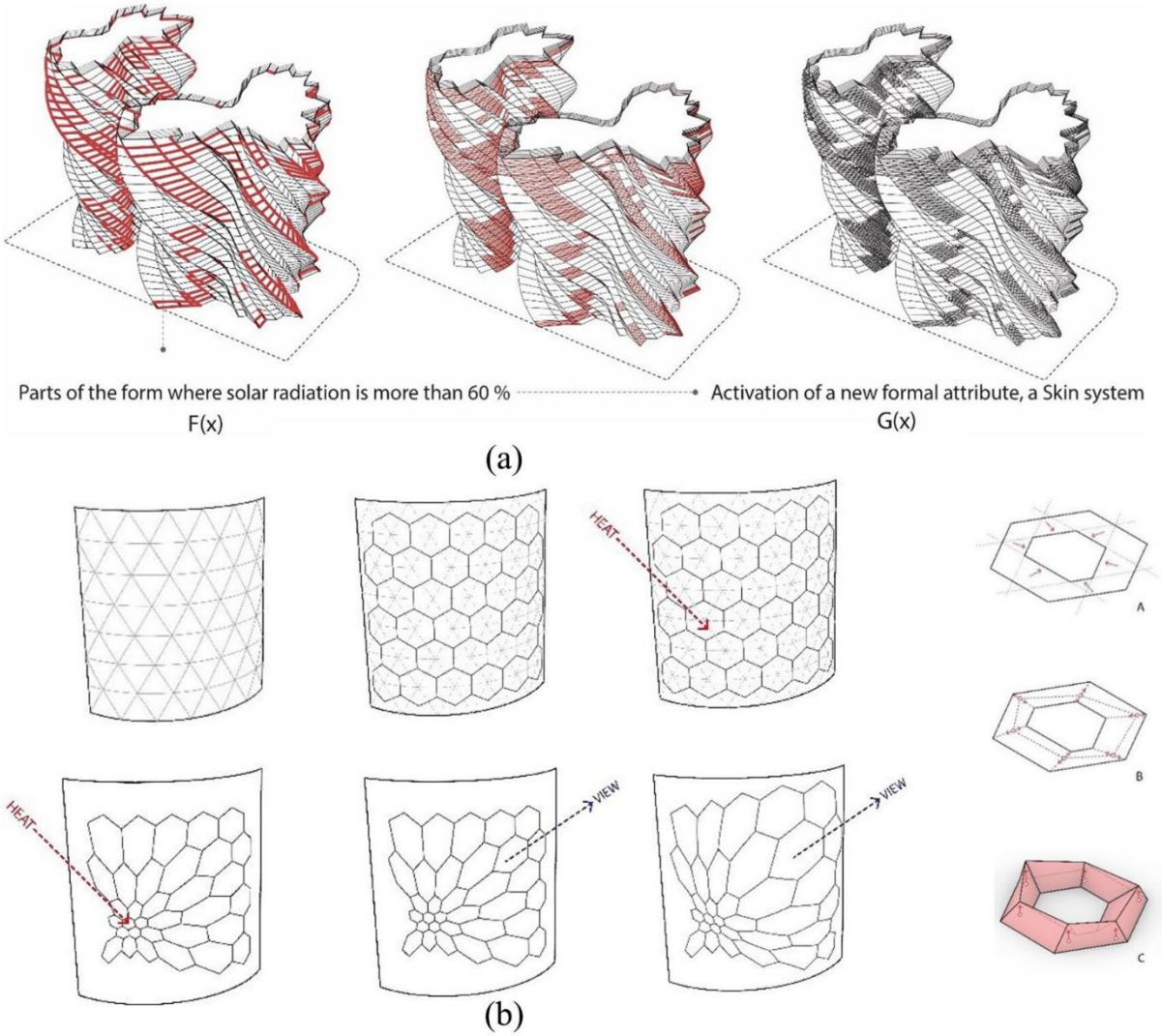

Figure 3-16 Illustration of (a) H-M-A process and effects (skin system); (b) algorithmic setup of the skin system. Source: Showkatbakhsh and Kaviani (2020)

Homeostatic Mechanism B affects areas of the buildings with no skin system. Its three main elements are as follows (Figure 3-17):

Setpoint: 30% of the solar radiation on the building surfaces with no skin system is the threshold after which a responsive feedback mechanism will be activated in order to counteract the deviation (30% is a design decision by the authors; this number can be modified accordingly in other scenarios).

Receptor: Building forms have been created algorithmically, allowing for the evaluation of the solar radiation on the building surfaces.

Effector: If the amount of solar radiation exceeds 30%, a new morphological attribute, indentation, will be activated on the exposed building surfaces (protrusions).

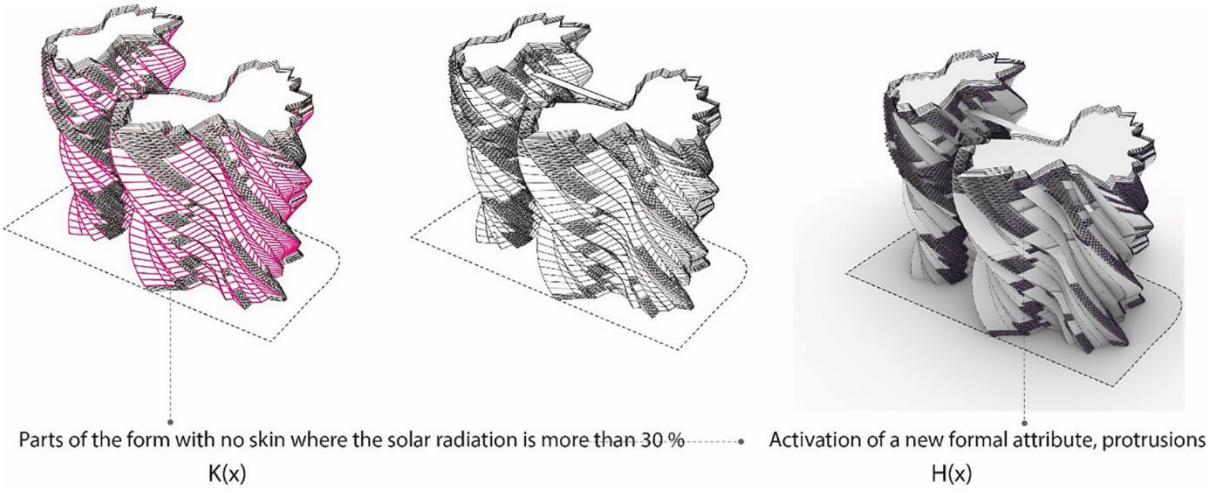

Figure 3-17 Illustration of mechanism B process and effects (protrusions). Source: Showkatbakhsh and Kaviani (2020)

Simulation Scenarios and the Importance of Combined Mechanisms:

The authors conduct an ablation study across five scenarios, selectively activating or deactivating the two homeostatic mechanisms:

Scenario 1: Only **A** active

Scenario 2: Only **B** active

Scenario 3: Both mechanisms active

Scenario 4: Neither mechanism active

Scenario 5: Partial or reduced skin behaviour

3.3.3 Objectives:

Minimizing deviation from the target GFA

Maximizing self-shading (building shading building)

Minimizing ground impact shading

Maximizing view quality

This finding demonstrates that static form-finding with embedded homeostasis can achieve performance levels comparable to or better than complex mechanical facades.

3.3.4 Results

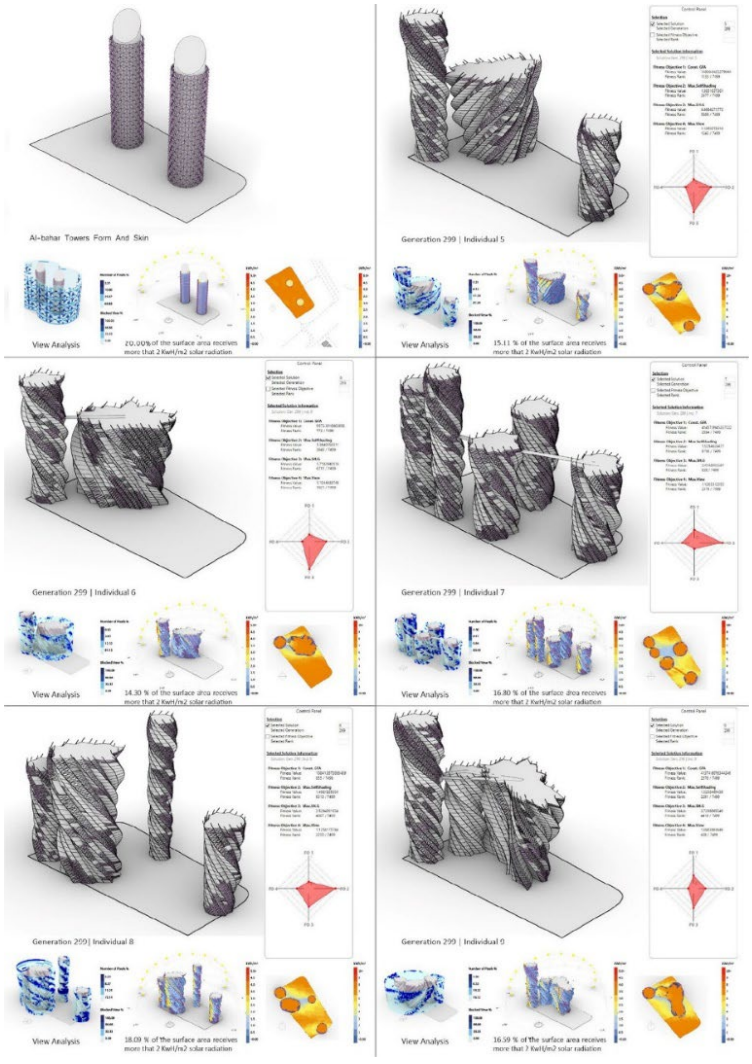

Figure 3-18 The Al-Bahr towers and the selected number of Pareto fronts and their performance measurements. All of the selected candidates are performing better than the Al-Bahr towers.

Remarkably, several evolved solutions surpass the real building in:

- shading efficiency,
- exposure to high-intensity solar radiation,
- façade performance without kinetic elements.

Figure 3-18 shows the measurement criteria based on which the case studies will be compared to the generated solutions in four ways, (1) morphological illustrations, (2) the percentage of the building surface area that receives more than 2 Kwh/m2 solar radiation, (3) the percentage of the skin that blocks the view from inside to outside and(4) the shadow on the ground (solar radiation analysis were carried out by Ladybug Tools).

3.3.5 Conclusion:

Analytically, this demonstrates a shift from the typical “evaluate → select → reproduce” paradigm toward a more biologically aligned loop that includes check → respond → evolve. This turns evolution from a purely stochastic search into a regulation-guided morphogenetic system.

The research has undertaken the analysis of a generative design system, using principles of regulation and adaptation, to conceive building clusters that are capable of adjusting to high levels of solar radiation. The generative design workflow was modified to facilitate the application of homeostatic principles in its process to generate morphological characteristic in the phenotypes for adaptation to extreme solar radiation.

The case study chosen was The Al-Bahr Towers, because of both the excessive solar radiation which they are subjected to and their use of contemporary systems to regulate temperature. The investigation concluded that the generative design system produced a set of design proposals with morphological characteristics that perform better (based on the measurement criteria) than the case study at a significant level.

Limitations identified throughout the research were primarily related to the long time required for the comparative simulations due to the inclusion of additional conditional statements. There were also some slight errors in the computation which resulted in excessive application or dismissal of skin, leading to 10 per cent of solutions being

considered anomalies despite the skin being chosen for its capacity to adapt to complex generated forms.

In order to establish the maximum efficacy of the design mechanism to embed principles of homeostasis, additional research is necessary. Although using feedback loops by including additional conditional statements would add to the required computation time, this addition would allow more solutions to be generated within the simulation in the correct performance range.

04

FRAMEWORK OF ALGORITHM

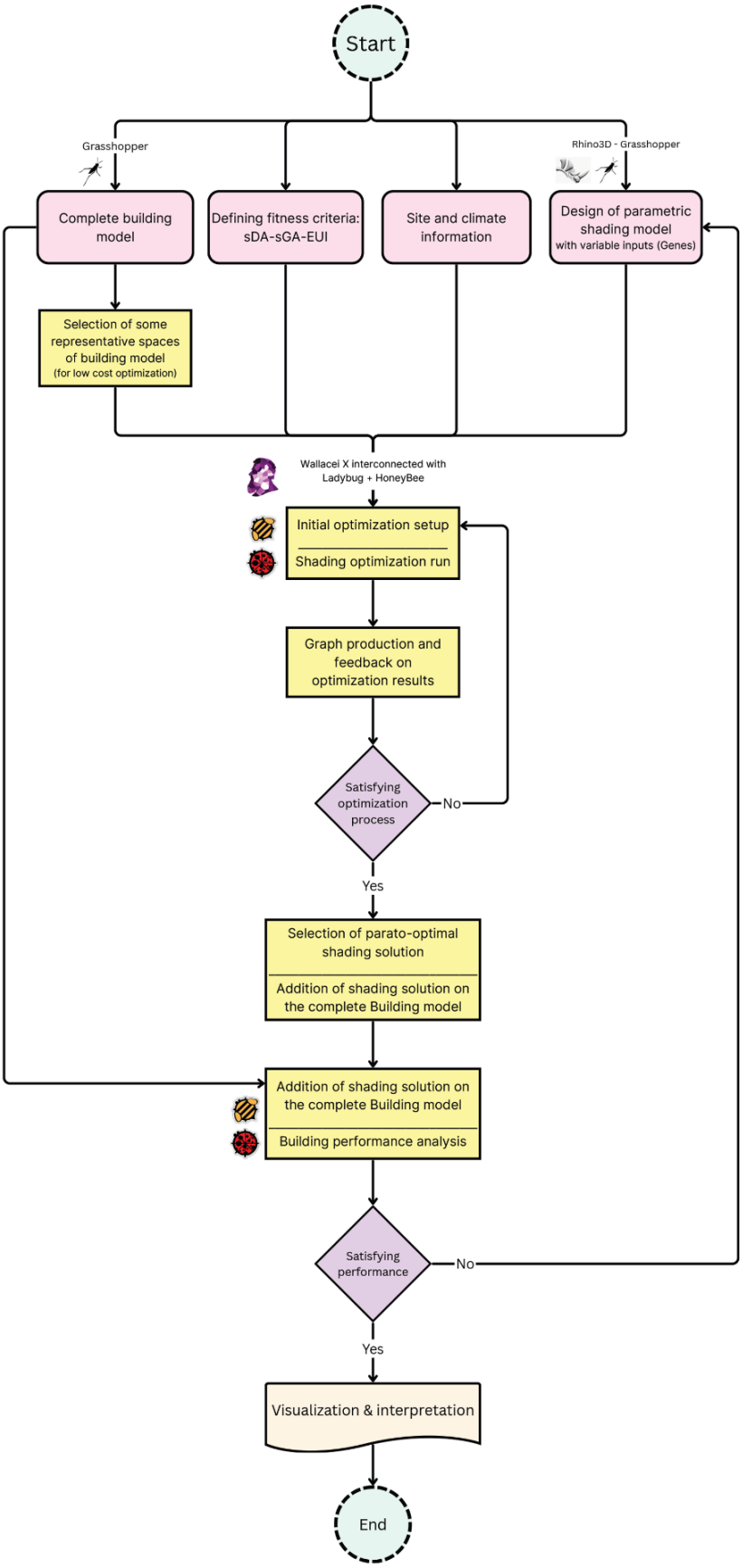

Figure 4-1 Overview of the performance-driven façade optimization workflow from parametric modeling to Pareto-optimal solution selection and evaluation.

This chapter describes our development of the simulation-based algorithm used to evaluate building energy performance in this research, with a particular focus on the role of computational tools and their integration within a parametric workflow. The algorithm is implemented through the combined use of Ladybug Tools, Honeybee, and OpenStudio, enabling environmental data processing, building energy modelling, and performance evaluation within a unified simulation framework.

Ladybug Tools are employed to access and process climatic data and to support the preliminary interpretation of environmental conditions relevant to building performance. These tools operate within the Grasshopper environment, allowing weather-driven inputs to be directly linked to the parametric geometry and enabling iterative performance assessment during model development.

Honeybee functions as the intermediary layer between the parametric model and the energy simulation platform. Through Honeybee, geometric, material, and operational parameters are translated into simulation-ready building models, ensuring a consistent and traceable connection between design variables and simulation inputs.

Building energy simulations are executed using EnergyPlus as the core calculation engine, with OpenStudio employed as the model authoring and workflow management framework. OpenStudio is adopted to facilitate structured model definition, simulation control, and systematic handling of EnergyPlus outputs. Compared to direct text-based EnergyPlus workflows, OpenStudio provides more efficient access to time-series and performance data without altering the underlying simulation engine, which is essential for supporting the analytical requirements of the proposed algorithm. This structured workflow enables precise evaluation of energy demand, heat transfer through building elements, and heating and cooling loads over time.

Wallacei plugin based on the NSGA-2 algorithm (Deb et. al., 2001) as the primary evolutionary algorithm is used for our multi-objective optimization and Gaining insights, seeing trends, and understanding the 'why' behind the optimization so was used in this thesis for our multi-objective optimization.

By integrating these tools within a single algorithmic framework, this chapter outlines how simulation models are constructed, parameterized, and executed. The emphasis is placed on the structure of the algorithm and the specific function of each tool,

providing a clear foundation for the analyses and results presented in the following chapters.

4.1 Simulation Tools:

4.1.1 Ladybug

Ladybug is a parametric environmental analysis plugin for Grasshopper developed to support environmentally conscious design decisions during the early and intermediate stages of architectural design. Unlike conventional building performance simulation tools that operate as standalone applications, Ladybug is embedded directly within the Rhino/Grasshopper modelling environment, enabling continuous interaction between geometry and environmental data.

At its core, Ladybug imports standard EnergyPlus Weather (EPW) files and translates raw climatic data into designer-friendly, interactive 2D and 3D visualizations. These visual outputs allow designers to interpret environmental conditions—such as solar radiation, temperature, wind, and sunlight availability—directly within the geometric modelling context, rather than through abstract tables or external reports (Roudsari and Pak, 2013) .A key contribution of Ladybug lies in addressing what the authors describe as the “data–design disconnection” in conventional workflows, where environmental analysis is often detached from form generation. By running entirely inside Grasshopper, Ladybug enables near-instantaneous feedback on design modifications, allowing environmental information to actively inform design exploration rather than merely validate final solutions.

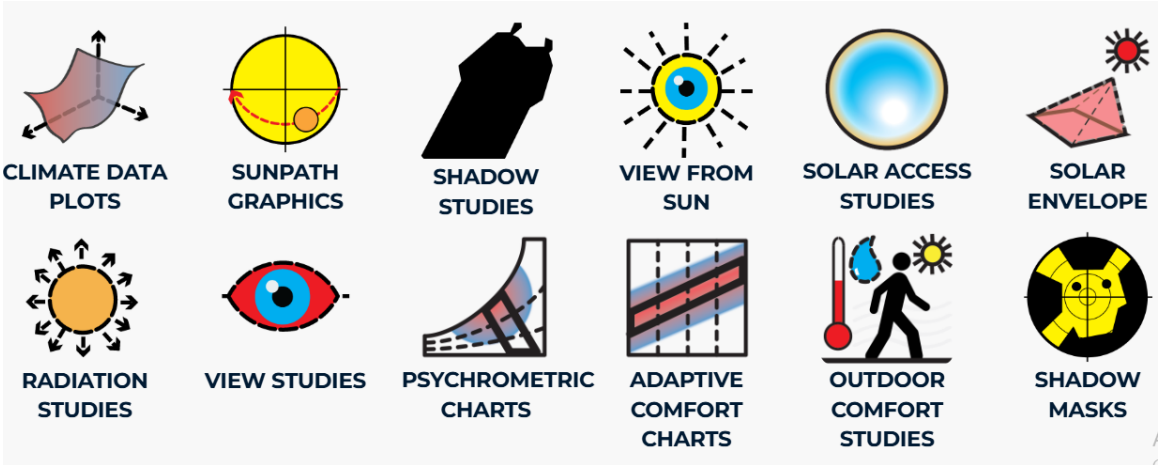

Figure 4-2 Ladybug features.Source: Ladybug

Overview of Ladybug Components Used in the Simulation Workflow

Within the Ladybug Tools environment, climatic data are obtained using the LB Download Weather component. The LB Download Weather component is used to download standard weather files required for building performance simulation.

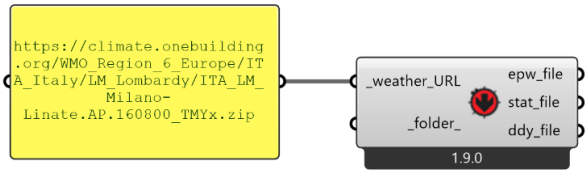

Figure 4-3 Ladybug Download weather component.

The _weather URL input receives direct a link to a weather file hosted on the One Building (https://climate.onebuilding.org) climate database and specifies the location and dataset to be downloaded. The folder input defines the local directory in which the downloaded weather files are stored.

The component generates three main outputs. The epw_file output provides the EnergyPlus Weather (EPW) file, containing hourly climatic data such as air temperature, solar radiation, wind speed, and humidity. This file serves as the primary climatic input for the energy simulation workflow and is directly used in subsequent Honeybee and OpenStudio simulations.

The stat_file output contains the corresponding STAT file, which summarizes long-term climatic characteristics and design conditions derived from the EPW dataset. In this research, both the EPW and STAT outputs are utilized as core climatic inputs; their specific roles and applications within the simulation and analysis process are discussed in detail in later sections of this chapter.

The ddy_file output provides design day definitions primarily used for peak load calculations; however, this output is not directly employed within the scope of the proposed algorithm.

4.1.2 Honeybee

Honeybee is an open-source environmental simulation plugin that extends the Rhino/Grasshopper 3D modeling environment with robust building performance analysis capabilities. It connects parametric models to validated engines like Radiance (for light and daylight simulation) and EnergyPlus (via OpenStudio for energy modeling). Honeybee enables architects and engineers to evaluate daylight, thermal comfort, and energy use interactively within their design workflow.

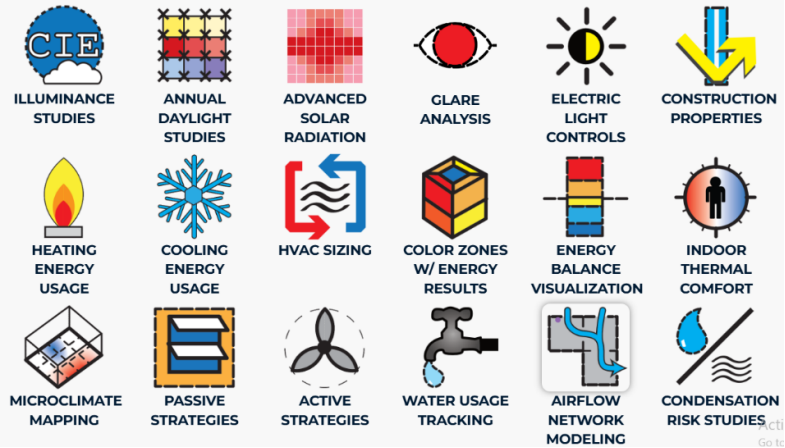

Figure 4-4 Honeybee Features. Source: Ladybug

Step 1: Thermal Zone Generation and Algorithmic

Thermal Zone Definition in Honeybee:

In Honeybee, thermal zones are defined based on the principle that energy simulation should represent spaces with relatively uniform thermal behavior rather than purely architectural divisions. Each thermal zone is modelled as an independent control volume in which indoor conditions, internal gains, and operational patterns are assumed to be spatially uniform and represented by average values. This assumption underpins whole-building energy simulation engines such as EnergyPlus, allowing energy balance calculations without computationally intensive fluid dynamics modelling. Honeybee incorporates this zone-based logic into a parametric, geometry-driven workflow, where zones are defined as closed volumes bounded by building elements. Internal surfaces enable heat exchange between adjacent zones, while external surfaces interact directly with climatic conditions through the building envelope.

Architectural Zoning versus Thermal Zoning:

Architectural zoning and thermal zoning follow different logics and serve distinct roles in design and simulation. Architectural zoning is guided by spatial organization, function, and design intent, aiming to support usability and programmatic clarity. Thermal zoning, in contrast, is determined by energy and environmental performance factors such as orientation, exposure, internal gains, occupancy, and control strategies, which may require subdividing or grouping architectural spaces based on their thermal behavior. Within the Honeybee framework, thermal zoning is a critical modelling decision that directly affects simulation accuracy. Therefore, in this research, thermal zones are defined to balance physical realism, analytical accuracy, and computational efficiency, avoiding both oversimplification and unnecessary complexity.

generation of thermal zones:

The generation of thermal zones follows a structured, algorithmic workflow designed to ensure geometric consistency, correct thermal adjacency, and reliable energy simulation outcomes.

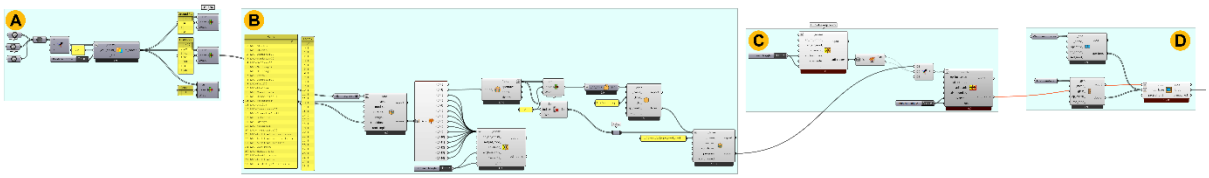

Figure 4-5 Creating Zones Algorithm in 4 sections A/B/C/D.

As shown in Figure 4-5 the process begins with the architectural geometry developed in Rhino, where individual spaces are modeled as closed Breps representing distinct spatial volumes (section A). These Breps are subsequently internalized within the Grasshopper environment, allowing them to be accessed, manipulated, and processed parametrically.

Once internalized, all zone Breps are subjected to a geometric intersection process by Honeybee to intersect solid components. This step is essential to eliminate overlaps, resolve shared boundaries, and ensure that adjacent spaces possess coincidence and

topologically consistent surfaces. By intersecting all Breps prior to thermal processing, the algorithm guarantees that shared faces between neighboring zones are explicitly

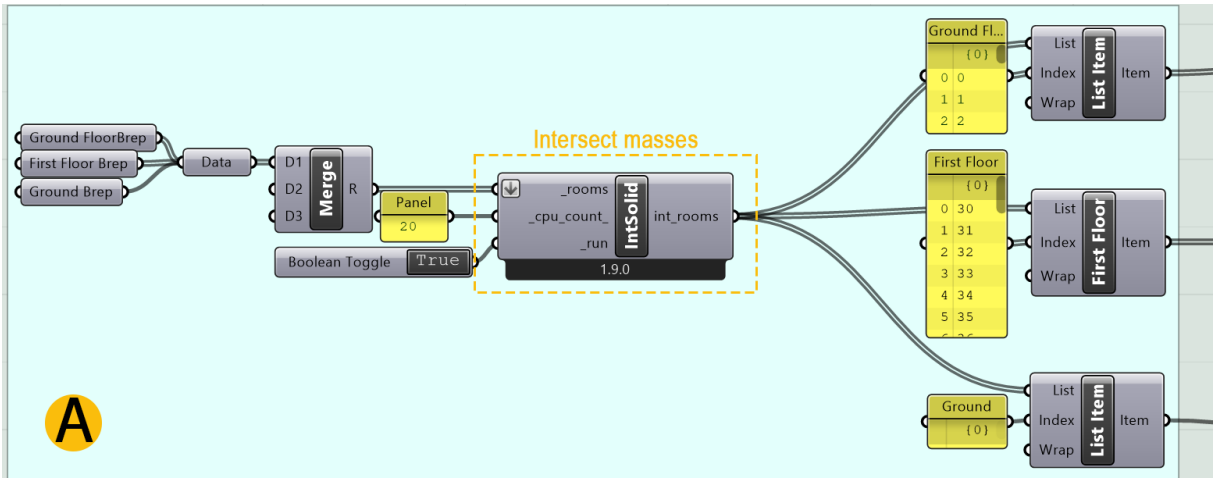

Figure 4-6 Section A the process of internalizing Rhino Breps and intersecting them.

defined, which is a prerequisite for accurate adjacency detection in energy simulation.

Following the intersection process, the algorithm evaluates the resulting faces to identify surfaces that separate sub-zones belonging to the same architectural space. In these cases, air boundary conditions are assigned to the corresponding faces. The application of air boundaries allows the zones to remain thermally distinct for calculation purposes while permitting air mixing and preventing the introduction of artificial thermal resistance between adjacent sub-zones. This approach preserves the intended thermal continuity of large architectural spaces that have been subdivided for simulation of accuracy.

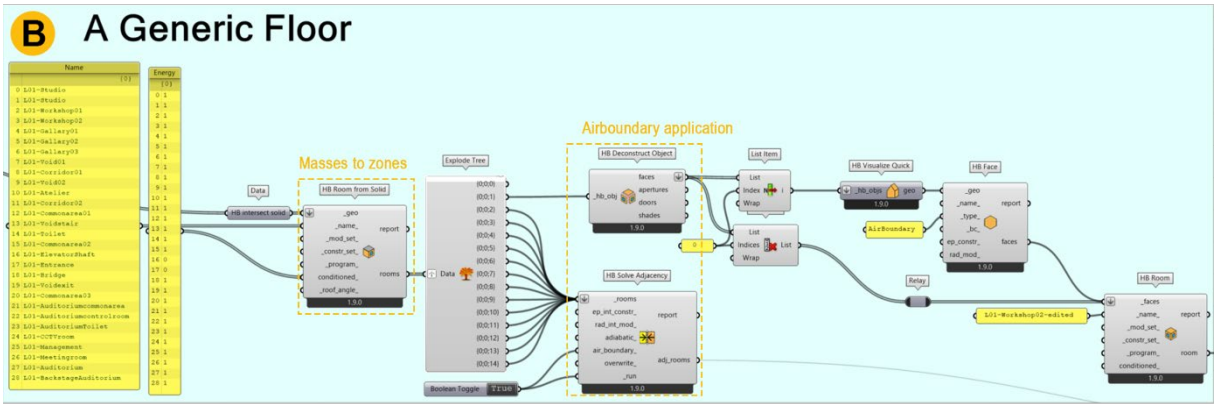

Figure 4-7 Zones classification and add air boundaries algorithm.

The next step involves executing the Solve Adjacency operation within the Honeybee framework. During this stage, the algorithm automatically analyzes the spatial relationships between adjacent zones and classifies their shared faces according to boundary conditions. Internal faces are identified as inter-zone partitions, while external faces are correctly assigned as walls, roofs, or floors exposed to outdoor conditions or ground contact. This automated adjacency resolution ensures that each zone has a complete and physically coherent set of boundary conditions before being passed to the energy simulation engine.

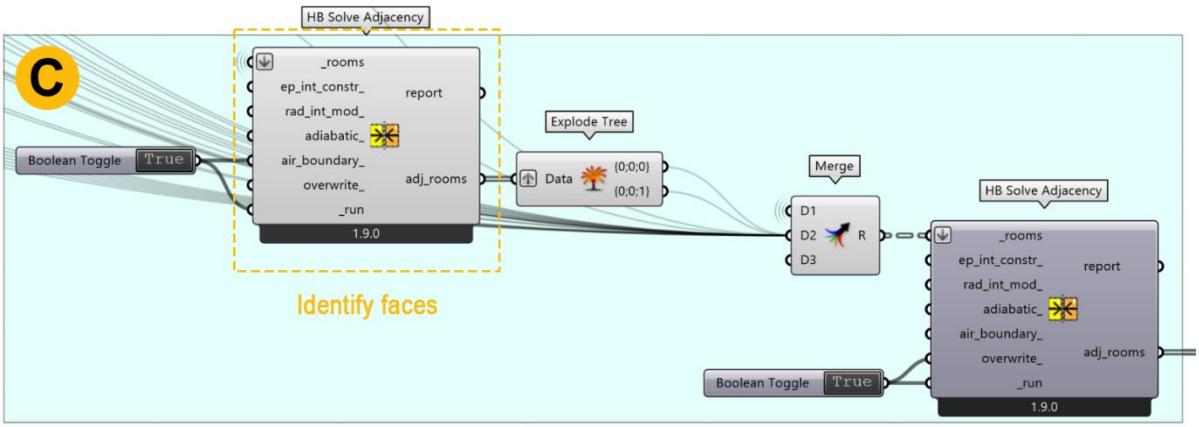

Figure 4-8 Honeybee solve adjacency component algorithm.

In the final step of the algorithm, architectural sub-surfaces are incorporated into the generated thermal zones. Openings such as windows, doors, and other facade elements are imported from Rhino and referenced within Grasshopper as surface geometry. These sub-surfaces are then assigned to their corresponding Honeybee Rooms, where they are recognized as apertures or doors associated with specific zone faces. This process ensures that each thermal zone accurately represents the architectural envelope, including transparent and operable elements, and allows their thermal and solar effects to be explicitly accounted for in the subsequent energy simulation.

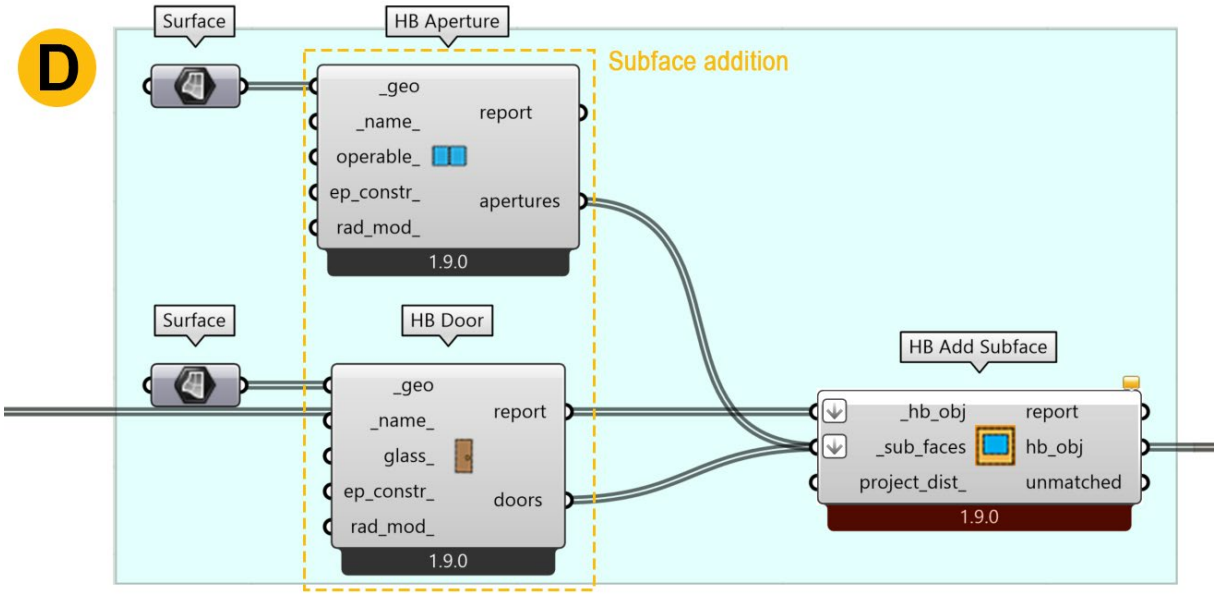

Figure 4-9 Honeybee add subface algorithm.

Step 2: Program Assignment to Thermal Zones

Following the generation of thermal zones, the second phase of the algorithm focuses on assigning appropriate usage programs to each zone. This phase defines internal loads, occupancy patterns, schedules, and thermal control parameters, which are critical for accurately representing operational energy demand.

In step A, the thermal zones generated across the building are classified according to

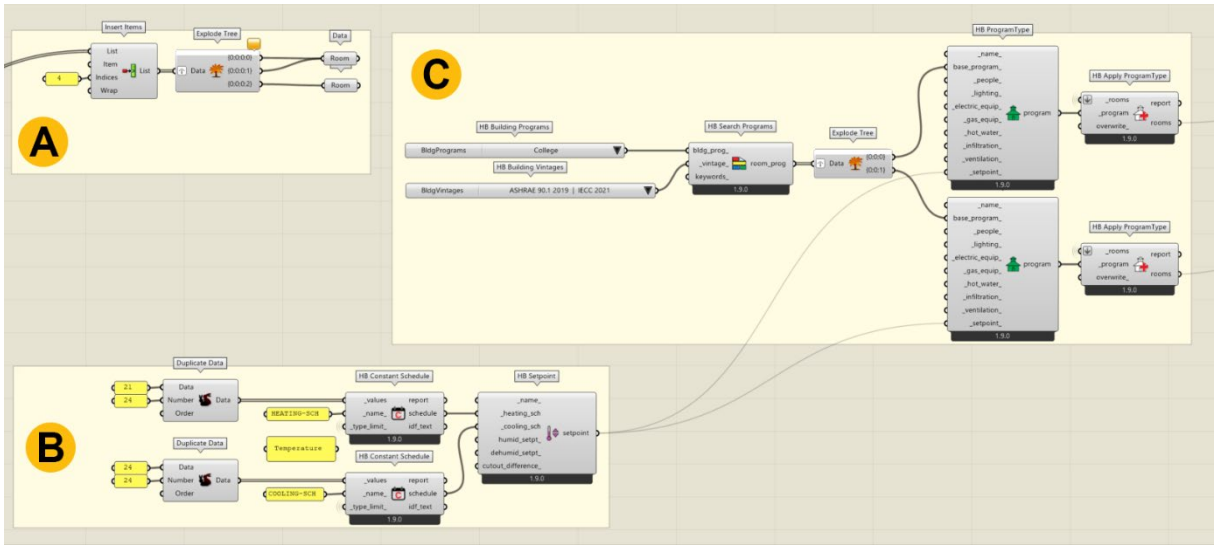

Figure 4-10 Program assignment workflow showing zone classification, ASHRAE based setpoint definition, and program type allocation using Honeybee in 3 steps(A,B,C).

their architectural and energy function. Based on spatial use and operational similarity.

This initial classification provides a logical basis for program assignment and ensures that zones with comparable occupancy behavior and internal load characteristics are treated consistently within the simulation framework.

In step B, indoor temperature control limits are defined at the building level using the

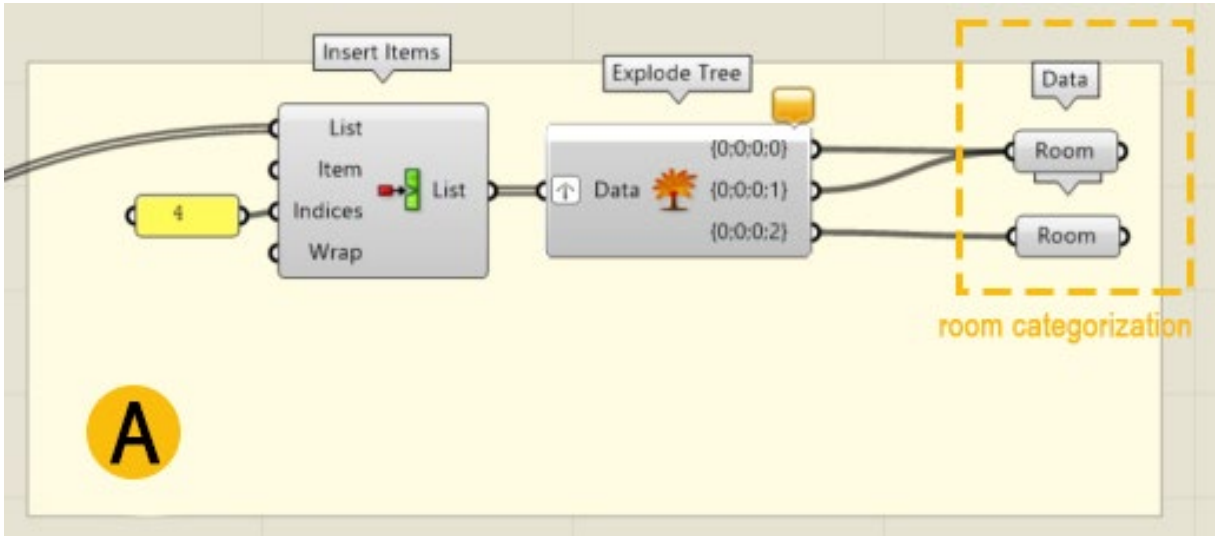

Figure 4-11 Room categorization algorithm.

HB Setpoint component. Heating and cooling setpoints are specified with guidelines, establishing acceptable minimum and maximum indoor temperatures for winter and summer conditions. These setpoints define the operational boundaries within which all conditioned zones are allowed to operate and directly influence heating and cooling energy demand. By applying consistent setpoint limits across the building, the model ensures comparability between zones while maintaining compliance with recognized comfort standards.

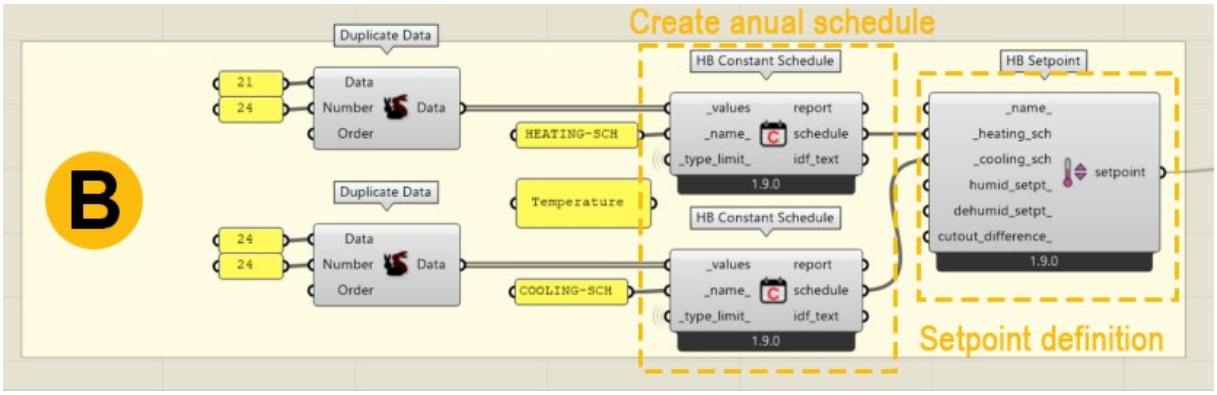

Figure 4-12 Definition of setpoint algorithm.

In step C, the functional zone categories defined in step A were mapped to standard program types using the HB Program Type component. This component assigns default schedules and internal load parameters—such as occupancy density, lighting power density, equipment loads, ventilation rates, and operating hours—based on ASHRAE reference standards embedded within Honeybee.

In the following section, the schedule outputs generated from the Honeybee programs are presented.

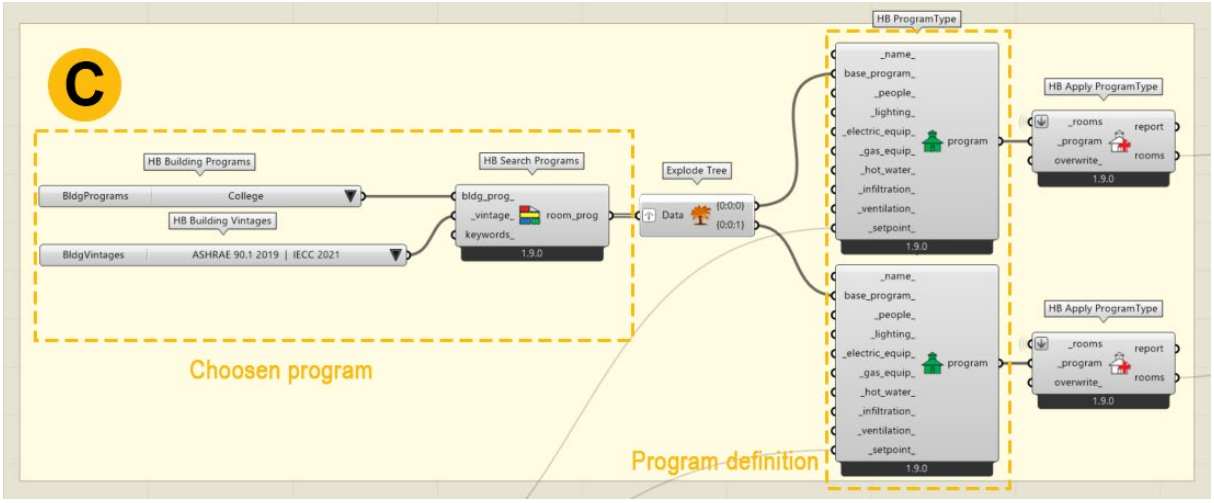

Figure 4-13 program Application algorithm.

In the following section, the schedule outputs generated from the Honeybee programs are presented.

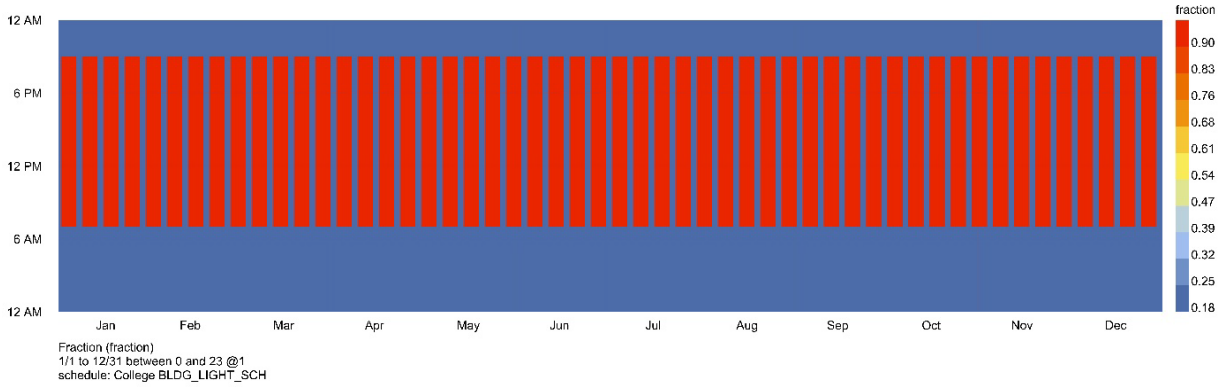

Figure 4-14 People occupancy Program schedule visualized by Ladybug Hourly Plot.

Figure 4-15 Lighting Program schedule visualized by Ladybug Hourly Plot.

Finally, all program-assigned zones were consolidated into a single data structure and passed to the subsequent stage of the algorithm, where construction assemblies and envelope properties are defined. This structured workflow ensures continuity between zoning, program definition, and construction modeling, which is discussed in the following section.

Step 3: Material Definition and Construction Set Assignment

Following thermal zoning and program assignment, the third phase of the algorithm focuses on defining material properties and assembling construction sets for the building envelope. This phase translates architectural and regulatory assumptions into physically explicit layer-based constructions, enabling accurate calculation of heat transfer through opaque building elements.

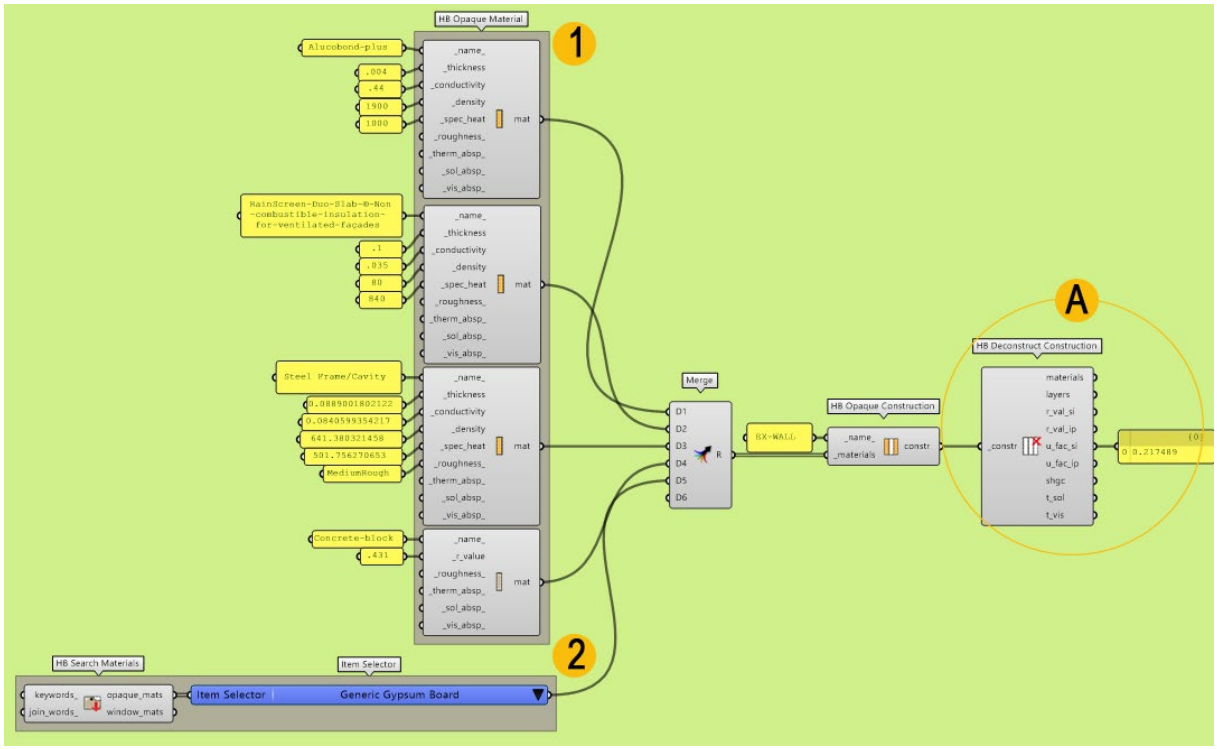

Figure 4-16 Honeybee material and construction set assignment algorithm.

In this workflow, individual construction assemblies are defined separately for each major envelope component, including external walls, roofs, internal floors, ceilings, and ground-contact elements. For each element type, material layers are specified using Honeybee material components, where key thermo-physical properties such as thickness, thermal conductivity, density, and specific heat capacity are assigned in accordance with reference standards and design assumptions. This modular approach allows material definitions to remain transparent, editable, and reusable across different construction assemblies.

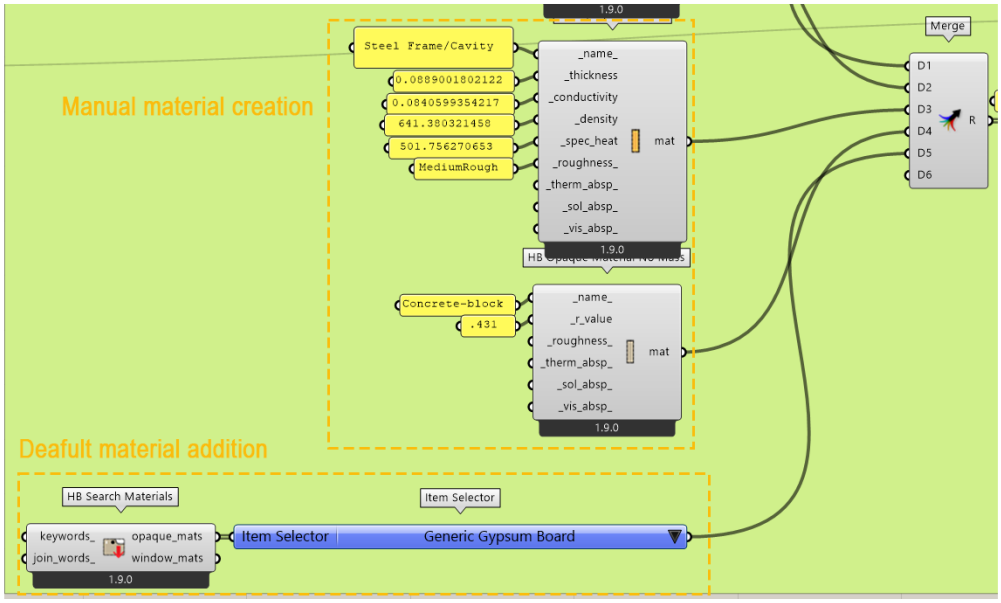

Figure 4-17 Opaque wall construction workflow in Honeybee

Once material layers are defined, they are combined into layered constructions using Honeybee construction components. Each construction represents a complete build-up corresponding to a specific envelope of condition, such as exterior exposure, interior adjacency, or ground contact. These constructions are then grouped into a unified construction set, which functions as a container linking the appropriate construction to each surface type within the thermal model.

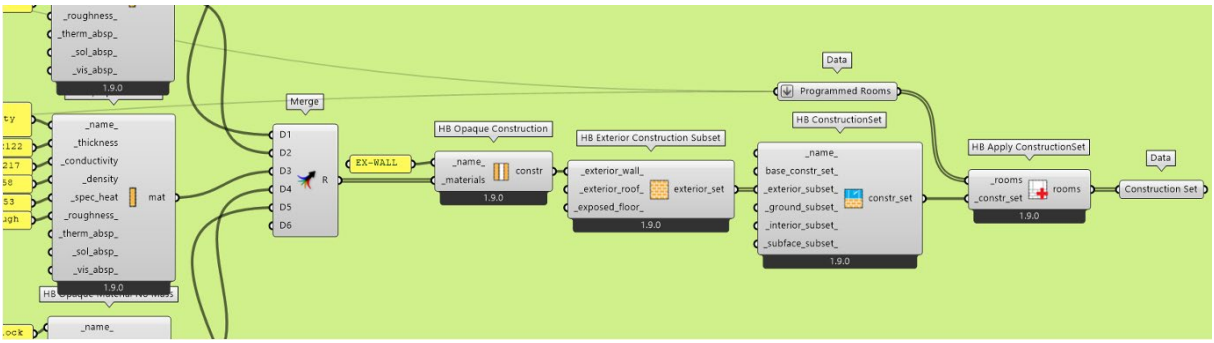

Figure 4-18 Create a Construction Set object containing all energy constructions needed to create an

The Construction Set is subsequently assigned to the previously defined Honeybee Rooms, ensuring that walls, roofs, floors, and ceilings are automatically matched with their corresponding constructions based on surface boundary conditions identified during the adjacency resolution phase. This structured assignment guarantees consistency between geometric zoning, program definition, and material performance, while avoiding manual and error-prone surface-by-surface specification. By

centralizing material and construction logic within a single Construction Set, the algorithm maintains a clear separation between geometric modelling, operational assumptions, and physical envelope properties. This approach enhances model transparency, reduces the risk of inconsistent material assignments, and provides a robust foundation for subsequent energy simulation and performance analysis.

4.1.3 Honeybee Energy

Honeybee provides a structured interface for building energy simulation. Honeybee does not perform numerical calculations itself; instead, it organizes geometric, thermal, and operational information into a coherent energy model suitable for execution by external simulation frameworks.

Energy simulation in Honeybee is based on a zone-level approach, where each Honeybee Room represents a thermal zone enriched with loads, schedules, constructions, boundary conditions, and simplified system assumptions. Idealized HVAC definitions and ventilation strategies are employed to support comparative and performance-driven analysis rather than detailed mechanical system design. At this stage, Honeybee functions as the interface between parametric architectural modeling and dynamic energy simulation.

Energy Plus

EnergyPlus is a dynamic whole-building energy simulation engine developed by the U.S. Department of Energy. It computes building thermal and energy behavior under time-varying climatic conditions by solving coupled heat and mass balance equations at an hourly or sub-hourly timestep (Crawley et al., 2001).

EnergyPlus adopts a zone-based approach in which each thermal zone is treated as a control volume with uniform indoor conditions. Within this research, EnergyPlus functions exclusively as the numerical calculation engine. All geometric, material, and operational inputs are defined upstream and passed through an intermediate framework, which executes the annual simulation and generates raw energy performance outputs.

EnergyPlus work within the Grasshopper workflow

Annual energy simulations are executed through the HB Annual Loads component (Figure 4-19, label 1), which translates the parametric Honeybee model into an EnergyPlus-compatible input file and runs an hourly annual simulation using an ideal approach. In this configuration, EnergyPlus computes the theoretical heating and cooling energy required to maintain the defined indoor setpoints without explicitly modeling HVAC system efficiencies, allowing the analysis to focus on the impact of architectural form, envelope properties, and operational assumptions (Crawley et al., 2001).

The simulation workflow is implemented within the Grasshopper environment using Ladybug and Honeybee as the primary interfaces, with EnergyPlus acting as the underlying calculation engine. Climatic boundary conditions are provided via EPW files imported using LB Download Weather, while thermal zones, constructions, schedules, and internal loads are assembled through the HB Model component. The overall process and component relationships are illustrated in Figure 4-19.

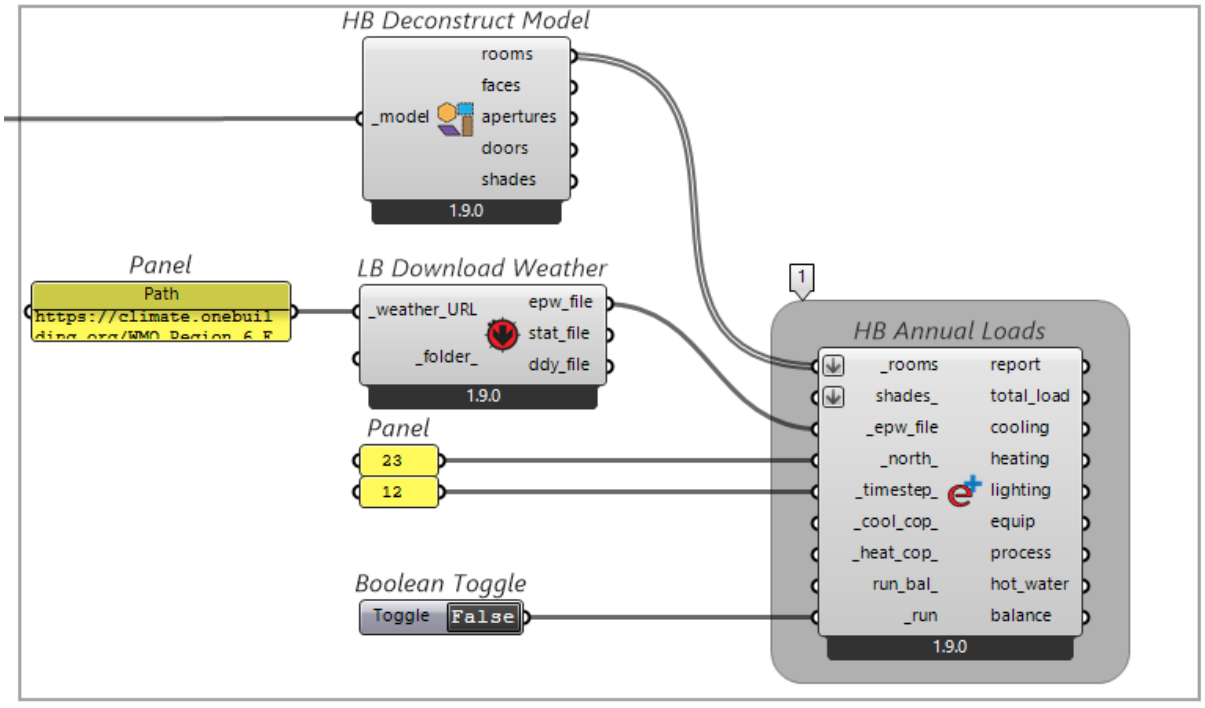

Figure 4-19 Energy simulation workflow using Honeybee–EnergyPlus integration.

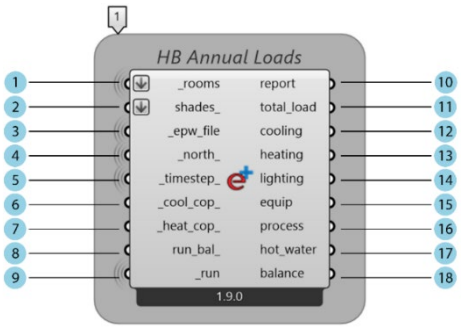

Figure 4-20 HB Annual Loads component, highlighted in Figure 4-19

Item	Description	Default Value
1	Honeybee Rooms to be simulated for annual thermal load estimation	N/A
2	Shading geometries associated with the rooms, used to account for solar obstruction	None
3	EPW weather file defining the climatic conditions for the annual simulation	N/A
4	North orientation of the model, used to adjust solar calculations	World Y
5	Simulation timestep used for the annual load calculation	Fitness 1 hour
6	Coefficient of performance (COP) for cooling, used to approximate cooling system effects	N/A
7	Coefficient of performance (COP) for heating, used to approximate heating system effect	N/A
8	Toggle to run a thermal balance calculation instead of a load calculation	False
9	Boolean toggle to execute the annual load simulation	False
10	Summary report on the simulation process and results	N/A
11	Total annual thermal load (heating, cooling, lighting, equipment, and service hot water loads)	N/A
12	Annual cooling load estimate	N/A
13	Annual heating load estimate	N/A
14	Annual lighting load estimate	N/A
15	Annual equipment load estimate	N/A
16	Annual process load estimate	N/A
17	Annual service hot water load estimate	N/A
18	Thermal balance results for the simulated rooms	N/A

Table 4-1 Summary of inputs, parameters, and outputs of the HB Annual Loads component used for annual thermal load and energy demand estimation.

Open Studio

OpenStudio is an open-source building energy modeling framework developed by the U.S. Department of Energy and the National Renewable Energy Laboratory. It provides an object-oriented data model and workflow infrastructure for organizing building energy models and managing simulation execution (Guglielmetti et al., 2011).

In this research, OpenStudio is used implicitly as an intermediate modeling layer integrated into the Grasshopper environment through Honeybee. While EnergyPlus performs numerical calculations, OpenStudio structures the energy model, manages simulation execution, and organizes results into standardized outputs, including SQL databases.

Step 4: OpenStudio work within the Grasshopper workflow

The OpenStudio workflow is constructed through a layered integration of parametric modeling and simulation components, as illustrated in Figure 4-21(A–C).

- **Input Model Assembly (A–B)**

  As shown in Figure 4-21-A and Figure 4-21-B, building geometry, thermal zones, shading elements, constructions, schedules, and operational assumptions are defined parametrically using Honeybee components within the Grasshopper environment. These elements are assembled into a complete Honeybee model representing the physical and operational characteristics of the building.

- **Model Translation (C)**

  In Figure 4-21-C, the assembled Honeybee model is translated into an OpenStudio Model (OSM) using the HB Model to OSM component. This translation converts parametric building data into an object-oriented OpenStudio structure, including zones, surfaces, internal loads, schedules, and simulation parameters.

How simulations are executed

Once the OpenStudio Model is generated, OpenStudio manages the simulation execution workflow, as illustrated in Figure 4-21-C. This includes linking the model to climatic data (EPW files), applying global simulation controls such as timestep and

orientation, and preparing the model for annual simulation. The structured workflow allows simulations to be executed automatically and consistently across multiple parametric iterations.

- **Data Flow and Outputs (D)**

  As shown in Figure 4-21, simulation results are written to an **SQL results database** managed by OpenStudio. This database serves as the primary source for post-processing within Grasshopper. From it, annual energy use, end-use breakdowns, and **Energy Use Intensity (EUI)** values are extracted and visualized. In this research, EUI constitutes the primary energy performance indicator used for evaluation and optimization, while additional load components are retained for diagnostic analysis.

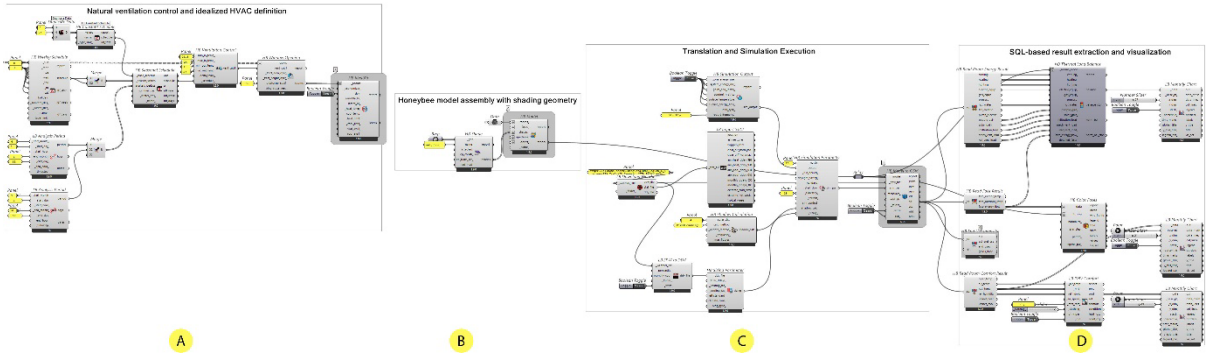

Figure 4-21 Energy simulation workflow: (A) natural ventilation and idealized HVAC definition; (B) Honeybee model assembly with shading; (C) OpenStudio model translation and simulation execution; (D) SQL-based result extraction and visualization.

A) Natural ventilation control and idealized HVAC definition

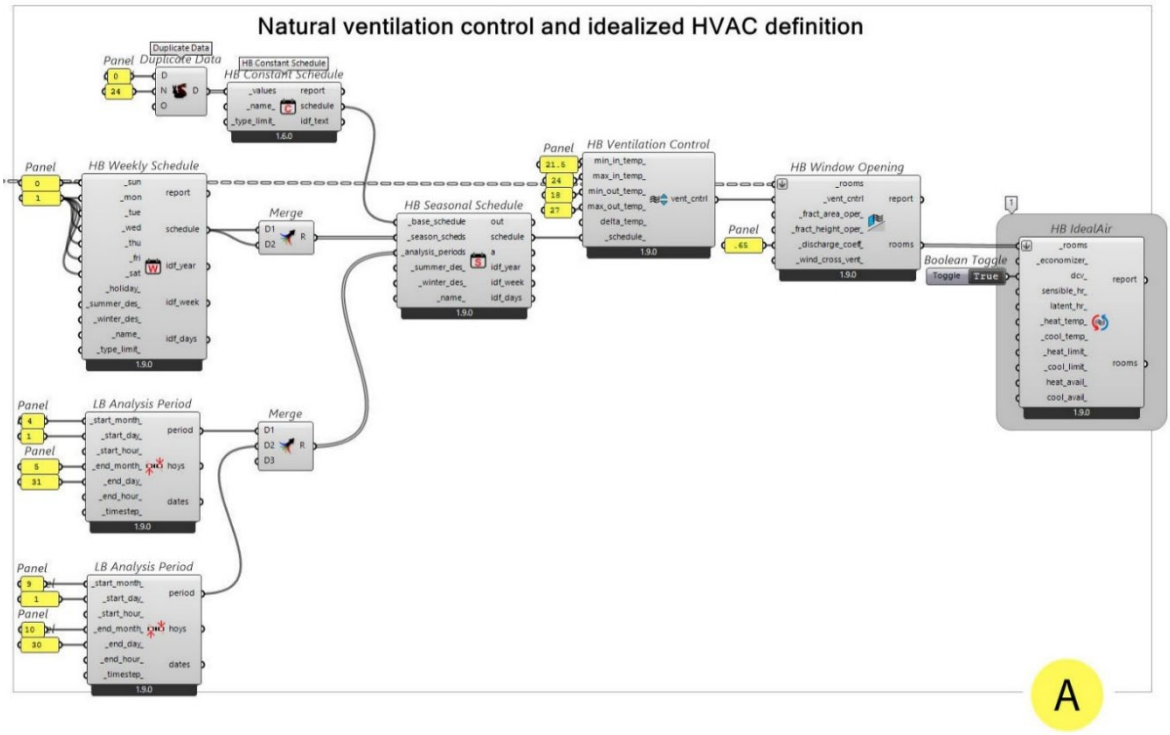

Figure 4-22 Zone-level definition of natural ventilation control and idealized HVAC operation using Honeybee components, including schedules, temperature-based ventilation logic, operable windows, and the HB Ideal Air system.

In the first phase of the workflow, natural ventilation control and thermal zone conditioning are defined at the room level. Operational schedules governing ventilation availability are established using HB Weekly Schedule, HB Seasonal Schedule, and HB Constant Schedule, which together define when natural ventilation is permitted.

Temperature-based control logic is then implemented through HB Ventilation Control, where minimum and maximum indoor and outdoor temperature thresholds regulate the activation of ventilation to ensure operation only under favorable thermal conditions. Operable window behavior is subsequently specified using HB Window Opening, including parameters such as opening fraction, discharge coefficient, and cross-ventilation potential.

These controls are coupled with an HB Ideal Air component (Figure 4-22, label 1), which supplies heating and cooling as required to maintain specified setpoints without explicitly modeling mechanical equipment. This approach isolates the building's thermal demand by decoupling load calculation from system efficiency, providing a stable and computationally efficient basis for annual energy performance assessment.

B) Honeybee model assembly with shading geometry

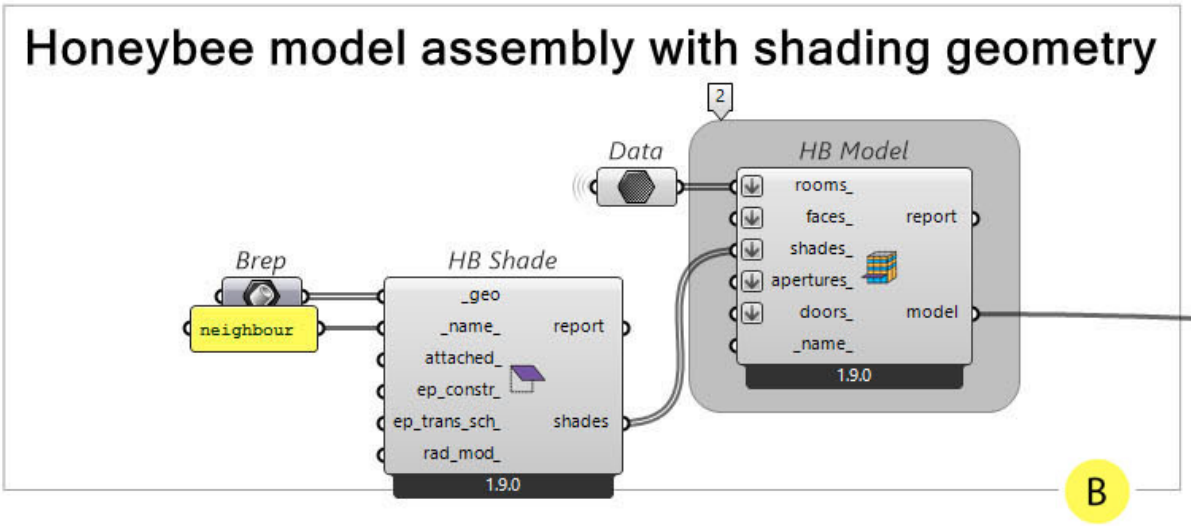

Figure 4-23 Assembly of Honeybee Rooms into a single building model with contextual shading geometry, showing the integration of thermal zones and external shading elements using the HB Model and HB Shade components prior to energy simulation.

In the second phase, the conditioned Honeybee Rooms generated in the previous step are consolidated into a single building-level representation using the HB Model component (Figure 4-23, label 2). This operation aggregates all thermal zones, faces, apertures, and doors into a coherent model suitable for energy simulation.

External context and neighboring obstructions are introduced separately through the HB Shade component, where surrounding geometries are defined as non-thermal shading elements. These shading objects are associated with the building model to account for their influence on solar access and façade exposure without being treated as conditioned spaces.

By integrating rooms and shading geometry within the HB Model, the workflow ensures that both internal thermal behavior and external solar obstruction effects are consistently represented at the building scale prior to simulation execution.

C)Translation and simulation execution

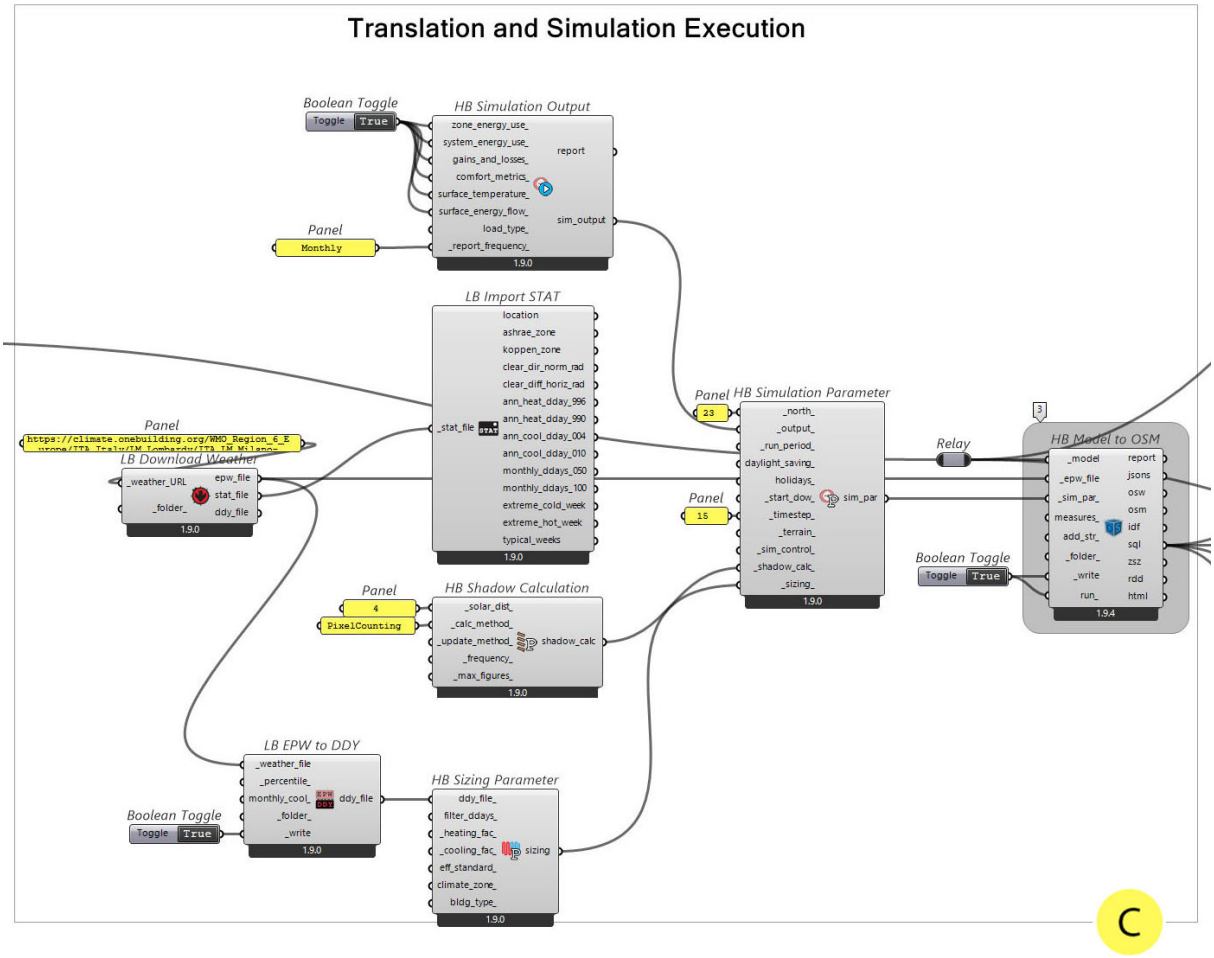

Figure 4-24 Translation of the parametric Honeybee model into an OpenStudio model and execution of the annual energy simulation with defined parameters and outputs.

In this study, the HB Model to OSM component which is highlighted in Figure 4-24 serves as the primary interface for translating the parametric Honeybee model developed in Grasshopper into the OpenStudio simulation environment (Figure 4-24). This component converts the fully defined Honeybee model, including geometry, constructions, schedules, internal loads, and simulation settings into a structured OpenStudio Model (OSM), ensuring that all parametric inputs are transferred into an object-oriented, simulation-ready format (Guglielmetti, Macumber, and Long, 2011).

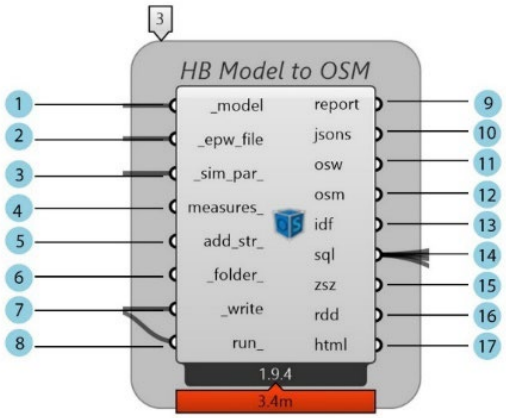

Figure 4-25 HB Model to OSM component, highlighted in Figure 4-24

Item	Description	Default Value
1	The Honeybee Model contains all geometry and energy properties to be exported and simulated.	N/A
2	EPW weather file path used for climate-driven simulation	N/A
3	Honeybee *SimulationParameter* defining run period, timestep, outputs, etc. If empty, defaults are used.	None (defaults applied)
4	Optional list of OpenStudio Measures to apply during export/workflow execution.	None
5	Optional additional EnergyPlus IDF text (advanced use) to append objects not supported by the interface.	None
6	Optional target folder to write exported files and results.	Default component run folder
7	Boolean toggle to write JSON(s) and the OpenStudio model/workflow files to disk.	False
8	Boolean (or integer “2” for silent) to translate and run the simulation, so result files are generated and returned.	N/A
9	Diagnostic log of export/run process (warnings, errors, completion info).	—
10	File paths to Honeybee JSON files (Model + SimulationParameter) written by the component.	—
11	OpenStudio Workflow file path (generated when measures are used or an OSW is required).	— / None if not needed
12	OpenStudio Model file path (.osm) generated from the Honeybee model.	—
13	EnergyPlus input file path (.idf) generated for EnergyPlus execution.	—
14	SQL results database generated after a successful run (primary results container in this study).	— / None unless run_ is True
15	CSV of detailed zone sizing / design-day load information (only produced when running).	— / None unless run_ is True
16	Result Data Dictionary listing all possible EnergyPlus output variables available for reporting.	—
17	HTML Summary Report(s) generated by EnergyPlus/OpenStudio (if requested).	—

Table 4-2 Inputs and Outputs of HB Model to OSM component

Simulation outputs and reporting frequency are defined via HB Simulation Output, enabling targeted extraction of energy and comfort-related results. Climatic boundary conditions are introduced through LB Import STAT and LB Download Weather, while HB Simulation Parameter specifies global simulation settings such as orientation, run

period, timestep, and terrain. Solar interaction and design-day–based system sizing are regulated using HB Shadow Calculation and HB Sizing Parameter, respectively. The assembled model is then executed through OpenStudio, with results written to an SQL database for automated post-processing and performance evaluation within the Grasshopper environment.

D)SQL-based result extraction and visualization

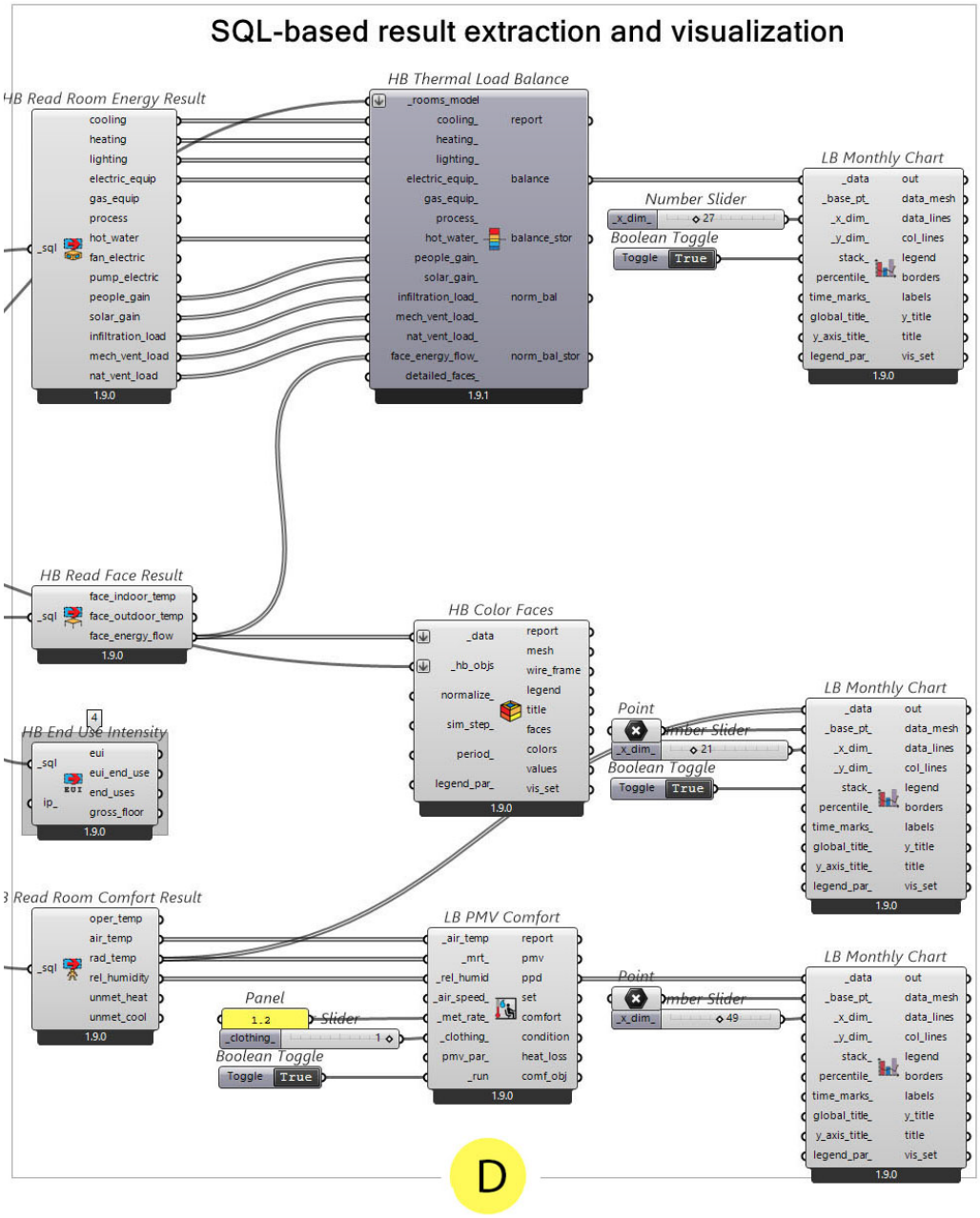

Figure 4-26 Simulation results are read from the OpenStudio SQL file, processed into energy and comfort metrics, and visualized using Ladybug charts and surface-based color mapping.

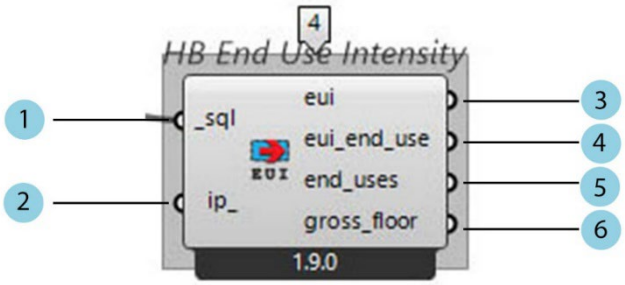

Figure 4-27 HB End use intensity component, highlighted in Figure 4-26

In the final phase, simulation results are retrieved directly from the SQL output database generated during the simulation run. The SQL file acts as a structured repository containing time-series and aggregated performance data at room, surface, and building levels.

The HB End Use Intensity component is used to extract energy performance indicators from the SQL results database generated after simulation

Energy Use Intensity (EUI) is a widely used performance indicator in building energy analysis that represents the annual energy consumption per unit floor area. It is typically expressed in kWh/m²·year (SI units) and end-use energy breakdowns from the simulation of SQL output, consistent with ASHRAE- and LEED-based energy performance assessment methodologies.

EUI end uses refer to the subdivision of total EUI into individual functional categories of energy consumption. These typically include:

- **Heating EUI** – energy used for space heating
- **Cooling EUI** – energy used for space cooling
- **Lighting EUI** – energy used for interior lighting
- **Equipment EUI** – energy used by plug loads and appliances
- **Fans and Pumps EUI** – energy used for air and fluid movement
- **Domestic Hot Water EUI** – energy used for hot water production

This end-use breakdown enables a more detailed interpretation of simulation results by linking energy demand to specific building systems and operational functions. Energy-related results; including heating, cooling, lighting, equipment, ventilation, and internal gains; are extracted using HB Read Room Energy Result and further processed through HB Thermal Load Balance to decompose thermal contributions and evaluate heat balance and storage effects. Envelope-related outputs, such as surface temperatures and heat fluxes, are obtained via HB Read Face Result. Indoor comfort conditions are assessed through HB Read Room Comfort Result and LB PMV Comfort, enabling the analysis of operative temperature, thermal comfort indices, and discomfort periods. Finally, results are visualized using LB Monthly Chart and HB Color Faces allowing spatial and temporal interpretation of energy use, thermal behavior, and comfort performance across different zones and simulation periods.

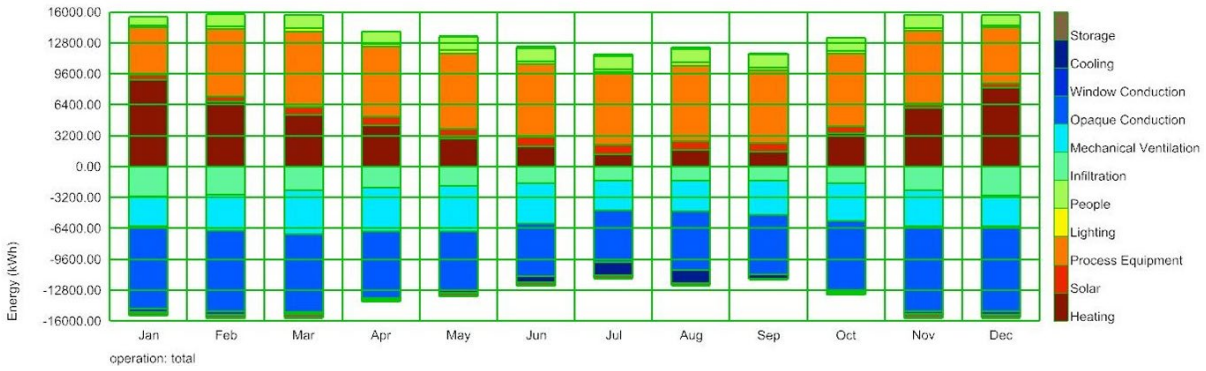

Figure 4-28 Monthly energy balance showing the contribution of heating, cooling, lighting, equipment, ventilation, solar gains, and thermal storage, derived from HB Read Room Energy Result and processed using HB Thermal Load Balance.

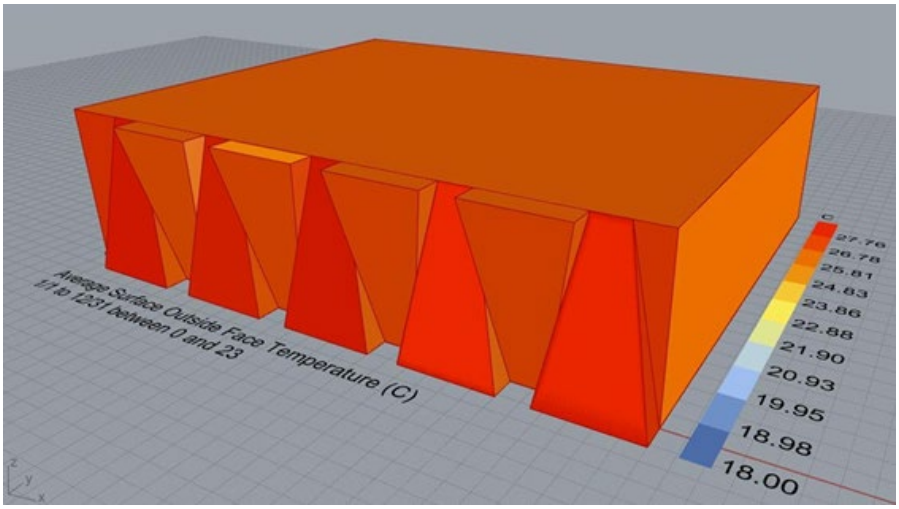

Figure 4-29 Spatial distribution of exterior surface temperatures obtained using HB Read Face Result,

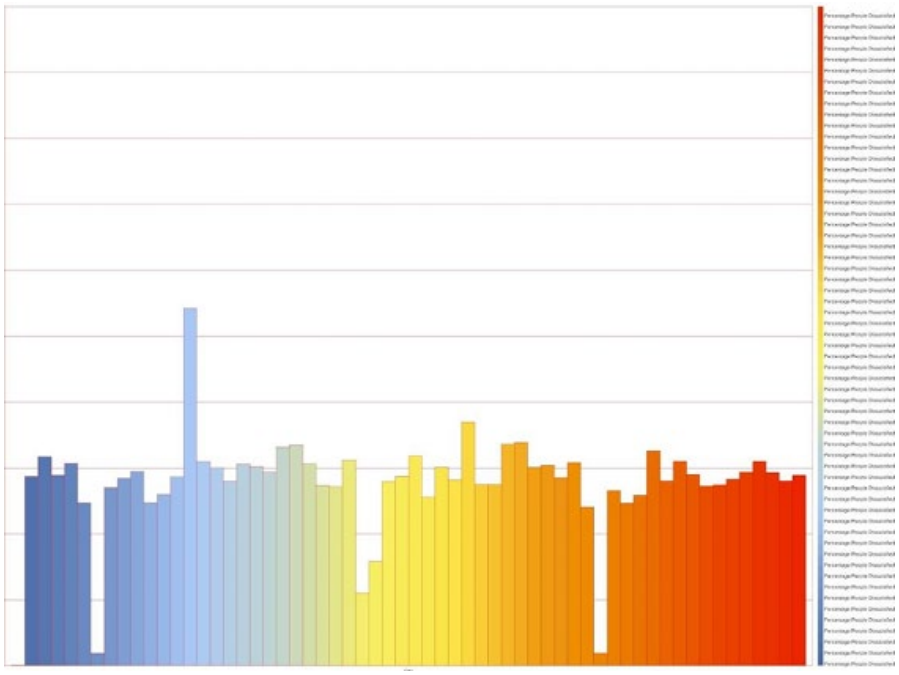

Figure 4-30 Thermal comfort performance evaluated using HB Read Room Comfort Result and LB PMV Comfort, showing operative temperature trends and the percentage of occupants dissatisfied (PPD) over the simulation period.

4.1.4 Honeybee Radiance

Daylight simulation is a computational process that numerically models the behavior of natural light within and around a building using physically based algorithms. In this study, daylight simulation is performed using a Radiance-based engine via Honeybee and Ladybug, driven by climate data from EPW weather files. The simulation calculates illuminance, and glare-related quantities at discrete sensor points under defined sky and time conditions.

Daylight simulation itself does not evaluate performance; rather, it generates raw, quantitative daylight data based on geometry, materials, sky models, and sensor placement.

Step 5: **Daylight simulation**

A) Daylight Sensor Grid Generation and Operation

The purpose of this workflow (Figure 4-31) is to prepare a geometrically and contextually accurate building model for daylight simulation by defining exterior

obstructions, generating sensor grids on interior surfaces, and associating these grids with the Honeybee model. This ensures that daylight metrics are evaluated at representative locations within occupied spaces while accounting for surrounding shading effects.

Method

First, surrounding buildings and contextual obstructions are modeled using HB Shade, where neighboring geometries are defined as external shading elements. These shades are connected to the HB Model component to ensure that their impact on daylight availability is included in the simulation.

Weather data is introduced through HB Wea From EPW, which converts the EPW file into a Radiance-compatible WEA format, providing sky and solar data required for daylight calculations.

Interior analysis surfaces are selected and discretized using LB Generate Point Grid, where sensor points are generated based on a specified grid size and offset distance. The grid size controls sensor density, while the offset distance moves sensors away from surfaces to avoid self-intersection errors during ray tracing.

The generated points are then converted into a Radiance-compatible sensor grid using HB Sensor Grid, where sensor directions are defined to represent the measurement orientation within the space. Finally, the sensor grids are linked to the building model using HB Assign Grids and Views, ensuring that all subsequent daylight simulations reference the same spatial sampling framework.

Metrics & Standards

Sensor grid generation follows best practices aligned with LEED v4/v4.1 daylight simulation guidelines, which require spatially distributed sampling across regularly occupied floor areas. A grid spacing of 0.5 m provides a resolution higher than the commonly accepted 0.6–1.0 m range used in LEED daylight assessments, improving spatial accuracy. An offset distance of 0.8 m positions sensors near work-plane height,

consistent with LEED and IES recommendations for occupied zones and Radiance-based daylight analysis.

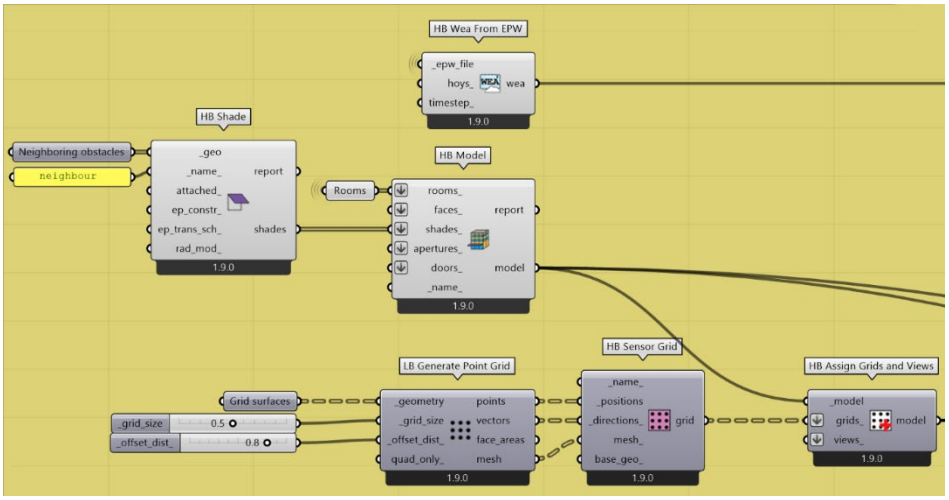

Figure 4-31 Honeybee-based daylight simulation setup integrating climate data, building geometry, shading, and sensor grids.

B) Daylight Factors Considered in This Study

Analytical Approach	Evaluation Objective	Daylight Metric	Description	Reference Standard
Static	Quantification of daylight availability at specific moments	Illuminance (lux)	Horizontal illuminance evaluated at equinox dates (March & September) at 9:00 and 15:00, within the range 300–3000 lux, to assess compliance with LEED daylight criteria under representative sky conditions.	LEED v4/v4.1 IEQ Daylight
Static	Assessment of daylight penetration efficiency	Daylight Factor (DF)	Ratio of indoor illuminance to simultaneous outdoor illuminance under overcast sky conditions, used to evaluate daylight potential independent of climate variability.	CIE / BRE
Dynamic	Annual daylight availability	Daylight Autonomy (DA)	Percentage of occupied hours during which a minimum illuminance threshold (300 lux) is met by daylight alone at each sensor point	IES / LEED
Dynamic	Spatial daylight performance	Spatial Daylight Autonomy (sDA300/50%)	Percentage of floor area achieving at least 300 lux for a minimum of 50% of annual occupied hours; primary LEED daylight performance metric	LEED v4/v4.1
Dynamic	Useful daylight range assessment	UDI (300–3000 lux)	Percentage of time when illuminance remains within the useful range, avoiding under-lit and over-lit conditions.	Nabil & Mardaljevic
Dynamic	Insufficient daylight identification	UDI-Low (<100 lux)	Fraction of occupied time when daylight levels are insufficient, indicating dependence on artificial lighting.	IES
Dynamic	Excessive daylight / glare risk	UDI-Up (>3000 lux)	Fraction of occupied time with excessive illuminance, associated with visual discomfort and glare potential.	IES
Dynamic	Annual direct sun exposure	ASE1000,250	Percentage of floor area receiving more than 1000 lux of direct sunlight for over 250 occupied hours per year; used to identify glare and overheating risk.	LEED v4/v4.1
Dynamic	Annual glare performance	Spatial Glare Autonomy (sGA)	Percentage of sensors that remain below the glare threshold for a defined fraction of occupied hours,	IES / Honeybee

Table 4-3 Daylight Factors Considered in This Study.

1)What is Illuminance?

Illuminance is a photometric quantity that describes the amount of visible light falling on the surface. It represents how well a space is lit and is measured in lux, where:

1 lux = 1 lumen per square meter (lm/m²)

The purpose of this analysis is to evaluate whether the indoor spaces achieve adequate daylight availability without excessive glare, in accordance with LEED v4 / v4.1 daylight performance requirements. The focus is on identifying the proportion of occupied areas that receive illuminance levels suitable for visual comfort and functional use.

Method

A point-in-time, grid-based daylight simulation as illustrated in Figure 4-32 is performed using a climate-based sky model for September at 15:00. Sensor grids are generated over the analysis surfaces and assigned to the building model. Illuminance values are computed at each sensor point using a Radiance-based simulation, accounting for building geometry, material properties, and sky conditions.

Metrics and Standards

Daylight performance is evaluated using horizontal illuminance (lux) at the work-plane level. In accordance with LEED v4/v4.1 (IEQ Credit: Daylight), acceptable daylight conditions are defined by illuminance values between 300 and 3000 lux, ensuring sufficient visual comfort while limiting over-illumination.

Point-in-time simulations are conducted for March and September at 9:00 and 15:00, representing equinox conditions and typical occupied hours permitted under LEED guidelines. Compliance is achieved when at least 75% of the regularly occupied floor area falls within the 300–3000 lux range, indicating successful daylight performance and eligibility for the LEED daylight credit.

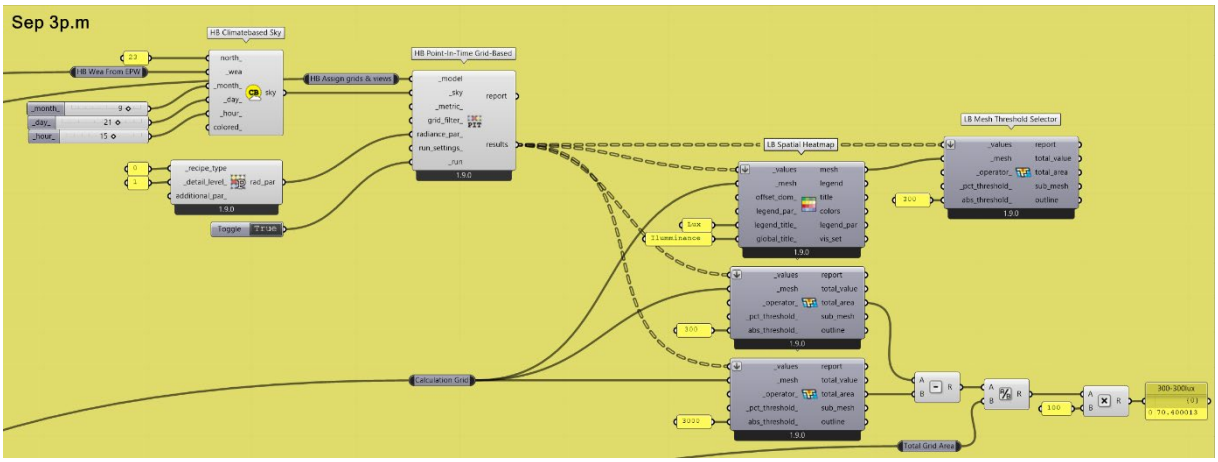

Figure 4-32 Point-in-time daylight simulation workflow for September at 15:00, evaluating indoor illuminance distribution against LEED thresholds.

2)What is Daylight Factor?

The Daylight Factor (DF) is a static daylight performance metric that expresses the ratio between indoor illuminance at a given point and the simultaneous outdoor horizontal illuminance under a standard CIE overcast sky, expressed as a percentage.

DF (%) = (Indoor Illuminance /Outdoor Illuminance) ×100

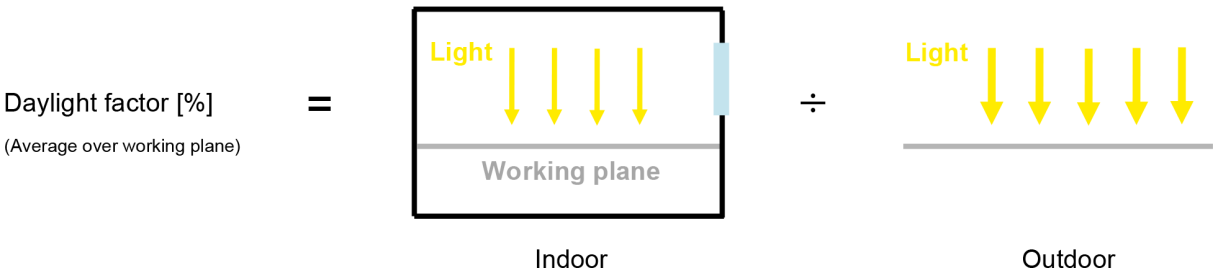

DF is independent of orientation and time of day and is therefore commonly used to evaluate the intrinsic daylighting potential of a space based on geometry, glazing, and material properties.

The Daylight Factor analysis is conducted to evaluate the availability and spatial distribution of diffuse daylight within the studied spaces under standardized overcast sky conditions. This metric provides an orientation- and climate-independent assessment of baseline daylight sufficiency.

Method

The analysis is performed using a grid-based Radiance workflow in Grasshopper as shown in Figure 4-33. Sensor grids are generated on interior floor surfaces and assigned to the building model. Daylight Factor values are computed using the HB Daylight Factor component, with simulation parameters defined through HB Radiance Parameter and HB Recipe Settings. Spatial distributions are visualized using LB Spatial Heatmap, and area-based classification is quantified via LB Mesh Threshold Selector.

Metrics & Standards

Daylight Factor (DF) is defined as the ratio of indoor illuminance to simultaneous outdoor horizontal illumination under a CIE overcast sky, expressed as a percentage. According to widely accepted daylighting guidelines and design practice:

- **DF < 2%** → insufficient daylight
- **DF = 2–5%** → adequately daylit space
- **DF > 5%** → well-daylit space, with potential glare risk if excessive

These thresholds are commonly referenced in architectural daylight assessments and are used here to classify daylight performance across the floor area.

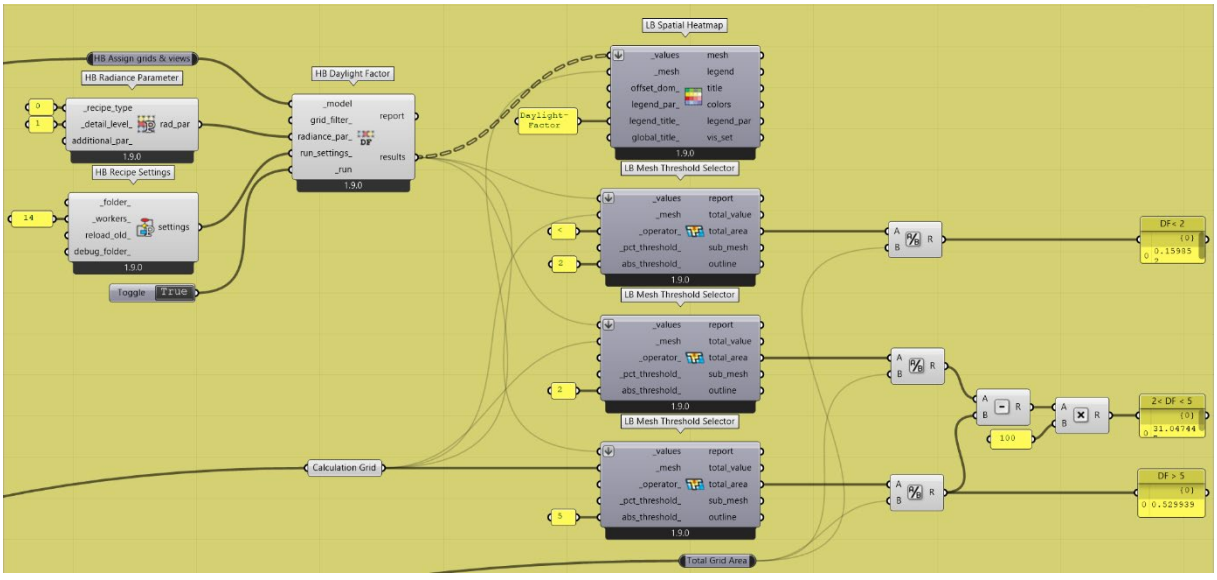

Figure 4-33 Daylight Factor simulation workflow

3)Daylight Autonomy

The purpose of this analysis is to evaluate the extent to which occupied spaces are adequately daylit by natural light throughout the year, using climate-based daylight metrics compliant with LEED v4/v4.1 Indoor Environmental Quality (IEQ) – Daylight requirements.

Method

Annual daylight performance was simulated using HB Annual Daylight based on a climate-based Radiance workflow (Figure 4-34). A sensor grid was generated across occupied floor areas and assigned to the building model using HB Assign Grids and Views.

Daylight Autonomy (DA) and Spatial Daylight Autonomy (sDA) were computed assuming a 300-lux illuminance threshold during occupied hours, defined through HB Constant Schedule. Results were post-processed and visualized using LB Spatial Heatmap, while compliance areas were quantified using LB Mesh Threshold Selector and HB Spatial Daylight Autonomy.

Metrics & Standards

Daylight Autonomy (DA): Percentage of occupied hours in which a point receives at least 300 lux from daylight alone.

Spatial Daylight Autonomy (sDA300/50%): Percentage of regularly occupied floor area that achieves ≥300 lux for at least 50% of annual occupied hours.

LEED v4/v4.1 Pass Threshold:

- sDA300/50% ≥ 55% → minimum compliance

- sDA300/50% ≥ 75% → exemplary performance
  (Source: USGBC, LEED v4/v4.1 BD+C IEQ Credit: Daylight).

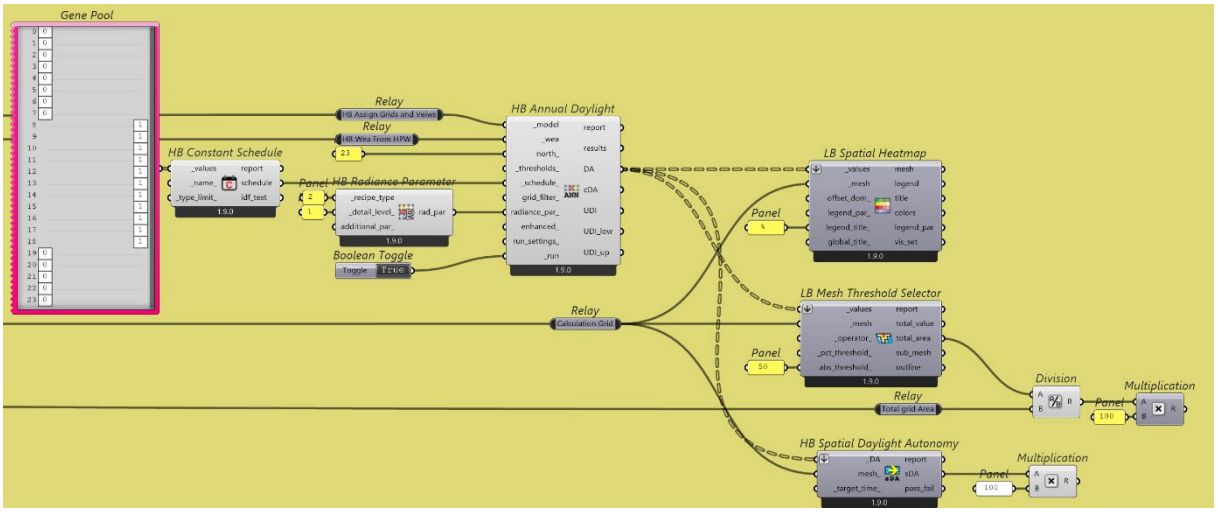

Figure 4-34 Parametric Honeybee workflow for annual daylight simulation and evaluation of UDI and sDA metrics.

Useful Daylight Illuminance (UDI)

The purpose of the Useful Daylight Illuminance (UDI) analysis is to evaluate the quality of daylight distribution within the occupied spaces by distinguishing between insufficient, useful, and excessive daylight levels. This assessment complements sDA and ASE metrics by providing a more nuanced understanding of visual comfort and potential glare risk across the floor area.

Method

UDI metrics were calculated using HB Annual Daylight, combined with HB Spatial Daylight Autonomy, based on sensor grids generated across interior spaces. Annual illuminance values at each sensor point were processed and visualized using LB Spatial Heatmap, while area-weighted percentages were quantified through LB Mesh Threshold Selector. Separate threshold filters were applied to isolate UDI, UDI Low, and UDI Up conditions across the same calculation grid.

Metrics & Standards

UDI classifies daylight performance based on horizontal illuminance ranges as defined in climate-based daylighting literature and adopted in LEED-aligned workflows:

UDI Low (Figure 4-36): Illuminance < 100 lux (insufficient daylight)

UDI (Useful, Figure 4-35): 300–3000 lux (visually comfortable and usable daylight)

UDI Up (Figure 4-37): Illuminance > 3000 lux (excessive daylight with potential glare or visual discomfort)

While LEED v4/v4.1 does not directly award credits based on UDI, these thresholds are widely used to support interpretation of sDA (300/50%) and ASE (1000/250) compliance by identifying over- and under-lit zones.

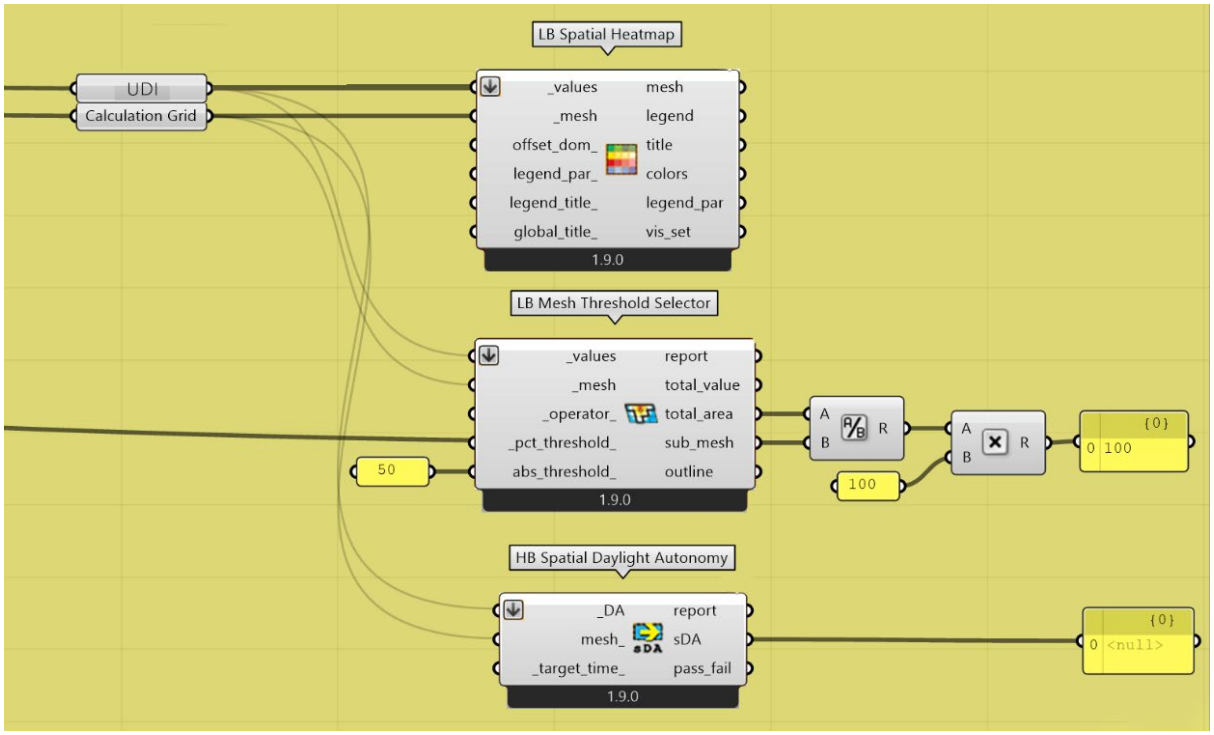

Figure 4-35 Workflow for annual daylight performance evaluation, illustrating UDI

UDI Low

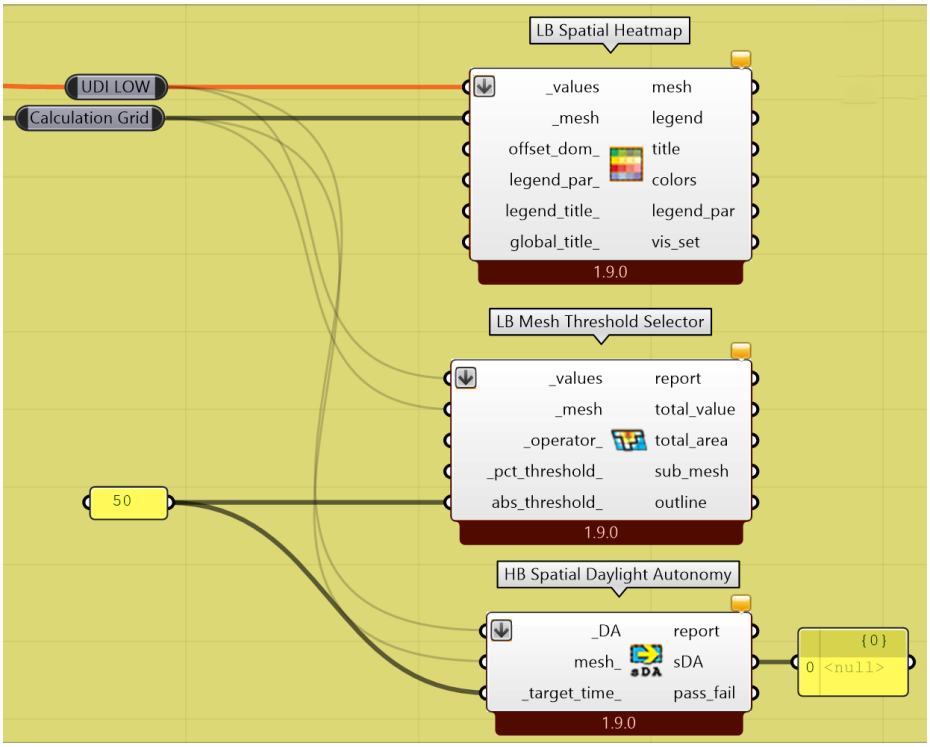

Figure 4-36 Workflow for annual daylight performance evaluation, illustrating UDI Low

UDI UP

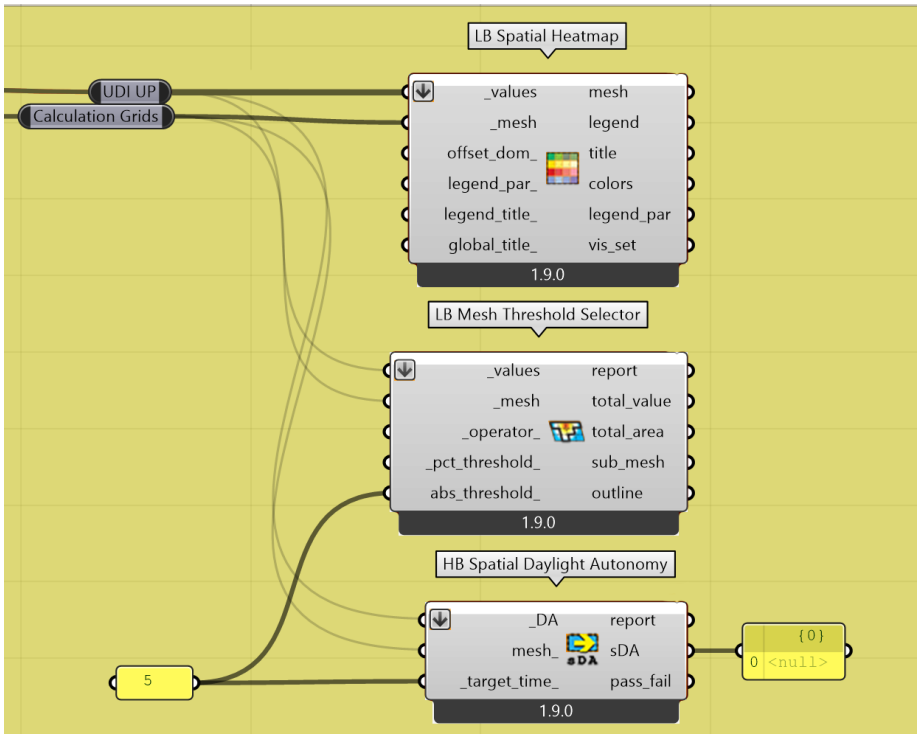

Figure 4-37 4 37 Workflow for annual daylight performance evaluation, illustrating UDI Up

4)Annual Sunlight Exposure (ASE)

ASE measures the percentage of floor area that receives direct sunlight exceeding a specified illuminance level for more than a defined number of hours per year. ASE is used to assess the risk of excessive direct sunlight, which can cause glare and thermal discomfort, and is a mandatory control metric in LEED daylight evaluation. The workflow is represented in Figure 4-38.

Method

ASE is calculated using HB Direct Sun Hours with annual weather data. Direct sunlight hours exceeding the illuminance threshold are identified at each sensor point, and spatial aggregation is performed using LB Mesh Threshold Selector and LB Spatial Heatmap.

Metrics & Standards

According to LEED v4 / v4.1 – IEQ Daylight Credit:

$ASE_{1000,250}$: Percentage of floor area receiving ≥1000 lux of direct sunlight for more than 250 hours per year

Pass Criterion:

- ASE ≤ 10% → acceptable level of direct sunlight (LEED compliant)
- ASE > 10% → excessive direct sunlight, indicating potential glare risk

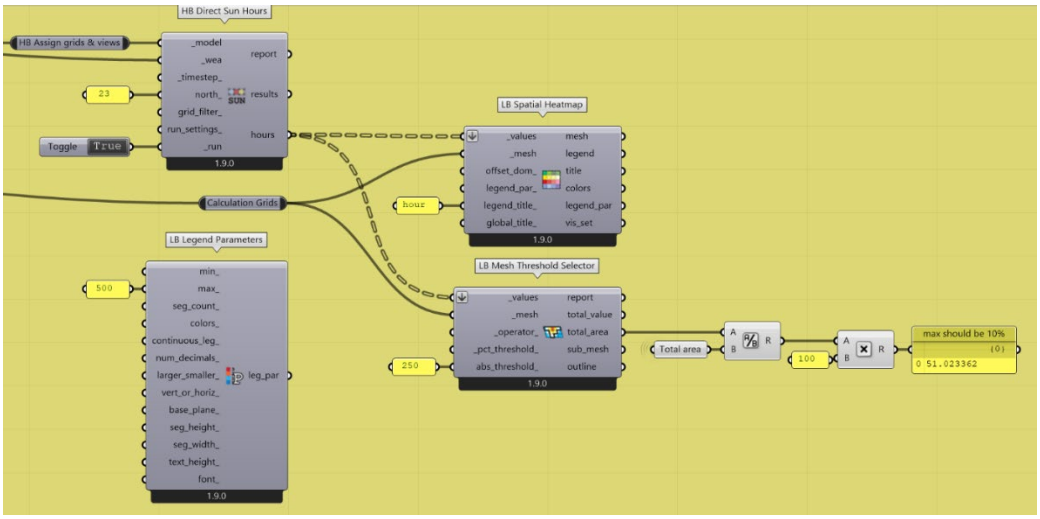

Figure 4-38 Workflow for Annual Sunlight Exposure (ASE) assessment, showing calculation of direct sun hours on the sensor grid

5)Spatial glare autonomy(sGA)

The purpose of evaluating Spatial Glare Autonomy (sGA) is to assess whether high daylight availability leads to visual discomfort due to glare, and to verify that daylight performance remains visually acceptable across occupied spaces.

Method

sGA is calculated using a climate-based glare simulation workflow in Honeybee–Radiance as shown in Figure 4-39. Sensor grids previously defined for daylight analysis are assigned to the building model and evaluated using HB Imageless Annual Glare and HB Annual Glare Metrics. For each sensor point, glare conditions are computed over occupied hours based on Radiance-based glare calculations, and compliance is evaluated relative to a defined glare threshold.

Metrics & Standards

Spatial Glare Autonomy (sGA) is defined as the percentage of sensor points within a space that do not exceed a specified glare threshold for a given fraction of occupied hours.

In the LEED v4 / v4.1 Daylight (IEQ Credit) framework:

sGA is used as a supporting control metric alongside Spatial Daylight Autonomy (sDA). Excessive glare indicates overexposure even if sDA targets are met. While LEED does not prescribe a fixed pass value for sGA, best-practice guidance requires that glare occurrence be limited so that spaces achieving sDA are not visually uncomfortable, often interpreted as glare occurring in no more than 10% of occupied hours for compliant areas.

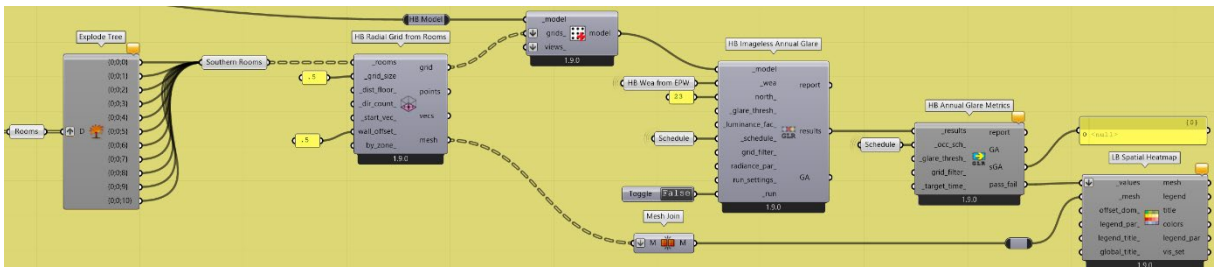

Figure 4-39 Spatial Glare Autonomy (sGA) workflow illustrating image-based annual glare simulation, glare metric evaluation, and spatial mapping of glare-compliant sensor areas.

4.2 Optimization Tool (Wallacei)

The theoretical explanations in the following were gathered generally as the whole concepts learned commonly through the Wallacei video tutorials and articles published on their official website, Wallacei group in the McNeel grasshopper forum and finally participation in optimization workshops by our team.

Here's the explanation of Wallacei components:

X Component:

Wallacei X is the primary component of the Wallacei platform. Through Wallacei X, the user can run an evolutionary algorithm, analyze the results, run selection methods, export phenotypes, all within one user interface. Additionally, Wallacei X incorporates the JMetal, LiveCharts and HelixToolkit open-source libraries.

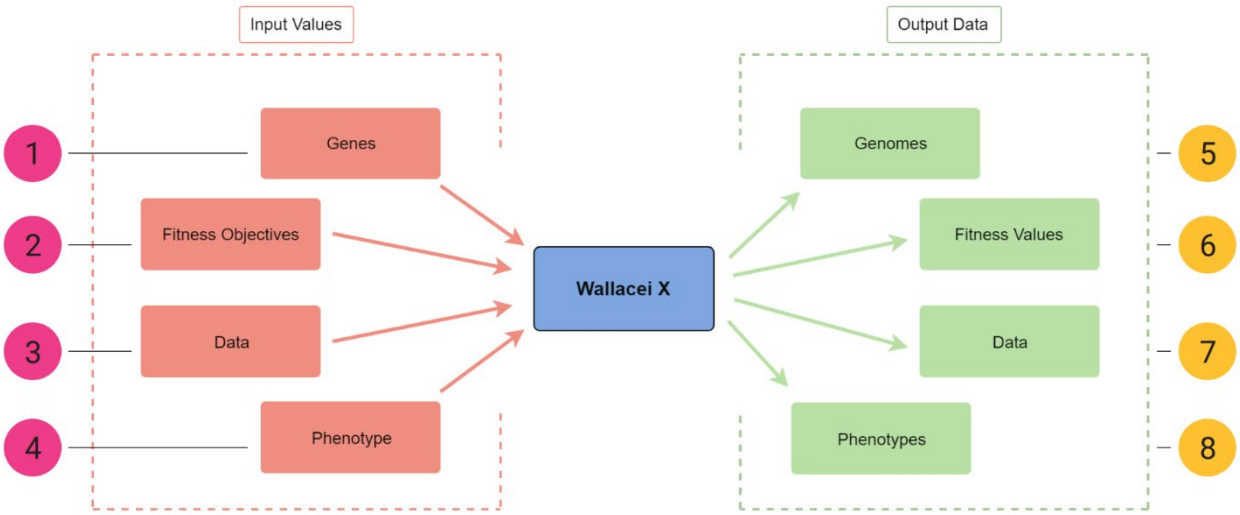

Figure 4-40 Wallacei X component in Grasshopper. Source: Showkatbakhsh et al. (2018).

1) Genes are comprised of slides or genepools. Rename the slides/genepools with prefix 'wlc_' for automated selection (by right clicking the Wallacei X component and clicking 'Select all Sliders').
2) Fitness Objectives are values contained within a 'number' component. Rename the fitness objectives with prefix 'wlc_' for automated selection (by right clicking the Wallacei X component and clicking 'Select all Objectives').
3) Any data type to be saved for every solution in the population (it is recomended only numerical data is inputted to avoid CPU overload causing grasshopper/rhino to crash).

4) The phenotypes that will be exported through the solver. Any data type is accepted such as Breps, Meshes or Numbers (the phenotypes can be inputted after you run the simulation).
5) This outputs the genomes of all solutions in the population. To access the Genome, use the 'Decode Genome' component to extract numerical values comprising each solution's genome
6) This outputs the fitness values of all solutions in the population. The list structure is as follows {A; B}[i], where 'A' is the generation number, B' is the solution number and 'i' is the fitness values for each fitness objective
7) This outputs the input data of all solutions in the population.
8) This outputs the phenotypes of the exported solutions. To access the geometry within the phenotype, use the 'Decode Phenotypes' or 'Distributor' components, which will output the data into different streams (numbers, meshes, breps, etc.)

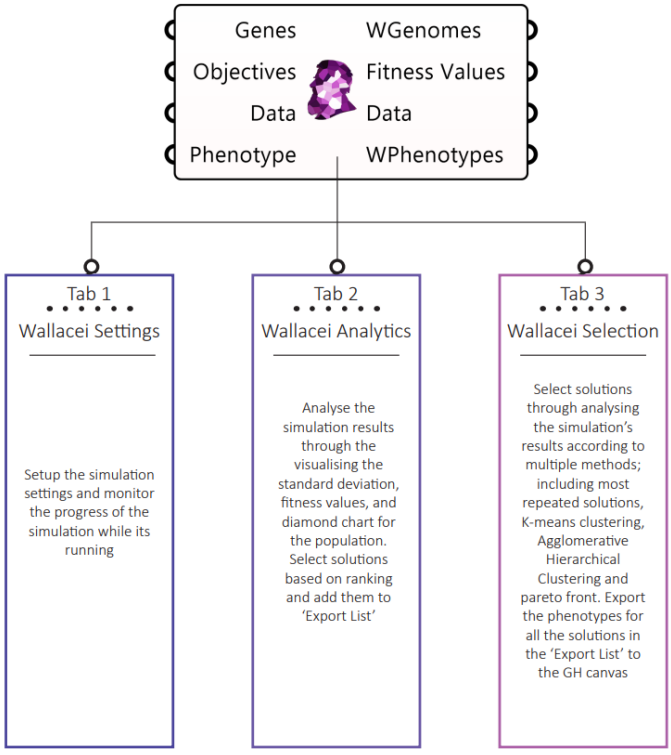

Figure 4-41 Wallacei X component, tabs general explanation.

Tab 1: Tab 1 of the Wallacei X user interface is the primary tab for setting up the simulation parameters before running the evolutionary algorithm.

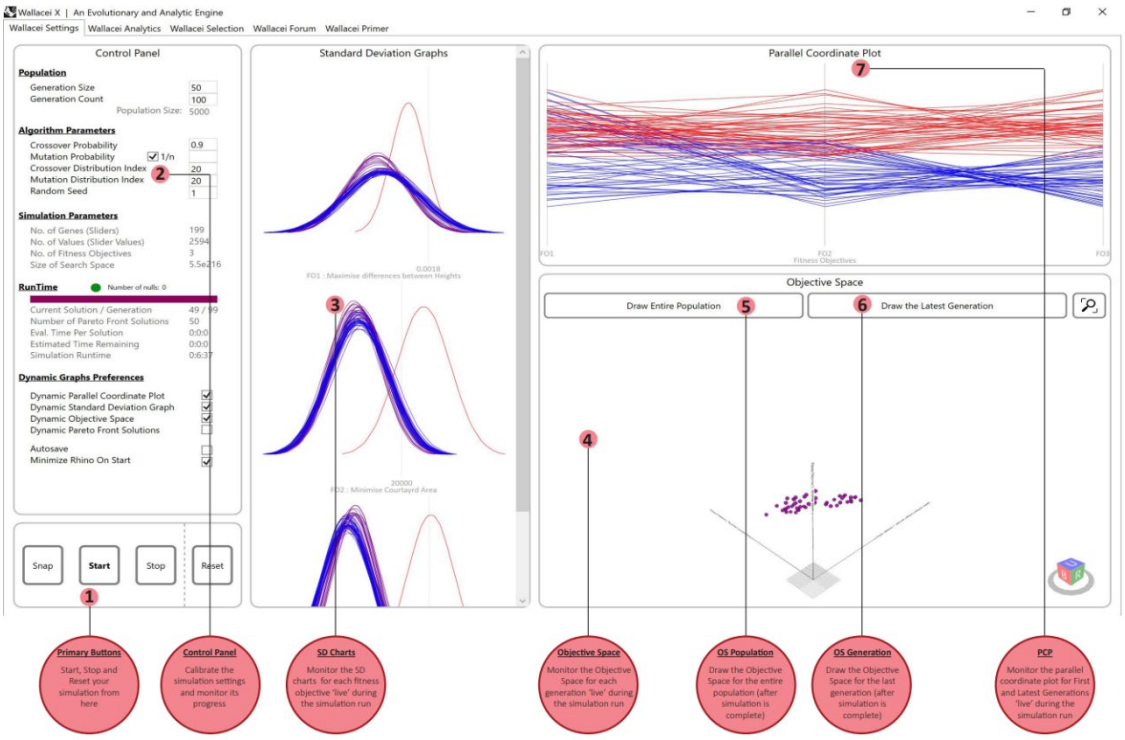

Figure 4-42 Wallacei X components, Tab 1 interface.

Control Panel:

Population: Set the generation size (how many individuals per generation) and generation count (how many generations in the simulation) for your simulation.

Algorithm Parameters: Crossover Probability (0.0 to 1.0) - the percentage of solutions in the generation that will reproduce for the next generation.

Mutation Probability (0.0 to 1.0) - The percentage of mutations taking place in the generation (Deb et. al. recommends the mutation probability to be 1/n, where ‘n’ is the number of variables (sliders) in the design problem. As such, the default value is 1/n).

Crossover and Mutation Distribution Index (0 to 100) - A large distribution index value gives a higher probability for creating offspring near parent solutions and a small distribution index value allows distant solutions to be selected as children’s solutions.

Dynamic Graphs Preferences: Toggle to allow Wallacei to draw the different graphs live as the simulation is running. The SD graphs draw the first generation and the latest 50 generations, the Parallel Coordinate Plot draws the first and latest generation and the Objective Space draws the latest generation. The primary aim of these 'live graphs' is to give the user an indication of the simulation's performance in the early stages of the simulation's runtime.

SD Charts:

Dynamically draws the Standard Deviation chart for each fitness objective independently. The Curves are coloured from red (first generation) to blue (latest generation). The SD charts display the curves for the FIRST generation and the latest FIFTY generations. This is to minimise simulation runtime while simultaneously providing the user with a clear representation of the simulation's progress.

Objective Space:

Dynamically draws the objective space for each generation in the simulation. The objective space can display up to 6 dimensions, X, Y, Z, Colour, Size, and Transparency. The Pareto Front solutions are represented in the objective space as yellow cubes.

Objective Space - Draw entire population:

Once the simulation is complete, this button becomes enabled allowing the user to display the objective space for all the solutions in the population.

Objective Space - Draw Latest Generation:

Once the simulation is complete, this button becomes enabled allowing the user to display the objective space for last generation in the population.

Parallel Coordinate Plot:

Dynamically draws the parallel coordinate plot for the simulation. To reduce simulation runtime, the parallel coordinate plot is drawn for the first and latest generation in the simulation (red to blue).

Tab 2: Tab 2 of the Wallacei X user interface is the primary tab for analysing the simulation's results and cross-referencing the different fitness objectives to one another

Figure 4-43Wallacei X components, Tab 2 interface.

Primary Buttons:

Snap: Takes a screenshot of your screen and saves it to the desktop. It is recommended you maximize the user interface window before taking a screen shot for best results.

Draw: Draws the graphs for all solutions in the population. This is the primary button for this tab as it enables all other features available within Tab 2.

Select: Highlights the selected solution in the graphs as well as the Diamond Fitness Chart of the selected solution.

Add: Adds the selected solution to the 'Export List' located in tab 3.

Selection:

Users can select a solution using one of two methods. The first is by inputting the generation and solution number; the second is by inputting the fitness objective and the solution's fitness rank. Once the selection fields have been filled, click 'Select' to display the solution in the graphs.

Diamond Fitness Chart:

Draw the diamond fitness chart for the selected solution. Each axis on the diamond chart represents a fitness objective. The closer the point to the center of the diamond chart the fitter the solution.

Standard Deviation Chart (red to blue - first generation to last generation):

Draws the standard deviation chart for all generations in the population for each fitness objective independently. Double clicking the chart maximises it to full screen

Fitness Value Chart (red to blue - first generation to last generation):

Draws the fitness value chart for all solutions in the population for each fitness objective independently. Double clicking the chart maximises it to full screen

Standard Deviation Trendline Chart:

Plots the standard deviation values for each generation as a line chart (first to last generation are plotted from left to right) for each fitness objective independently. Double clicking the chart maximises it to full screen

Mean Value Trendline Chart:

Plots the mean fitness value for each generation as a line chart (first to last generation are plotted from left to right) for each fitness objective independently.

Tab 3: Tab 3 of the Wallacei X user interface is the primary tab for analysing the results of the simulation for the purpose of selection and export. To start analysing through any of the methods provided, you must first 'DRAW PARALLEL COORDINATE PLOT'.

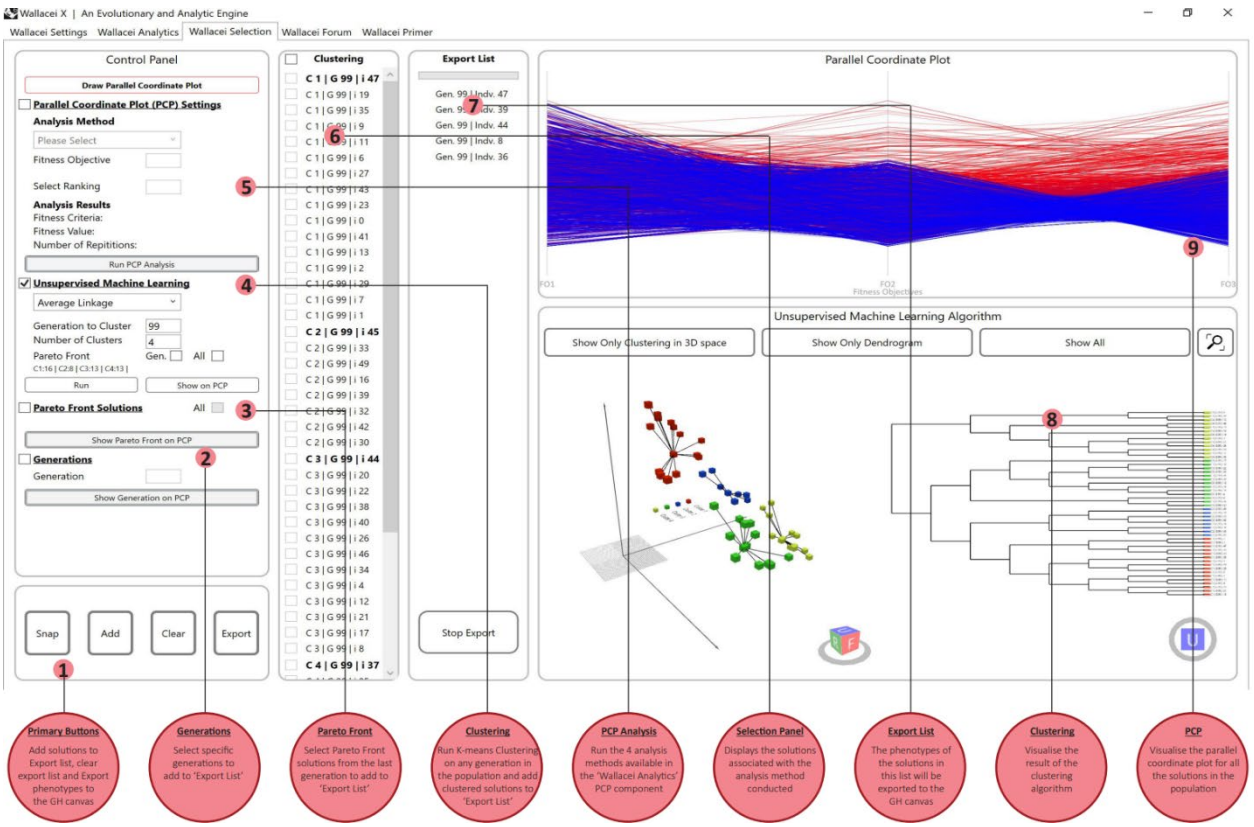

Figure 4-44 Wallacei X components, Tab 3 interface.

Primary Buttons:

Snap: Takes a screenshot of the screen and saves it to the desktop. It is recommended to maximize the user interface window before taking a screen shot for best results.

Add: Adds the selected solutions from panel (6) to the export list (panel (7)).

Clear: Clears the solutions in the 'Export List' (panel (7))

Reset: Exports on the phenotypes of the solutions added to the 'Export List' (panel (7)).

Parallel Coordinate Plot Analysis:

The parallel coordinate plot analysis provides four analytic methods to reorder the solutions in the population

- Most repeated fitness values
- Solutions with most repeated fitness values
- Relative difference between fitness ranks
- average fitness rank

Unsupervised Machine Learning

Cluster solutions generated by simulation. The user can cluster solutions from any given generation, or the Pareto front of any given generation, or the Pareto front of the entire population, using two primary clustering algorithms – K-means Clustering and Agglomerative Hierarchical Clustering (which includes within it three sub clustering methods; Single Linkage, Average Linkage and Complete Linkage). The user can also display the clustered solutions on the parallel coordinate plot. The order of the clustered solutions in the selection panel (panel (6)) is according to each solution's distance from the cluster's center. The solution highlighted in bold is the cluster center.

Pareto Front Solutions:

Displays the Pareto front solutions of either the final generation or of the entire population (by calculating dominance values of all the solutions in the population) in the selection panel (6). The pareto front solutions can be displayed in the parallel coordinate plot to compare them with the remaining solutions in the population.

Generations

Displays the generations in the selection panel (6). This is for users who wish to export complete generations (as opposed to only solutions within generations).

Selection Panel:

Solutions corresponding to the analytic method chosen are displayed here. Users can add specific solutions from this list to the 'Export List' (panel (7)).

Export List:

These are the solutions that will be exported to the canvas. When a user clicks the ‘Export’ button, a popup will appear with a estimated export time. Please note that this is an estimation only.

Clustering Viewport:

Display the results of the Clustering algorithm. Kmeans clustering will display the results on the objective space only, however when running the Hierarchical clustering, the results can be displayed in the objective space as well as the Dendogram (which is the typical representation method for hierarchical clustering)

Parallel Coordinate Plot:

Displays the Parallel coordinate plot for ALL solutions in the population (red to blue - first solution to last solution). Double clicking the chart maximises it to full screen. Reminder: to utilise any of the selection methods in tab 3, the parallel coordinate plot must first be drawn.

Fitness Value Component:

This is how its related component comes into action:

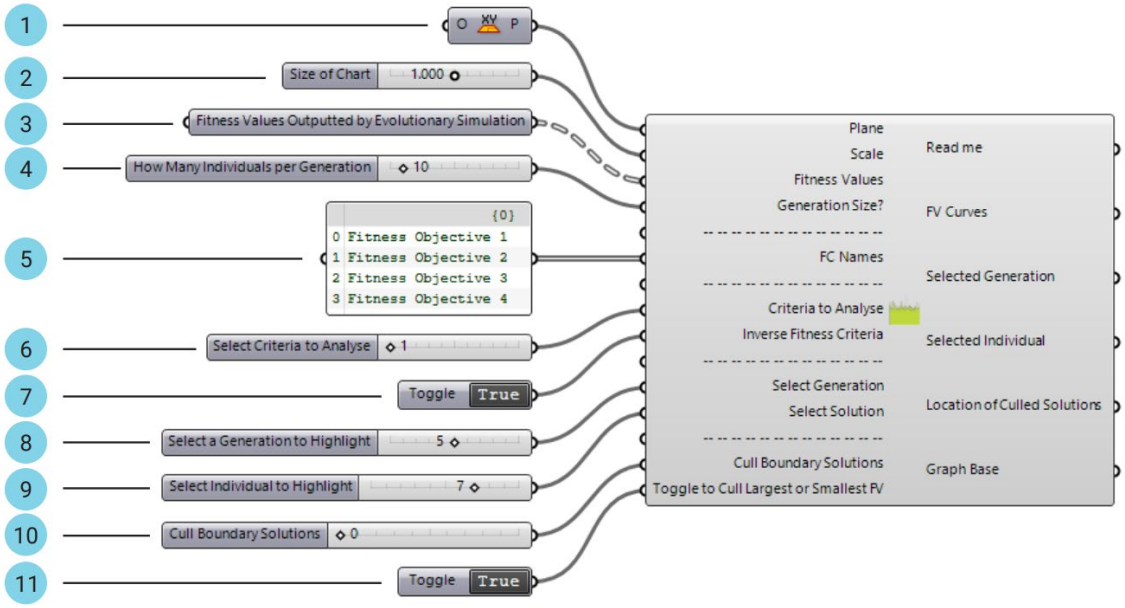

Figure 4-45 Overview of inputs in Fitness Value Component.

Item	Description	Default Value
1	Plane that defines the orientation the graph will be displayed	World XY
2	Value that controls the size of the graph	1.0
3	Fitness Values outputted by the evolutionary simulation	N/A
4	Define the how many individuals are in each generation	N/A
5	Input the names of the fitness objectives (the default is ‘Fitness Objective ‘x’)	Fitness Objective 'x'
6	Select which criteria to display the graph for	N/A
7	Toggle if you wish to inverse the fitness values (this is for display purposes only)	False (not inversed)
8	Select the generation you want to highlight	N/A
9	Select the solution in the above generation you want to highlight	N/A
10	Select the number of 'extreme' solutions you want to cull from the graph	0
11	Toggle to switch beteen culling largest or small values	False

Table 4-4 Explanation of inputs in Fitness Value Component.

Users can inverse the fitness values displayed on the Y-axis (this only affects how the fitness values are displayed, and does not impact the graph), as well as cull ‘extreme’ solutions from the population. This is required in cases where an ‘extreme’ solution (or solutions) has remapped the graph to a domain that makes it impossible to properly assess the fitness values of the remaining solutions in the population. Finally, users

can highlight a specific solution in the population through selecting the generation and individual number of the desired solution.

Mean Fitness Trendline Component:

This is how its related component comes into action:

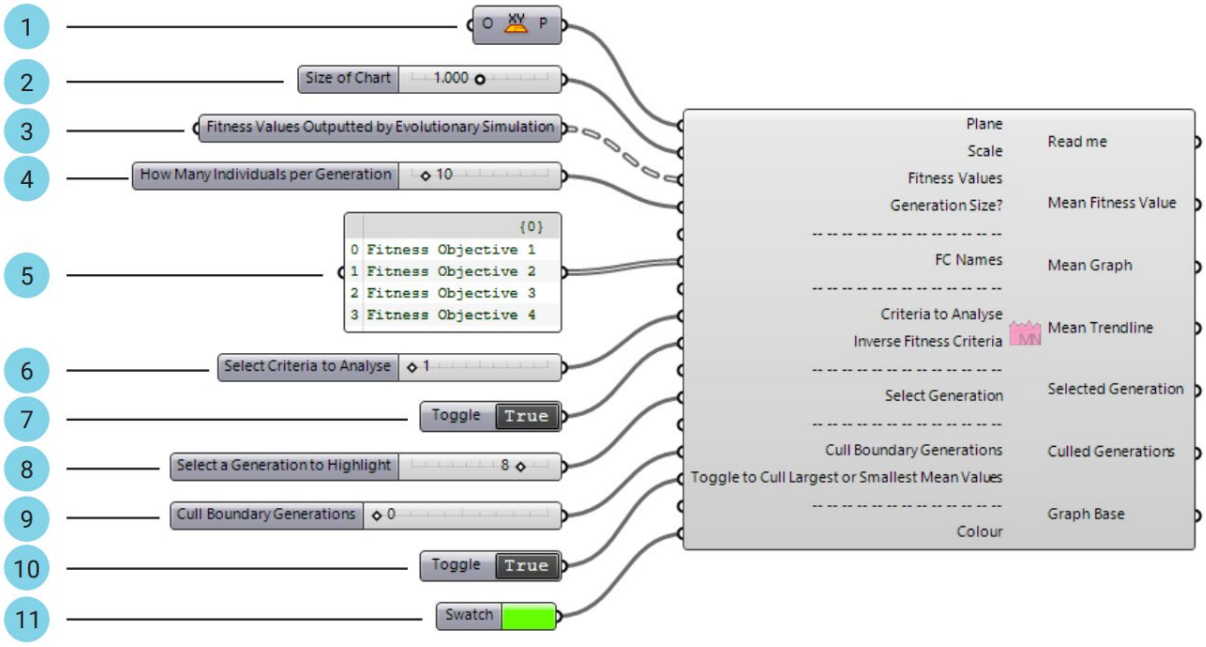

Figure 4-46 Overview of inputs in Mean Fitness Trendline Component.

Item	Description	Default Value
1	Plane that defines the orientation the graph will be displayed.	World XY
2	Value that controls the size of the graph.	1.0
3	Fitness Values output by the evolutionary simulation.	N/A
4	Define how many individuals are in each generation.	N/A
5	Input the names of the fitness objectives (the default is ‘Fitness Objective ‘x’)	Fitness Objective 'x'
6	Select which criteria to display the graph for	N/A
7	Toggle if you wish to inverse the fitness values (this is for display purposes only)	False (not inversed)
8	Select the generation you want to highlight	N/A
9	Select the number of 'extreme' generations you want to cull from the graph	0
10	Toggle to switch beteen culling largest or small values	False
11	Select the Colour of the graph	Green

Table 4-5 Explanation of inputs in Mean Fitness Trendline Component.

Users can inverse the values displayed on the Y-axis (this only affects how the fitness values are displayed, and does not impact on the graph), as well as cull ‘extreme’ generations from the population. This is required in cases where an ‘extreme’

generation (or generations) has remapped the graph to a domain that makes it impossible to properly assess the mean fitness values of the remaining generations in the population. Users can highlight a specific generation in the population through selecting the generation's number in the population. Users can control the colour of the graph through using a 'swatch' component. Finally, the chart displays the 'trendline', which is represented through a dashed line that calculates the variance of mean values from the mean.

Standard Deviation Component:

This is how its related component comes into action:

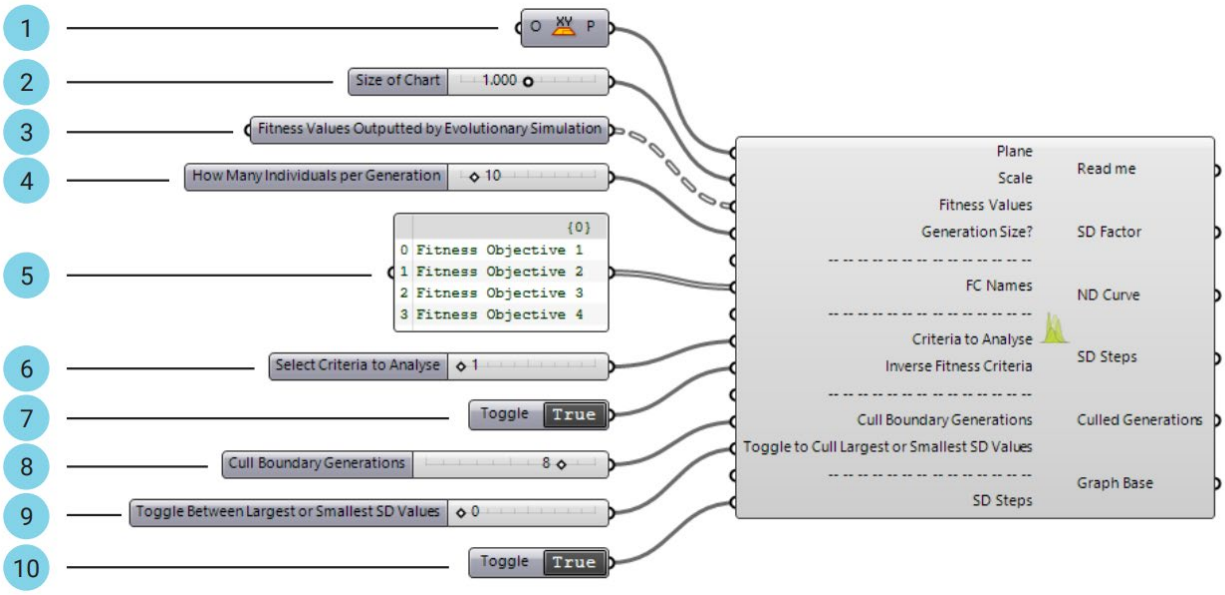

Figure 4-47 Overview of inputs in Standard Deviation Component.

Item	Description	Default Value
1	Plane that defines the orientation the graph will be displayed	World XY
2	Value that controls the size of the graph	1.0
3	Fitness Values outputted by the evolutionary simulation	N/A
4	Define the how many individuals are in each generation	N/A
5	Input the names of the fitness objectives (the default is 'Fitness Objective 'x')	Fitness Objective 'x'
6	Select which criteria to display the graph for	N/A
7	Toggle if you wish to inverse the fitness values (this is for display purposes only)	False (not inversed)
8	Select the number of 'extreme' generations you want to cull from the graph	0
9	Toggle to switch beteen culling largest or small values	False
10	Toggle to display the Standard Deviation Steps per Generation	True

Table 4-6 Explanation of inputs in Standard Deviation Component.

Users can inverse the values displayed on the X-axis (this only affects how the fitness values are displayed, and does not impact the graph), as well as cull ‘extreme’ generations from the population. This is required in cases where an ‘extreme’ generation (or generations) has remapped the graph to a domain that makes it impossible to properly assess the mean fitness values of the remaining generations in the population. Finally, users can switch on/off the SD steps displayed on the chart, this is for visual clarity and does not affect the calculation of the standard deviation.

Standard Deviation Trendline Component

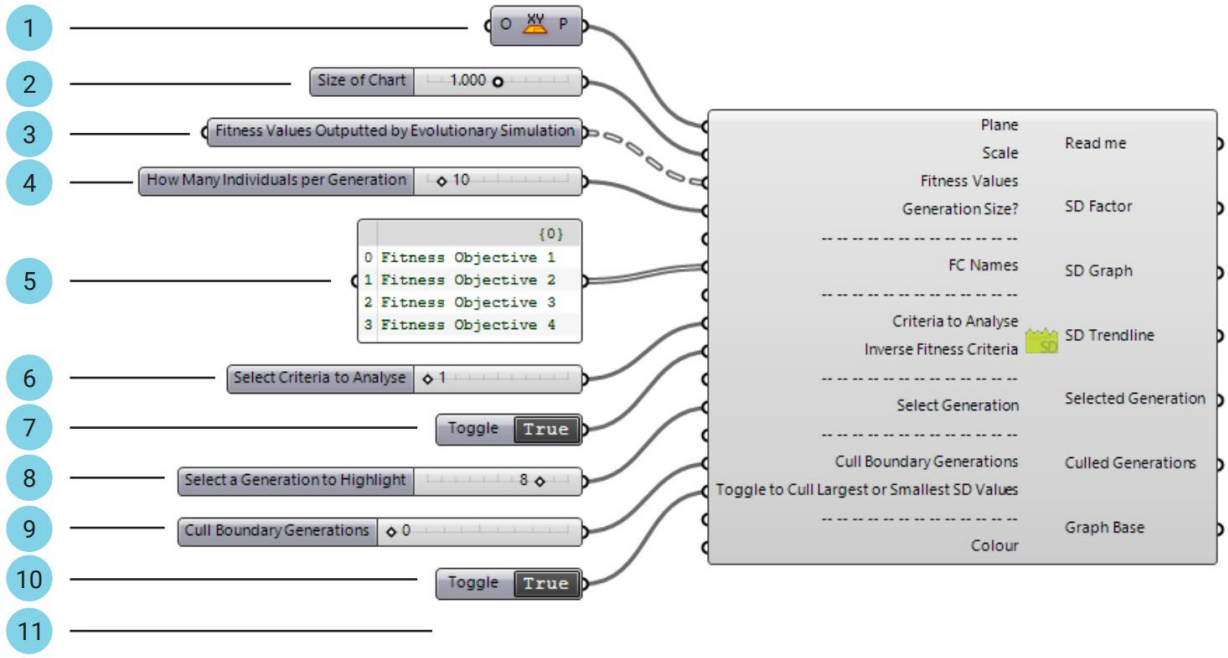

Figure 4-48 Overview of inputs in Standard Deviation Trendline Component.

This is how its related component comes into action:

Item	Description	Default Value
1	Plane that defines the orientation the graph will be displayed	World XY
2	Value that controls the size of the graph.	1.0
3	Fitness Values outputted by the evolutionary simulation.	N/A
4	Define the how many individuals are in each generation.	N/A
5	Input the names of the fitness objectives (the default is ‘Fitness Objective ‘x’)	Fitness Objective 'x'
6	Select which criteria to display the graph for.	N/A
7	Toggle if you wish to inverse the fitness values (this is for display purposes only)	False (not inversed)
8	Select the generation you want to highlight	N/A
9	Select the number of 'extreme' generations you want to cull from the graph	0
10	Toggle to switch beteen culling largest or small values	False
11	Select the Colour of the graph	Green

Table 4-7 Explanation of inputs in Standard Deviation Trendline Component.

Users can inverse the values displayed on the Y-axis (this only affects how the fitness values are displayed, and does not impact on the graph), as well as cull ‘extreme’ generations from the population. This is required in cases where an ‘extreme’ generation (or generations) has remapped the graph to a domain that makes it impossible to properly assess the standard deviation values of the remaining generations in the population. Users can highlight a specific generation in the population through selecting the generation’s number in the population. Users can control the colour of the graph through using a ‘swatch’ component. Finally, the chart displays the ‘trendline’, which is represented through a dashed line that calculates the variance of SD values from the mean SD value.

Parallel Coordinate Plot Component

This is how its related component comes into action:

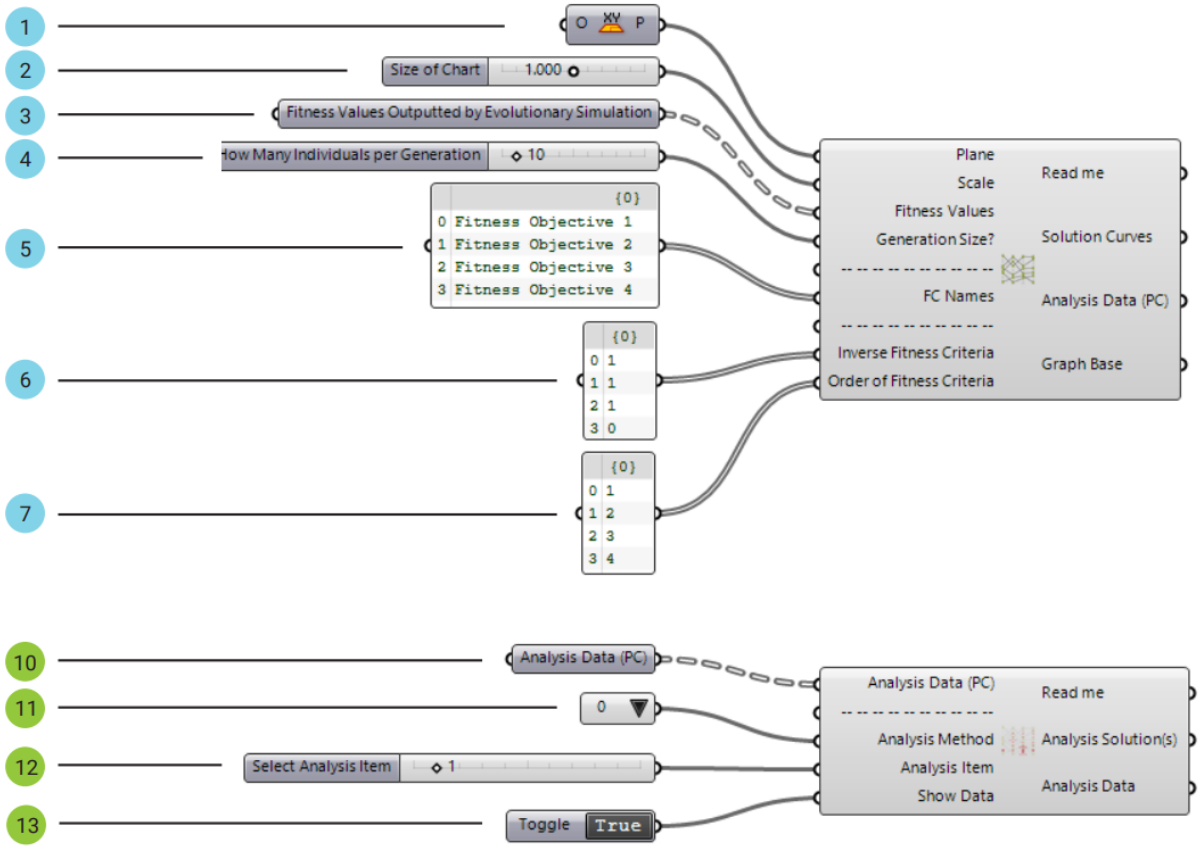

Figure 4-49 Overview of inputs in Parallel Coordinate Plot Component.

Item	Description	Default Value
1	Point in the xy plane to define the base of the Objective Space	World XY
2	Value that controls the size of the graph.	1.0
3	Fitness Values outputted by the evolutionary simulation.	N/A
4	Define the how many individuals are in each generation.	N/A
5	Input the names of the fitness objectives (the default is ‘Fitness Objective ‘x’)	Fitness Objective 'x'
6	Insert list of Boolean values to inverse Fitness values (1=inverse // 0=do not inverse	0
7	list of numbers (1,2…n (1 is 1st objective, n is last objective)) to reorder objectives	1,2,3…n
10	The analysis data outputted by the 'Wallacei_PCP' component	N/A
11	Select analysis method (there are 4 analysis methods numbered 0,1,2 or 3)	0
12	Select the solution to analyse according to the selected analysis method	0
13	Toggle to show the analysis data in the Rhino viewport	True

Table 4-8 Explanation of inputs in Parallel Coordinate Plot Component.

Figure 4-50 PCP Analysis, Method 0.

The methods of analysis provided in the PCP-A are the following:

0) Most repeated fitness values: This presents the most repeated fitness values in the population (from most repeated to least repeated) and outputs the corresponding data.

Figure 4-51-51 PCP Analysis, Method 1.

1) Solutions with most repeated fitness values: This extracts and highlights the solutions associated with the most repeated fitness values calculated in method 0'. Through this, the user can highlight the frequency of repeated fitness values across the simulation.

Figure 4-52 PCP Analysis, Method 2.

2) Relative difference between ranks: This method orders the solutions according to the relative difference between the fitness ranks of the different objectives. In this method, the 'fittest' solution is the one that has the same rank for all fitness objectives.

Figure 4-52 PCP Analysis, Method 3.

3) Average Fitness Rank: This method orders the solutions according to their mean fitness by calculating the mean fitness rank of each solution's fitness objectives (the 'fittest' solution is the one with the lowest mean rank).

Diamond Fitness Component:

This is how its related component comes into action:

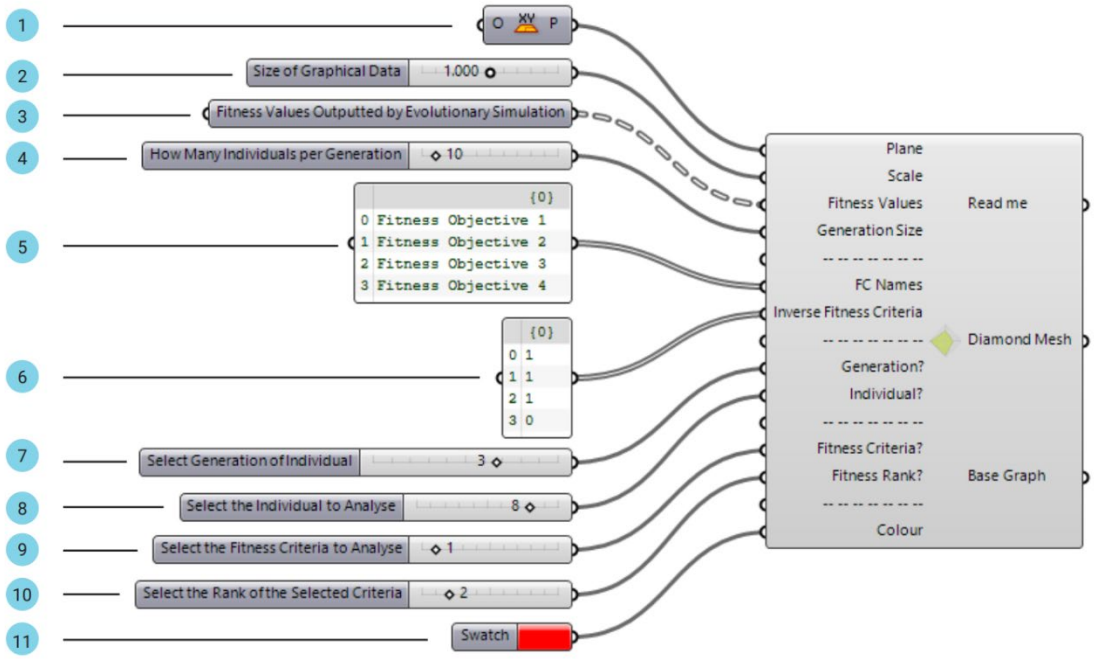

Figure 4-53 Overview of inputs in Diamond Fitness Component.

Item	Description	Default Value
1	Plane that defines the orientation the graph will be displayed	World XY
2	Value that controls the size of the graph.	1.0
3	Fitness Values outputted by the evolutionary simulation.	N/A
4	Define the how many individuals are in each generation.	N/A
5	Input the names of the fitness objectives (the default is ‘Fitness Objective ‘x’)	Fitness Objective 'x'
6	Insert list of Boolean values to inverse Fitness values (1=inverse // 0=do not inverse	0
7	Selection method 1 - Select the generation to analyse	N/A
8	Selection method 1 - Select the solution in the generation above	N/A
9	Selection method 2 - Select the fitness objective to analyse	N/A
10	selection method 2 - Select the ranking from the objective above	N/A
11	Select the colour of the graph	Red

Table 4-9 Explanation of inputs in Diamond Fitness Component.

The first selection method allows a user to select a solution by calling the generation and individual number of that solution (for example, generation 5, individual 3). This is primarily useful when a solution is highlighted through the analysis of the other components in Wallacei analytics. The second selection method, however, allows users to select a solution according to their rank in the population. In this case, a user selects the objective to analyse, followed by the ranking to select (for example, fitness objective 2, ranking 0). Through this method, users can quickly select the fittest solutions across the entire simulation and extract their location in the population. Users can inverse the fitness values (by using a boolean value of 1 or 0) to display the true fitness value for each solution. Finally, users can modify the colour of the diamond chart (by selecting a colour, the chart creates multiple variations of the selected colour to better differentiate between adjacent surfaces).

Objective Space and Pareto Front Components

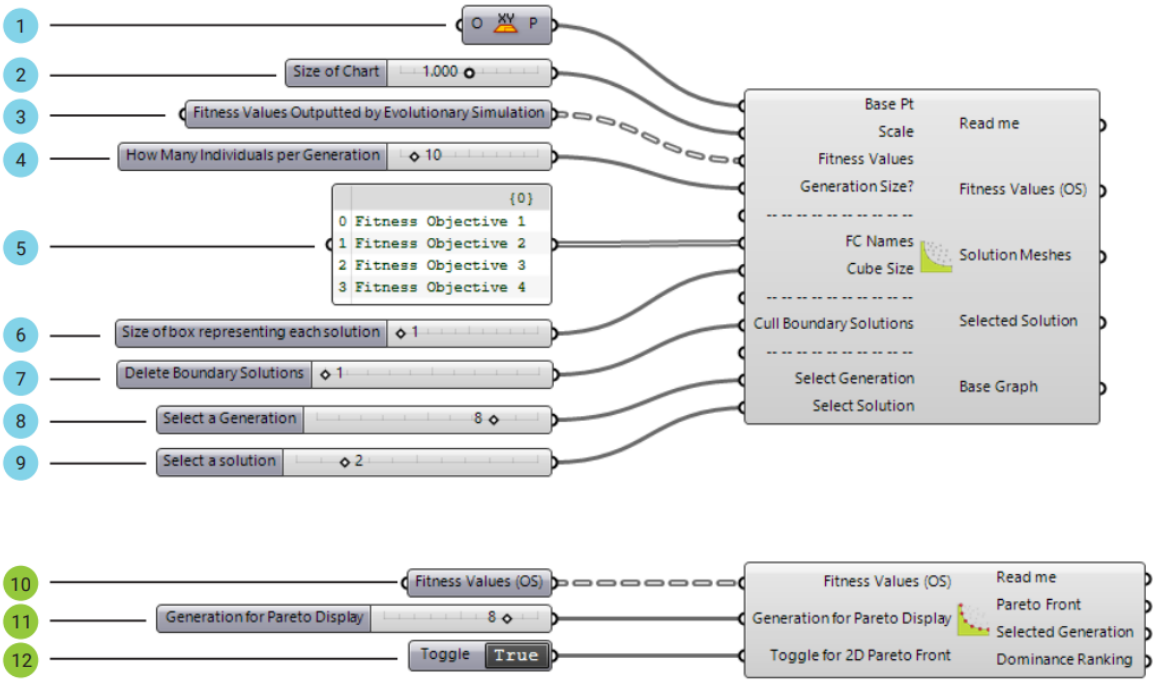

Figure 4-54 Overview of inputs in Objective Space and Pareto Front Components.

This is how its related component comes into action:

Item	Description	Default Value
1	Point in the xy plane to define the base of the Objective Space.	World XY
2	Value that controls the size of the graph.	1.0
3	Fitness Values outputted by the evolutionary simulation.	N/A
4	Define the how many individuals are in each generation.	N/A
5	Input the names of the fitness objectives (the default is ‘Fitness Objective ‘x’)	Fitness Objective 'x'
6	Size of cubes in the Objective space.	1
7	Select the number of 'extreme' solutions you want to cull from the graph	False (not inversed)
8	Select the generation you want to highlight	N/A
9	Select the solution in the above generation you want to highlight	N/A
10	The fitness values outputted by the 'Wallacei_Objective Space' component	N/A
11	Select the generation to display the 'pareto front' mesh	N/A
12	Toggle to display a 2d representatiuon of the front the xy, yz and xz planes	N/A

Table 4-10 Explanation of inputs in Objective Space and Pareto Front Components.

Users are able to cull ‘extreme’ solutions from the population. This is required in cases where an ‘extreme’ solution (or solutions) has remapped the objective space to a domain that makes it impossible to properly assess the distribution of solutions in the objective space. Users are able to highlight a specific solution in the objective space

through selecting the solution by its generation and individual number in the population. The Pareto Front component calculates the non-dominance value for any generation within the population and draws the pareto front for any given generation.

Our alternative demonstration method for Objective Space:

In contrast to the main wallacei X component that was written by C# programming language being fast, the native chart components were developed by Python which has made them very slow specially when it comes to producing some or all graphs at the same time. As a result, we have written some short algorithms by native built-in

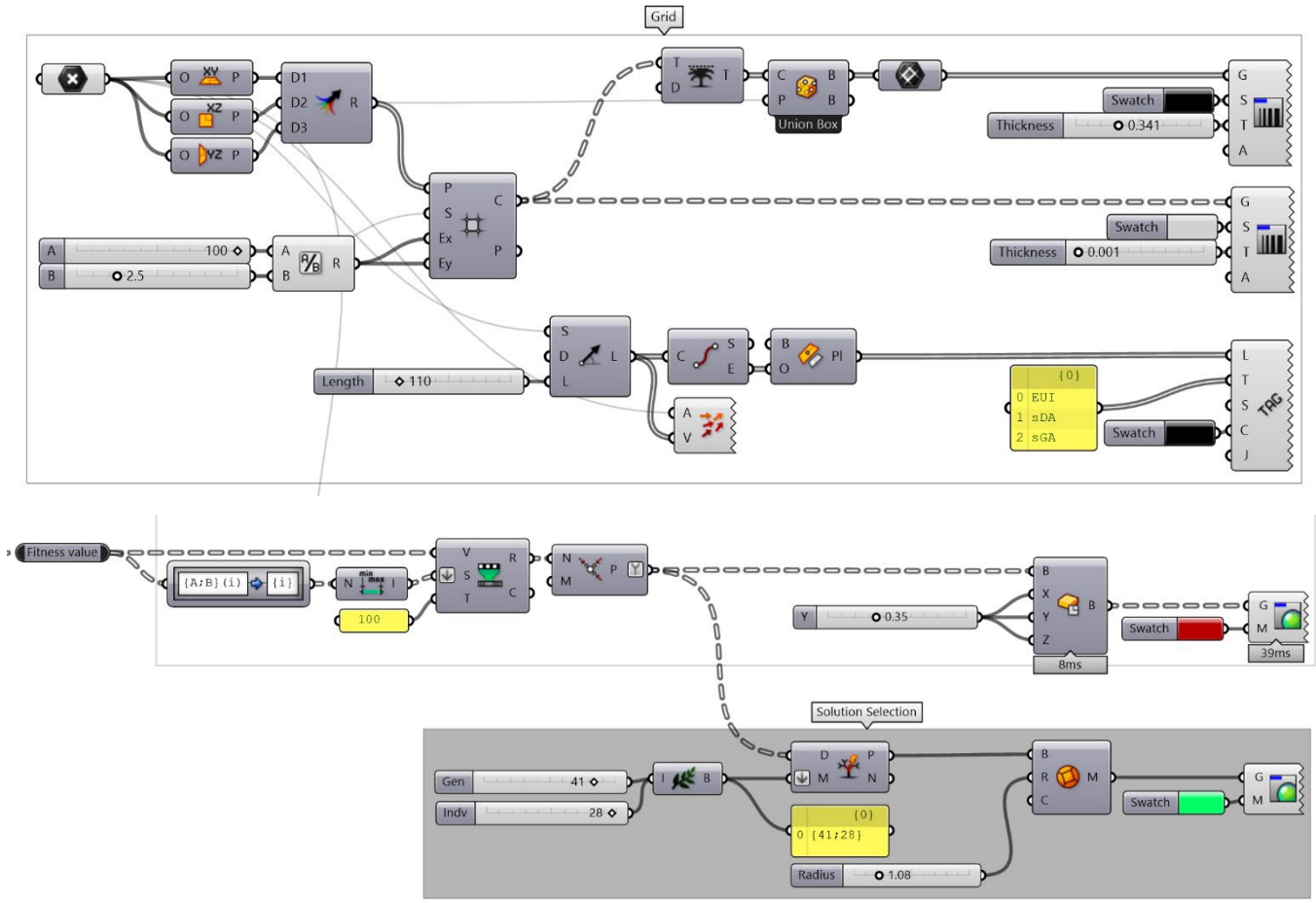

Figure 4-55 Algorithm to demonstrate Objective Space by built-in Grasshopper components.

grasshopper components which uses fitness values of individuals in each generation and produce these graphs.

05

RESULTS ON
EXISTING CASE STUDY

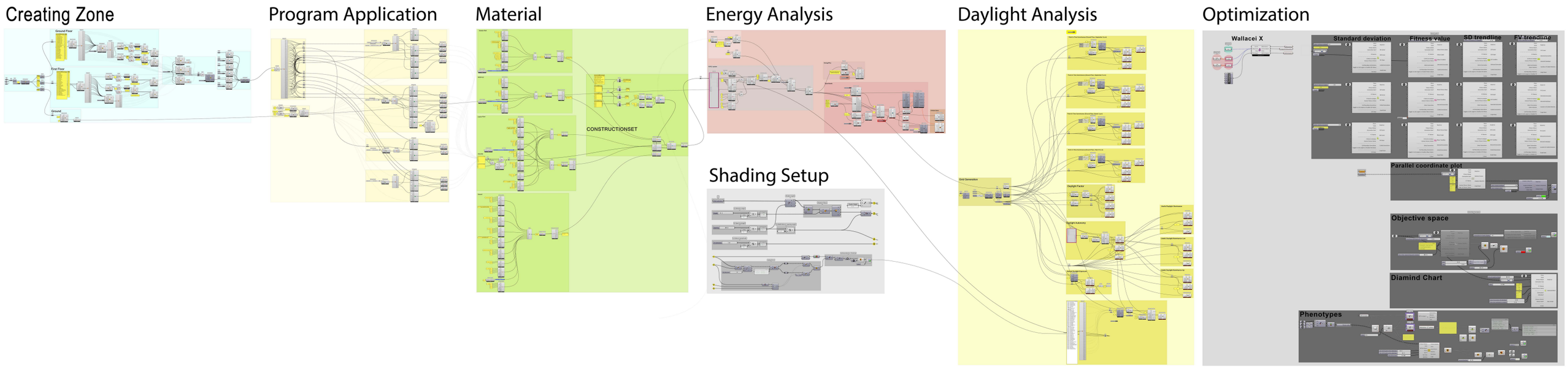

Figure 5-1 Overall computational workflow developed for the shading generating and energy simulation within an optimization algorithm to test on the case study.

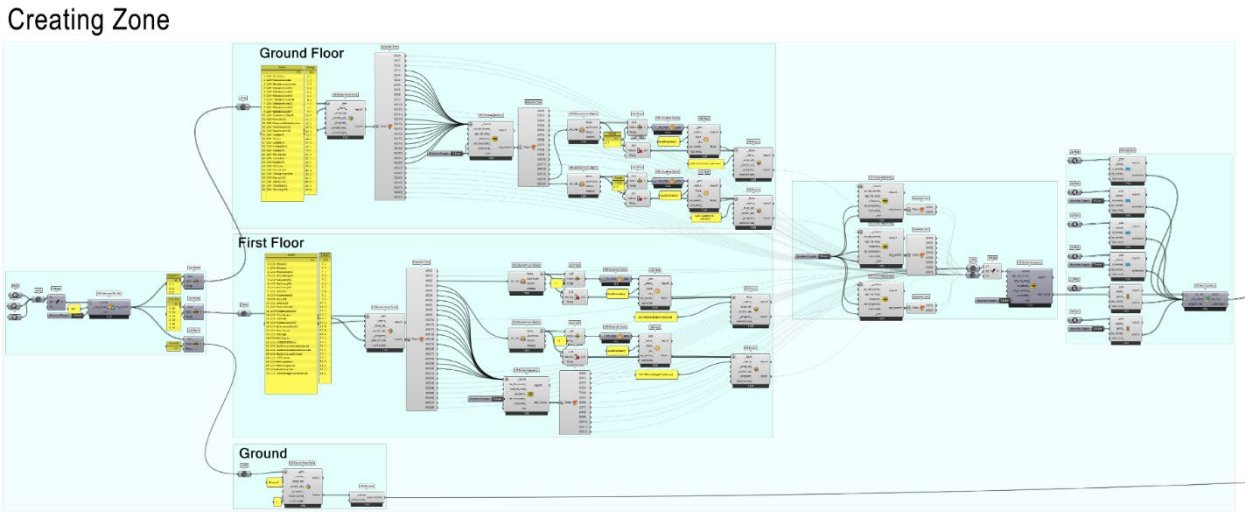

Figure 5-2 First step of the framework: zone creation algorithm (refer toFigure 5-1)

Program Application

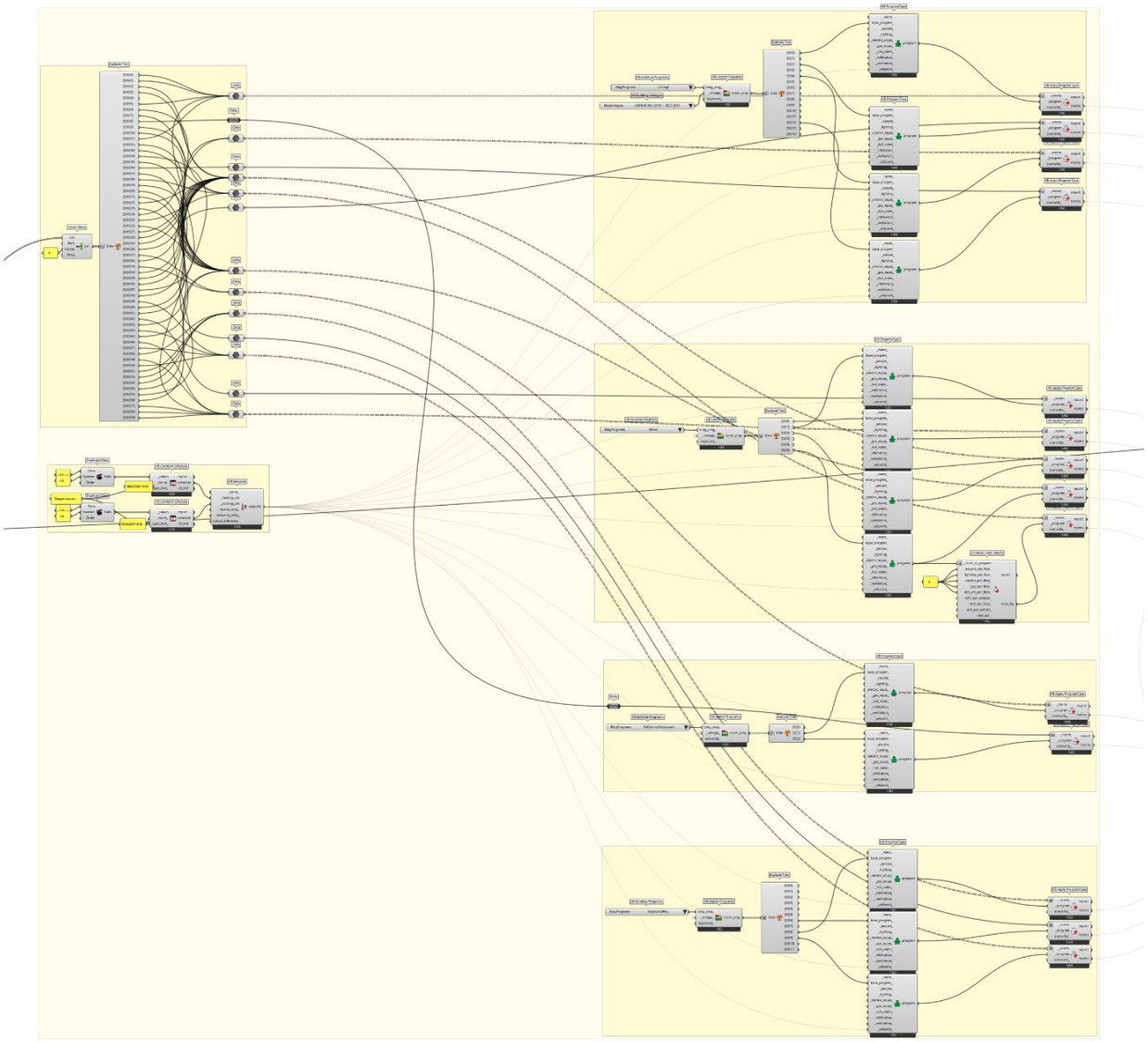

Figure 5-3 Second step of the framework: Program assignment process algorithm

(refer to Figure 5-1)

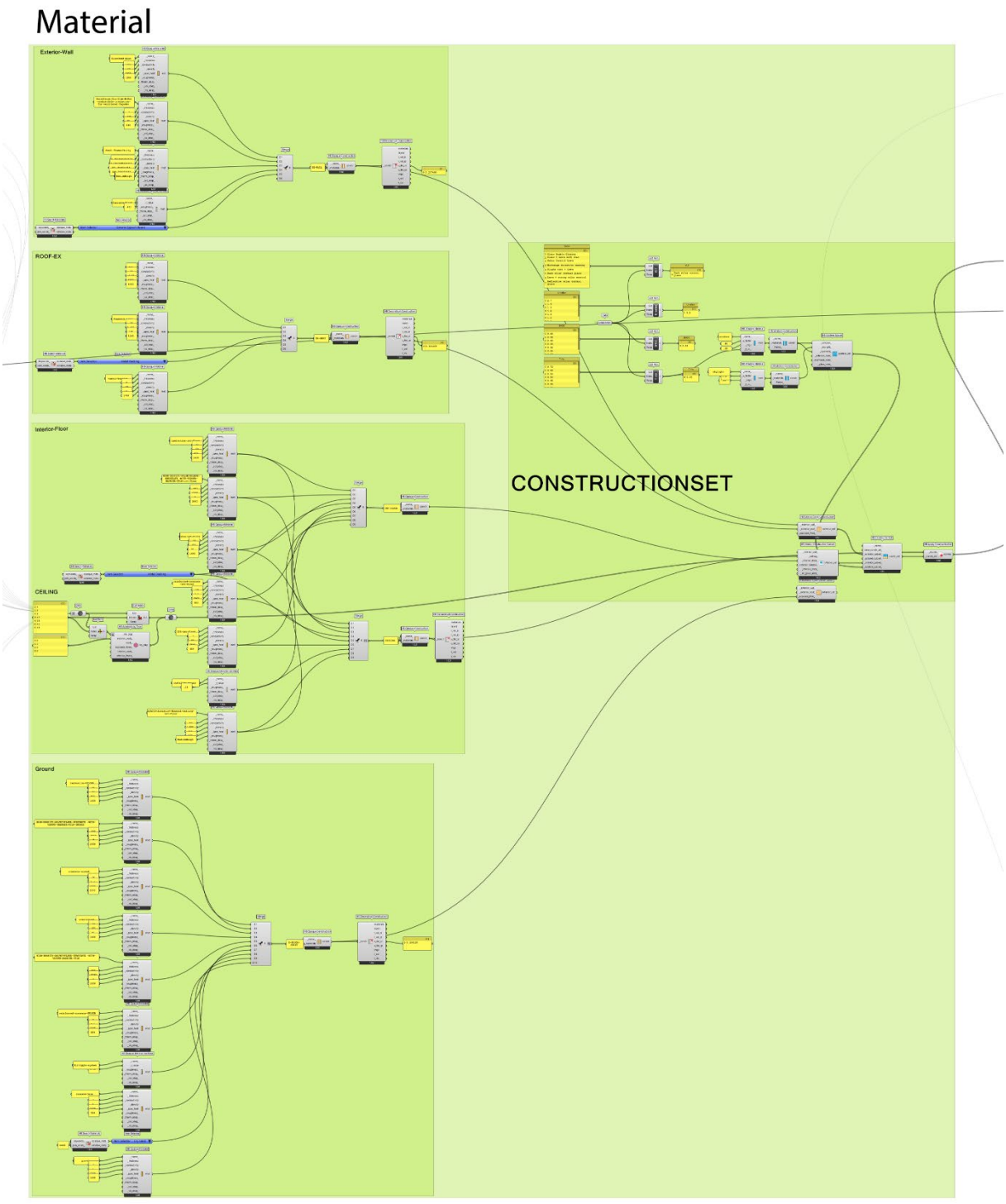

Figure 5-4 Third step Material and construction set configuration in the framework.(refer to Figure 5-1)

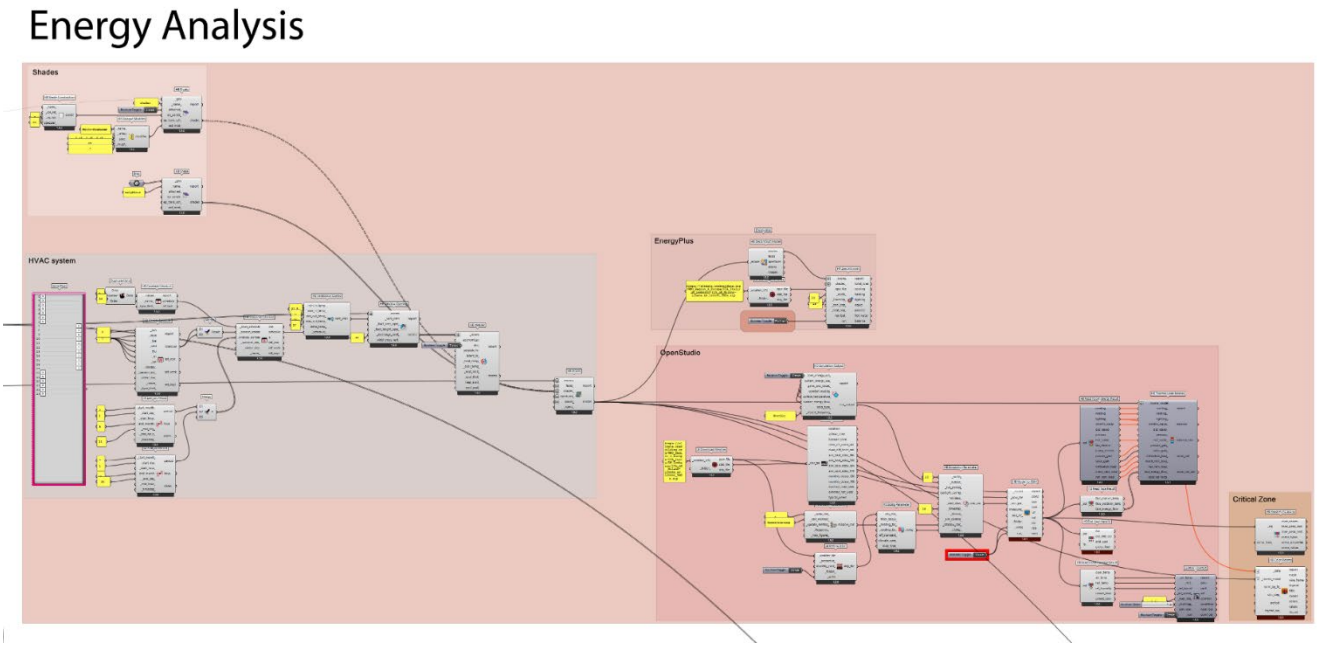

Figure 5-5 step four: Energy analysis stage of the framework (refer to Figure 5-1)

Daylight Analysis

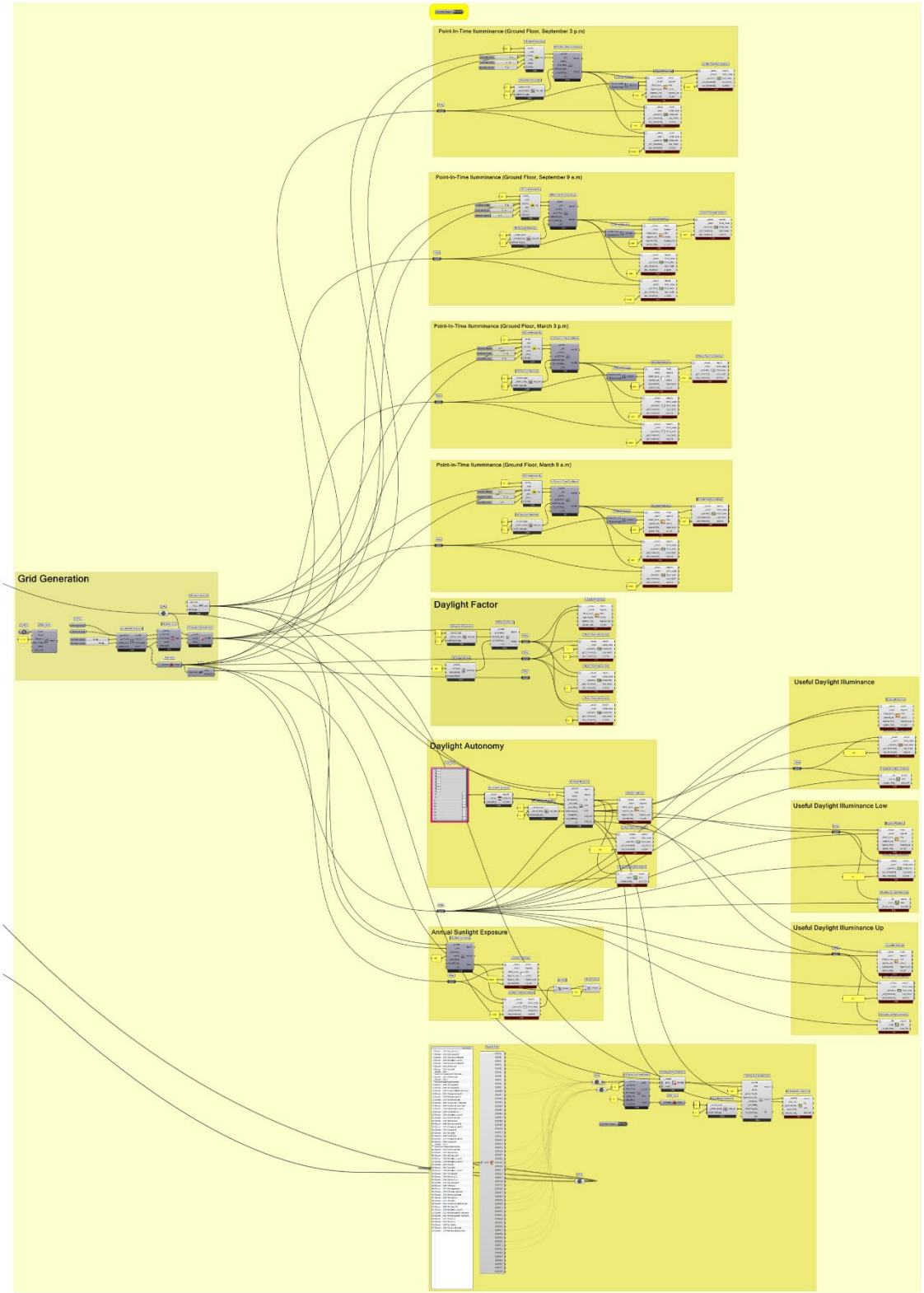

Figure 5-6 Step 5: Daylight analysis framework (refer to Figure 5 1

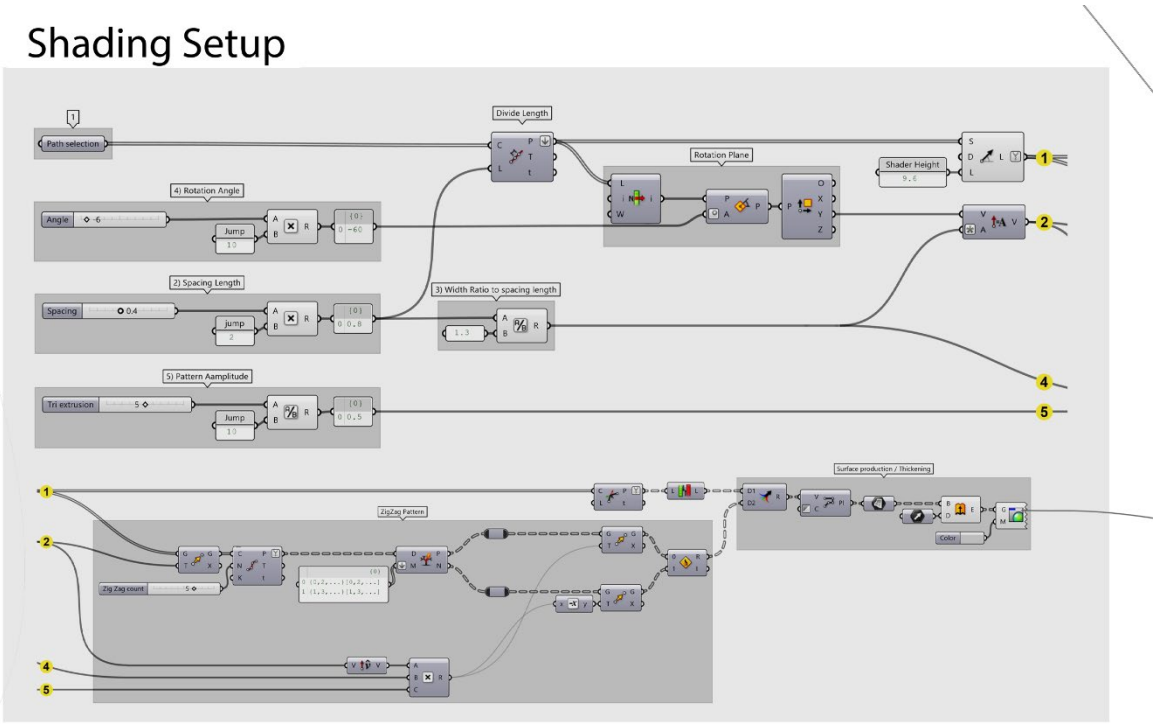

Figure 5-7 Shading setup stage of the framework, defining geometric parameters and controling variables for the external shading system (refer to Figure 5 1)

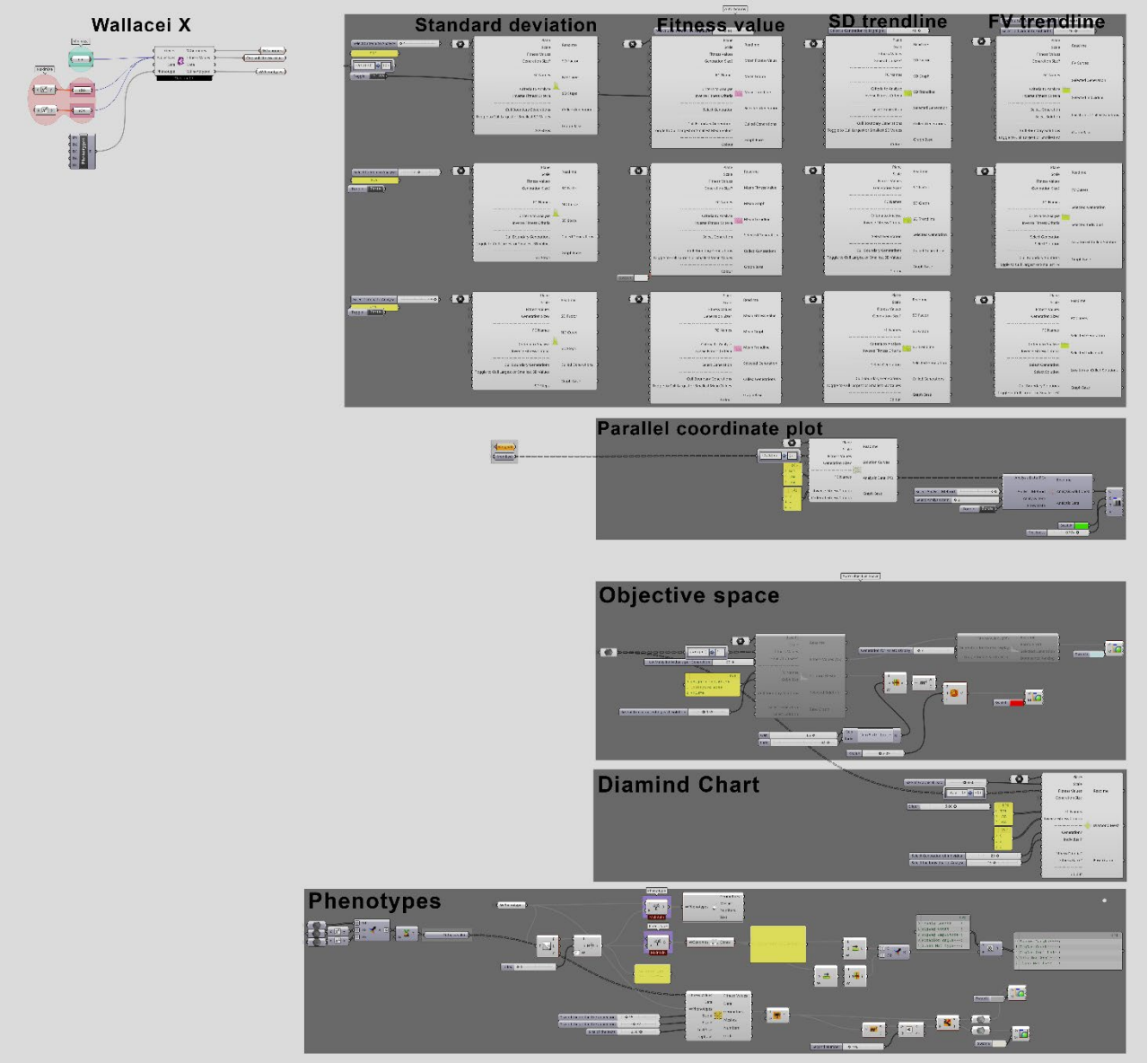

Figure 5-8 Optimization stage of the framework and related resulting charts production

Case Study Description:

The proposed optimization algorithm is applied in this chapter to a real-world case study with representative geometric, climatic, and functional parameters. The aim is not to redesign the building, but to test the robustness and performance of the proposed optimization framework in a real-world architectural scenario. The case study chosen is a mid-rise cultural and mixed-use building in Milan, Italy. The building was originally developed as part of an integrated sustainable building technology studio.

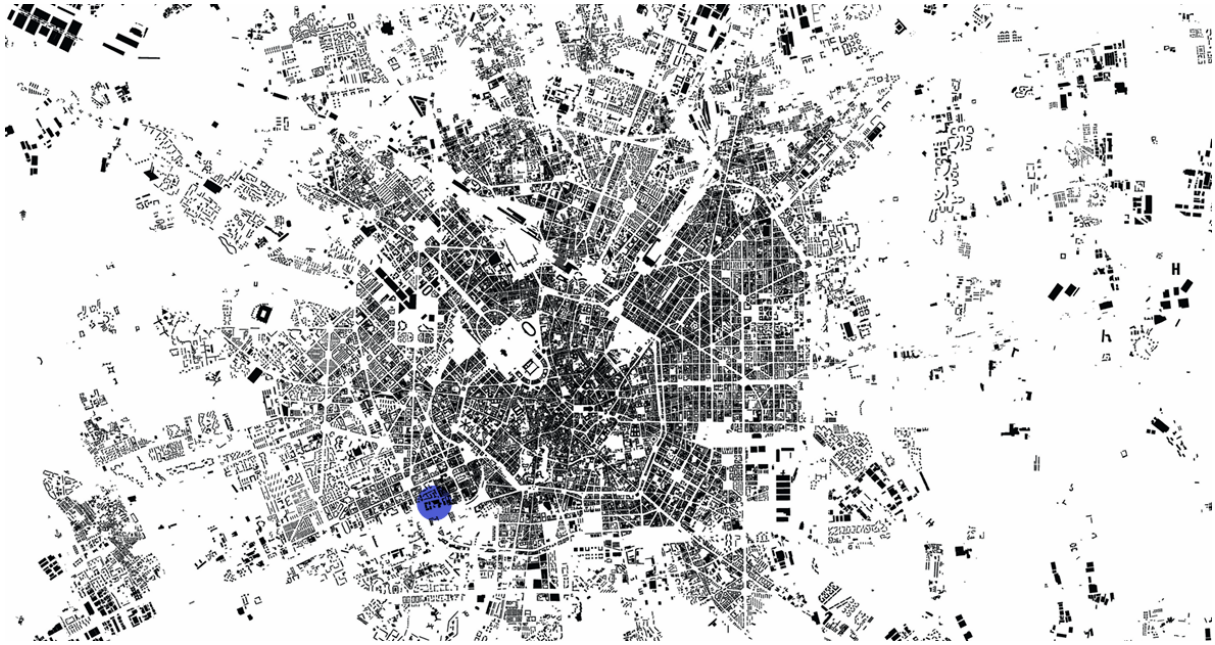

Figure 5-9 Urban morphological map of Milan. The blue marker indicates the case study site location.

The building is in a historically industrial area, which was defined by large manufacturing plants such as Zust, Riva Calzoni, Schlumberger, Nestlé, and General Electric. The original complex was built in the 1920s by the Compagnia Generale Elettrica as an electric turbine production plant. From a performance point of view, the building is characterized by several factors that make it an interesting candidate for testing façade optimization strategies. The deep plan layout hinders uniform daylight distribution, while the presence of opaque and highly transparent façade elements creates conflicting requirements for thermal performance, solar gain, and visual comfort. Additionally, the mixed-use layout leads to varying internal loads and occupancy schedules for different zones.

These factors create a complex relationship between energy demand, daylight availability, and solar access, providing an interesting scenario for testing the effectiveness of the proposed performance-driven optimization algorithm.

Figure 5-10 Zoomed-in view of the case study site, illustrating its constrained urban position between transport infrastructure and dense surrounding fabric

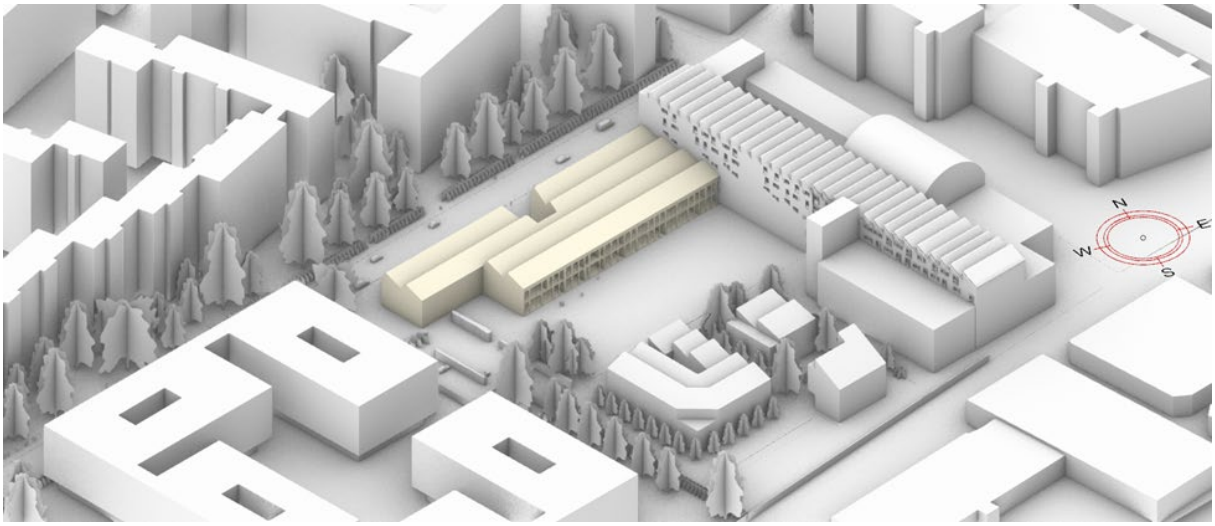

Figure 5-11 Three-dimensional massing representation of the case study building and its surrounding urban context.

Climatic Conditions:

The case study is set in Milan, Italy (45.45° N, 9.28° E), and has a cold and humid climate with strong seasonal variation. The annual outdoor temperature varies from about −2 °C in winter to above 30 °C in summer.

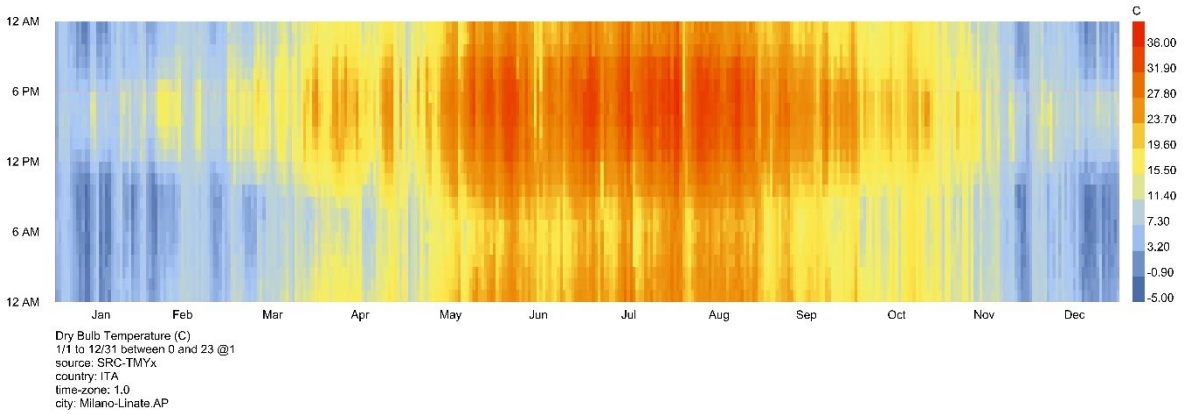

Figure 5-12 Annual dry-bulb temperature heatmap for Milan (EPW data), illustrating hourly temperature variation across the year.

The climatic boundary conditions for the simulation were set using a standard EPW weather file for Milan, ensuring that the environmental conditions are consistent with the framework of the performance assessment. Although a short period of the year is within adaptive thermal comfort conditions without the use of mechanical conditioning, the overall climatic conditions require both heating and cooling systems, as well as solar control during the respective seasons. The psychrometric chart shows that passive design alone cannot provide indoor thermal comfort conditions throughout the year, thus underlining the importance of envelope characteristics in controlling thermal loads and solar gains.

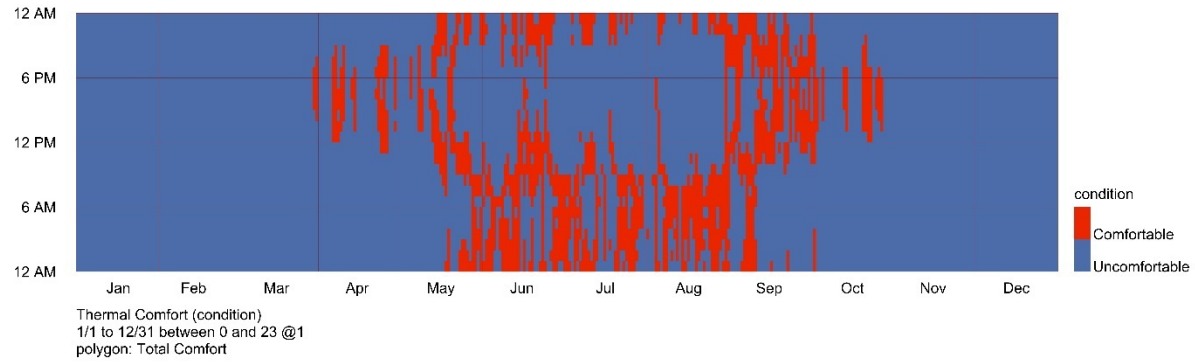

Figure 5-13 Annual thermal comfort distribution for Milan, indicating hourly periods classified as comfortable and uncomfortable based on the total comfort polygon.

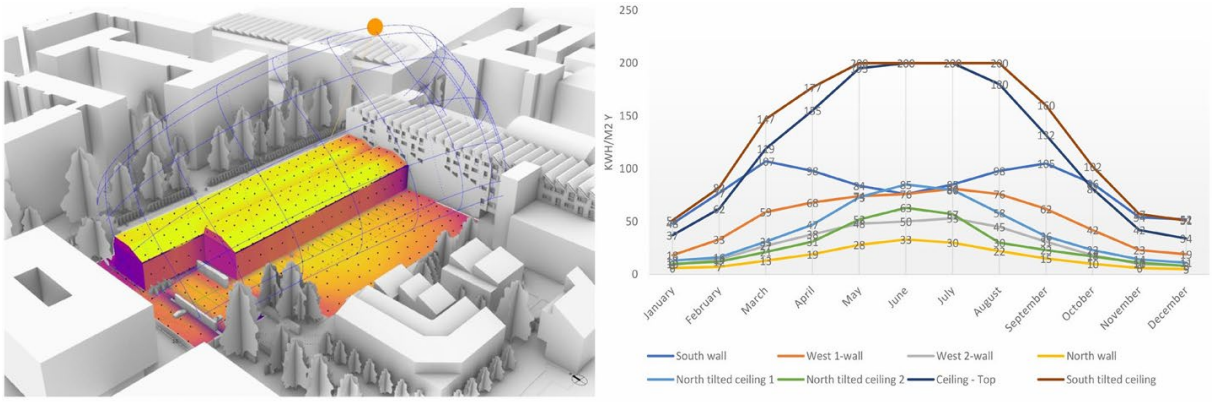

Figure 5-14 Solar radiation analysis of the case study building in Milan. (Left) Spatial distribution of annual incident radiation. (Right) Monthly radiation values (kWh/m²) for each façade and roof orientation. Solar radiation analysis of the case study building in

Solar radiation mapping shows a strong asymmetry in façade exposure. The roof surfaces and south façades receive the maximum annual solar radiation, especially during the cooling season, thus increasing the risk of overheating and glare. The north façade is mainly exposed to diffuse solar radiation, with no direct solar incidence. In this case, solar control measures were considered a priority for the south façade, while the north façade was not considered a critical surface for solar control measures.

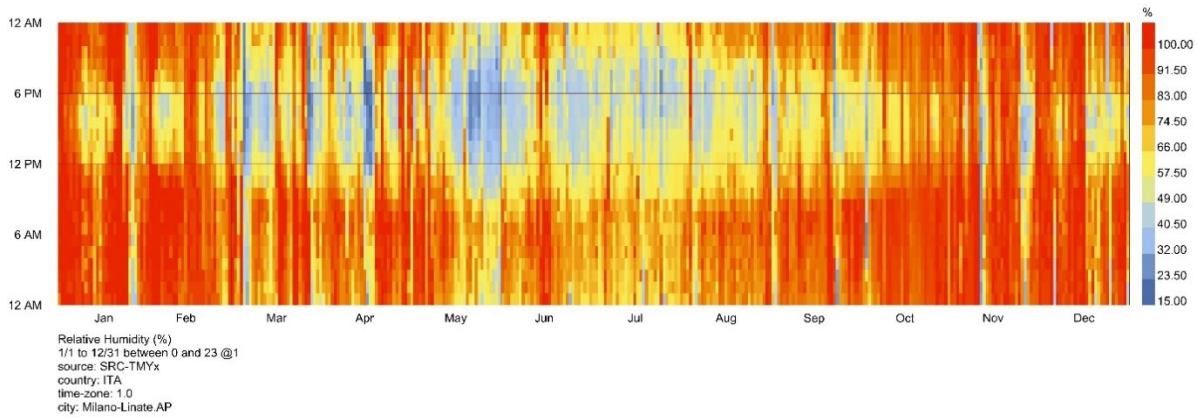

Figure 5-15 Annual hourly relative humidity (%) for Milan based on EPW weather data, demonstrating seasonal and daily variability in ambient moisture conditions."

The annual relative humidity profile indicates seasonal variation, with periods of increased fluctuation in specific months. Overall, the average humidity levels remain within or close to the defined comfort range for a considerable portion of the year. This suggests that, although Milan exhibits relatively high humidity, conditions are generally compatible with indoor comfort, while still requiring careful envelope design to prevent moisture-related performance issues.

The wind analysis indicates a relatively high frequency of calm conditions throughout the year (approximately 24–33%), with the highest occurrence during the autumn period. Prevailing winds predominantly originate from the North and North-East directions. Strong wind events are generally infrequent, with only occasional higher-speed occurrences during spring. Overall, wind conditions remain moderate, suggesting limited potential for consistent wind-driven natural ventilation.

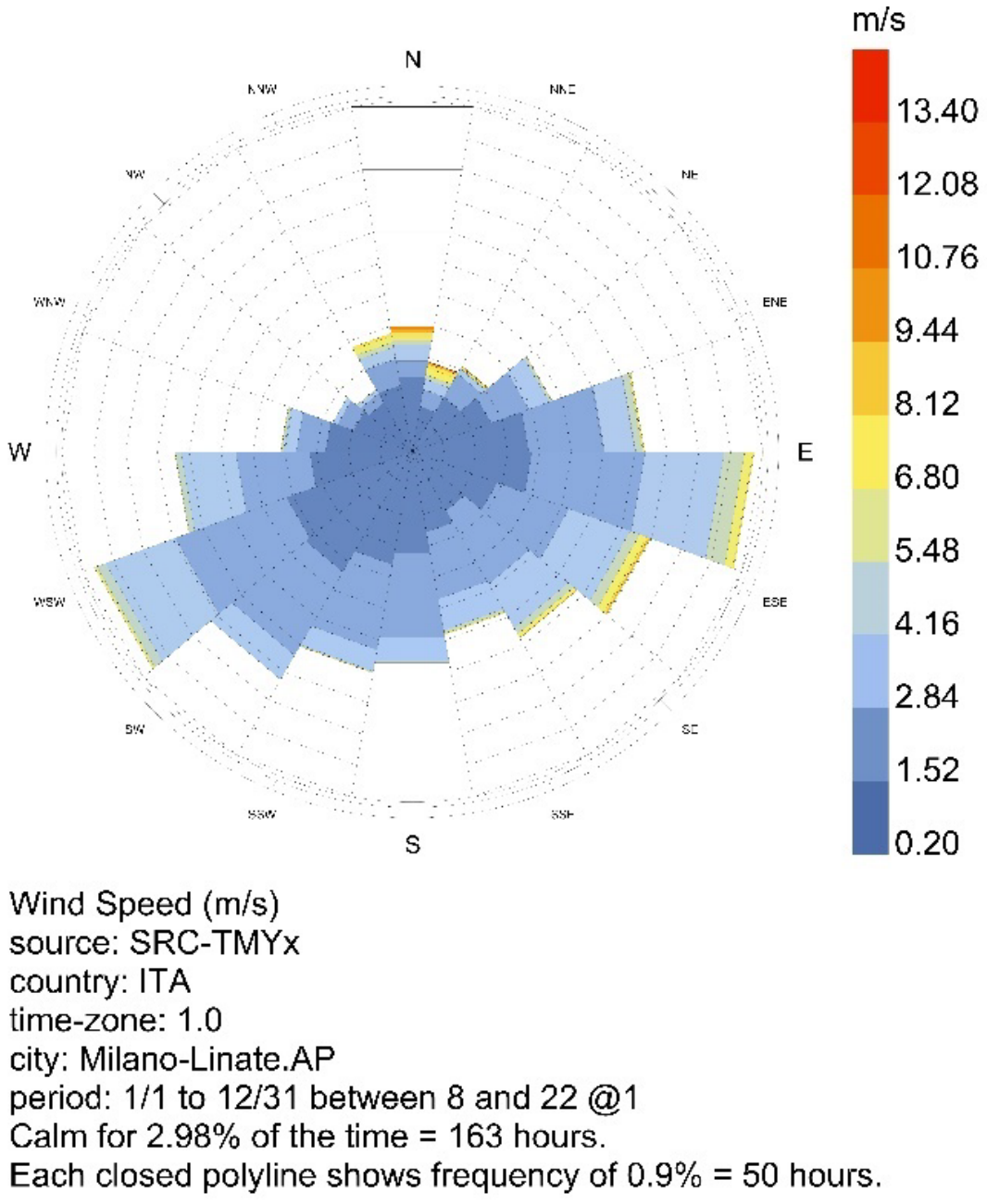

Figure 5-16 Annual wind rose for Milan (Linate EPW data), illustrating prevailing wind directions and corresponding wind speed distribution (m/s).

In conclusion, Because of the high density of the surrounding urban blocks, the potential for cross-ventilation was low. Consequently, natural ventilation was not considered a major optimization variable for this study, and the analysis concentrated on façade geometry, glazing characteristics, and solar control variables as major

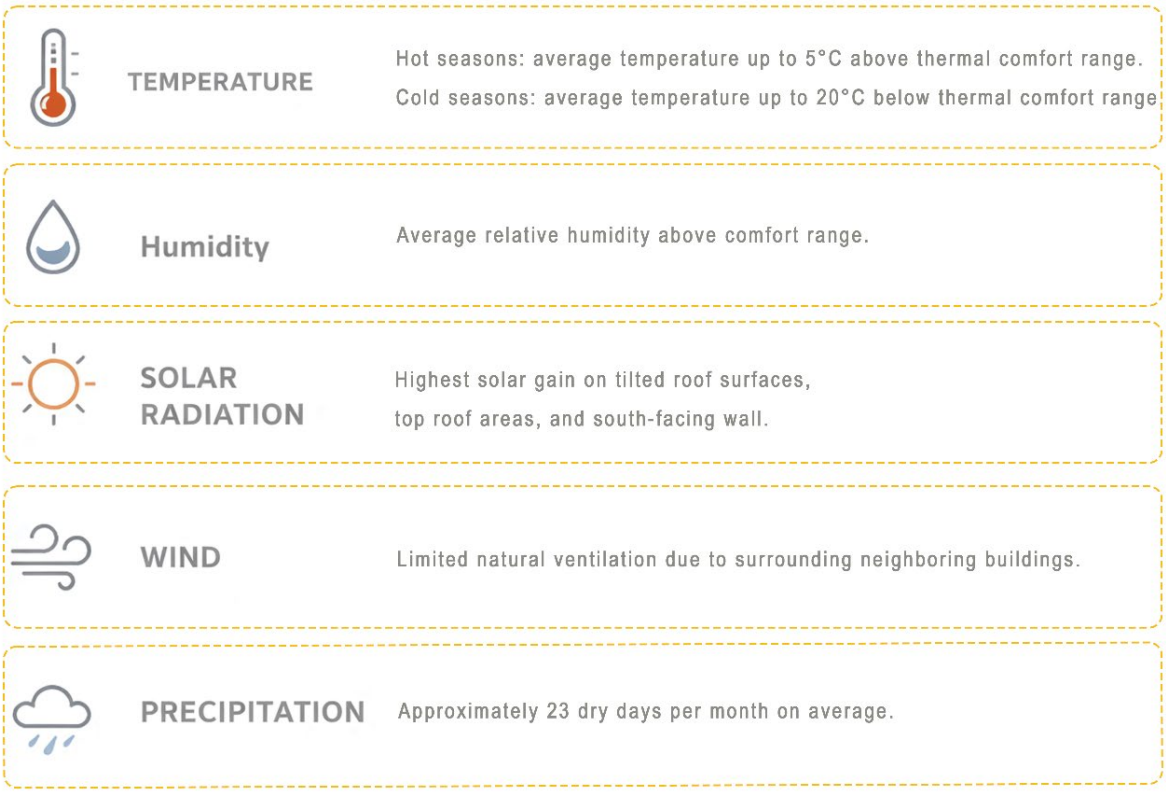

Figure 5-17 Summary of primary climatic parameters affecting the case study site in Milan.

Building Typology:

The case study building is a cultural complex with exhibition areas, ateliers, offices, commercial spaces, restaurants, and public paths on two main levels.

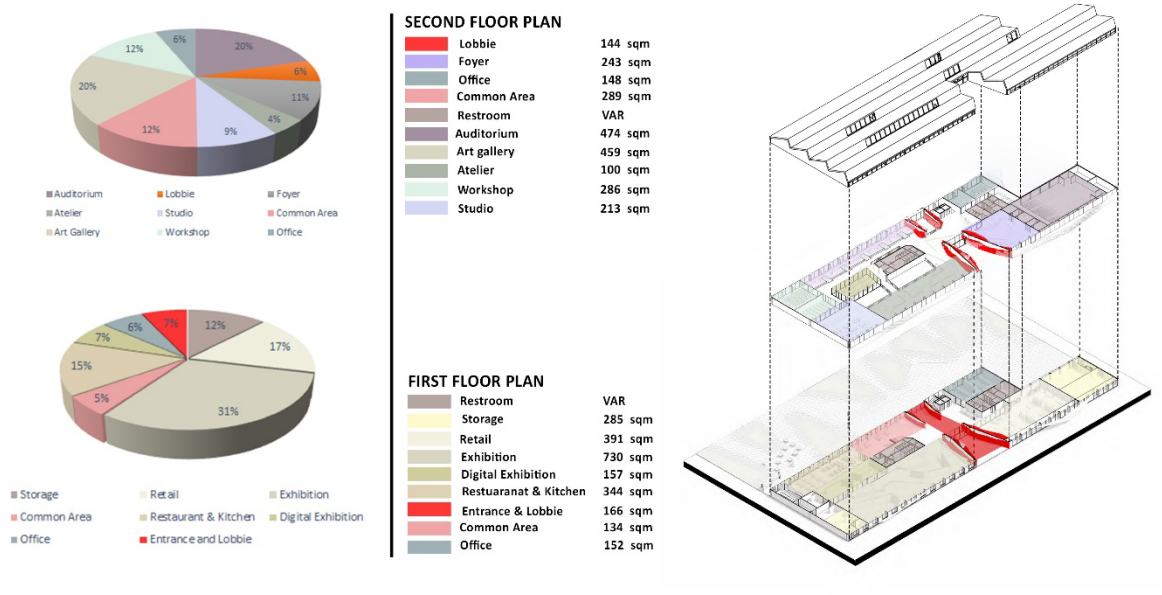

Figure 5-18 Functional area distribution and vertical spatial organization of the case study building.

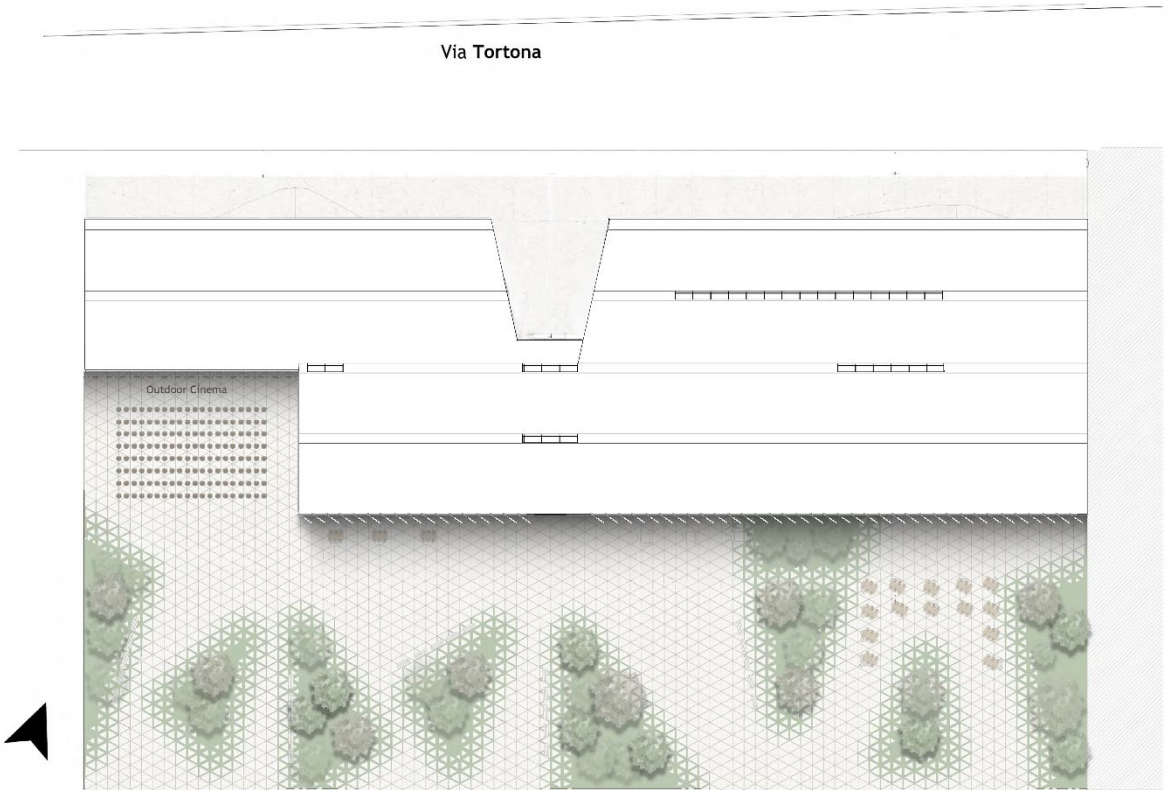

Figure 5-19 Site plan of the case study building.

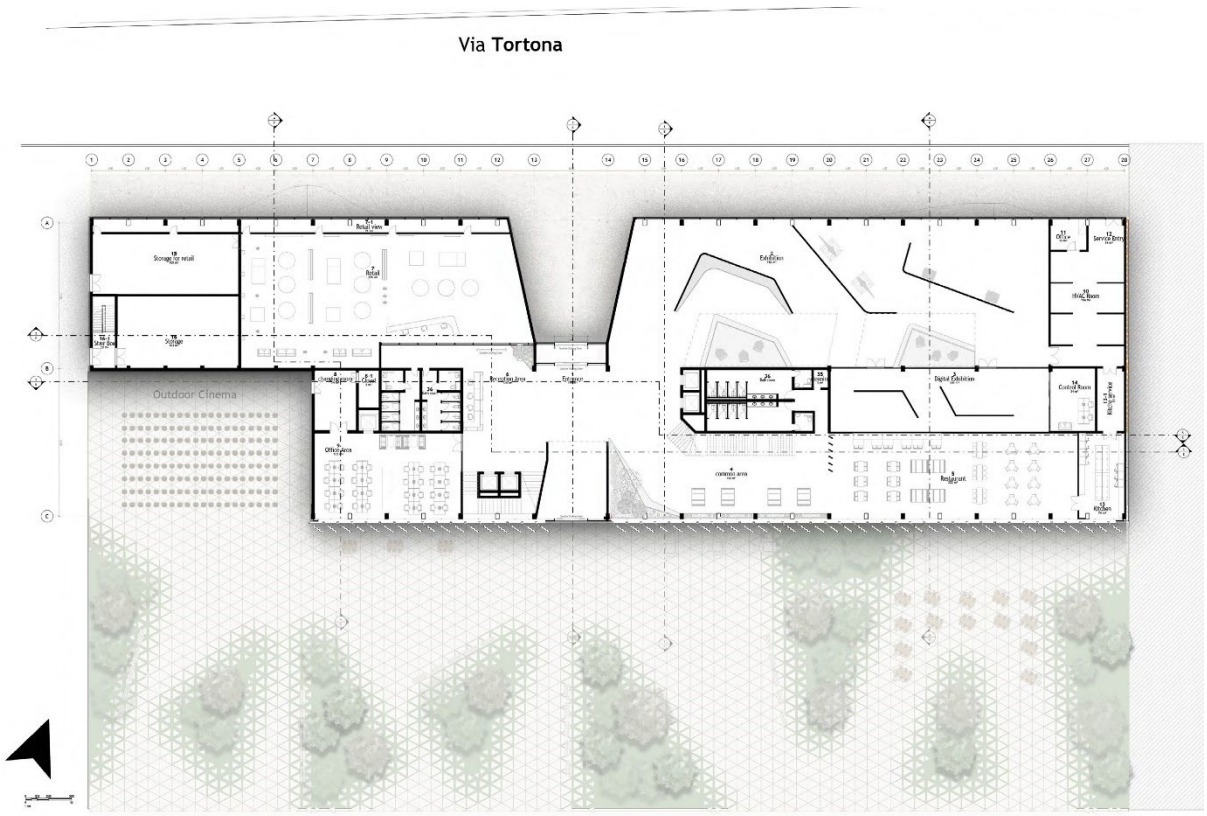

Figure 5-20 Ground floor plan of the case study building.

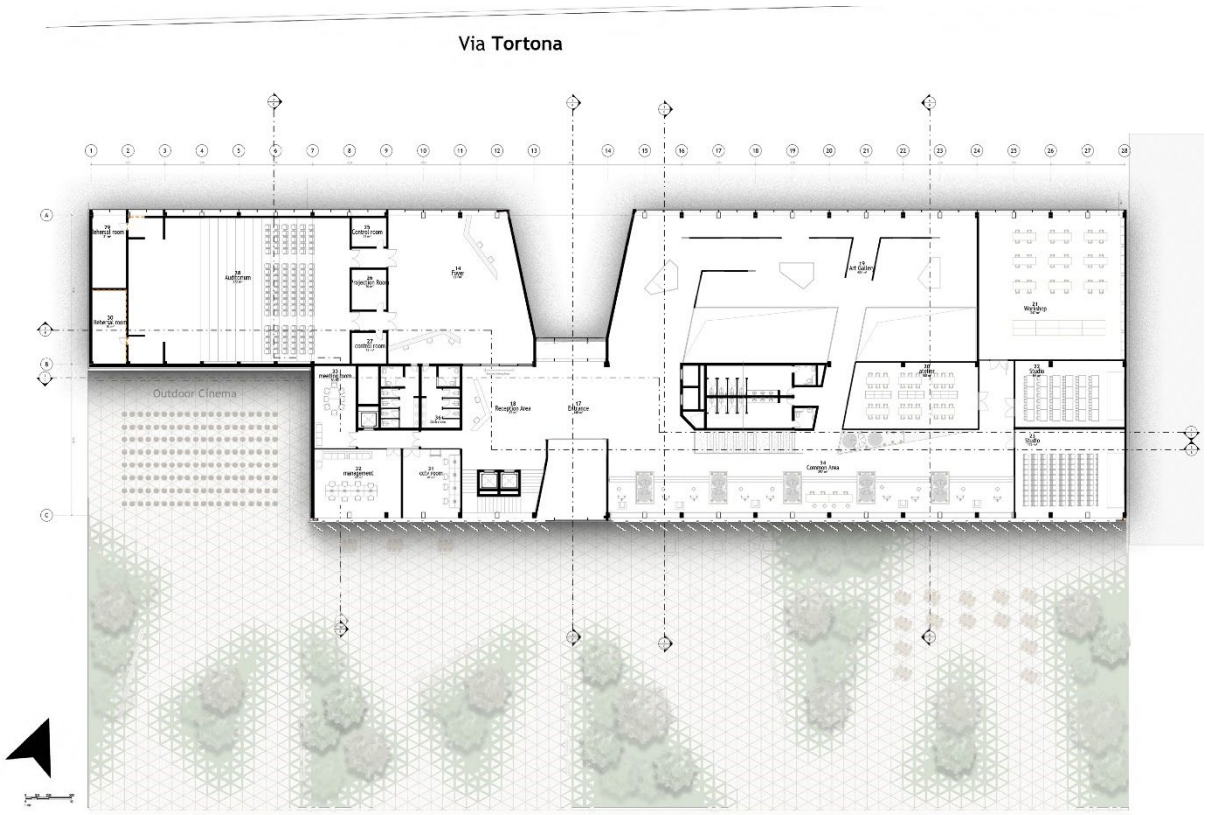

Figure 5-21 First floor plan of the case study building.

Figure 5-22 Rendered view of the south façade before the adoption of the optimized shader.

.

Figure 5-23 Rendered perspective view of the south façade before the adoption of the optimized shader.

Building Envelope and Baseline Configuration:

The building envelope combines a reinforced concrete masonry unit (CMU) structural system with a ventilated cladding assembly. The CMU walls serve as the primary load bearing, thermal mass, acoustic insulation, and fire-resistant components, establishing a strong structural core. On the exterior, a rear-ventilated façade assembly with aluminum composite panels is mechanically attached to a secondary substructure with integrated thermal insulation. This multi-layered system improves thermal, moisture, and durability performance while keeping the overall weight of the exterior envelope relatively low.

The façade design features large rectangular glazed areas that are aligned with the structural grid. Three different geometric window arrangements—square, horizontal, and vertical scales—were considered in the evaluation stage. The final design features vertically oriented rectangular windows that are in sync with the structural rhythm of the building.

The baseline window-to-wall ratio (WWR) is set at 80% on the north façade and 85% on the south façade, with about 10% roof glazing. Double-glazed units (U-value 1.2 W/m²K) are used as the baseline glazing system for performance evaluation.

To facilitate a controlled evaluation of the optimization process, certain parameters are maintained constantly in all simulation runs. These include the internal layout arrangement, structural system, HVAC system type, and occupancy rate.

Role of the Case Study in Algorithm Validation:

Based on the definition of site context, geometric configuration, and baseline performance parameters, the case study provides a controlled experimental setting for testing the proposed optimization framework. The chosen building example is not meant to be a site-specific or prescriptive design solution but instead provides a realistic architectural setting with complex geometry and mixed-use operational characteristics to test the algorithm against.

In this setting, the boundaries of algorithmic intervention were specifically limited to parameters related to the building envelope. The optimization procedure was limited to the geometry and configuration of external shading devices on solar-exposed

façades, specifically testing variations in louver angle, depth, and spacing. Window-to-wall ratios, glazing properties, HVAC systems, and occupancy rates were held constantly to isolate the performance effect of the shading optimization. The overall methodological workflow—including baseline model definition, fitness criteria setup, parametric shading generation, multi-objective optimization, and final performance evaluations illustrated in the research flowchart (Figure 4-1), which outlines the integration of the parametric modelling environment with the energy simulation engines and the iterative optimization loop adopted in this study.

By setting these boundaries of intervention, the performance differences can be primarily attributed to the optimization algorithm itself rather than to cumulative design modifications. Accordingly, the results of this chapter are interpreted as indicative of methodological robustness and computational validity, while the optimization procedure is considered transferable to different climatic conditions and building types.

5.1 Parametric Zones Modeling

In the presented case study, an initial architectural zoning scheme was developed based on the functional and spatial organization of the building **(refer to Figure 5-2)** While this architectural zoning provided a clear representation of program distribution, several zones exhibited large floor areas and complex geometries that were not suitable for accurate thermal modelling. In such cases, representing extensive spaces as single thermal zones would have introduced unrealistic assumptions of uniform thermal behavior, potentially increasing simulation error.

To address this issue, a refined thermal zoning strategy was implemented within the Honeybee framework. Selected architectural zones with excessive area or heterogeneous exposure conditions were subdivided into smaller thermal zones to better capture spatial variations in heat transfer, solar gains, and internal conditions. As a result of this process, the total number of thermal zones across two floors increased from 32 architectural zones to 60 Honeybee thermal zones.

In locations where a single architectural space was subdivided into multiple Honeybee zones, air boundary conditions were applied between adjacent thermal zones.

The use of air boundaries allows zones to be thermally separated for calculation purposes while permitting air mixing and preventing the introduction of artificial thermal

resistance between sub-zones. This approach ensures continuity of thermal behavior within the original architectural space while still allowing the simulation engine to resolve local thermal differences more accurately.

Overall, the increase in the number of thermal zones was intentionally introduced to improve the spatial resolution of energy simulation. By distributing energy flows more evenly across smaller, behaviorally consistent zones, the model achieves a more homogeneous representation of thermal conditions and reduces numerical smoothing effects associated with oversized zones. This zoning strategy therefore enhances the reliability of simulation outputs while maintaining consistency with the original architectural intent.

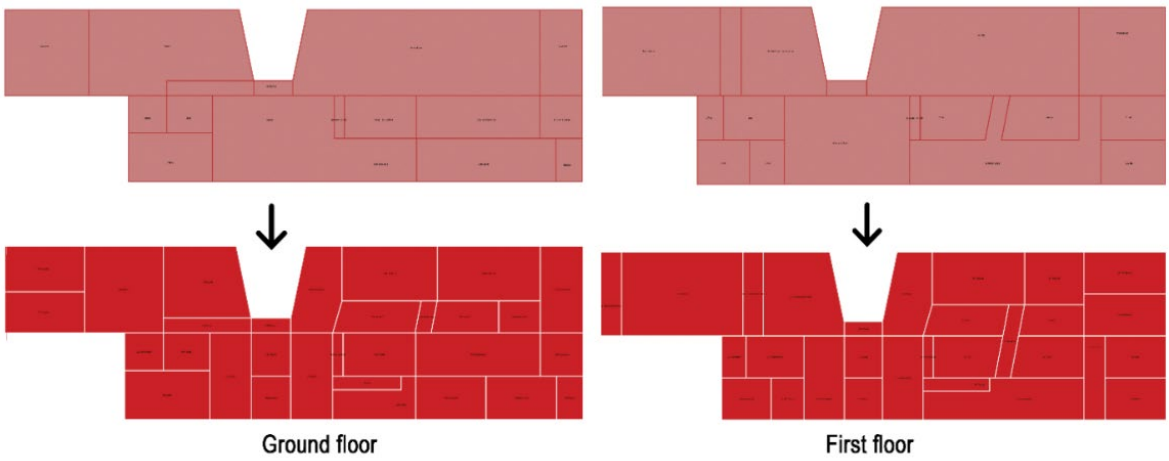

Figure 5-24 Ground floor and First floor transition from architectural to thermal.

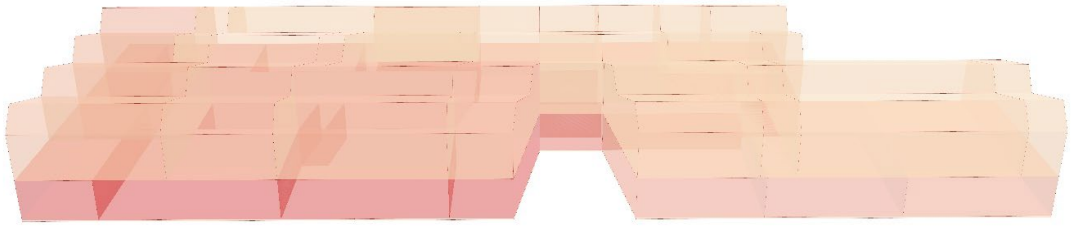

Figure 5-25 Intersected Zones 3D Modeling.

Thermal Boundary Condition Definition

After defining the zones and performing the intersection process, the faces associated with each zone were clearly identified, and geometric overlaps were removed. This step ensures a clean and unambiguous surface definition as a prerequisite for reliable thermal modeling.

Subsequently, boundary conditions were assigned to all zone surfaces to enable accurate energy simulation. The architectural zones were first converted into Honeybee Rooms, providing a thermal representation compatible with energy analysis. The Solve Adjacency component (explained in section 4.1.2) was then employed to automatically identify spatial relationships between rooms and classify their surfaces as external walls, internal walls, air boundaries, roofs, and floors.

Following the definition of surface boundary conditions, openings were introduced into the model. Doors and windows were assigned to their corresponding wall surfaces, completing the geometric and thermal definition of the building envelope. This step ensures that openings are correctly integrated into the thermal model and that their influence on heat transfer, solar gains, and energy performance is accurately captured in subsequent simulations.

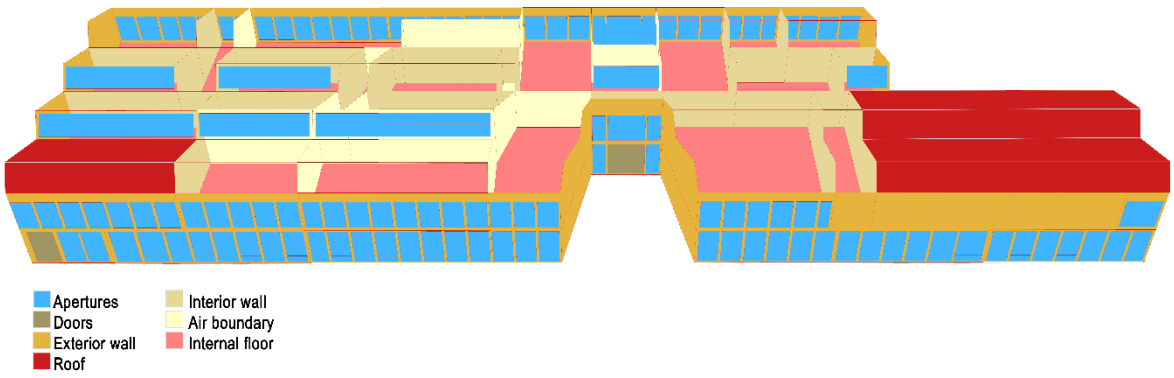

Figure 5-26 Boundary condition of case study.

5.2 Parametric shader modeling

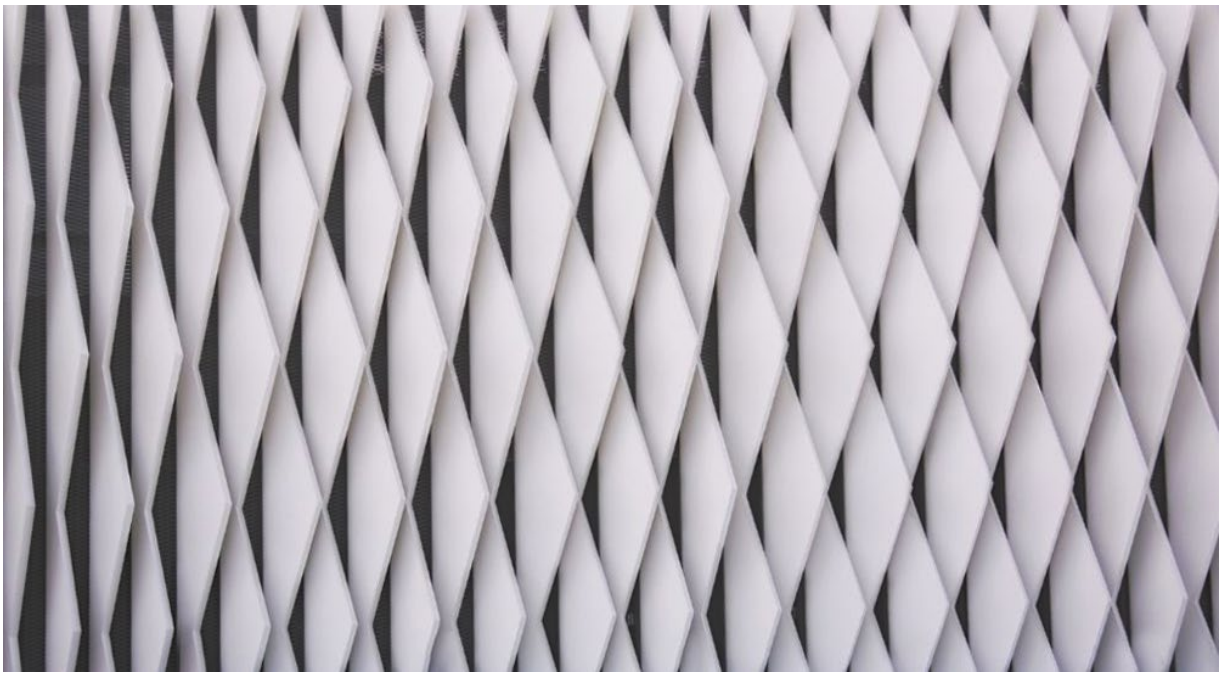

Figure 5-27 Visualization of the parametric shading system.

Figure 5-6 represents a general overview of 3D visualization from the parametric shading system modeled to be used on southern facade of the case study for this test.

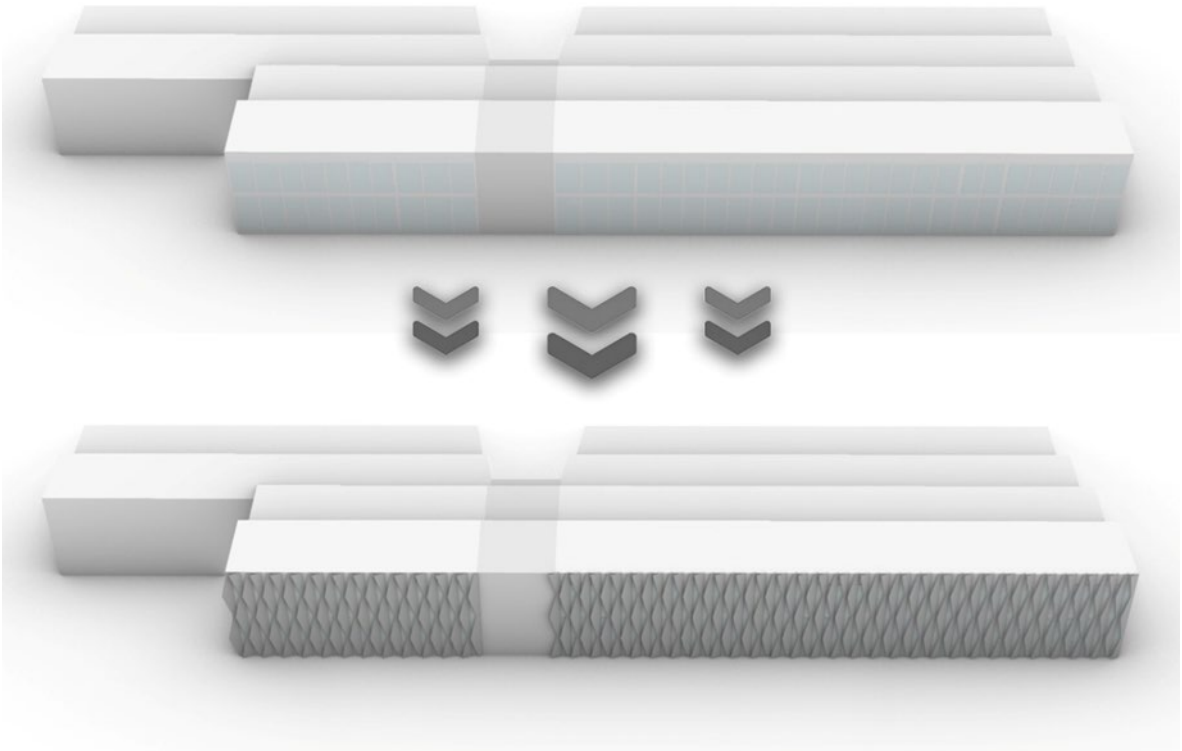

. Figure 5-28 Existing and transformed mode of the case study.

The existing situation of the design project without shadings and after addition of the shading system in one possible mode out of the various possibilities is shown on the Figure 5-7.

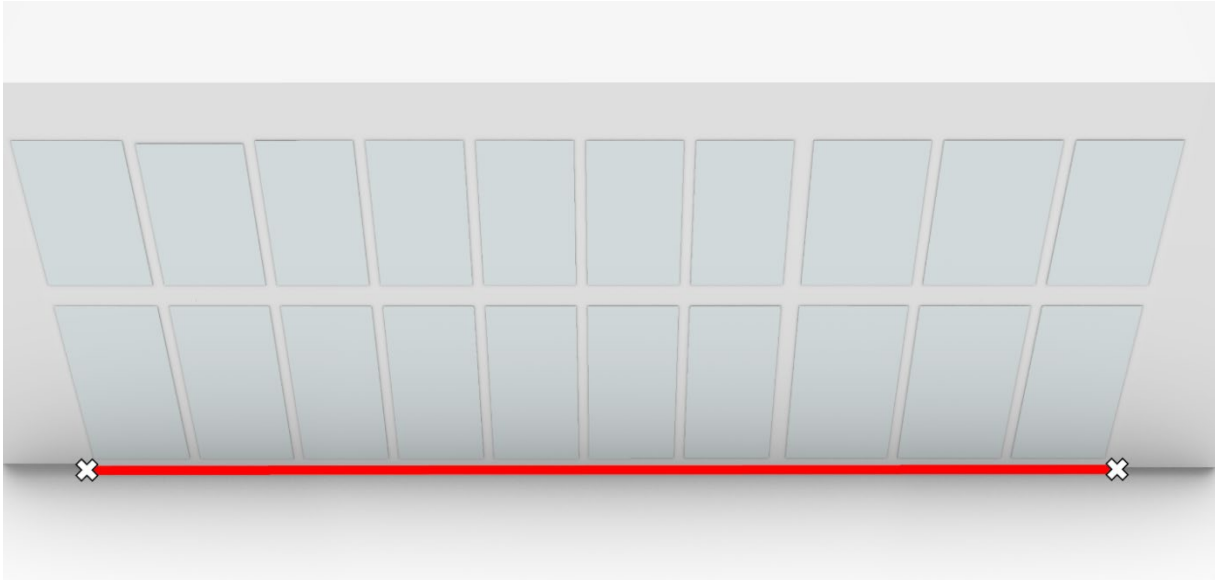

Figure 5-29 Variable input of the parametric shading model

The parametric shading model being considered for this optimization test can be simply created by the user only with drawing lines wherever needed, and its algorithm gets activated.

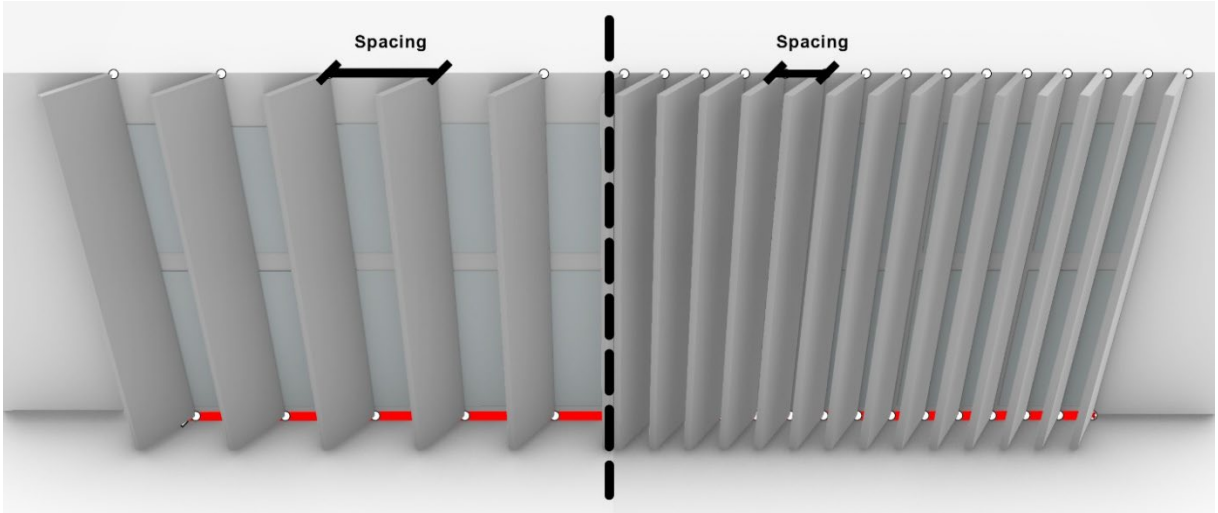

Figure 5-30 Variable input of the parametric shading model.

One of the inputting parameters which will vary during the optimization is the spacing size between the shading components.

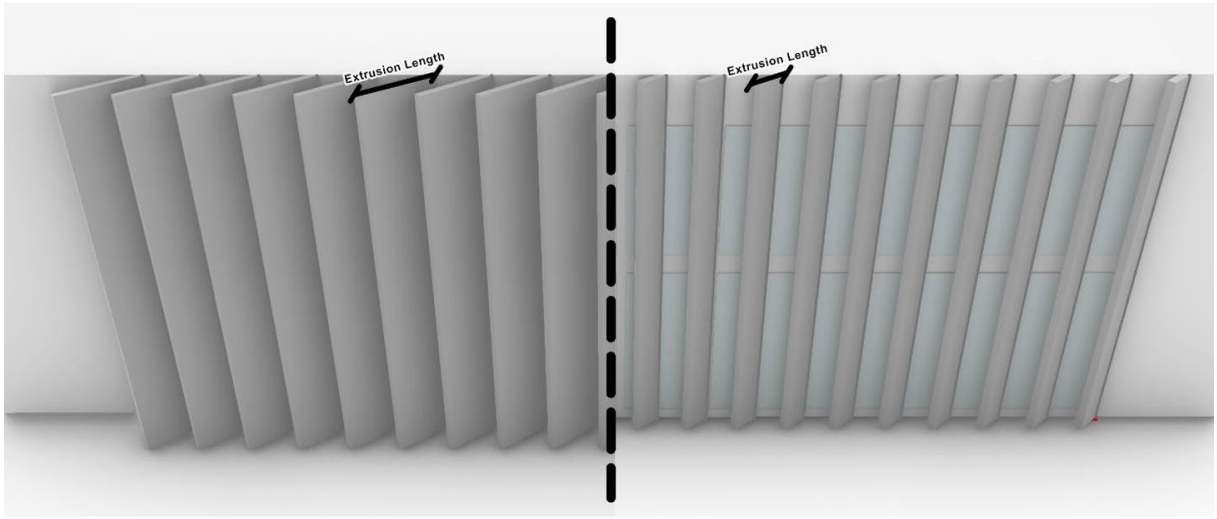

Figure 5-31 Variable input of the parametric shading model.

The next one is the extrusion length (or width) of the shaders.

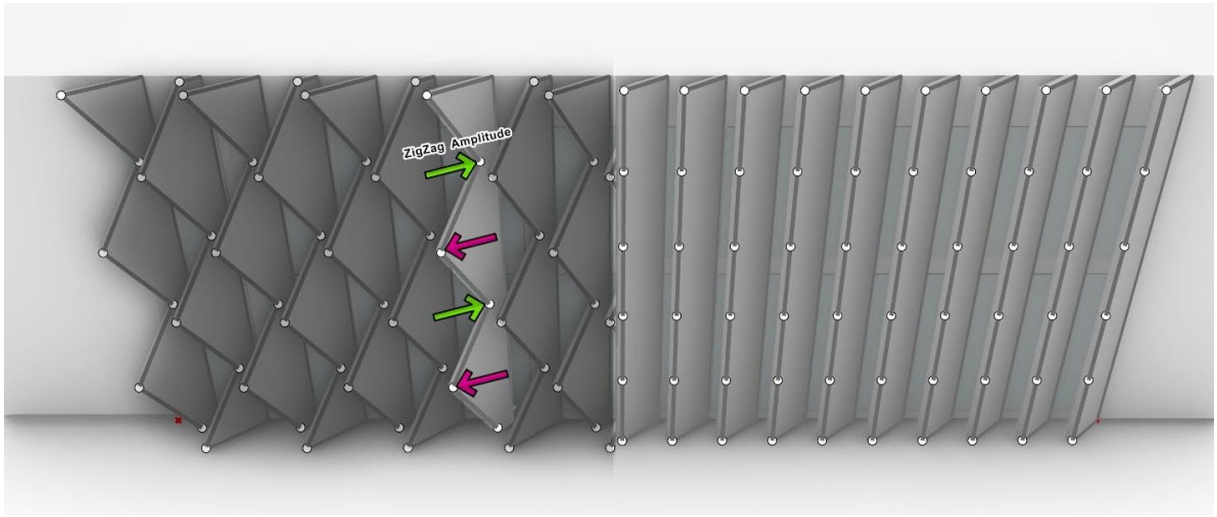

Figure 5-32 Variable input of the parametric shading model.

Zig zag amplitude which gives different patterns with different results.

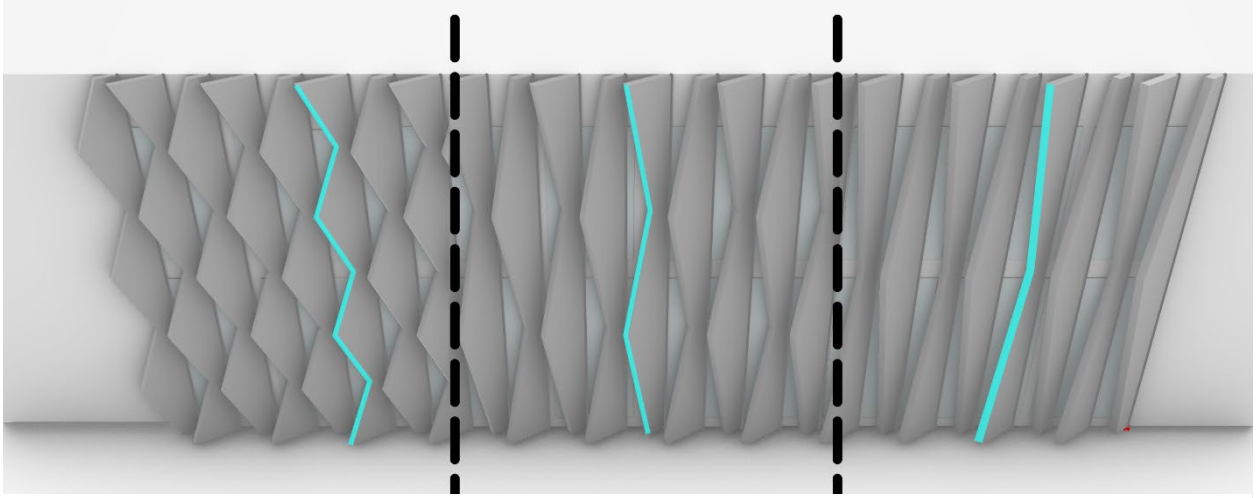

Figure 5-33 Variable input of the parametric shading model.

The count of these zig zag variations.

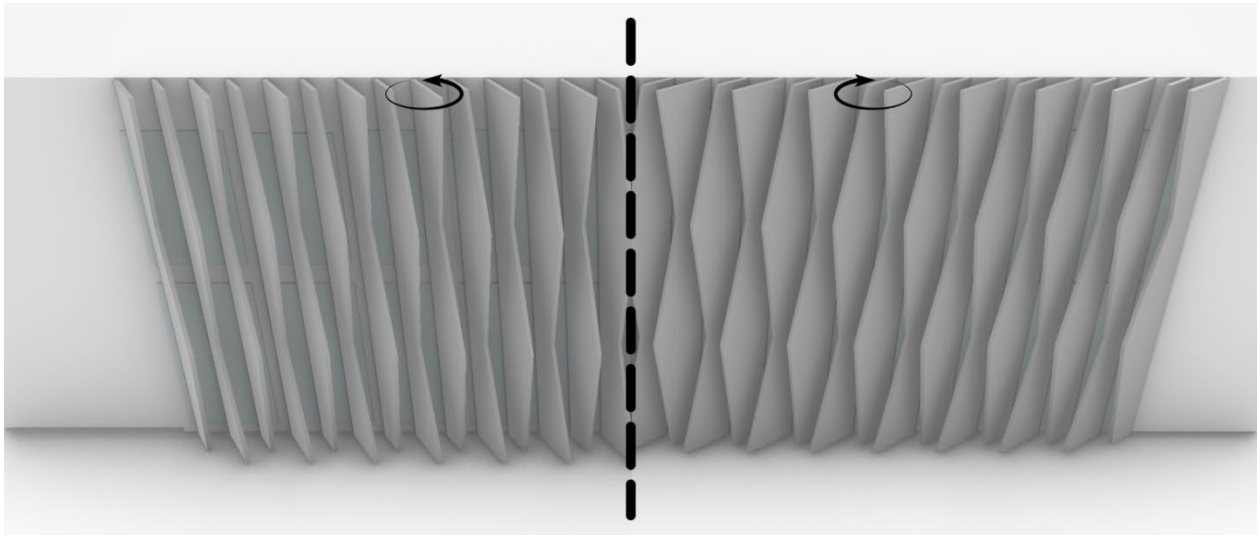

Figure 5-34 Variable input of the parametric shading model.

Rotation to give different results for solar radiation orientation.

The algorithm for this parametric shading system is attached below and explained part by part.

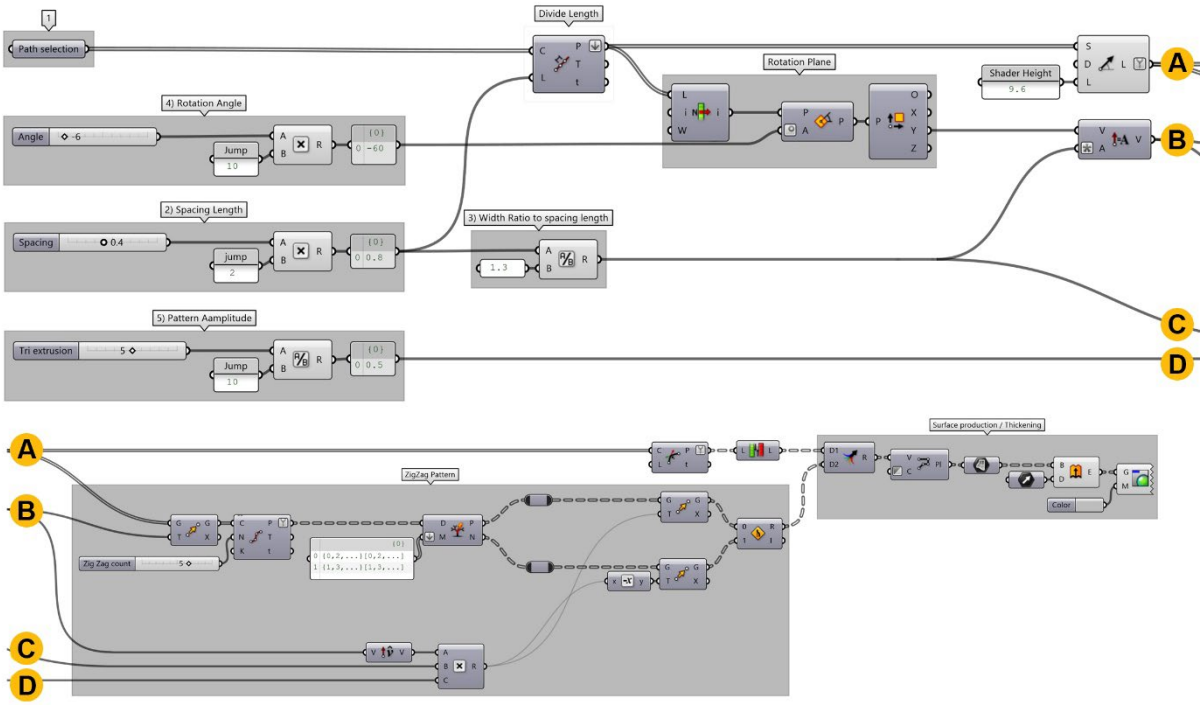

Figure 5-35 algorithm of the shading system model

The orange circles represent the continuity of the algorithm connection.

The algorithm blown up:

Figure 5-36 algorithm blow-up 1

1) At this stage, the user only needs to draw and select a single line (path) or multiple ones to define the extent and direction of the shading system. The algorithm automatically generates the shading elements along the selected path, without requiring the user to specify orientation or additional geometric constraints. Based on the chosen path, tangent and normal vectors are computed correctly at each point, ensuring robust geometric behavior regardless of whether the path is straight or curved. As a result, even for paths with varying curvature or direction, a stable local coordinate framework is established, allowing the shading system to be generated consistently and uniformly along the entire path.

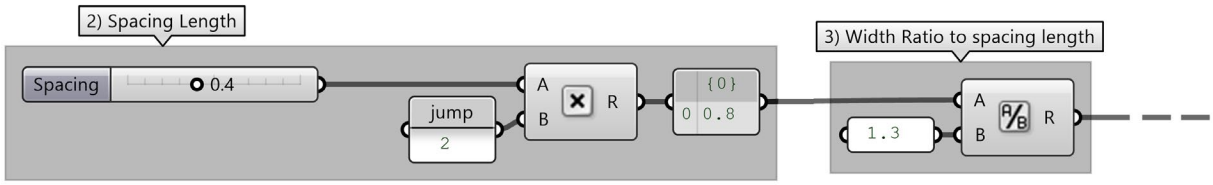

Figure 5-37 algorithm blow-up 2 & 3

2) Spacing number slider is one of the variables controlled during optimization process

This step controls the horizontal spacing between shading louvers, defined in meters. To improve optimization efficiency and avoid unnecessary expansion of the search space, the spacing parameter is discretized using a jump operation. Although the slider ranges from 0.2 to 0.7, after applying the scaling and jump mechanism it is interpreted as discrete spacing values from 0.4 m to 1.4 m at 0.2 m intervals. This approach reduces redundant evaluations while allowing the algorithm to explore a meaningful range of spacing configurations within the same number of generations.

By constraining the resolution of the spacing parameter, optimization avoids excessive redundancy, improves population diversity, and allows the algorithm to explore a wider range of meaningful configurations within the same number of generations.

3) In this step, the width of the shading louvers is controlled relative to the spacing length through a proportional ratio rather than an absolute dimension. By defining louver width as a function of spacing, the system ensures that geometric proportions scale consistently and logically as spacing values change. This relative control prevents excessive widening or narrowing of louvers and parametrically avoids geometric overlap or interpenetration between adjacent shading elements. As a result, the shading geometry remains coherent and constructible across all tested configurations, while maintaining stable proportions throughout the optimization process.

This avoids essentially creating null answers and errors during the optimization.

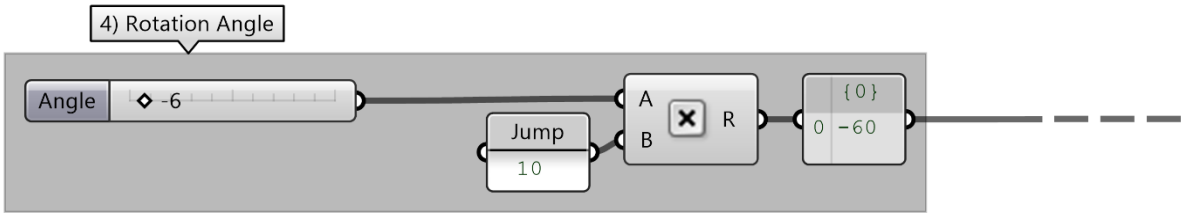

Figure 5-38 algorithm blow-up 4

4) The rotation angle number slider is the next optimizing variable. This step controls the rotation angle of the shading louvers relative to the local reference frame defined along the path. The rotation angle is allowed to vary between −70° and +70°, enabling a wide range of orientations for solar control and daylight modulation. To prevent unnecessary expansion of the search space and improve optimization efficiency, the angle parameter is discretized using a jump operation, evaluating rotations at 10-degree intervals. This discretization ensures that the optimization explores meaningful angular variations while avoiding redundant intermediate rotations that produce negligible performance differences. As a result, the algorithm maintains a balanced exploration of louver orientations with controlled computational cost.

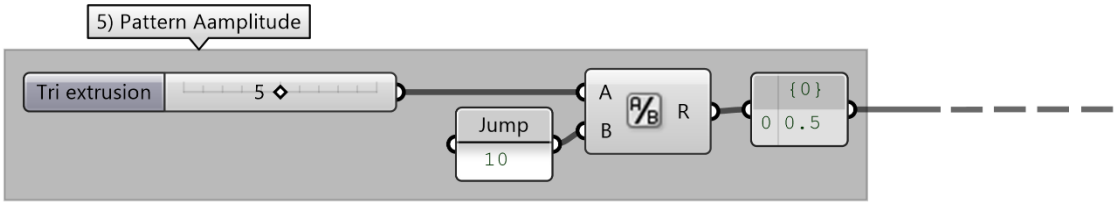

Figure 5-39 blow-up 5

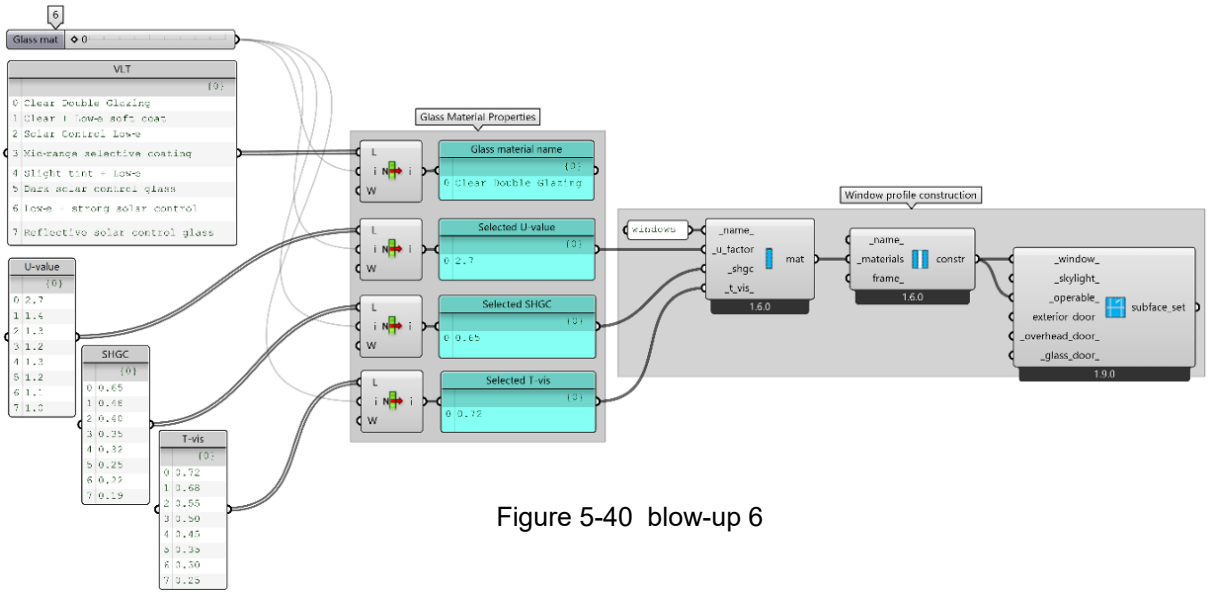

Figure 5-40 blow-up 6

5) This step controls the amplitude of the zigzag pattern, which defines the lateral offset of the shading geometry along the generated path. The amplitude parameter directly affects the depth and articulation of the pattern, influencing both shading performance and visual porosity. To maintain a structured and efficient search space, the amplitude value is discretized using a division and jump operation, resulting in 10 cm intervals between successive configurations. By evaluating the zigzag amplitude at regular 0.1 m steps, the algorithm avoids excessive geometric redundancy while still capturing meaningful variations in pattern depth. This controlled discretization enables consistent pattern generation and ensures stable geometric behavior throughout the optimization process.

6) This number slider functions as a discrete selector for predefined glass material types, controlling the optical and thermal properties of the window system. Rather than

varying glass parameters continuously, the slider indexes a library of realistic glazing options, each associated with a specific set of U-value, solar heat gain coefficient (SHGC), and visible transmittance (T-vis) values. By adjusting a single integer value, the user selects a corresponding glass material, and the linked U-value, SHGC, and T-vis properties are automatically assigned and propagated through the window construction definition.

This approach ensures that all evaluated glazing configurations remain physically consistent and industry-realistic, while also preventing unnecessary expansion of the search space. By treating glass properties as a categorical design variable rather than independent continuous parameters, the optimization avoids unrealistic combinations and maintains coherence between thermal and daylight performance inputs throughout the simulation workflow.

5.3 Baseline analysis before shading application

5.3.1 Zonal program & setpoint assignment

After completing the zoning process and converting architectural zones into Honeybee Rooms, the next critical step involved assigning an appropriate operational program to each room **(refer to Figure 5-3)**. This step is essential because thermal and energy behavior in building simulation is not governed by geometry alone, but by how spaces are used, occupied, and conditioned over time.

Each Honeybee Room was therefore assigned to a program that reflects its functional use and expected energy behavior. Program definitions were selected using the HB Search Program component, which provides access to a library of predefined operational templates derived from ASHRAE standards. These templates encapsulate typical assumptions for occupancy density, internal heat gains, lighting power density, equipment loads, ventilation rates, and operational schedules, thereby ensuring consistency with recognized performance benchmarks.

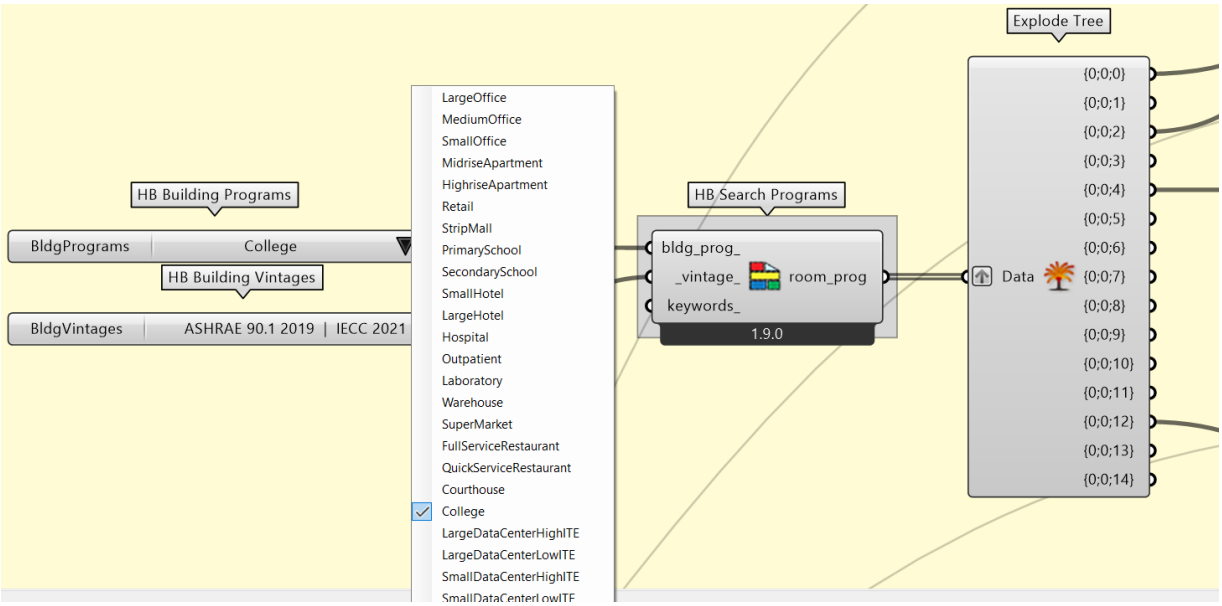

Figure 5-41 Overview of available options in the Honeybee HB Search Programs component.

The default program library available within the HB Search Program component includes a wide range of building typologies, such as office buildings, residential units, retail spaces, educational facilities, hospitality functions, healthcare environments, laboratories, warehouses, data centers, and food service establishments. These predefined programs serve as standardized representations of real-world building use patterns and are widely adopted in performance-based energy modelling.

Given the mixed-use nature of case study building, a selective program assignment strategy was adopted. Instead of applying a single operational program across the entire model, rooms with similar functional characteristics and energy-use profiles were grouped and assigned to one of four representative program categories: College, Retail, Full-Service Restaurant, and Medium Office. This strategy ensures that spaces with comparable patterns of occupancy, internal gains, and operational schedules share consistent behavioral assumptions, while still allowing thermal responses to vary as a function of geometry, orientation, and exposure conditions.

Following program selection, each chosen program was passed to the HB Program Type component, which generates a Program Type object encapsulating all schedules and internal loads defining the usage characteristics of space. These Program Type objects are subsequently assigned to Honeybee Rooms to specify default assumptions related to occupancy, lighting, equipment, ventilation, and operational schedules.

Within the HB Program Type component, a key input is the Setpoint parameter, which defines the temperature and humidity setpoints associated with the selected program. A Setpoint object is required for any conditioned space, as a Program Type without defined setpoints cannot be assigned to a mechanically conditioned Honeybee Room. In this study, heating and cooling setpoints were defined in accordance with ASHRAE (2002) guidelines. A heating setpoint of 21°C and a cooling setpoint of 24°C were applied consistently across all conditioned rooms. This standardized setpoint strategy establishes a clear and comparable operational baseline, ensuring that variations in energy performances are primarily driven by spatial configuration, envelope behavior, and programmatic use rather than by inconsistent thermal comfort assumptions. Once all operational programs, schedules, internal loads, and setpoints were fully defined, the HB Apply Program Type component was used to assign the Program Type objects to the Honeybee Rooms. Through this step, the programmatic and behavioral characteristics of each space were fully integrated into the thermal model, completing the operational definition of the building. The resulting model combines geometric, thermal, and usage-related information in a consistent manner, providing a robust foundation for baseline energy simulation and subsequent optimization and performance evaluation.

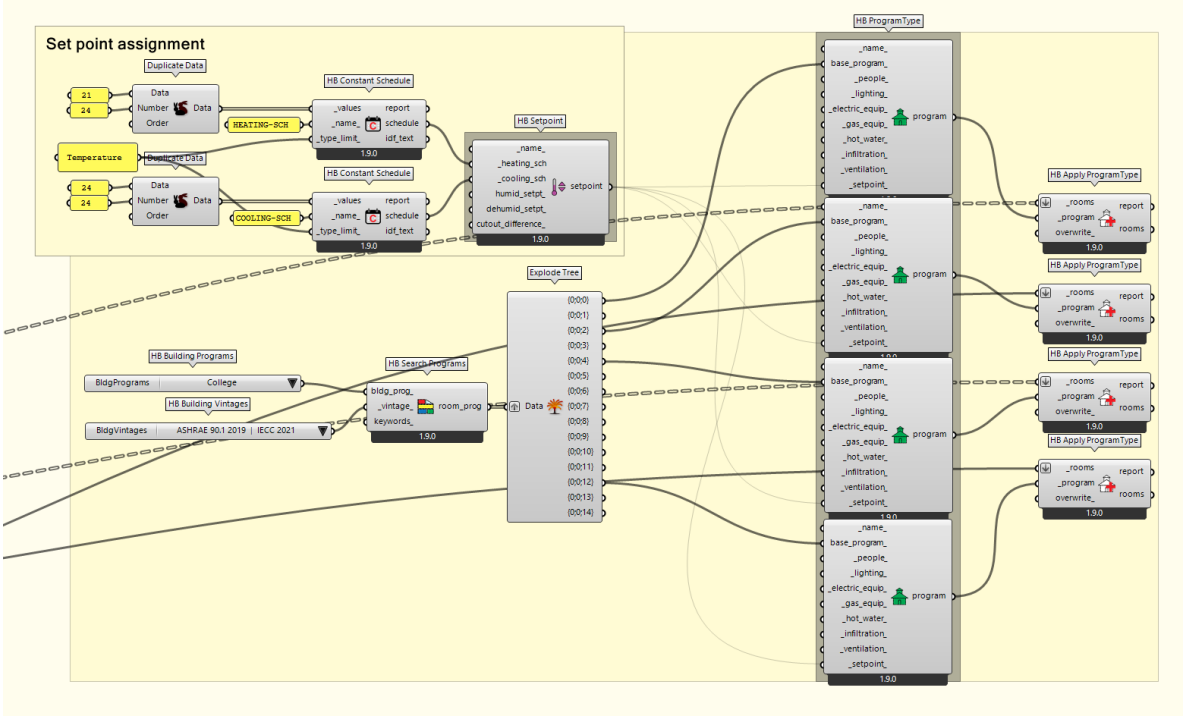

Figure 5-42 Assignment of heating and cooling setpoints and application of Honeybee program types.

The following figures present representative schedule profiles derived from the assigned program types, illustrating the temporal distribution of internal loads used in the energy simulations.

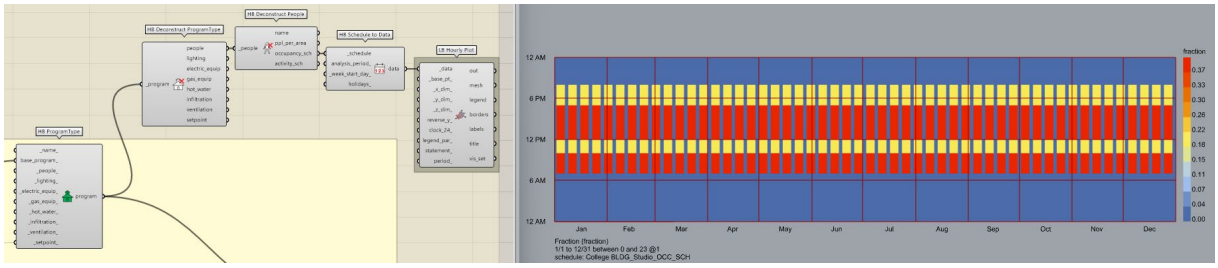

Figure 5-43 Workflow for extracting and visualizing People occupancy schedules from assigned Honeybee Program Types, showing the deconstruction of program data and the resulting hourly schedule profile used in the energy simulations.

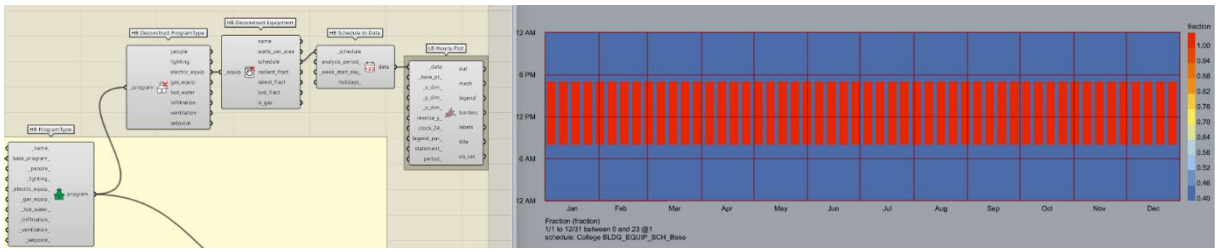

Figure 5-44 Workflow for extracting and visualizing Equipment schedules from assigned Honeybee Program Types, showing the deconstruction of program data and the resulting hourly schedule profile used in the energy simulations.

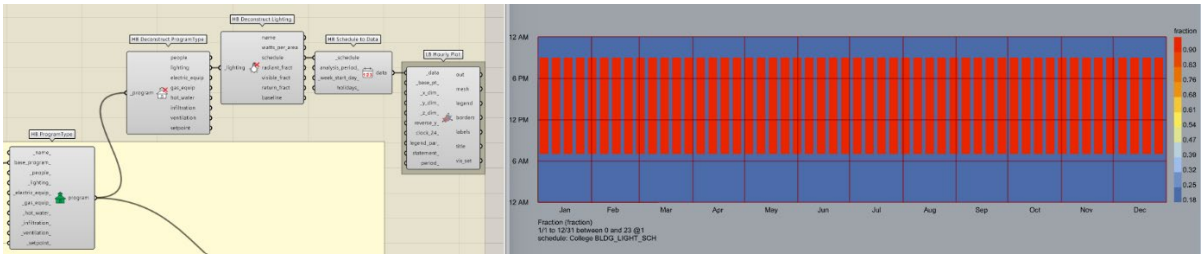

Figure 5-45 Workflow for extracting and visualizing lighting schedules from assigned Honeybee Program Types, showing the deconstruction of program data and the resulting hourly schedule profile used in the energy simulations.

.

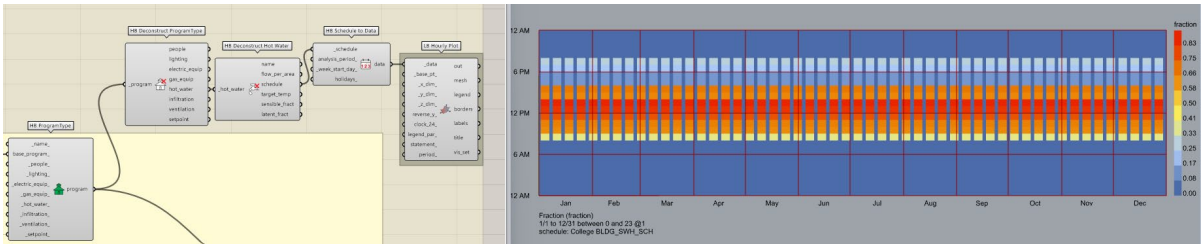

Figure 5-46 Workflow for extracting and visualizing Hot water schedules from assigned Honeybee Program Types, showing the deconstruction of program data and the resulting hourly schedule profile used in the energy simulations.

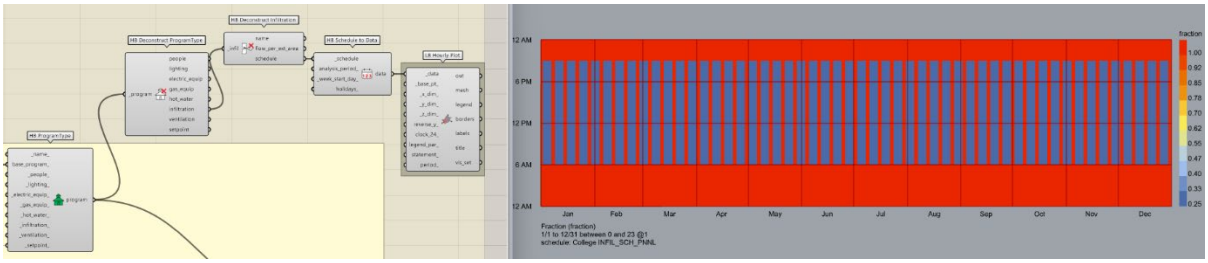

Figure 5-47 Workflow for extracting and visualizing People occupancy schedules from assigned Honeybee Program Types, showing the deconstruction of program data and the resulting hourly schedule profile used in the energy simulations.

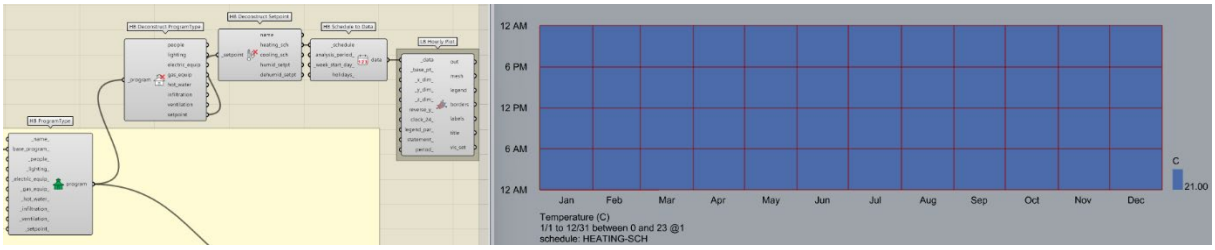

Figure 5-48 Workflow for extracting and visualizing Heating schedules from assigned Honeybee Program Types, showing the deconstruction of program data and the resulting hourly schedule profile used in the energy simulations.

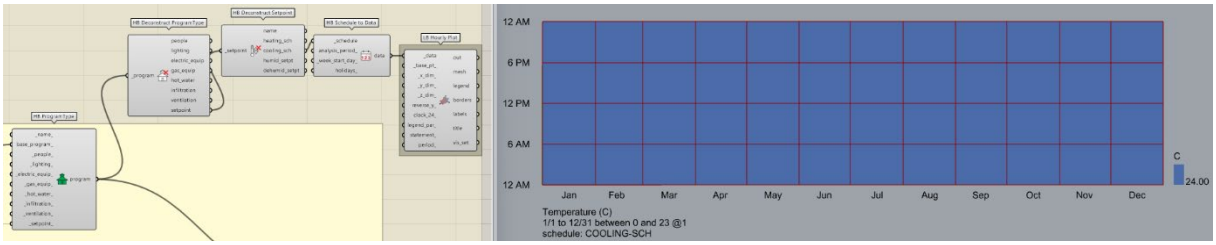

Figure 5-49 Workflow for extracting and visualizing Cooling schedules from assigned Honeybee Program Types, showing the deconstruction of program data and the resulting hourly schedule profile used in the energy simulations.

5.3.2 Definition of Material Properties for Baseline Simulation

After the operational programs and schedules were assigned to all Honeybee Rooms, the next step focused on defining the physical and thermal properties of the building's envelope and internal elements **(refer to Figure 5-4)**. While program assignments govern how spaces are used and conditioned, accurate energy simulation additionally requires a detailed description of how heat is transferred through walls, roofs, floors, and ground-contact surfaces.

This stage begins with the definition of material layers using Honeybee energy material components. Each material is characterized by its thermophysical properties, which determine how heat is stored and transmitted through individual layers and form the fundamental inputs for heat transfer calculations within the simulation engine.

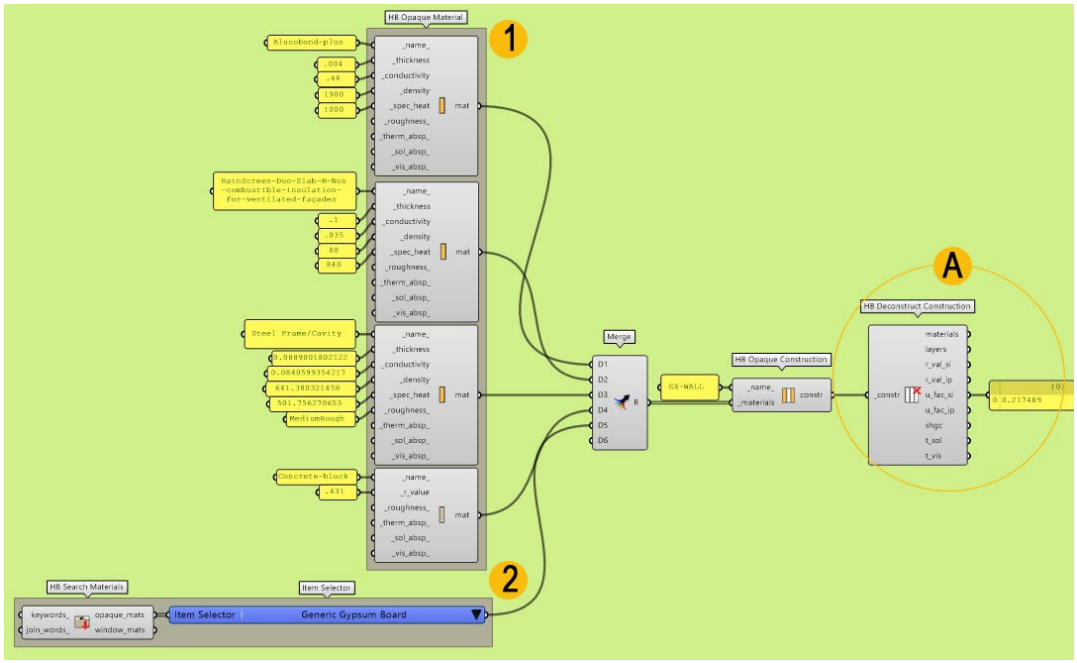

Figure 5-50 Opaque wall construction workflow in Honeybee, showing (1) manual material definition using HB Opaque Material and (2) use of default materials via HB Search Material, assembled into an HB Opaque Construction for energy simulation.

Material properties were assigned using two complementary approaches to balance modeling accuracy and standardization.

In the first approach, highlighted as (1) in Figure 5-50 **.** material definitions were created manually using the HB Opaque Material component, with properties specified from manufacturer technical data and product datasheets. Key thermophysical parameters—thermal conductivity, density, specific heat capacity, and layer thickness—were entered according to published specifications. In parallel, a second set of materials, highlighted as (2) in Figure 5-50, was derived from the default Honeybee material library, representing generic constructions consistent with EnergyPlus reference datasets and ASHRAE-aligned modelling conventions. Combining manual and library-based materials ensures project-specific accuracy while maintaining methodological consistency within the EnergyPlus simulation environment.

Following material definition and assignment, baseline construction performance was evaluated (A in Figure 5-50) using resulting U-values and thermal mass characteristics, which govern steady-state heat transfer and dynamic thermal response. Fixing envelope parameters at these stabilities a stable reference condition, allowing subsequent variations in energy demand and indoor thermal performance to be attributed to spatial configuration, operational behavior, and control strategies rather than inconsistencies in construction definition.

After defining material layers and assembling construction definitions for each building element, the workflow advanced to the Construction Set stage.

This step organizes the previously defined constructions into structured subsets, enabling consistent assignment of envelopes and internal constructions across all Honeybee Rooms. Constructions related to the external envelope were grouped using the HB Exterior Construction Subset, covering external walls, roofs, and exposed floors. Internal building elements were organized using the HB Interior Construction Subset, including internal walls, floors, ceilings, and internal openings. In addition, constructions for openings such as windows, skylights, and doors were defined separately using the HB Subface Subset.

These subsets were then combined within the HB construction Set component, which aggregates all construction definitions required to generate a complete energy model. The resulting Construction Set specifies default constructions for all relevant surface types and ensures consistent application across the model. Finally, the Construction Set was assigned to all Honeybee Rooms using the HB Apply Construction Set component. This step completes the physical and thermal definition of the building, establishing a coherent and simulation-ready model for baseline energy analysis.

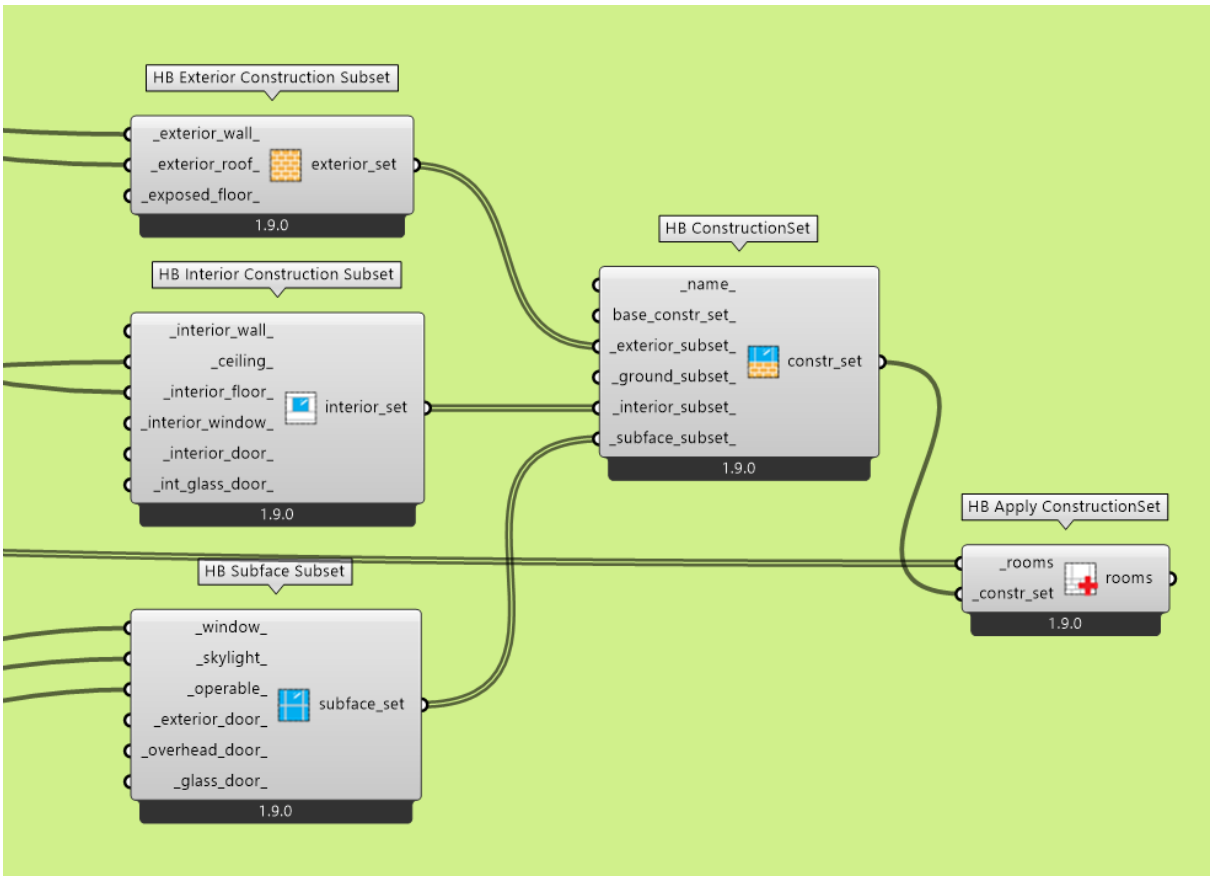

Figure 5-51 Construction set workflow in Honeybee, organizing envelope, interior, and sub-surface constructions and assigning them to rooms.

5.3.3 Energy results

This section presents the energy performance results derived from the annual simulations described in Chapter 4. Energy behavior is evaluated at the building level using Energy Use Intensity (EUI) as the primary performance indicator, extracted from OpenStudio simulation outputs. The results correspond to a 60-zone Honeybee energy model representing a multifunctional building and are used to assess overall energy demand and to support comparative interpretation of design scenarios.

Total Energy Use Intensity (EUI)

As it is illustrated bellow total Energy Use Intensity (EUI) of 181.4 kWh/m²·year. This value represents the aggregated annual energy demand for all modeled end uses, normalized by the gross floor area, including conditioned and unconditioned spaces.

Interpretation

Within the LEED framework**,** Energy Use Intensity is not assigned to fixed performance classes; instead, it is evaluated relative to a baseline building defined by ASHRAE standards. Therefore, the reported EUI of 181.4 kWh/m²·year cannot be directly classified as “pass” or “fail” under LEED, but serves as a comparative performance indicator used to quantify improvement against a reference model. As such, this value provides a consistent metric for optimization and scenario comparison rather than absolute certification grading.

From an Italian and Milan regulatory perspective, building energy performance is typically classified using (Global Non-Renewable Primary Energy Index) indicators rather than EUI. While a direct one-to-one conversion is not possible, an EUI of this magnitude is generally indicative of a medium energy performance level, broadly corresponding to Class C–D for complex, multifunctional buildings in the Milan climatic context. The result suggests that, while the building does not achieve high-performance or near-zero energy standards, it demonstrates a controlled and reasonable energy demand consistent with contemporary urban mixed-use developments.

Distinct Energy Use Intensity (EUI)

The breakdown of the total Energy Use Intensity (EUI = 181.4 kWh/m²·year) for the multifunctional building reveals a relatively balanced distribution across major end uses. Space heating (56.12 kWh/m²·year) and space cooling (53.84 kWh/m²·year)

constitute the dominant energy demands, together accounting for approximately 61% of the total EUI. Interior lighting (30.29 kWh/m²·year) and electric equipment (33.59 kWh/m²·year) represent significant internal loads, while domestic hot water and water-related systems contribute a comparatively minor share (7.57 kWh/m²·year).

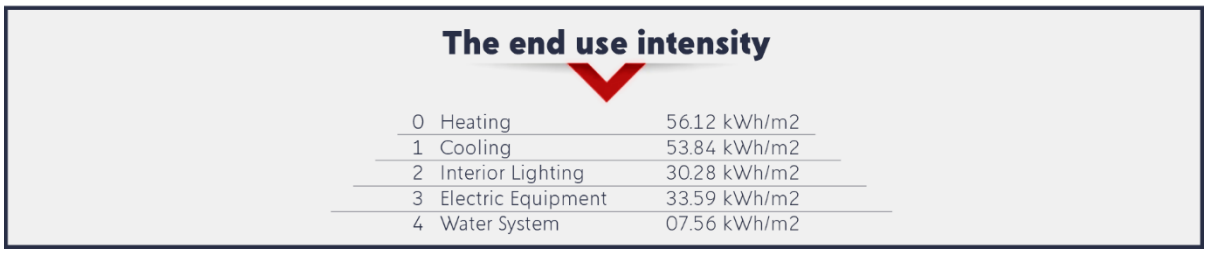

Interpretation

The comparable magnitude of heating and cooling demands indicates a strong sensitivity of the building's energy performance to envelope characteristics, solar gains, and ventilation strategies, rather than a heating- or cooling-dominated profile. The substantial contribution of lighting and equipment reflects the mixed-use nature of the building and highlights the importance of internal gains in driving both cooling loads and overall energy demand. From a performance perspective, these results suggest that further reductions in total EUI would most effectively be achieved through integrated strategies targeting envelope optimization, solar control, and daylight-responsive lighting, rather than focusing on a single end-use category alone.

Thermal Load Balance

The thermal load balance illustrates the monthly distribution of energy gains and losses across the building, disaggregated by end uses and physical mechanisms, including heating and cooling demand, solar gains, internal gains (people, lighting, equipment), ventilation and infiltration, and heat transfer through opaque and transparent envelope components. Positive values indicate heat gains to the zones, while negative values represent heat losses. Seasonal trends show dominant heating contributions during winter months and pronounced cooling loads during summer, with solar and internal gains peaking in warmer periods. The distinction between *balance* and *balance_stor* highlights the role of instantaneous heat exchange versus delayed effects associated with thermal mass.

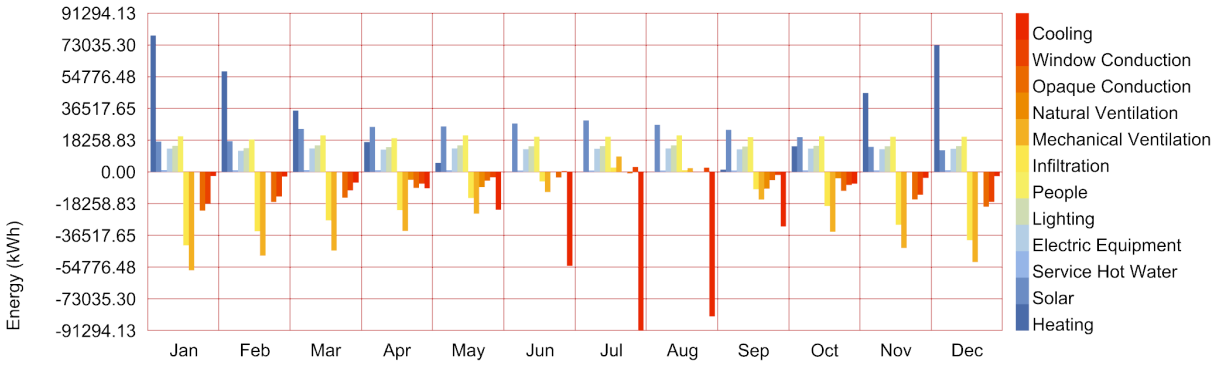

Figure 5-52 Monthly thermal load balance illustrates the relative contributions of heat gains and losses by source across the year.

Interpretation

- The building exhibits a cooling-dominated profile during summer months (June–September), with peak cooling demand occurring in July and August.
- Solar gains and window conduction are major contributors to summer cooling loads, indicating high solar exposure through glazing.
- Heating demand increases significantly during winter (December–February) due to conductive losses through glazing and opaque envelope elements.
- Internal gains (people, lighting, equipment) remain relatively constant throughout the year and function as stable base loads.
- Transitional months (March–May, October–November) show reduced thermal extremes and more balanced heat exchange.
- The baseline façade lacks seasonal adaptability, resulting in pronounced energy peaks during climatic extremes.

The baseline model exhibits a clear seasonal imbalance, with dominant cooling demand in summer driven by solar gains and window conduction, and increased heating demand in winter due to envelope heat losses. The absence of shading results in pronounced energy peaks under climatic extremes.

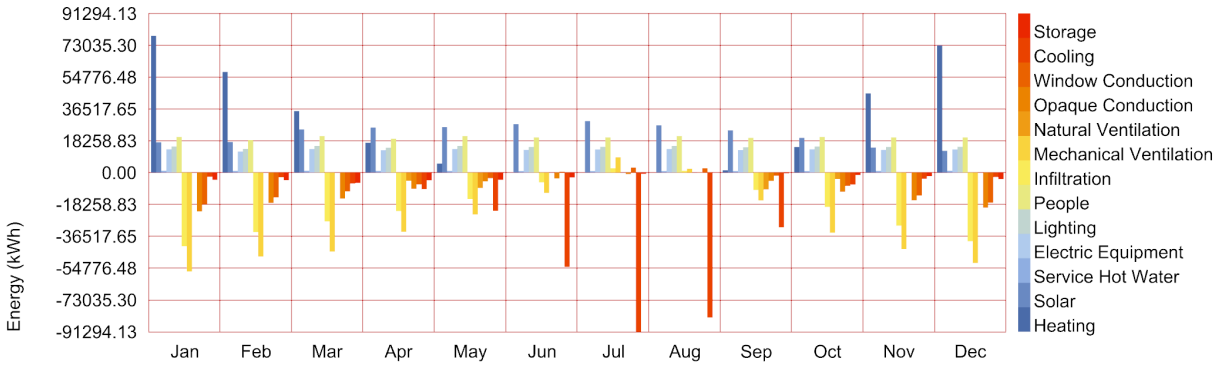

Figure 5-53 Monthly thermal load balance including balance_stor, illustrating the effect of thermal mass on heat storage and release alongside major heat gains and losses.

Interpretation

- Thermal storage (balance_stor) demonstrates a clear seasonal buffering effect.
- During summer, negative storage values indicate heat absorption by internal mass, reducing peak cooling loads temporarily.
- In winter, positive storage values reflect delayed heat release, contributing partially to heating demand reduction.
- The buffering effect is most evident during peak climatic months (July–August and December–January).
- Despite thermal inertia, solar gains and conductive losses remain dominant drivers of seasonal energy imbalance.
- Thermal mass improves temporal load distribution but does not fundamentally resolve overheating or heat-loss issues in the baseline configuration.

In summary, the incorporation of thermal storage highlights the moderating role of building mass in redistributing heat over time; however, its buffering capacity is insufficient to offset the substantial solar gains, and conductive losses present in the unshaded configuration. While thermal inertia reduces peak intensity to some extent, it does not eliminate the fundamental seasonal imbalance in energy demand, confirming that passive mass alone cannot ensure stable annual performance.

Percentage of People Dissatisfied (PPD).

This diagram illustrates the extraction of zone-level thermal conditions. The PPD trends confirm this relationship by quantifying the proportion of occupants likely to experience discomfort.

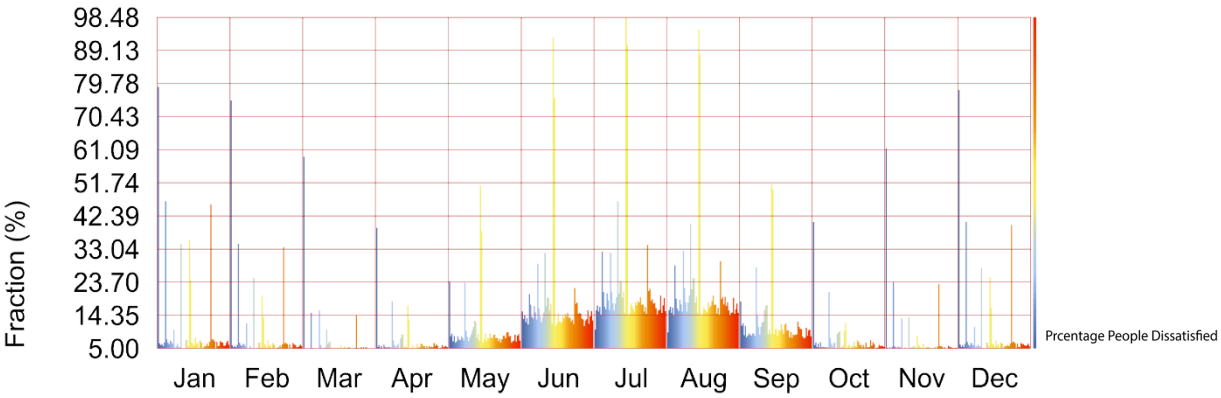

Figure 5-54 Monthly distribution of thermal comfort conditions based on PMV analysis, showing the fraction of occupied hours within comfort and discomfort ranges across the year.

Interpretation

- Summer months show a high fraction of discomfort hours, primarily due to overheating.
- Winter months also exhibit discomfort peaks, associated with underheating conditions.
- Transitional seasons demonstrate the highest proportion of thermally comfortable occupied hours.
- Percentage People Dissatisfied (PPD) increases significantly during peak summer and winter periods.
- The building's comfort performance is highly sensitive to seasonal climatic extremes.

- Without external shading or façade intervention, the baseline model does not maintain stable annual comfort conditions.
- Thermal comfort performance is seasonally unstable, with significant overheating in summer and underheating in winter. While transitional months show acceptable comfort levels, the baseline façade fails to ensure consistent annual indoor environmental quality.

Overall, the baseline thermal comfort analysis indicates significant seasonal instability, with elevated discomfort levels during both summer overheating and winter underheating periods. Although transitional months demonstrate acceptable comfort performance, the building fails to maintain consistent indoor environmental quality across the full annual cycle. These findings emphasize the limitations of the existing façade configuration and underline the necessity for performance-driven envelope optimization.

Mean Air Temperature

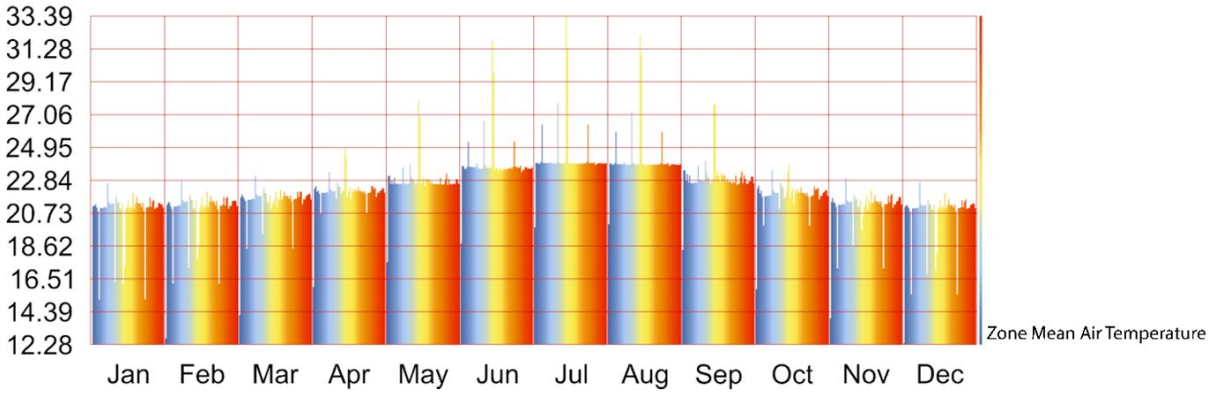

Figure 5-55 Monthly variation of zone mean air temperature (°C) across the year, illustrating seasonal thermal trends and peak summer conditions.

Interpretation

The zone mean air temperature varies annually between approximately 20.5 °C (winter minimum) and 24.0 °C (summer average peak), with short-term summer extremes exceeding 30 °C. While average values remain within moderate ranges, the summer spikes indicate intermittent overheating risk under unshaded conditions.

Annual Surface Heat Gain and Loss Distribution Across Building Envelope

The surface heat transfer distribution reveals significant solar-driven heat gains concentrated on exposed glazed façades, reaching intensities above +300 kWh/m², while other envelope components experience comparatively moderate gains or localized conductive losses. The non-uniform heat transfer pattern confirms that glazing surfaces are the primary drivers of façade-related thermal imbalance in the baseline configuration.

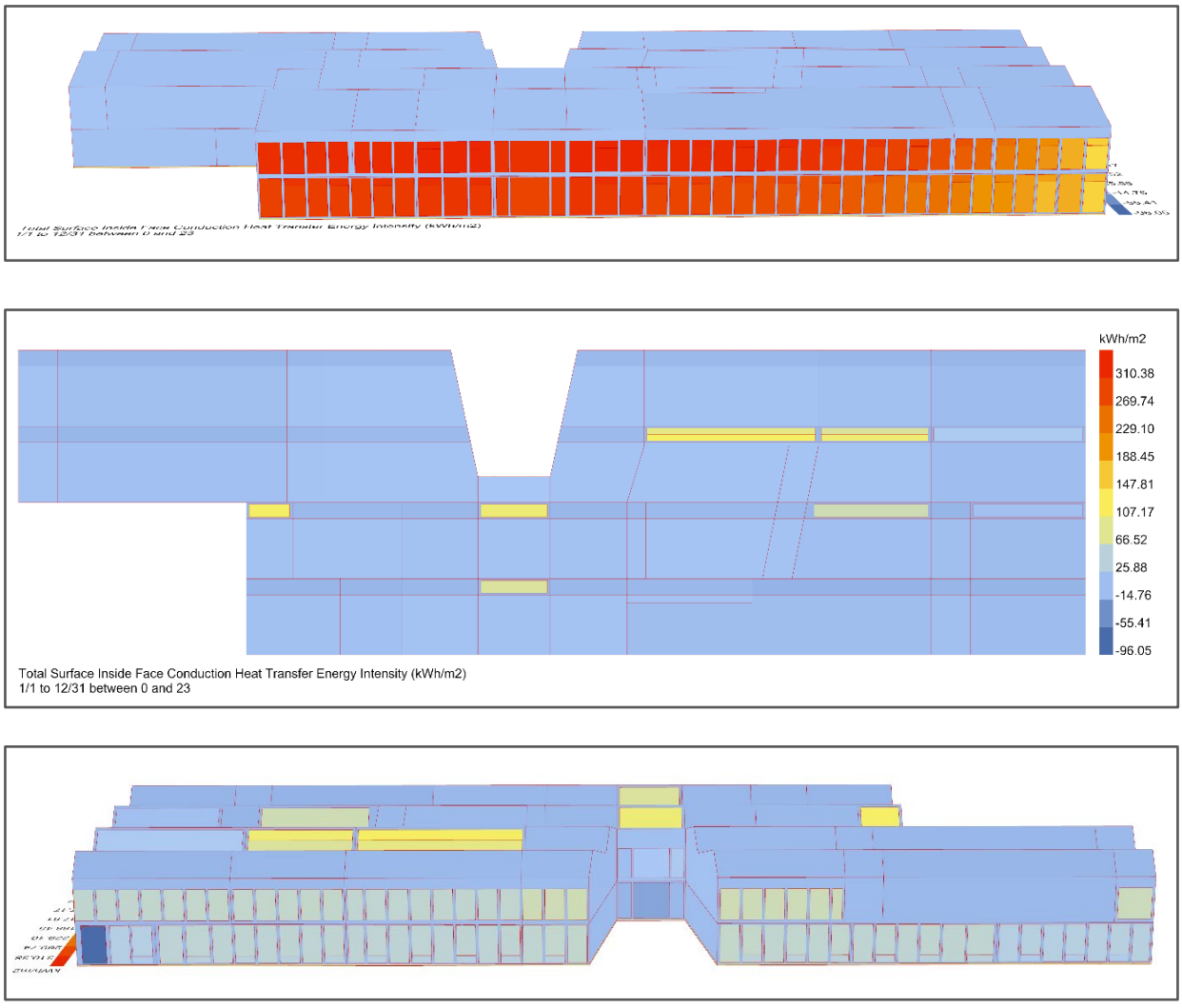

Figure 5-56 The heat loss (negative) or heat gain (positive) through each building surfaces (kWh).

Roon Energy Simulation Result

- Cooling: The room-level cooling energy intensity demonstrates significant spatial variability, with perimeter and solar-exposed zones reaching up to **200 kWh/m²**, while internally buffered areas remain below **70 kWh/m²**. The pronounced disparity confirms that façade exposure and glazing orientation are the dominant drivers of cooling demand in the unshaded configuration, highlighting critical zones for subsequent shading optimization.

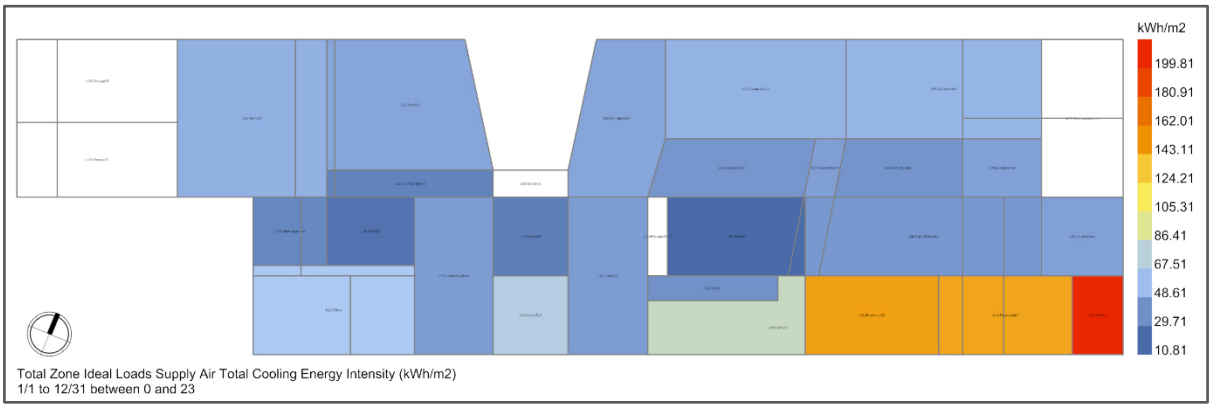

Figure 5-57 Total cooling energy intensity (kWh/m2), Ground Floor.

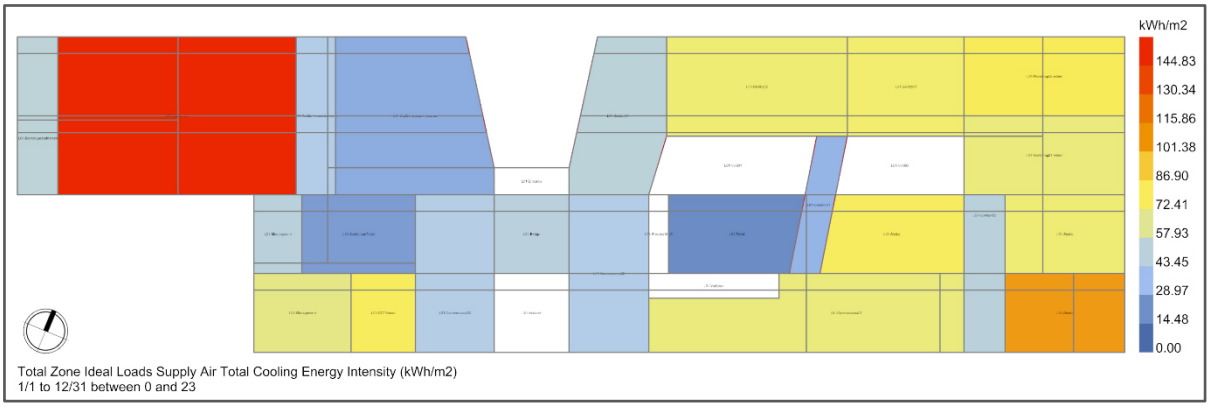

Figure 5-58 Total cooling energy intensity (kWh/m2), First Floor.

- Heating: The heating energy intensity demonstrates clear perimeter-driven demand, with exposed façade zones reaching up to **100 kWh/m²**, while internally buffered areas remain substantially lower.

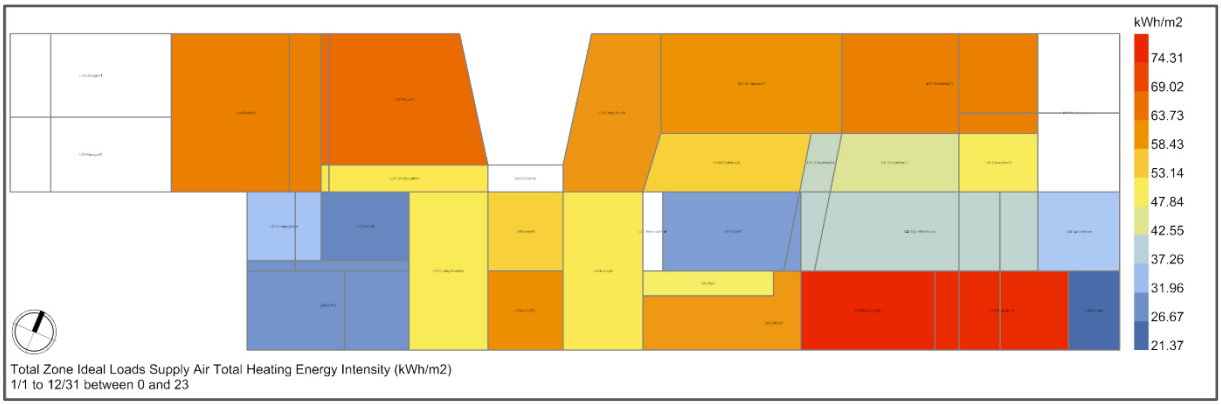

Figure 5-59 Total heating energy intensity (kWh/m2), Ground Floor.

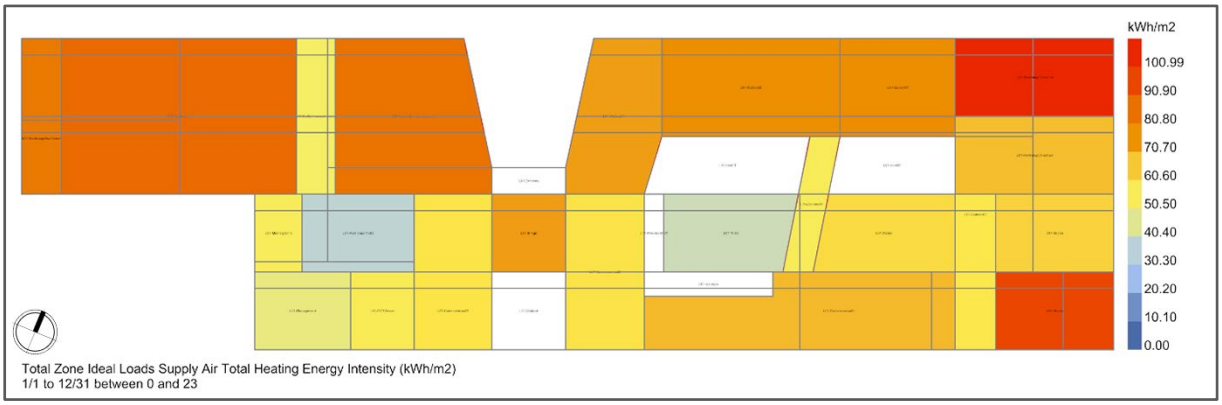

Figure 5-60 Total heating energy intensity (kWh/m2), First Floor.

- Lighting: The baseline lighting energy intensity ranges approximately between **0 and 50 kWh/m²**, with higher values observed in deeper or less daylight-exposed zones. Perimeter areas demonstrate comparatively reduced lighting demand due to natural daylight contribution.

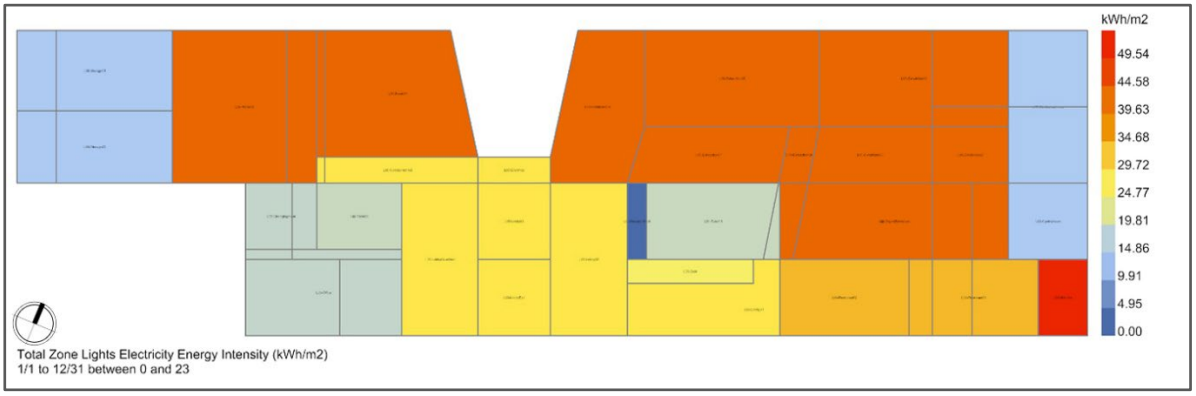

Figure 5-61 Total lights electricity energy intensity (kWh/m2), Ground Floor.

Figure 5-62 Total lights electricity energy intensity (kWh/m2), First Floor.

- Electric Equipment: Electric equipment energy intensity is primarily driven by functional program rather than envelope exposure. While most zones remain below **120 kWh/m²**, a single high-load space reaches approximately **580 kWh/m²**, significantly influencing internal heat gains. In contrast, typical occupied zones range between **10–50 kWh/m²**, contributing stable internal loads that affect overall thermal balance but are not climate-responsive.

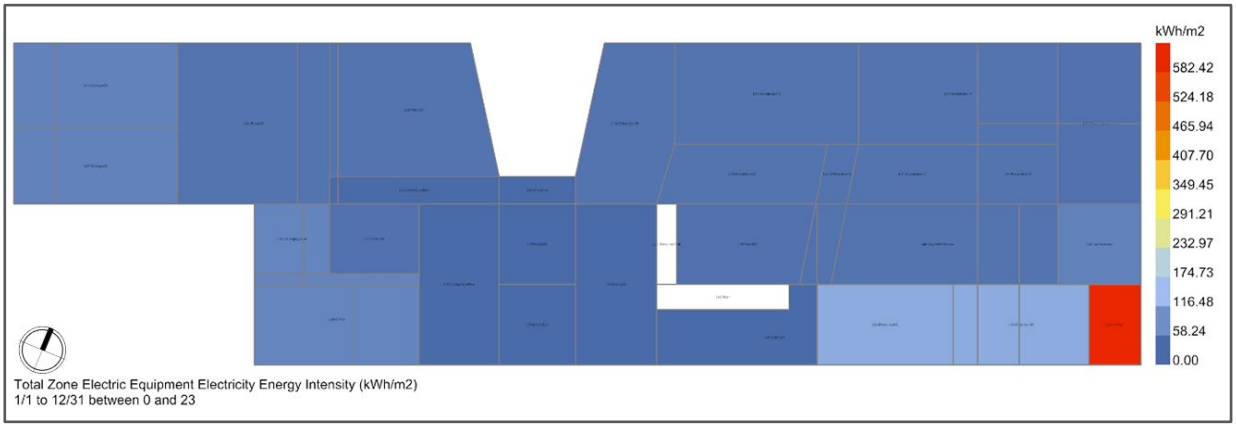

Figure 5-63 Total electric equipment energy intensity (kWh/m2), Ground Floor.

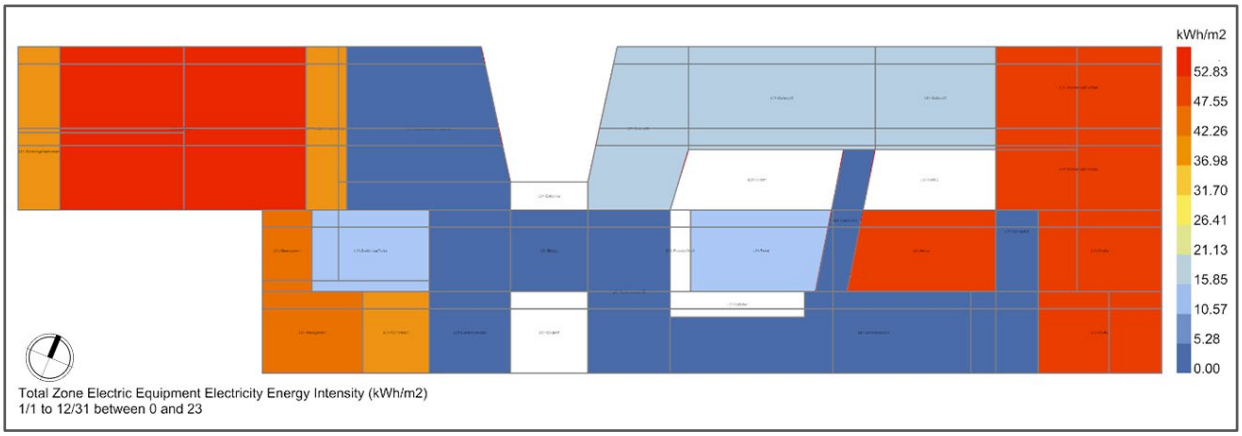

Figure 5-64 Total electric equipment energy intensity (kWh/m2), First Floor.

- Hot Water: Hot water heating energy intensity is primarily determined by functional programs rather than climatic exposure. While a limited number of zones exhibit concentrated high demand reaching approximately **500 kWh/m²**, the majority of spaces either show low or uniform values around **22 kWh/m²**.

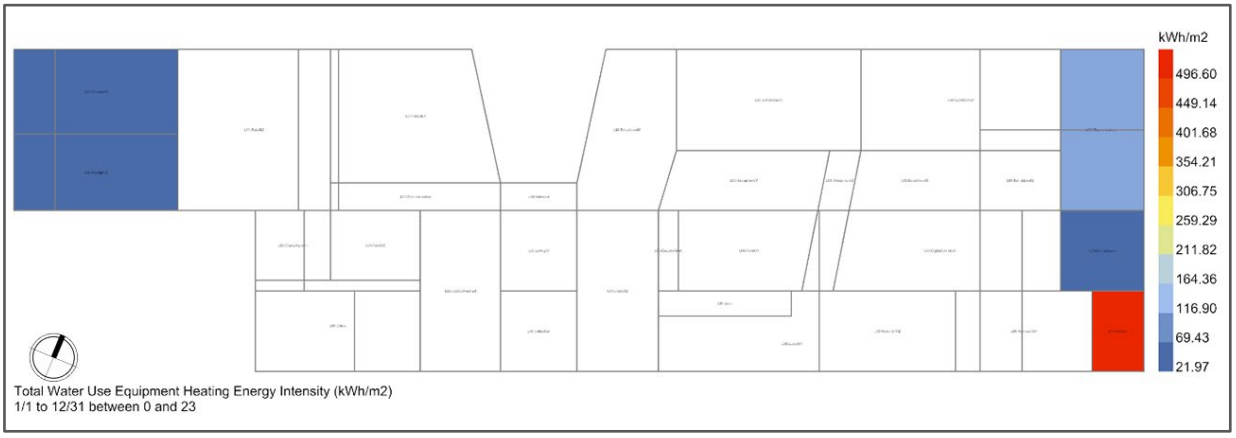

Figure 5-65 Total water uses equipment heating energy intensity (kWh/m2), Ground Floor.

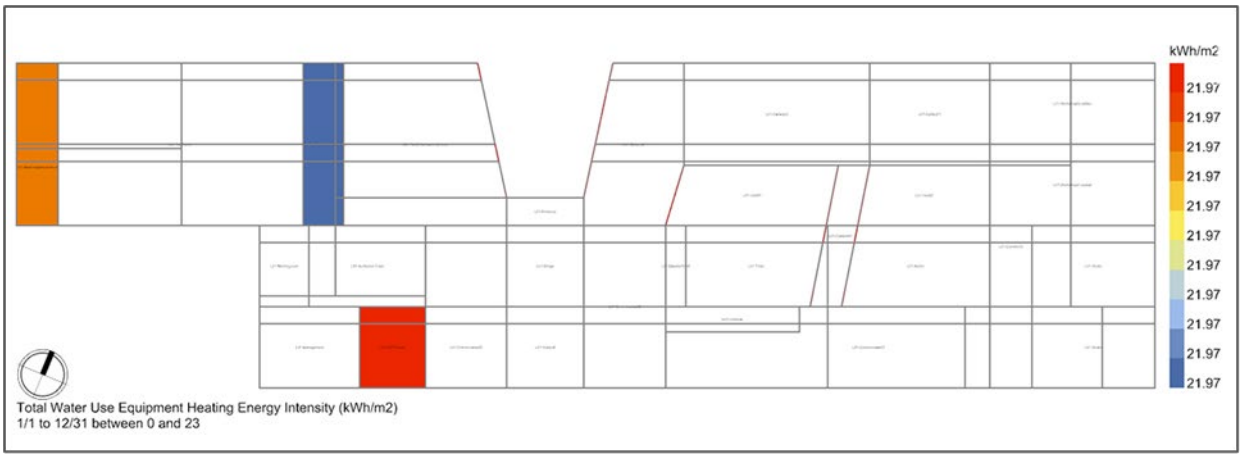

Figure 5-66 Total water uses equipment heating energy intensity (kWh/m2), First Floor.

- Solar Gain: Annual transmitted solar radiation through glazing reaches up to **190 kWh/m²** in exposed façade zones, confirming significant unmitigated solar penetration in the baseline configuration. The spatial concentration of solar gains aligns closely with high cooling demand areas, reinforcing glazing exposure as the primary driver of summer thermal imbalance. Core zones remain comparatively unaffected, highlighting the façade's dominant influence on solar-driven energy behavior.

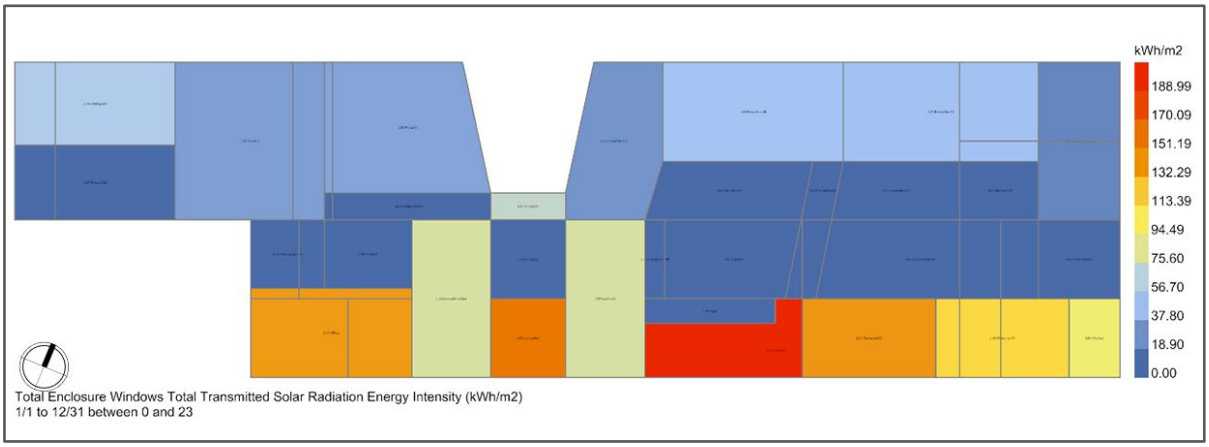

Figure 5-67 Total enclosure windows total transmitted solar radiation energy intensity (kWh/m2), Ground Floor.

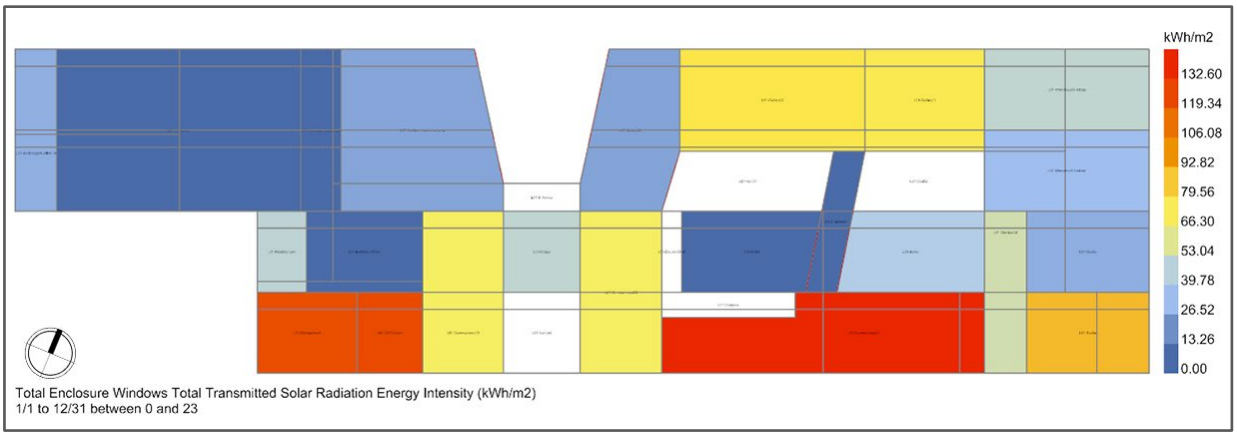

Figure 5-68 Total enclosure windows total transmitted solar radiation energy intensity (kWh/m2), First Floor.

5.3.4 Daylight Analysis

Daylight analysis in this chapter focuses on the interpretation of simulated daylight performance outcomes using established quantitative metrics and evaluation thresholds. The results are derived from previously executed daylight simulations and are assessed to determine daylight availability, spatial distribution, visual comfort, and compliance with recognized performance criteria, including LEED v4/v4.1.

The analysis examines key daylight indicators such as:

- Indoor Illuminance Distribution
- Daylight Factor
- Daylight Autonomy (DA)
- Spatial Daylight Autonomy (sDA)
- Useful Daylight Illuminance (UDI)
- Annual Sunlight Exposure (ASE)
- Spatial Glare Autonomy (sGA)

These results are aggregated and evaluated against accepted benchmarks to identify well-daylit areas, potential underlit zones, and regions susceptible to excessive daylight or glare.

A) Indoor Illuminance Distribution

For September, the analysis indicates that approximately 79.7**%** of the evaluated area falls within the acceptable illuminance range. This result suggests that, under late-summer equinox conditions, the building provides adequate daylight for a substantial portion of occupied spaces, while limiting excessive illuminance that could lead to visual discomfort or glare.

September at 9:00 AM

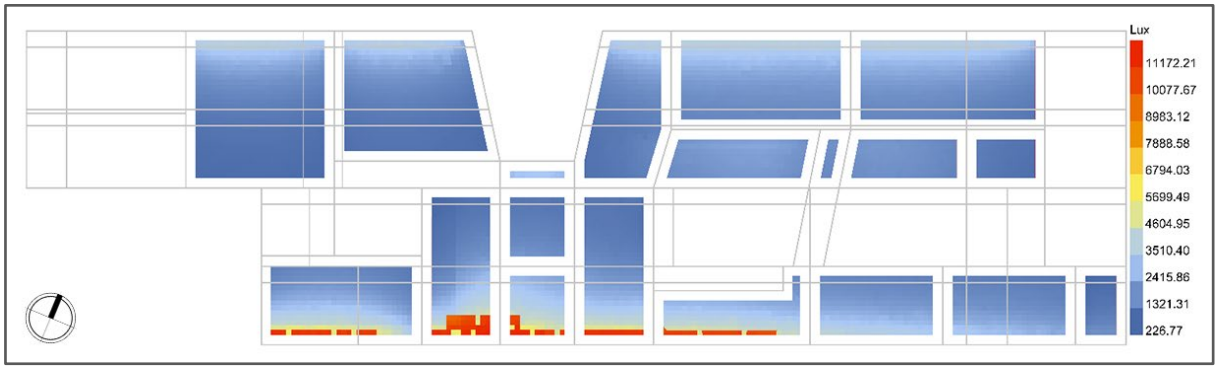

Figure 5-69 Point-In-Time Illuminance (Ground Floor, September 9 A.M).

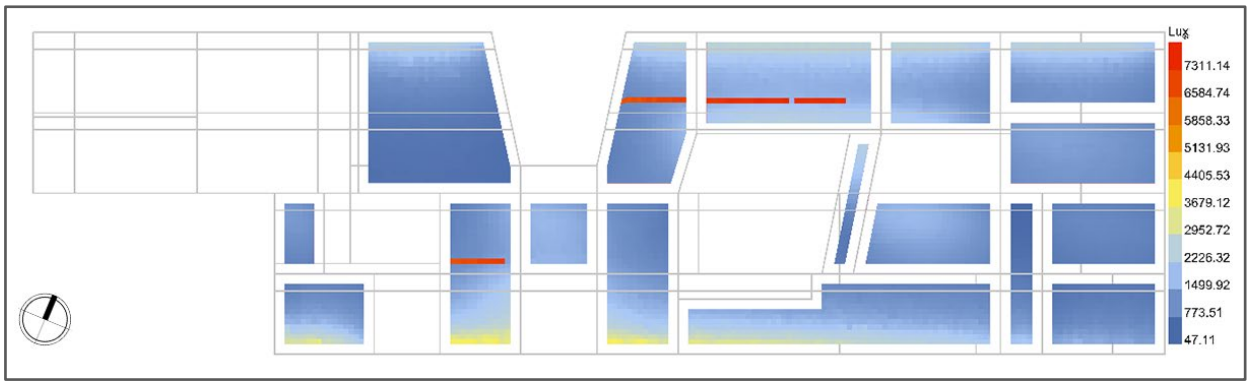

Figure 5-70 Point-In-Time Illuminance (Fisrt Floor, September 9 A.M).

September at 15:00

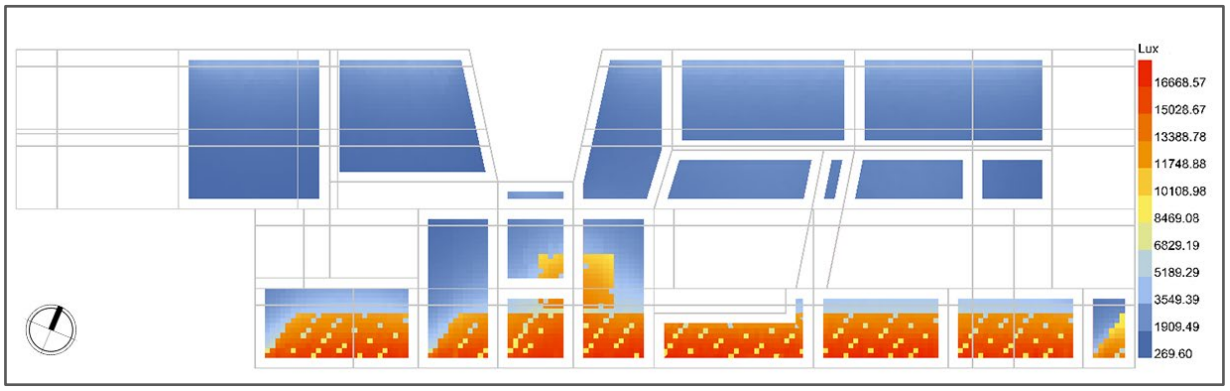

Figure 5-71 Point-In-Time Illumminance (Ground Floor, September 3 P.M).

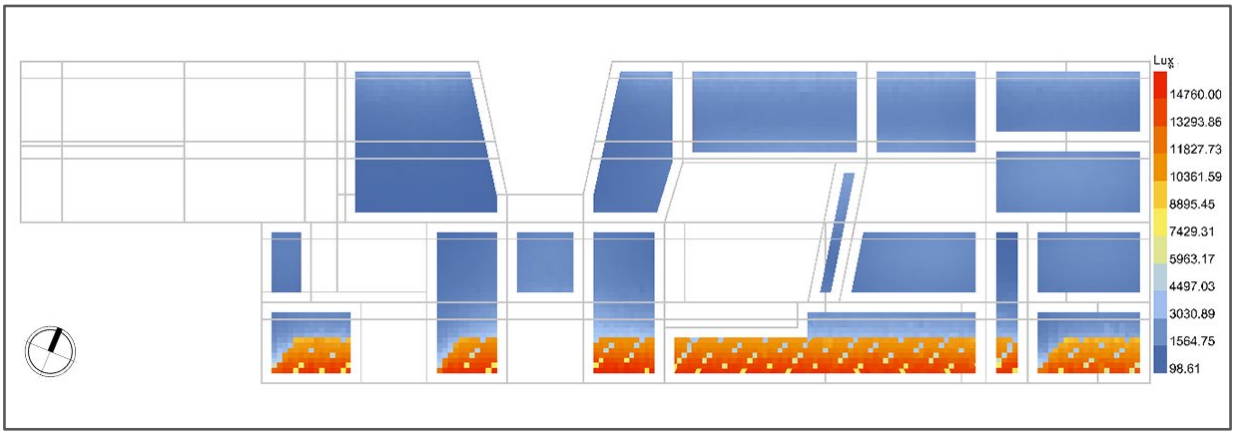

Figure 5-72 Point-In-Time Illumminance (First Floor, September 3 P.M).

In March, the percentage of compliant areas increases to approximately 83.22%, reflecting more favorable daylight distribution under spring equinox conditions. The higher compliance in March can be attributed to lower solar altitudes and reduced risk of over-illumination, resulting in a more balanced daylight penetration across interior spaces.

March at 9:00 AM

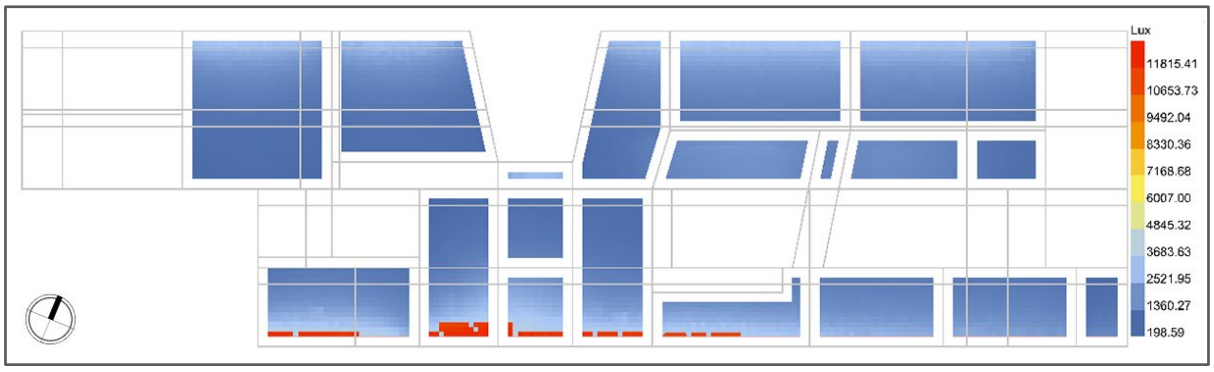

Figure 5-73 Point-In-Time Illuminance (Ground Floor, March 9 A.M).

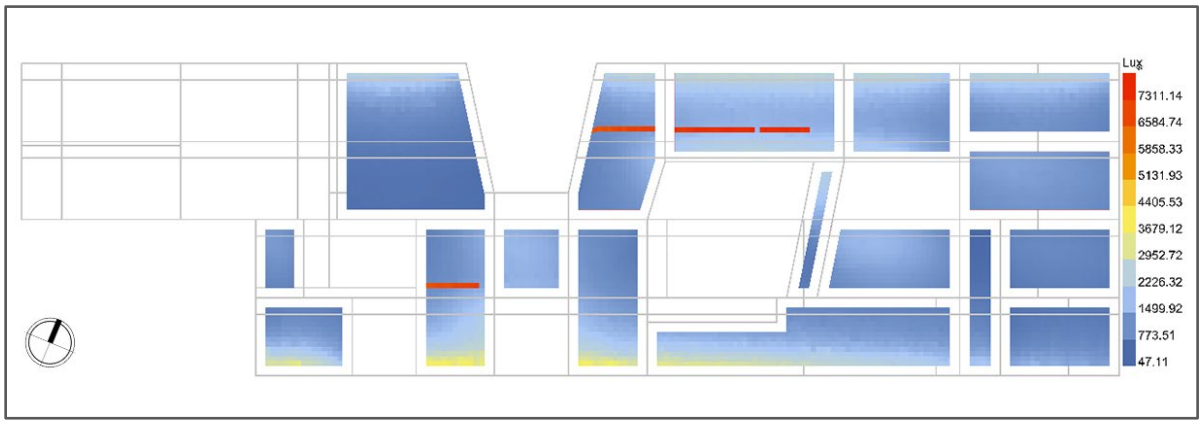

Figure 5-74 Point-In-Time Illuminance (First Floor, March 9 A.M).

March at 15:00

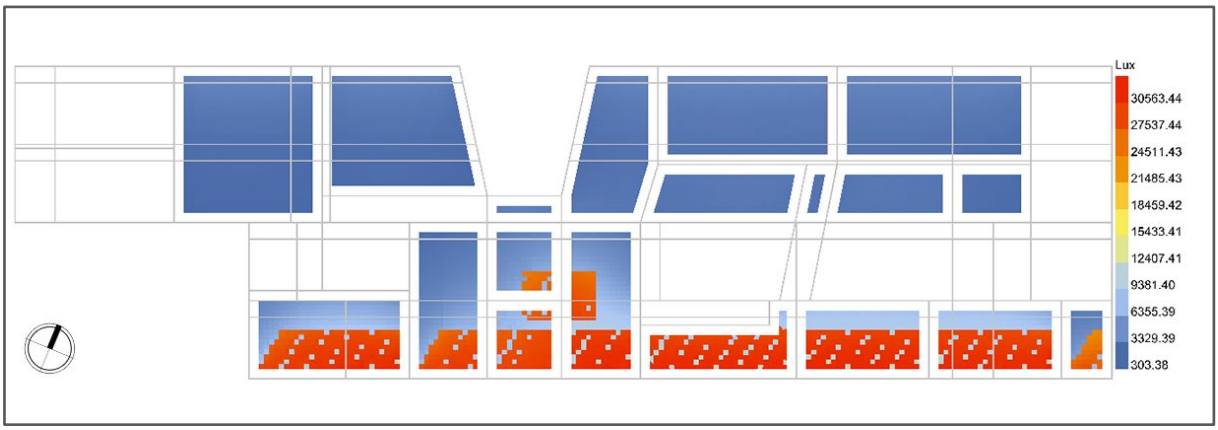

Figure 5-75 Point-In-Time Illuminance (Ground Floor, March 3 P.M).

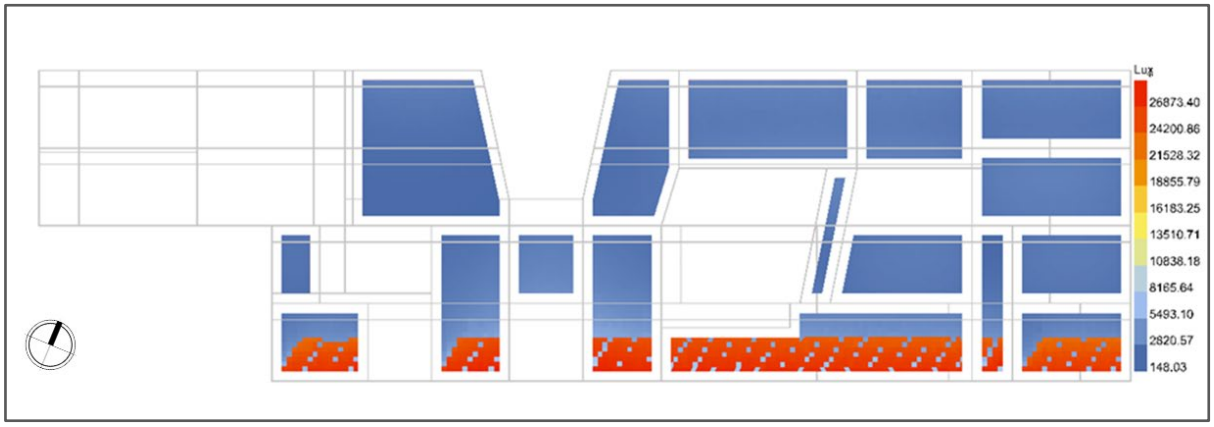

Figure 5-76 Point-In-Time Illuminance (First Floor, March 3 P.M).

Interpretation

Overall, the results demonstrate that the building achieves a high level of compliance with LEED daylight requirements for both evaluated periods. The slightly higher percentage in September suggests improved daylight penetration under late-summer solar angles, while the minor reduction in March may be attributed to differences in solar altitude and sky conditions. Overall, the values demonstrate that the design maintains adequate daylight availability throughout the year without excessive underlit or excessively illuminated areas, supporting visual comfort and reducing reliance on artificial lighting.

B) Daylight Factor

The analysis shows that 30.95% of the total analyzed area achieves a Daylight Factor between 2% and 5%, corresponding to adequately daylit conditions. The results indicate that nearly one-third of the space meets accepted daylight sufficiency criteria under overcast conditions.

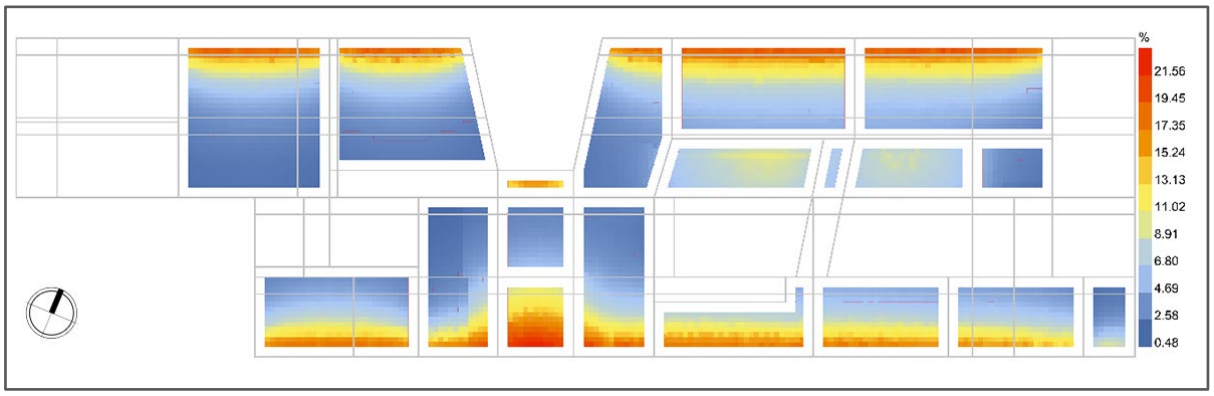

Figure 5-77 Daylight Factor between 2% and 5%, Ground floor.

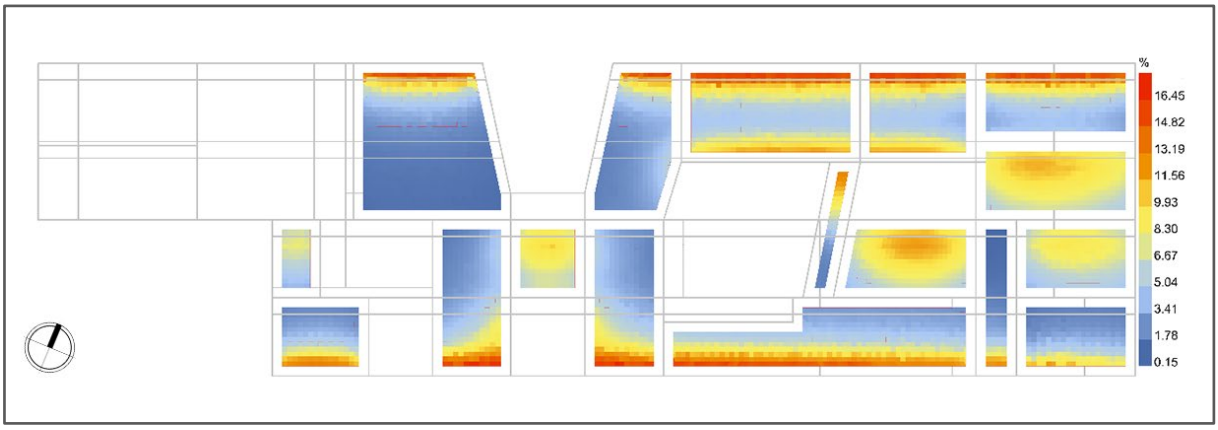

Figure 5-78 Daylight Factor between 2% and 5%, First floor.

Interpretation

Areas with DF values below 2% suggest a need for improved daylight access, while zones exceeding 5% may require glare mitigation strategies. Overall, the Daylight Factor provides a clear baseline assessment of daylight availability, which is complemented by climate-based metrics in subsequent analyses.

C) Spatial Daylight Autonomy (sDA)

The analysis yields an sDA300/50% value of 96.7%**,** indicating that nearly the entire occupied floor area receives sufficient daylight for more than half of the annual occupied hours. This result exceeds the LEED v4/v4.1 exemplary performance threshold (75%)**,** demonstrating excellent daylight availability across the analyzed spaces.

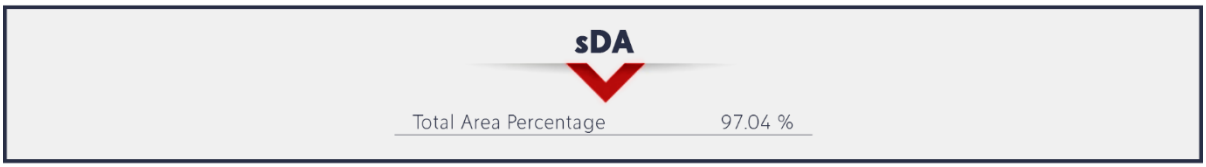

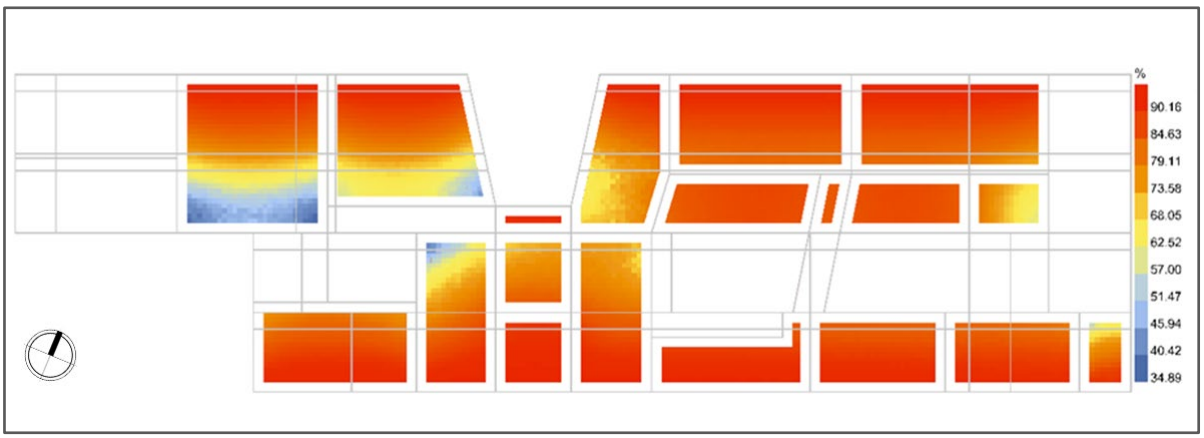

Figure 5-79 Daylight Autonomy (sDA300/50%): Percentage of regularly occupied floor area that achieves ≥300 lux for at least 50% of annual occupied hours. (Ground Floor)

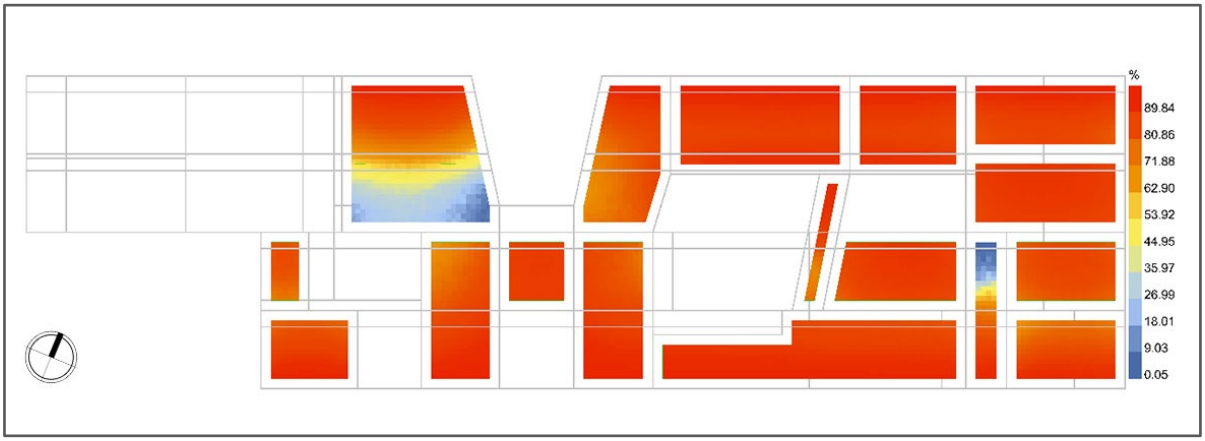

Figure 5-80 Daylight Autonomy (sDA300/50%), First Floor.

Interpretation

Higher sDA values indicate a larger proportion of floor area that is sufficiently daylit for most of the occupied year, reducing dependence on electric lighting and improving visual comfort. Values significantly above the LEED threshold reflect robust daylight availability but must be evaluated alongside glare metrics to avoid overexposure.

D)Useful Daylight Illuminance (UDI)

The annual simulation results indicate the following spatial performance; these values were computed as area-weighted percentages over the total sensor grid.

- **UDI Low (<100 lux)**: **0.12%** of the analyzed floor area→ Insufficient daylight; artificial lighting is usually required.

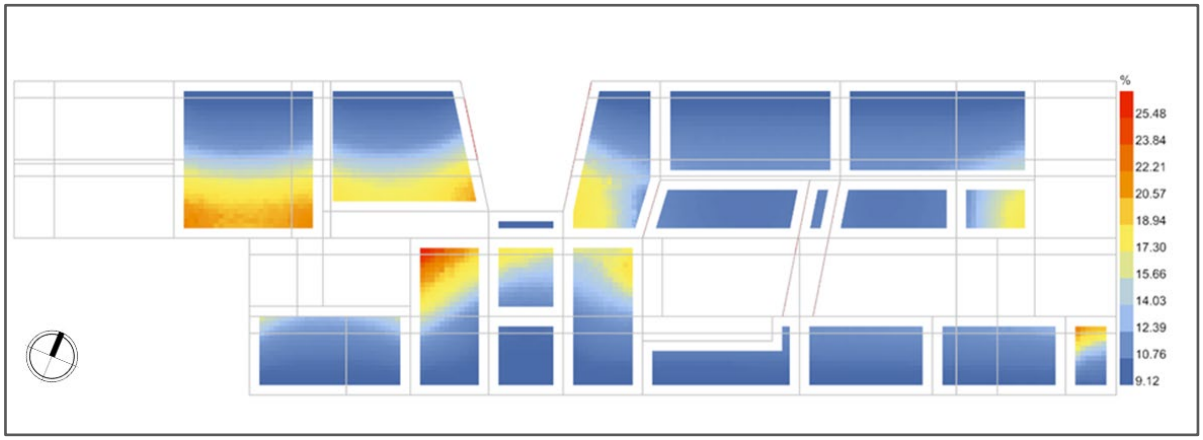

Figure 5-81 Percentage of DI-Low (< 300 lux), Ground Floor.

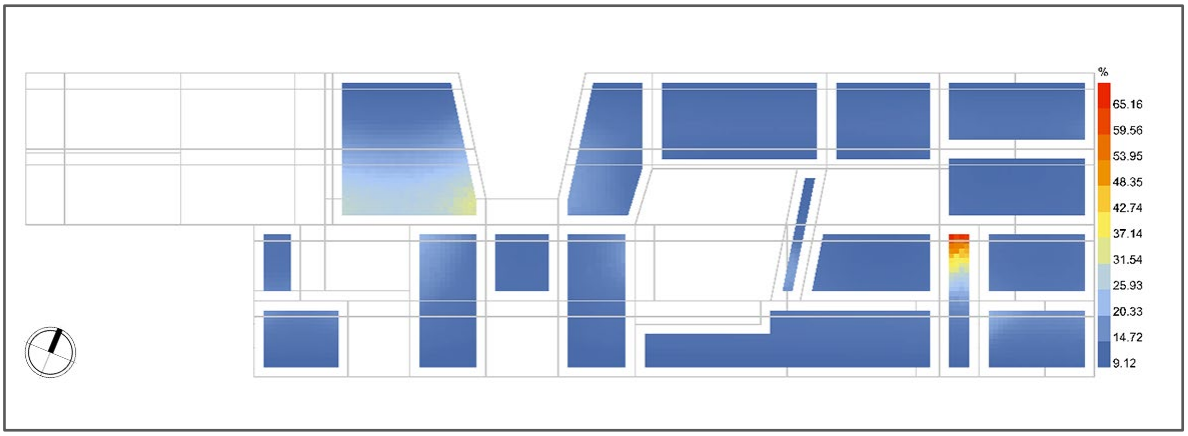

Figure 5-82 Percentage of DI-Low (< 300 lux), First Floor.

- **UDI (300–3000 lux)**: **82.74%** of the analyzed floor area→ Useful daylight; illuminance levels suitable for visual tasks without glare.

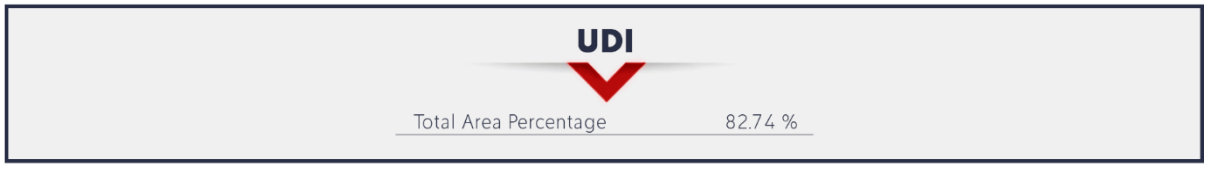

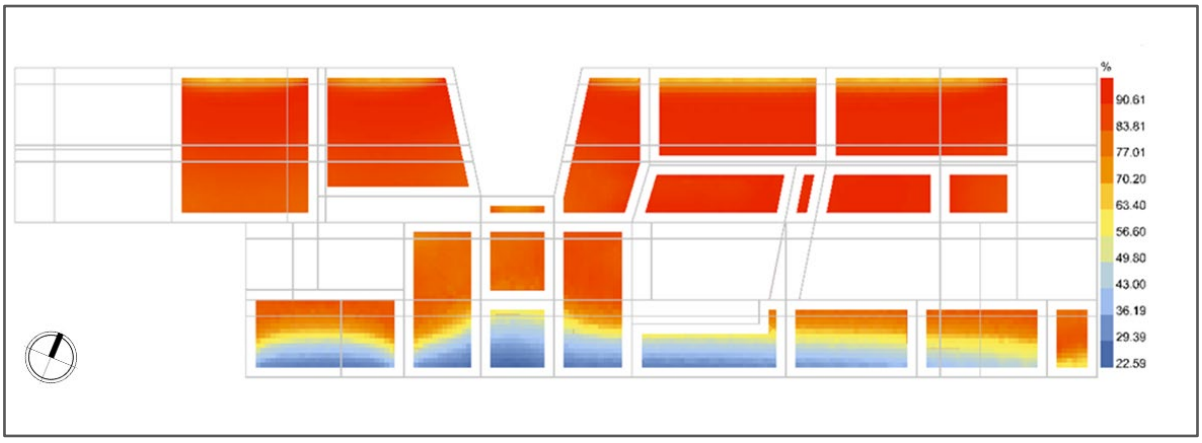

Figure 5-83 Percentage of UDI (300–3000 lux), Ground Floor.

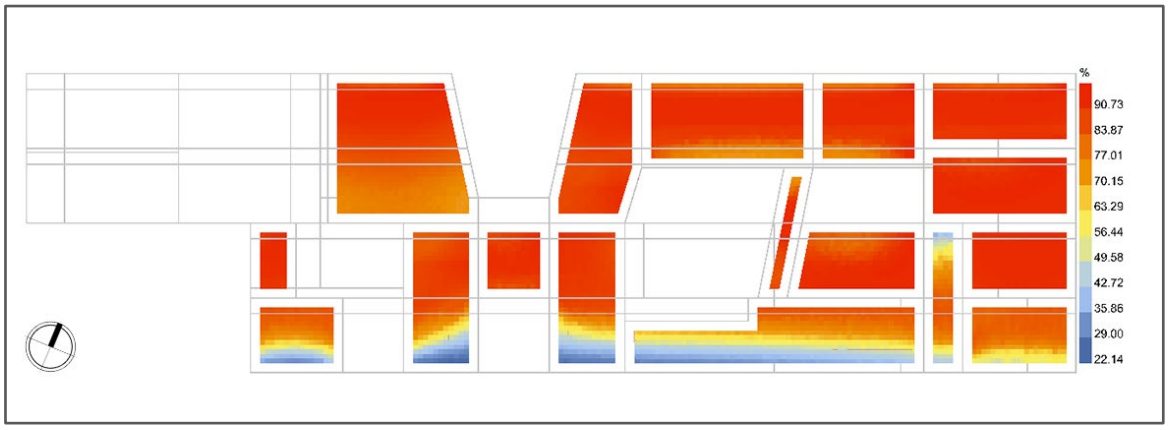

Figure 5-84 Percentage of UDI (300–3000 lux), First Floor.

- **UDI Up (>3000 lux)**: **46.47%** of the analyzed floor area→ Excessive daylight; potential risk of glare and visual discomfort.

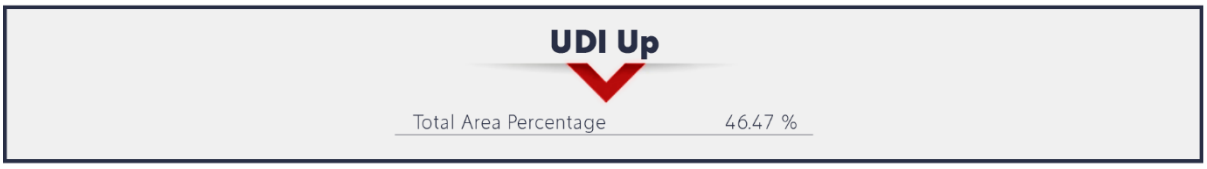

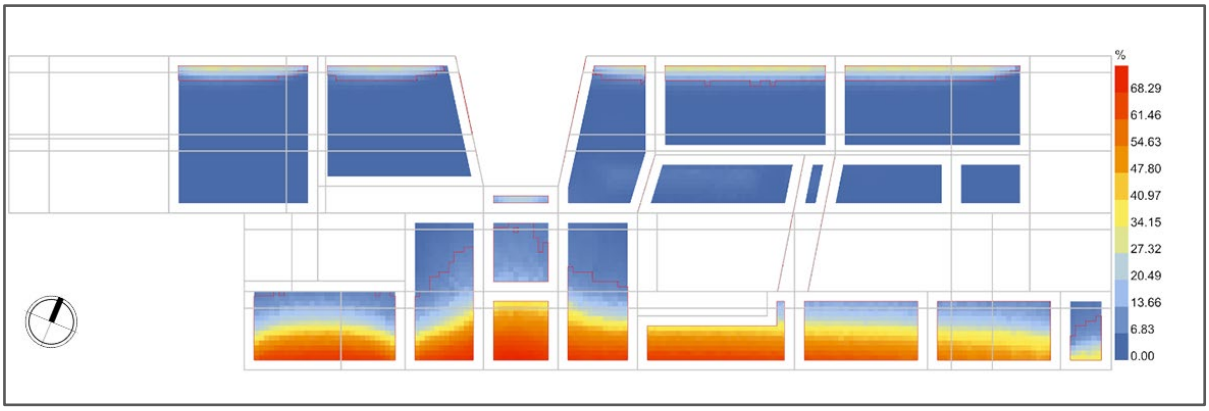

Figure 5-85 Percentage of UDI-up (> 3000 lux), Ground Floor.

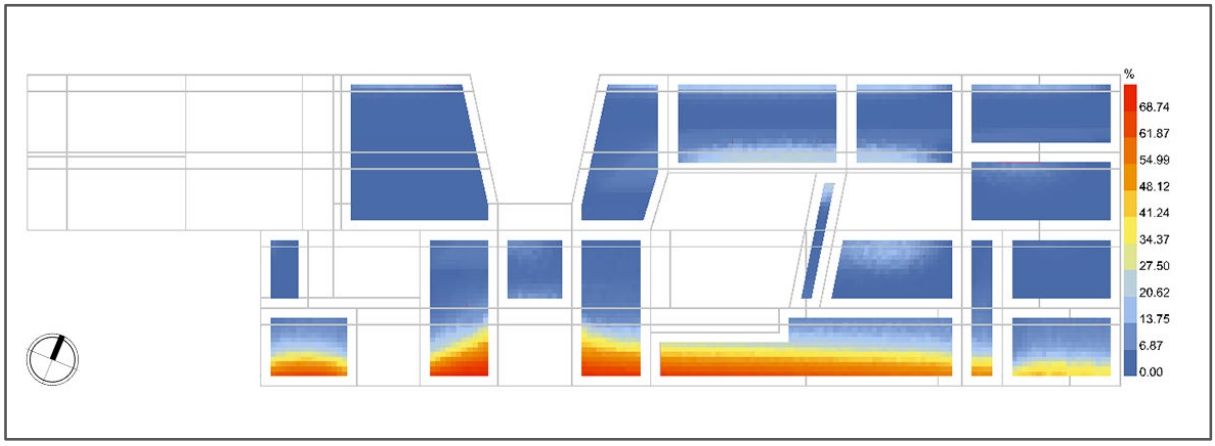

Figure 5-86 Percentage of UDI-up (> 3000 lux), First Floor.

Interpretation

The results show that daylight availability is generally effective, with most of the floor area receiving illuminance within the useful range (300–3000 lux), indicating good visual comfort and reduced reliance on artificial lighting. The negligible share of underlit areas confirms adequate daylight penetration. However, the relatively high proportion of excessively illuminated areas (>3000 lux) suggests a risk of glare and visual discomfort, highlighting the need for shading or daylight control strategies to moderate excessive solar exposure.

E) Annual Sunlight Exposure (ASE)

51.02% of the analyzed area is exposed to excessive direct sunlight (≥1000 lux for ≥250 h/year).

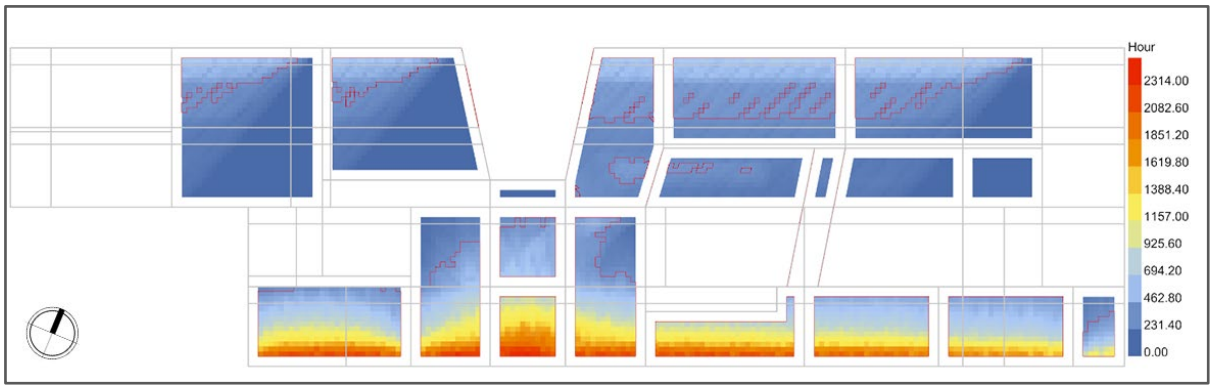

Figure 5-87 Spatial distribution of Annual Sunlight Exposure (ASE ≥ 250). Heatmap showing cumulative direct sunlight hours on the analysis grid, Ground Floor.

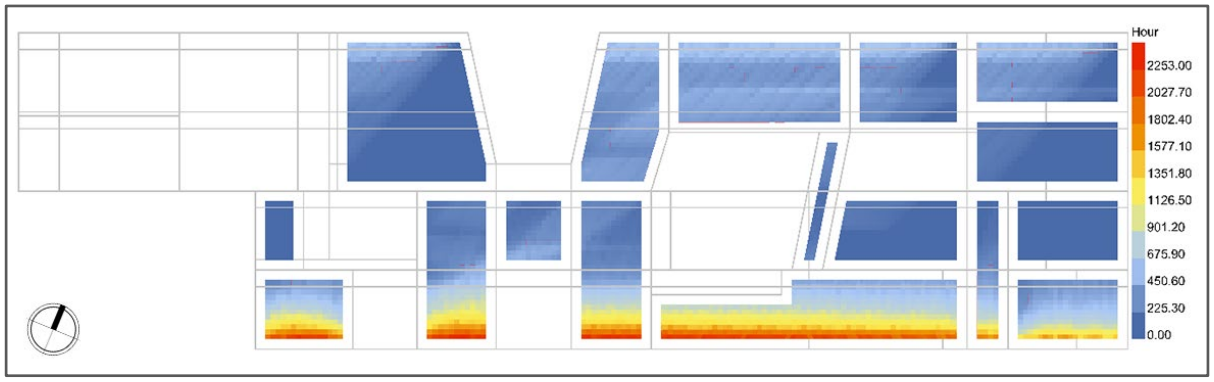

Figure 5-88 Spatial distribution of Annual Sunlight Exposure (ASE ≥ 250), First Floor.

Interpretation

The ASE value significantly exceeds the LEED maximum allowable threshold of 10%, indicating excessive direct sunlight penetration. This result highlights a high risk of glare and overheating, suggesting the need for design interventions such as external shading devices, glazing modification, or façade reconfiguration to comply with LEED daylight requirements.

F) Spatial Glare Autonomy (sGA)

Spatial glare autonomy as a percentage of the sensors for each analysis grid that does not exceed the glare threshold for a specified fraction of occupied hours.

sGA

Total Area Percentage	42.94 %

Distinct sGA

Zone 0	0%
Zone 1	0 %
Zone 2	21.05 %
Zone 3	0 %
Zone 4	0 %
Zone 5	17.01 %
Zone 6	3.24 %
Zone 7	0.38 %

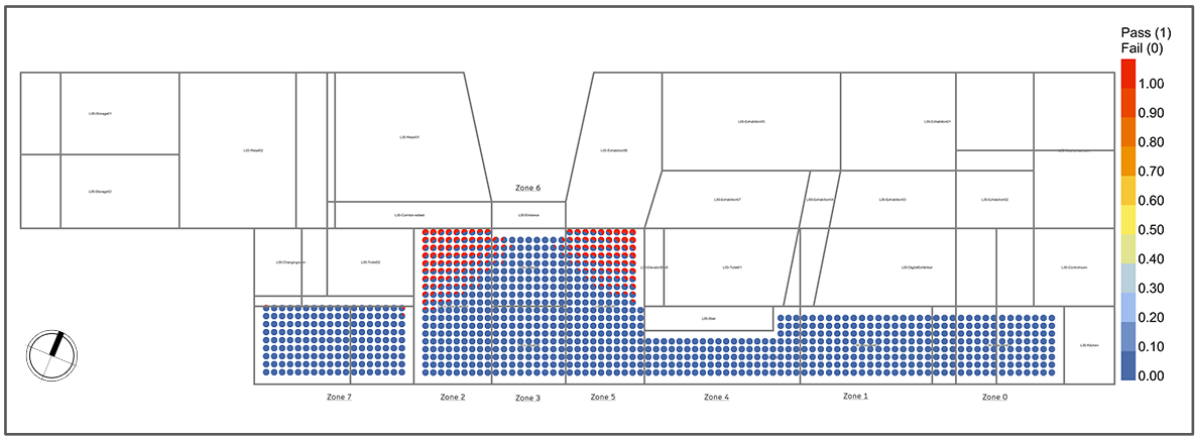

Figure 5-89 Spatial Glare Autonomy (sGA) pass/fail distribution across the analysis grids, showing the percentage of sensor points that remain below the glare threshold for the specified fraction of occupied hours (red = pass, blue = fail), Ground Floor.

Distinct sGA

Zone 0	94.71%
Zone 1	80.86 %
Zone 2	36.41 %
Zone 3	60.62 %
Zone 4	54.55 %
Zone 5	42.18 %
Zone 6	100 %
Zone 7	75.65 %
Zone 8	99.91%
Zone 9	85.26 %

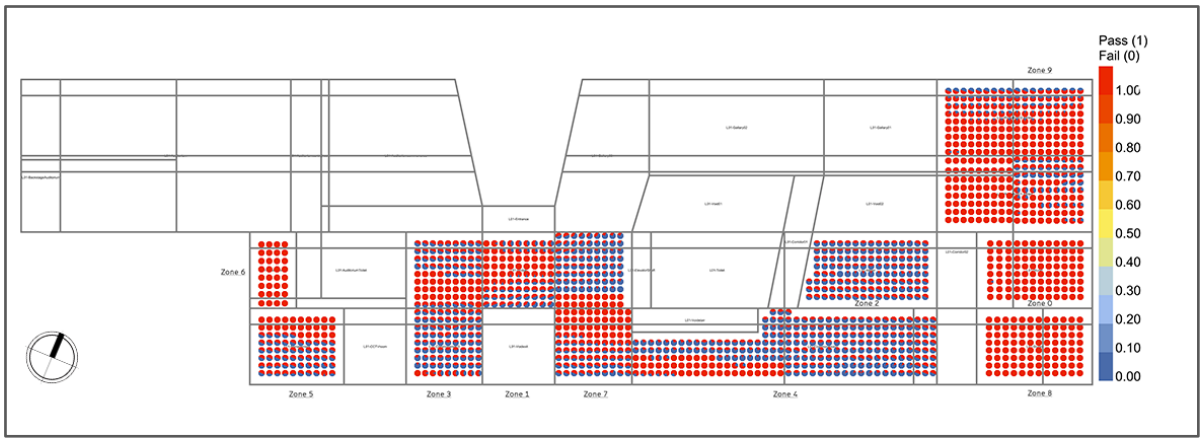

Figure 5-90 Spatial Glare Autonomy (sGA), First floor.

5.4 Optimization results on the representative spaces

Due to the computationally intensive nature of evolutionary optimization and the limited analytical value of performing full energy, daylight, and glare simulations for every iteration across the entire building, the scope of the optimization was strategically constrained. Instead of optimizing the full building model, the optimization process was conducted on two representative spaces with different functional programs, allowing for a substantial reduction in computational cost while preserving analytical relevance.

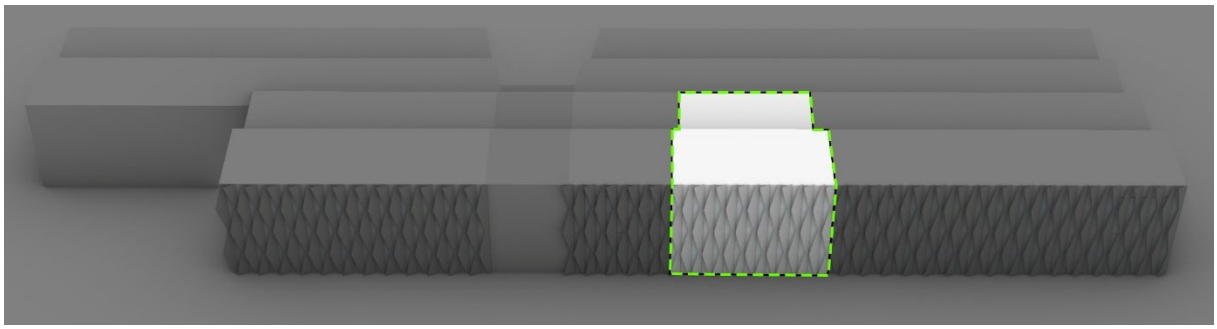

Figure 5-91 representative space for a faster optimization

Since external shading systems primarily affect south-facing spaces, two zones located on the southern façade were selected on two vertically adjacent floors. This configuration allows the optimization to capture both façade-related and vertical performance variations associated with shading design. The selected spaces include a Ground Floor space with a Medium Office (closed office) program and a First-Floor space with a college – Art Classroom program. These programs represent distinct occupancy patterns, daylight requirements, and glare sensitivity.

Following the optimization process, selected solutions extracted from the design space are subsequently applied to the entire building model, where comprehensive analysis is performed at the building scale. This two-stage approach combines the efficiency of localized optimization with the robustness of whole-building performance evaluation.

Since Wallacei operates exclusively within a minimization framework, both sDA and sGA objectives were inverted prior to optimization (1/sDA and 1/sGA, respectively). Consequently, lower fitness values in the mean trendline correspond to higher actual performance, representing increased spatial daylight autonomy and a greater proportion of glare-free conditions across the analyzed grid. Accordingly, downward trends observed in the fitness graphs should be interpreted as improvements in daylight availability and glare control rather than performance degradation.

Initial settings:

The initial values for the generation count and generation size were determined cautiously by reviewing comparable case studies in the literature and examining the ranges commonly adopted in similar optimization problems. However, given that optimization problems rarely share identical environmental, geometric, and performance conditions, these initial values were treated only as informed estimates rather than fixed standards.

More importantly, the final selection of the generation count and population size was guided by continuous monitoring of the mean fitness value trendline and the standard deviation (SD) trendline during the optimization process. By observing the convergence behaviour, stabilization of mean fitness values, and reduction of population diversity, decisions were made regarding an appropriate number of generations and population size that ensured sufficient convergence without unnecessary computational cost.

Generation count	*Number of generations in the simulation*	50
Generation size	*Number of individuals per generation*	30
Total population size		1500
Size of search space		34000
Crossover probability	*Percentage of solutions that reproduce in each generation*	0.9
Mutation probability	*The percentage of mutation 1/ (number of variables)*	1/n
Crossover distribution index	*Probability of similarity of the offspring to the parents*	20
Mutation distribution index	*Probability of similarity of the offspring to the parents*	20
Random seed	*Random seed in the simulation*	1

Table 5-1 Initial setting of optimization

Standard deviation:

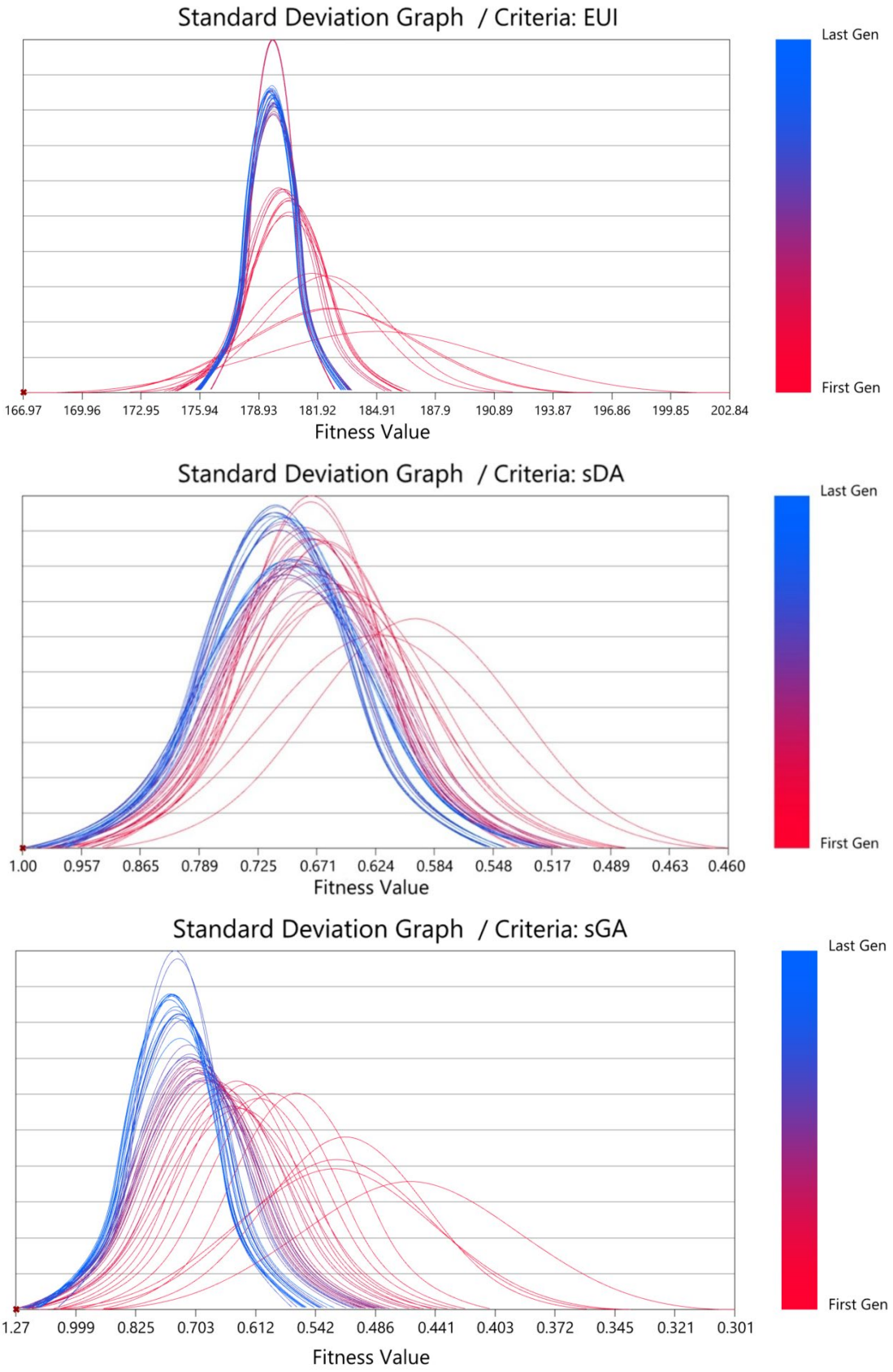

Figure 5-92 SD graph for EUI,sDA and sGA criteria

EUI: The Standard Deviation graph for the EUI fitness objective demonstrates a clear evolutionary transition from exploration to convergence across 50 generations. In the early generations (red curves), the SD distribution was wide and flat, indicating a high level of diversity within the population. This spread reflects the exploratory behavior of the NSGA-II algorithm, where a broad range of EUI values is investigated.

As optimization progresses toward the final generations (blue curves), the SD distributions become progressively narrower and more peaked, revealing a reduction in population diversity and increased convergence. This narrowing indicates that solutions are clustering more tightly around the mean, suggesting that the algorithm is refining and exploiting fitter regions of the solution space.

In addition, the leftward shift of both lower and upper bounds of the SD distributions is clearly observable. Since EUI is a minimization objective, this shift confirms a systematic improvement in mean fitness values, with later generations achieving lower EUI values compared to earlier ones. The simultaneous decrease in variability and improvement in mean performance indicates that the optimization process reaches a stable and well-converged state in the final generations, without evidence of erratic behavior or loss of optimization direction.

Overall, the SD graph confirms that the NSGA-II optimization effectively balances diversity preservation in early generations with convergence toward optimal EUI solutions in later generations.

sDA: For the sDA objective, the Standard Deviation graph shows a gradual reduction in dispersion from early (red) to later generations (blue), indicating a controlled convergence of solutions. The later generations exhibit a more compact distribution, suggesting that the population stabilizes around a narrower range of fitness values.

At the same time, the distribution shifts towards the left side of the fitness axis, corresponding to higher sDA performance, where values closer to 1.00 indicate a larger portion of the analyzed floor area meeting the sDA target. This behavior confirms that the optimization process successfully guides the population toward solutions with improved spatial daylight availability while maintaining convergence in the final generations.

Overall, the SD behavior for sDA reflects a stable optimization process, with sufficient early exploration followed by convergence toward higher-performing daylight solutions.

sGA: The SD graph for sGA shows a clear reduction in dispersion from early to late generations, indicating convergence of the population. The progressive shift of the distribution toward the left side of the fitness axis, where values closer to 1.00 represent glare-free conditions across a larger portion of the analysed grid, confirms continuous improvement in glare performance. The narrowing of the final generations suggests that the optimisation stabilises around high-performing, low-glare solutions.

Mean Value Trendline:

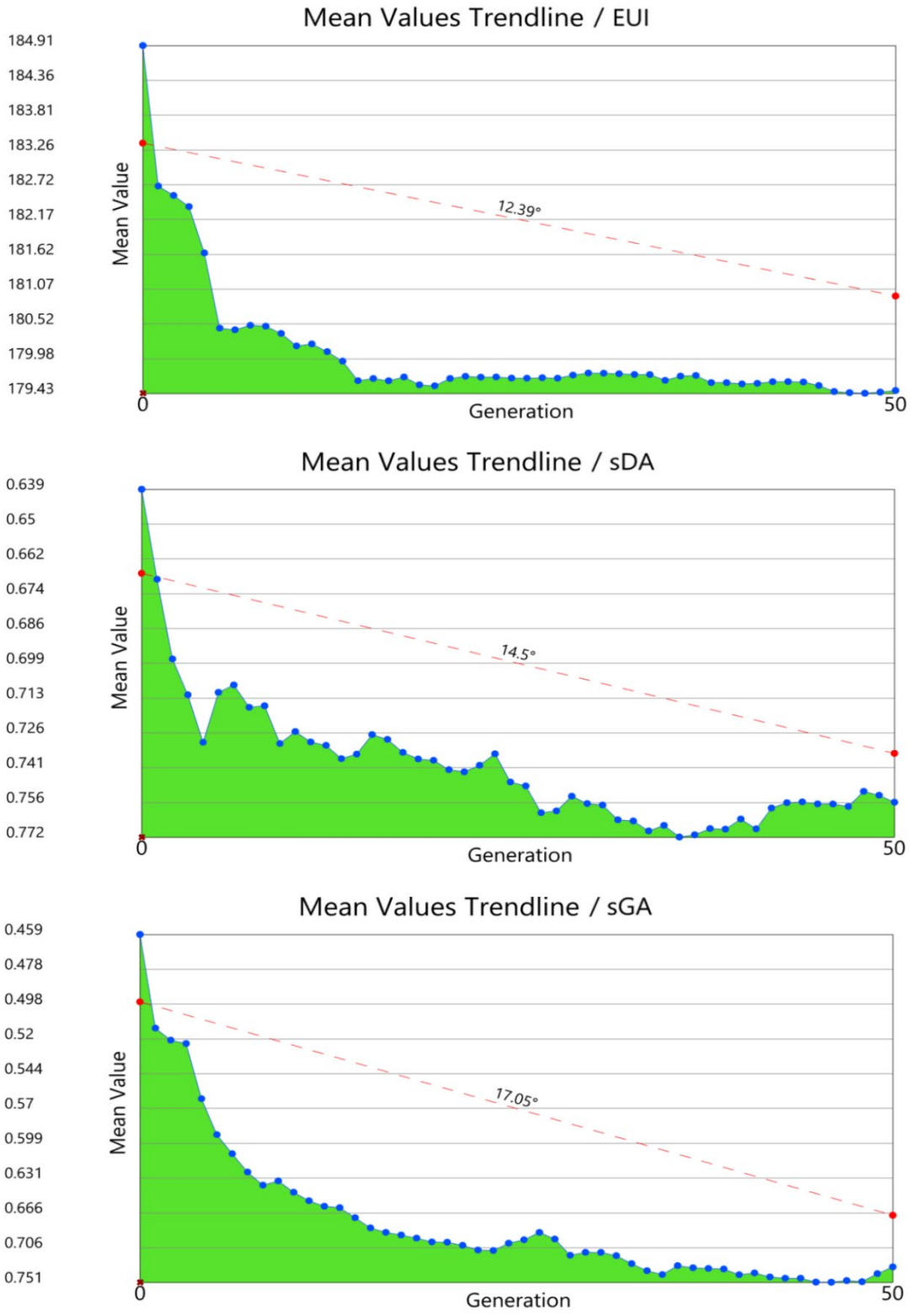

Figure 5-93 Mean value trendline chart for all criteria

EUI: The mean value trendline for EUI shows a clear downward trend across the 50 generations, indicating continuous improvement in the population's average performance. A sharp reduction in mean EUI is observed during the early generations, reflecting rapid optimisation, followed by a more gradual decrease and eventual stabilization in later generations.

The relatively flat behavior of the trendline toward the final generations suggests that the optimisation reaches a steady and stable state, with only minor fluctuations around the final mean value. Since EUI is a minimization objective, this consistent reduction in the mean confirms the effectiveness of the optimisation process in guiding the population toward lower energy use intensity values.

Since the last quarter of generations shows a flat mean fitness trend accompanied by stable standard deviation values (convergence plateau), the optimisation can be considered sufficiently converged, and further generations do not contribute to meaningful performance improvement.

SDA: The mean fitness trendline for sDA shows a clear downward trend, indicating progressive improvement under the pre-minimization formulation. After rapid improvement in the early generations, the trendline flattens toward the end, suggesting convergence and diminishing gains. This behavior confirms that optimization stabilizes solutions with higher spatial daylight autonomy.

sGA: The mean fitness trendline for sGA shows a consistent downward trend, indicating progressive improvement in glare performance under the pre-minimization formulation. After rapid improvement in the early generations, the trend stabilizes toward the end, confirming convergence toward solutions with a higher proportion of glare-free conditions.

Standard Deviation Trendline:

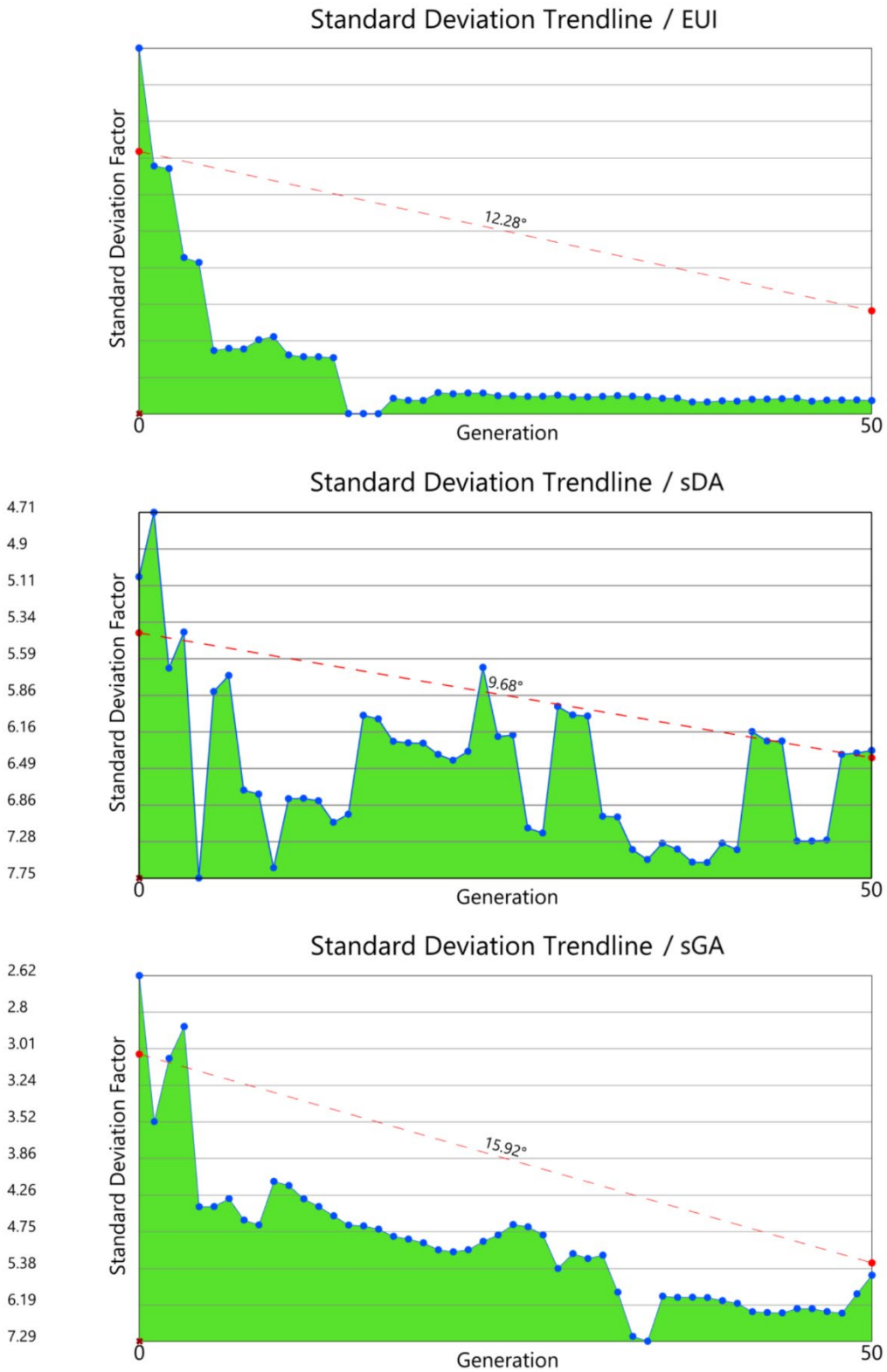

Figure 5-94 SD trendline chart for all criteria

For EUI, the SD decreases rapidly during the early generations and remains low and stable in the later stages, demonstrating strong convergence toward similar low-energy solutions. The sustained low variability in the final generations suggests that the population has reached a well-defined and stable solution space.

For sDA, the SD trendline shows higher variability and intermittent fluctuations throughout the optimization, reflecting the greater sensitivity of daylight availability to geometric changes. Despite this variability, the overall downward trend indicates progressive convergence, with diversity preserved longer before stabilizing in the final generations.

For sGA, the SD trendline exhibits a steady decrease with moderate fluctuations, indicating a controlled reduction in glare-related variability. The later generations show a narrower distribution, confirming convergence toward solutions that consistently improve glare performance across the analyzed grid.

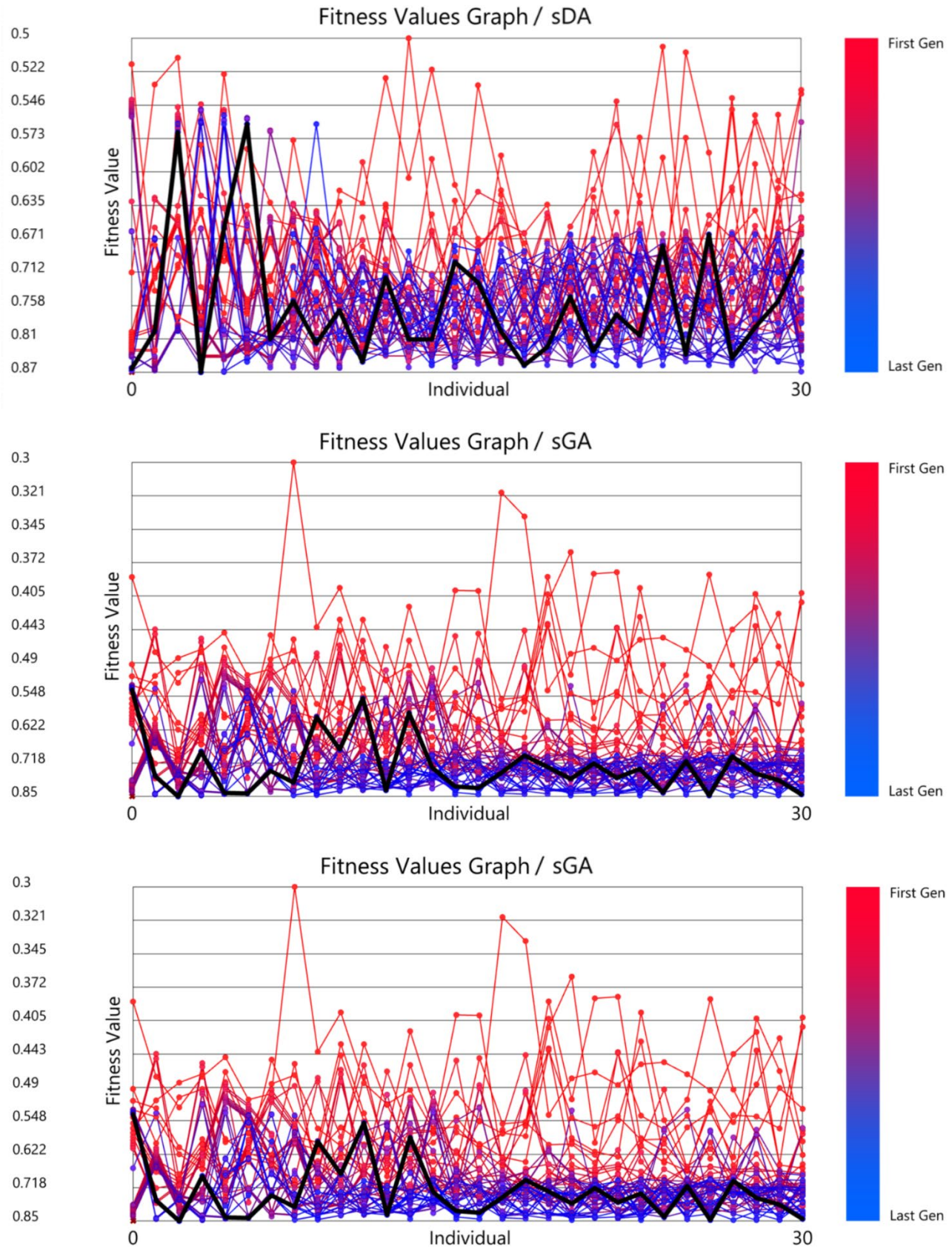

Figure 5-95 Fitness value graph for all criteria

The Fitness Values graphs illustrate a clear evolution in solution quality and population consistency across generations for all three objectives. For EUI, early generations (red polylines) exhibit wide dispersion and frequent extreme fitness values, indicating unstable and poorly performing solutions. As generations progress toward the final iterations (blue polylines), fitness values become more tightly clustered at lower ranges, demonstrating improved energy performance and reduced variability across individuals. In the case of sDA, the early generations show pronounced fluctuations between individuals, reflecting sensitivity of daylight performance to geometric variation, while later generations converge toward consistently lower fitness values under the pre-minimization formulation, indicating improved spatial daylight autonomy across the population. For sGA, a similar pattern is observed: early generations display scattered fitness values with occasional outliers, whereas later generations show a compact distribution with reduced spread, confirming convergence toward glare-robust solutions. The highlighted black polyline representing the selected final generation lies consistently within the densest cluster of low-fitness solutions for all objectives, confirming that the chosen population represents a stable, well-performing generation with balanced energy, daylight, and glare performance.

The Parallel Coordinate Plot reveals the multi-objective relationships and trade-offs among EUI, sDA, and sGA across the population. Each polyline represents a single solution evaluated simultaneously against all three fitness objectives, allowing emergent optimization behavior to be identified beyond individual objective trends.

For EUI, a wide spread of values is observed in the early generations, indicating significant variability in energy performance across the population. As the solutions evolve, a denser clustering of polylines emerges toward the lower end of the EUI axis, confirming convergence toward energy-efficient configurations. This clustering suggests that improved EUI is consistently achievable without extreme degradation in the other objectives.

The sDA axis exhibits a pronounced concentration of high-performing solutions, particularly among later generations, indicating that a large portion of the population converges toward higher spatial daylight autonomy. The slope patterns between EUI and sDA demonstrate that solutions with lower EUI frequently correspond to higher

sDA values, suggesting a synergistic relationship between energy efficiency and daylight availability rather than a direct conflict.

For sGA, the distribution shows moderate dispersion, reflecting the sensitivity of glare performance to geometric and material variations. Nevertheless, later-generation solutions increasingly align toward higher sGA performance, indicating that glare mitigation improves concurrently with EUI and sDA optimization. The absence of strong crossing patterns between sDA and sGA axes suggests that improvements in daylight autonomy do not systematically lead to increased glare disturbance within the optimized solution space.

Overall, the PCP demonstrates that the optimization process successfully identifies a coherent set of high-performing solutions that balance energy efficiency, daylight availability, and glare control. The concentration of later-generation solutions within favorable regions across all axes confirms the effectiveness of the multi-objective optimization strategy and supports the robustness of the selected final population.

Parallel Coordinate Plot:

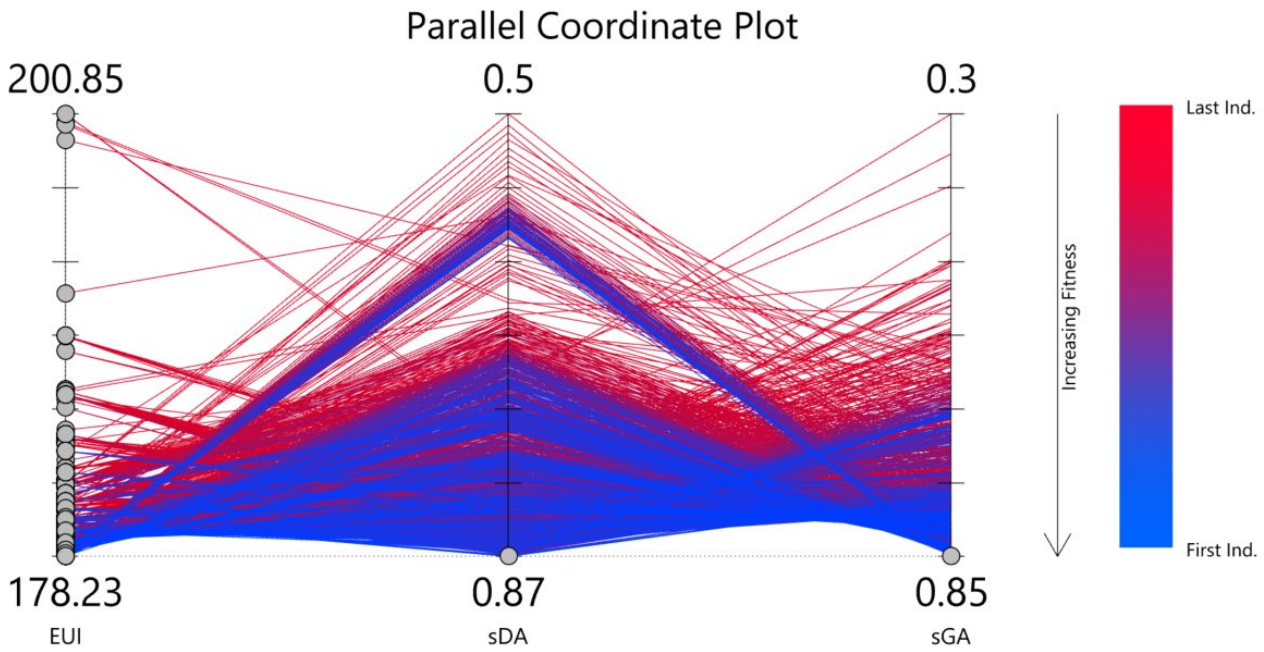

Figure 5-96 Parallel coordinate plot for all fitness objectives

The Parallel Coordinate Plot highlights the multi-objective behavior of the population across EUI, sDA, and sGA. Solutions with lower EUI values increasingly cluster in later generations, indicating convergence toward energy-efficient configurations. At the same time, higher sDA values are predominantly associated with these low-EUI solutions, suggesting a generally compatible relationship between energy efficiency and daylight availability within the optimized solution space.

In contrast, sGA exhibits a wider dispersion, particularly among higher-sDA solutions, indicating a partial trade-off between daylight availability and glare control. While several high-performing solutions achieve both acceptable sDA and sGA values, the PCP reveals that increases in daylight autonomy do not uniformly translate into improved glare performance.

Objective space:

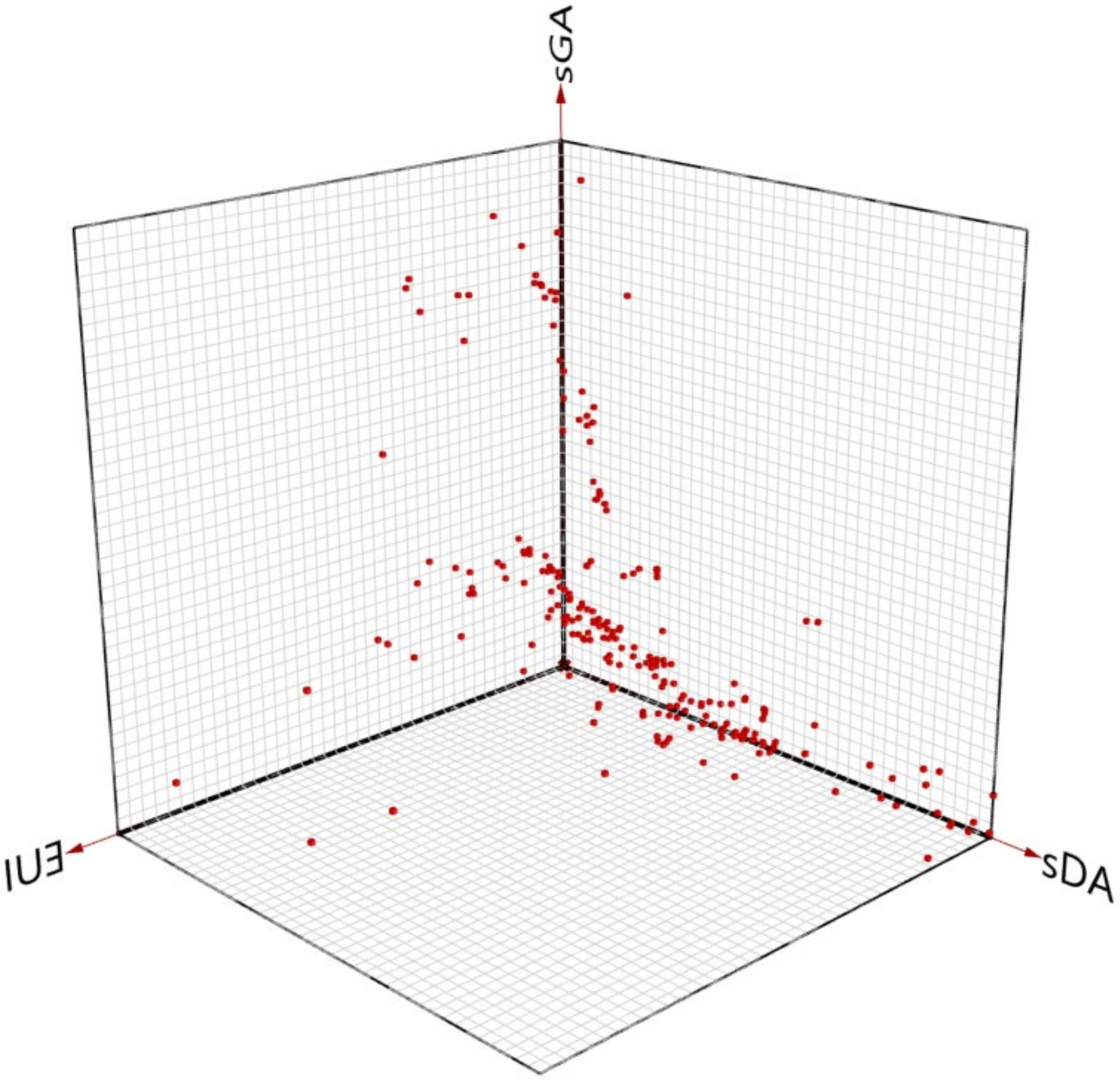

Figure 5-97 Objective space visualization for all fitness criteria

5.5 Optioneering (Solution selection)

A) By relative difference between fitness ranks:

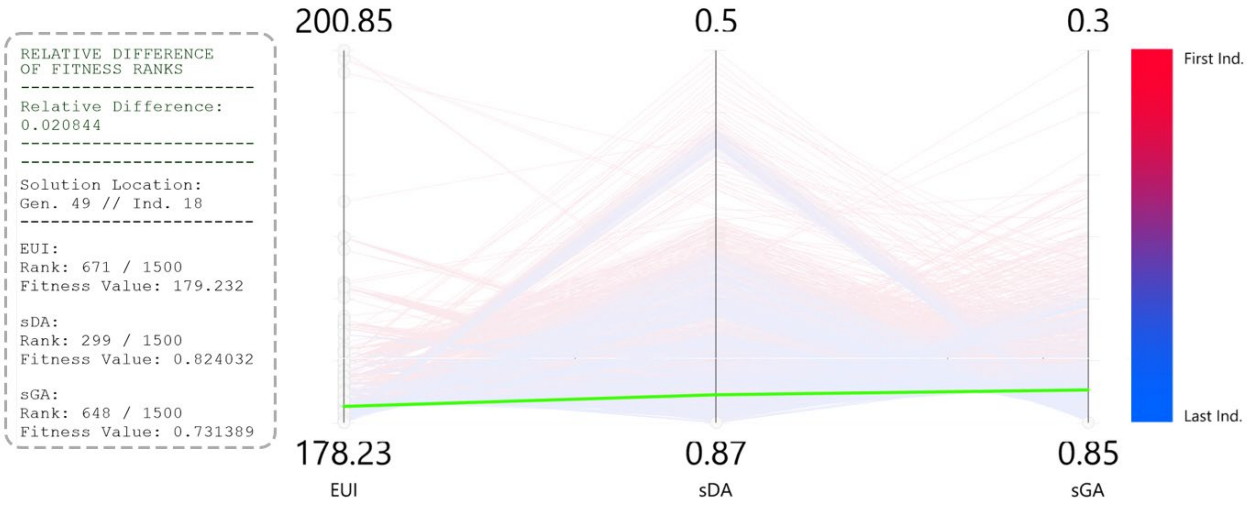

Figure 5-98 PCP analysis 1

Analysis method: relative difference between fitness ranks=0 ,

referring to the highlighted green polyline, identifying an equally balanced performance across all objectives, indicating no dominance bias toward any single objective.

B) By average fitness rank

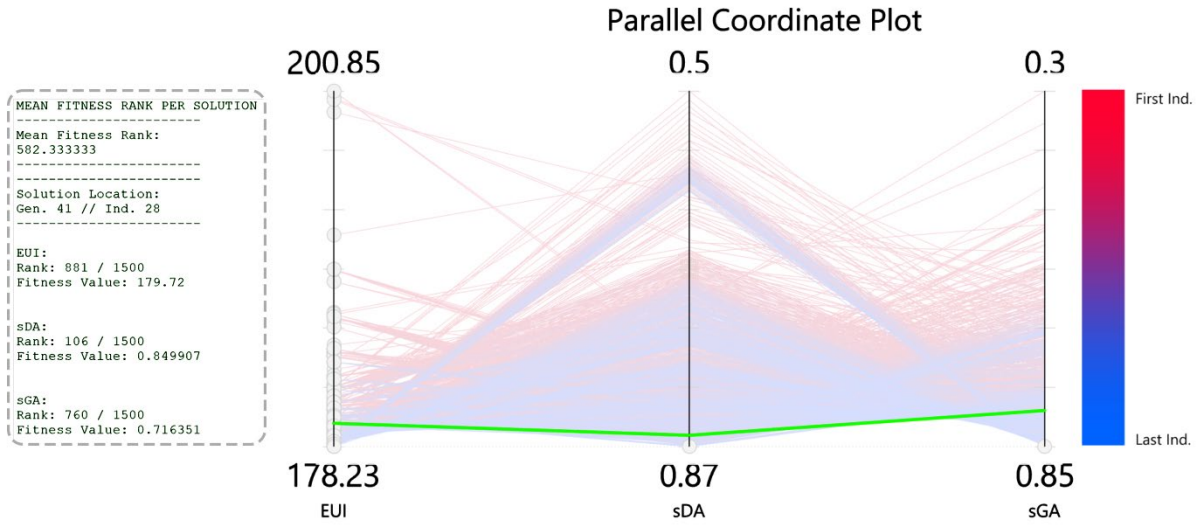

Figure 5-99 PCP analysis 2

C)Analysis method:

average fitness rank = 0,

referring to the highlighted green polyline, representing the best-performing compromise across EUI, sDA, and sGA

D)Best fitness rank in each objective:

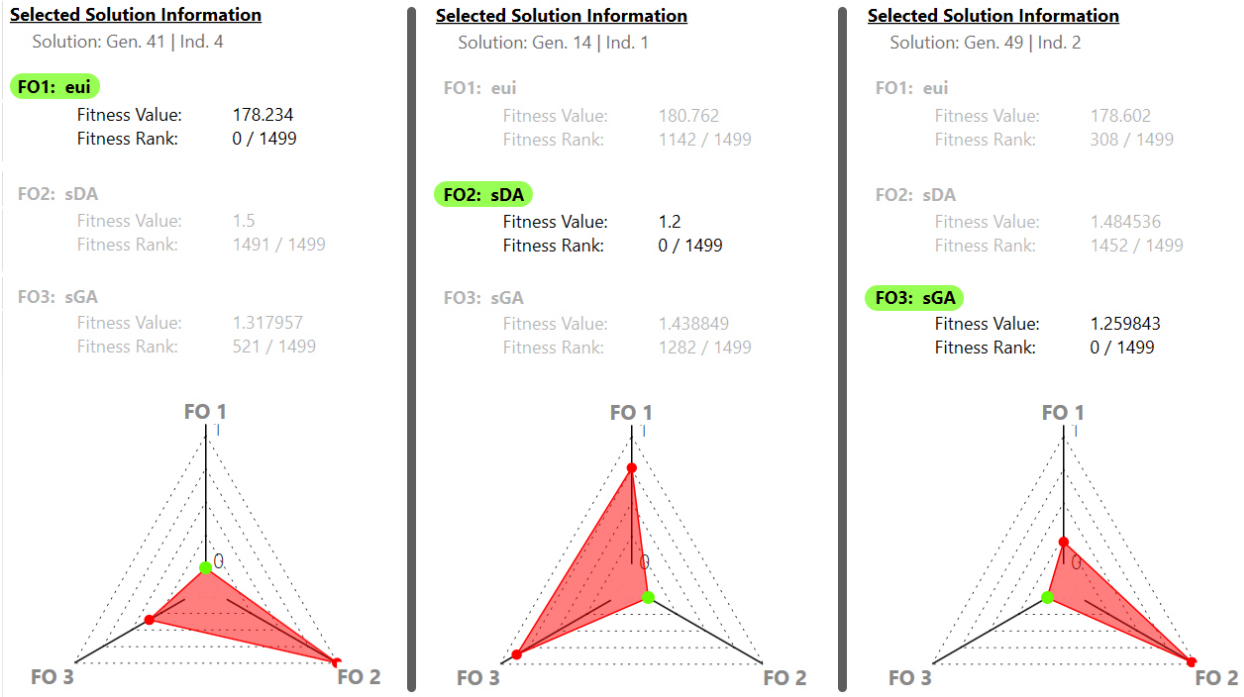

Figure 5-100 Diamond chart for each objective

E) Pareto Front clustering by k-means:

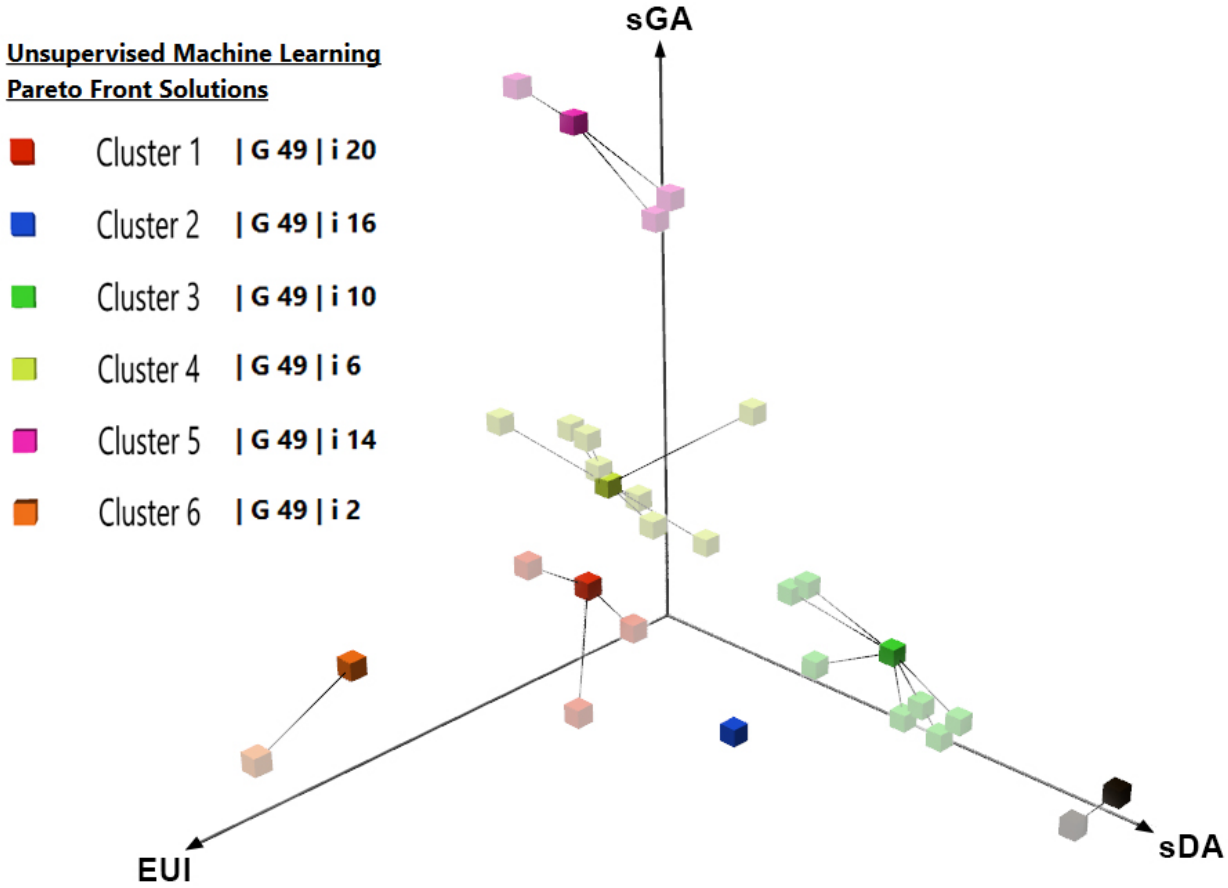

Figure 5-101 K-means clustering

Since a large portion of the solutions in the final generations converged onto the Pareto front, the resulting solution space became highly dense, with many solutions exhibiting very similar performance across the objectives. To reduce this redundancy and facilitate a more structured interpretation of the design space, a Pareto-front clustering approach based on k-means was employed.

By applying k-means clustering to the non-dominated solutions, the Pareto front was partitioned into groups of solutions with similar performance profiles. This process enabled the identification of representative clusters rather than treating each solution individually, thereby reducing visual and analytical congestion. The clustering strategy also supports a more systematic selection of candidate solutions by highlighting distinct performance regions within the Pareto front instead of relying on densely packed local optima.

Exported Phenotypes based on selected solutions:

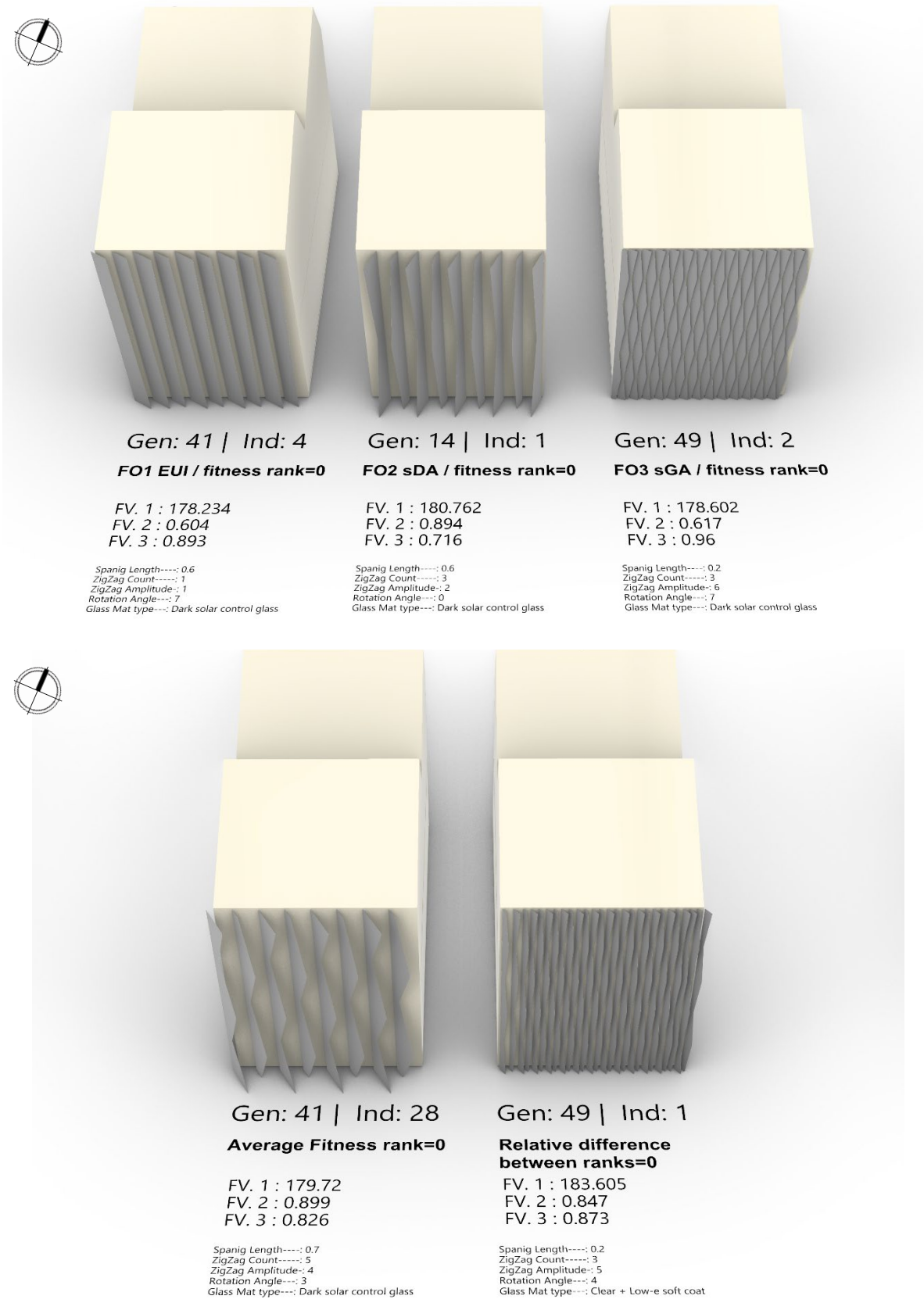

Figure 5-102 Exported phenotypes

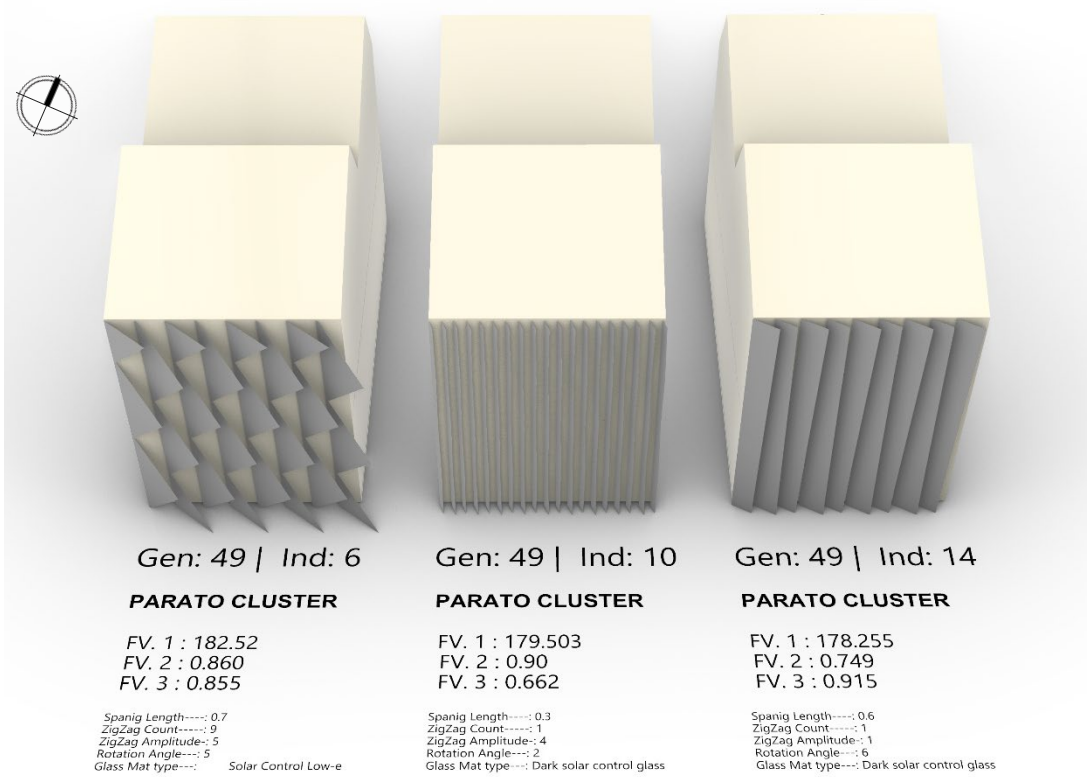

Figure 5-103 Exported phenotypes

5.6 Analysis for the whole building based on selected solutions:

Solution	Gen:41| Ind:4	Gen:14| Ind:1	Gen:49| Ind:2	Gen:41| Ind:28	Gen:49| Ind:1	Gen:49| Ind:6	Gen:49| Ind:10	Gen:49| Ind:14	Gen:49| Ind:16	Gen:49| Ind:20
Heating (kWh/m^2)	65.2	63.026	65.153	63.443	61.239	62.238	63.24	64.778	63.441	63.403
Cooling (kWh/m^2)	40.102	41.949	40.184	41.233	46.254	44.376	41.422	40.339	42.381	41.279
Interior lighting (kWh/m^2)	30.287	30.287	30.287	30.287	30.287	30.287	30.278	30.287	30.287	30.287
Electric equipment (kWh/m^2)	33.594	33.594	33.594	33.594	33.594	33.594	33.597	33.597	33.594	33.594
Water system (kWh/m^2)	7.566	7.566	7.566	7.566	7.566	7.566	7.566	7.566	7.566	7.566
EUI (kWh/m^2)	176.74	176.42	176.78	176.12	178.94	178.06	176.11	176.564	177.26	176.12
Average illuminance (September)(Lux)	88.155	84.324	86.952	87.213	88.058	87.557	86.7	89.865	87.962	86.091
Average illuminance (march) (Lux)	93.553	83.697	90.927	86.045	87.616	87.410	85.07	90.638	87.119	87.928
Daylight factor (%)	51.13	53.7	50.5	53.3	52.4	50.4	53.8	50	50.7	53
sDA (%) >75	94.158	96.531	91.892	94.616	95.925	93.746	96.488	94.885	96.067	94.639
UDI (%) ≥ 70٪	99.295	88.408	99.048	94.118	92.475	96.579	89.565	96.612	92.333	94.347
ASE (%) <10	11.75	16.73	11.82	14.94	14.25	13.82	15.70	12.47	14.18	15.07
sGA (%) >60	72.966	63.789	72.536	65.843	67.685	53.610	65.054	71.292	79.499	77.887

Table 5-2 Comparison of alternatives for the whole building

All the alternatives are analyzed on the complete building model and then compared in Table 5-2.

Analysis example for Gen.49 Ind.14 on the whole building.

Thermal Load Balance

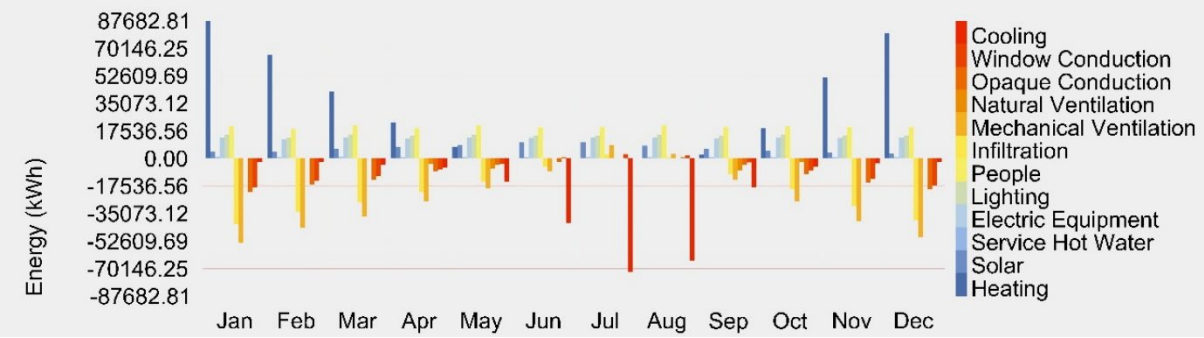

Figure 5-104 Monthly thermal load balance illustrates the relative contributions of heat gains and losses by source across the year.

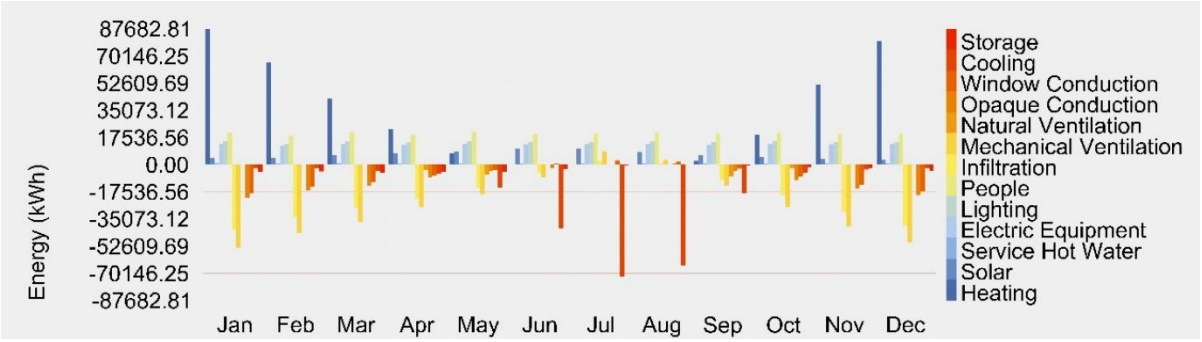

Figure 5-105 Monthly thermal load balance including balance_stor, illustrating the effect of thermal mass on heat storage and release alongside major heat gains and losses.

Percentage of People Dissatisfied (PPD).

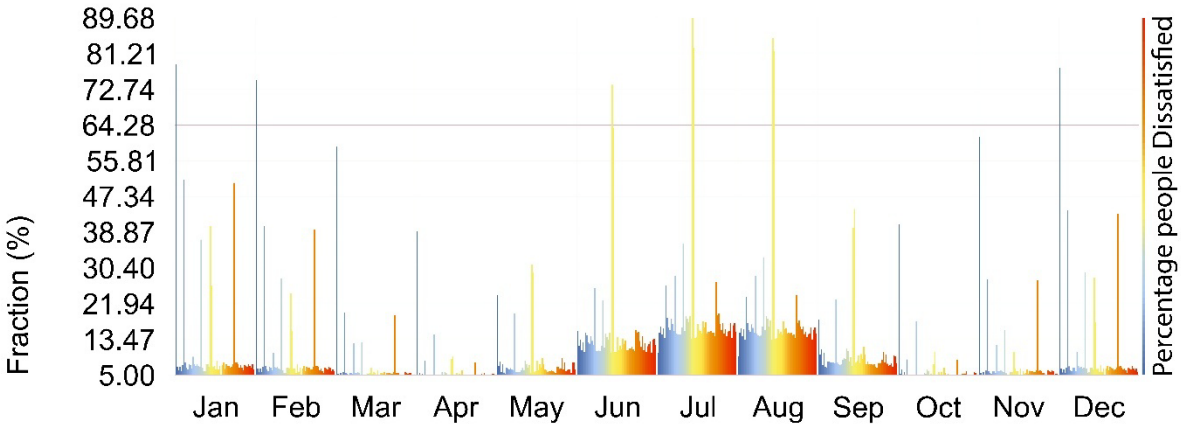

Figure 5-106 Monthly distribution of thermal comfort conditions based on PMV analysis, showing the fraction of occupied hours within comfort and discomfort ranges across the year.

Annual Surface Heat Gain and Loss Distribution Across Building Envelope

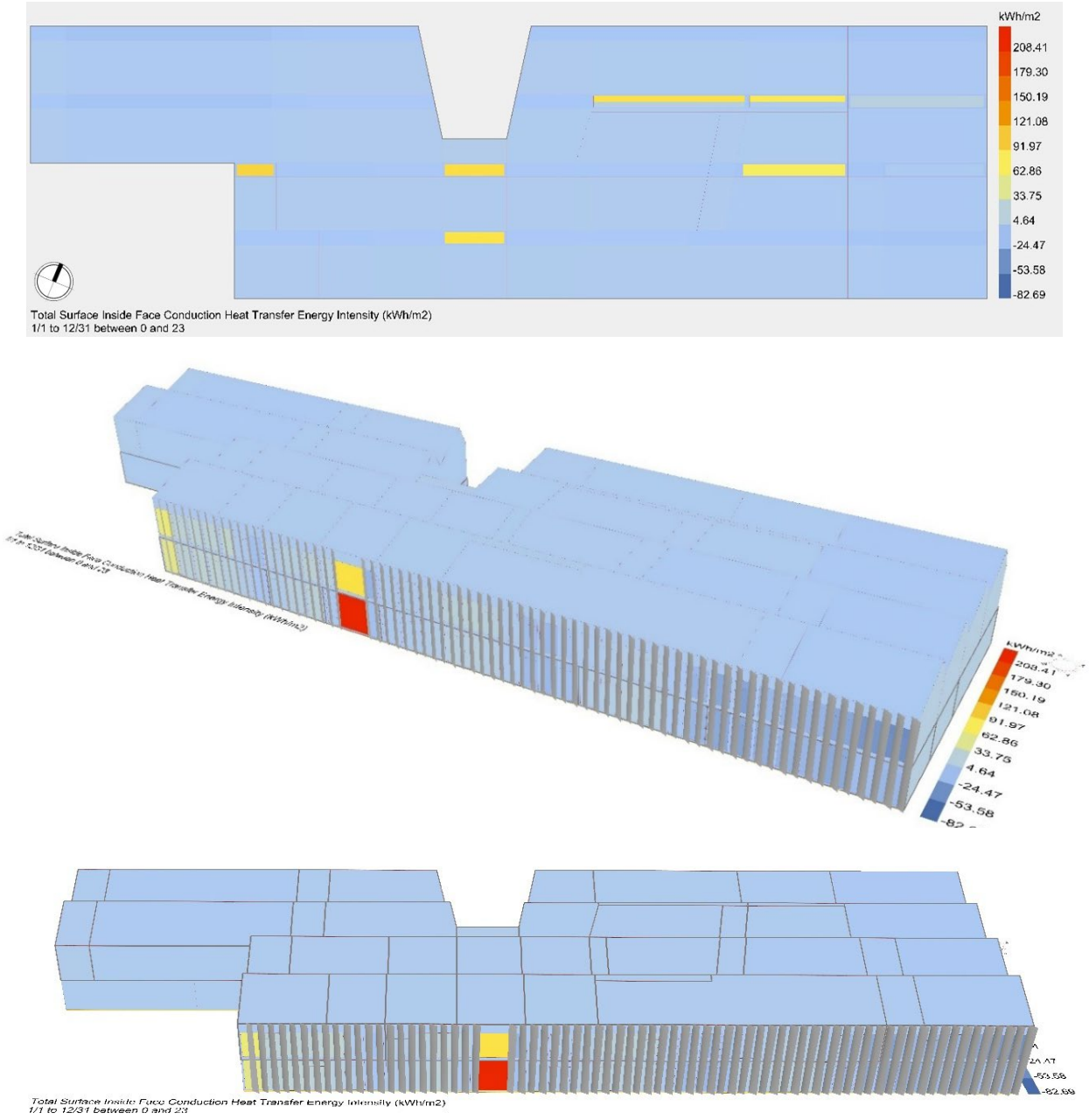

Figure 5-107 The heat loss (negative) or heat gain (positive) through each building surfaces (kWh).

Room Energy Simulation Result

- Cooling

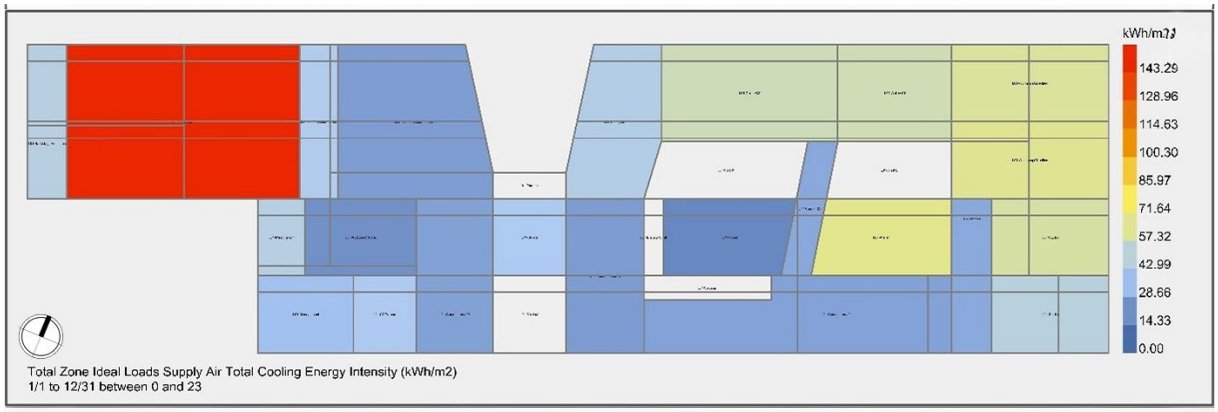

Figure 5-108 Total cooling energy intensity (kWh/m2), Ground Floor.

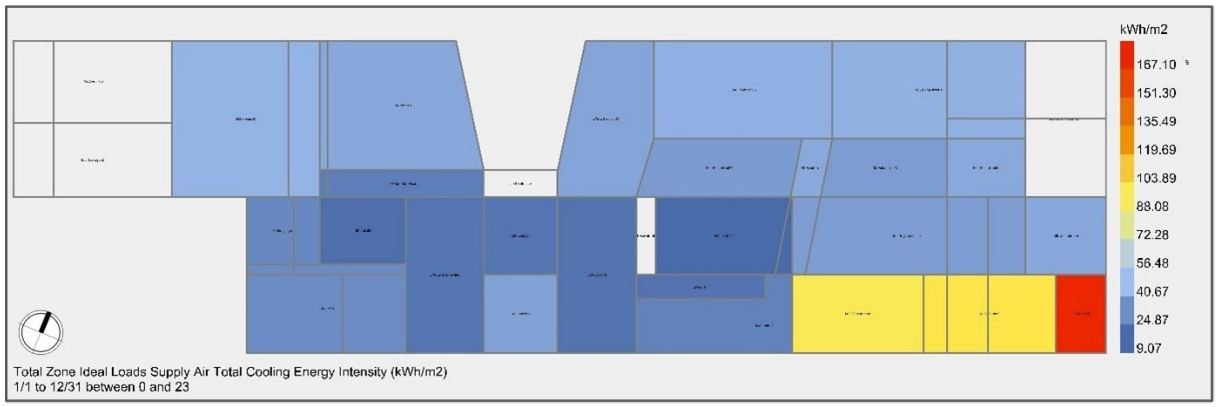

Figure 5-109 Total cooling energy intensity (kWh/m2),First Floor.

- Heating

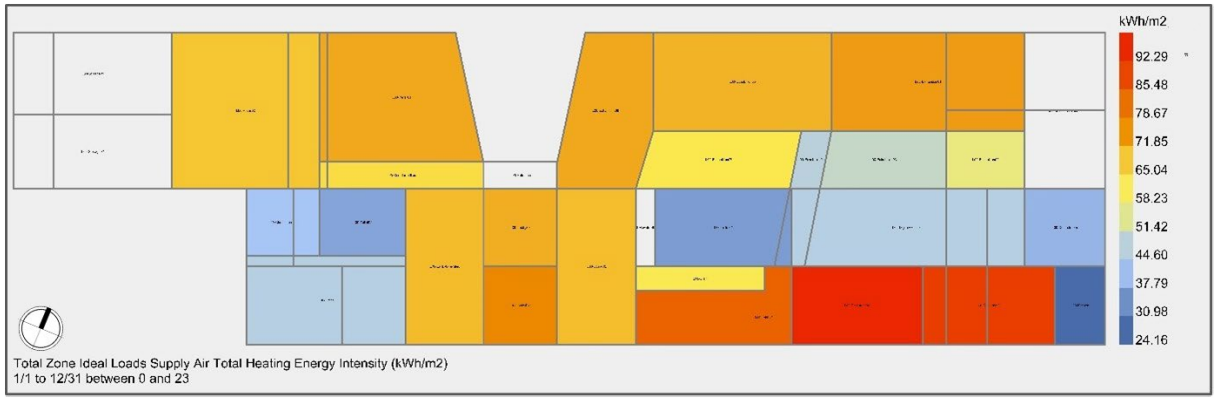

Figure 5-110 Total heating energy intensity (kWh/m2), Ground Floor.

Figure 5-111 Total heating energy intensity (kWh/m2), First Floor.

- Lighting

Figure 5-112 Total zone lights electricity energy intensity (kWh/m2), Ground Floor.

Figure 5-113 Total zone lights electricity energy intensity (kWh/m2), First Floor.

- Electric Equipment

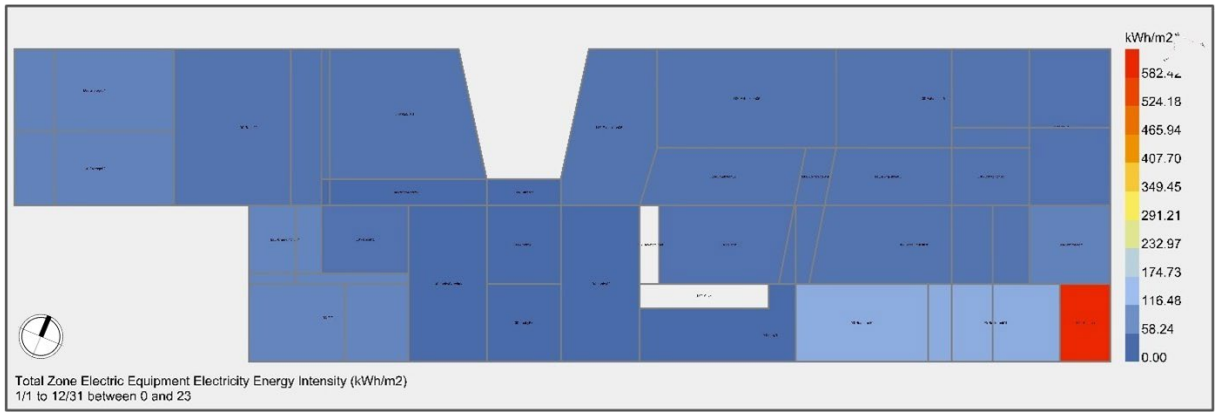

Figure 5-114 Total zone Electric Equipment energy intensity (kWh/m2), Ground Floor.

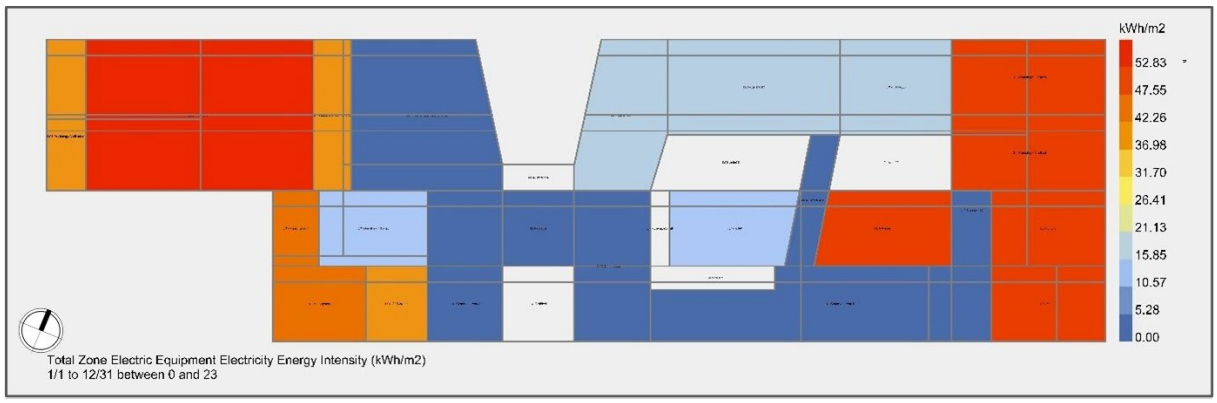

Figure 5-115 Total zone Electric Equipment energy intensity (kWh/m2), Ground Floor.

- Solar gain

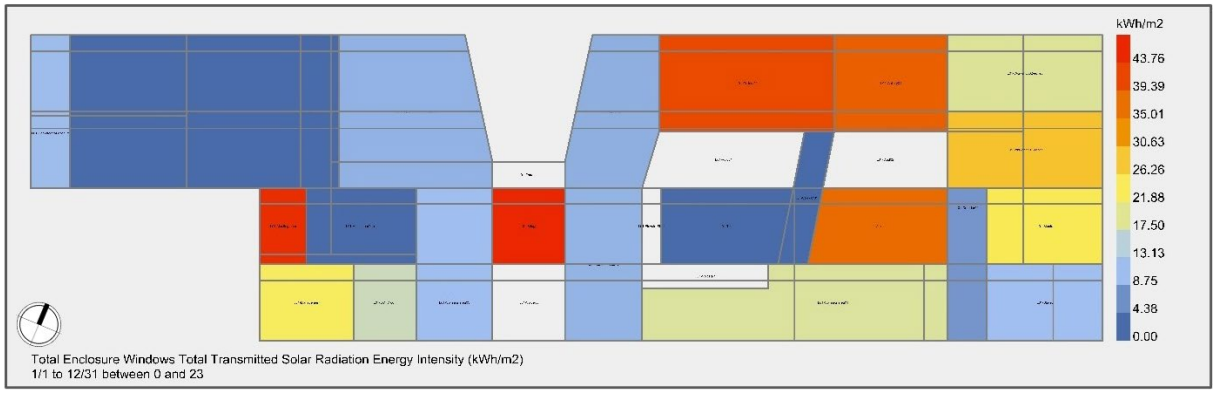

Figure 5-116 Window total transmitted solar radiation energy intensity (kWh/m2), Ground Floor.

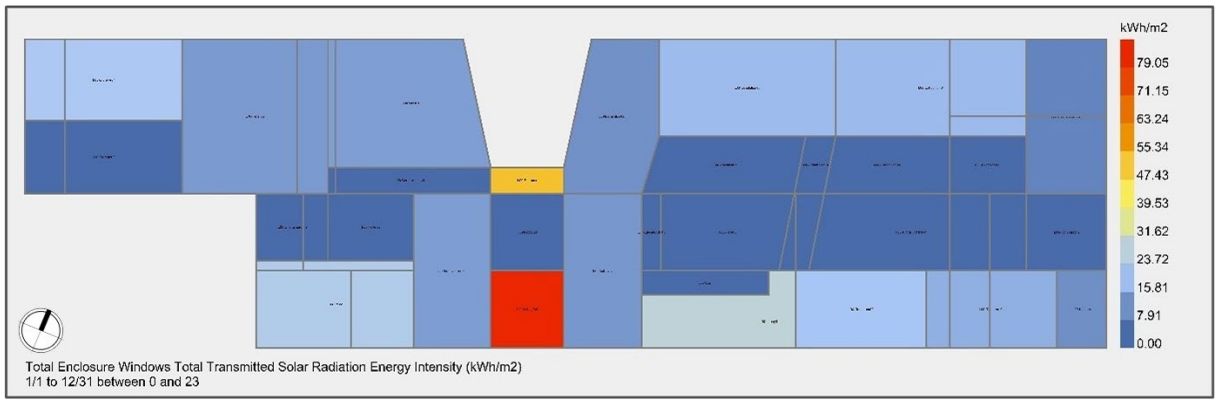

Figure 5-117 Window total transmitted solar radiation energy intensity (kWh/m2), First Floor.

Indoor Illuminance Distribution

September at 9:00

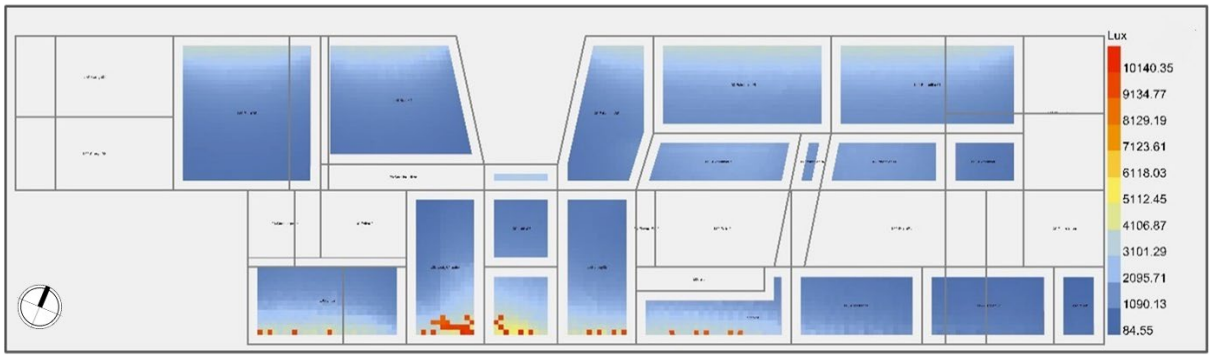

Figure 5-118 Point-In-Time Illuminance (Ground Floor, September 9 A.M)

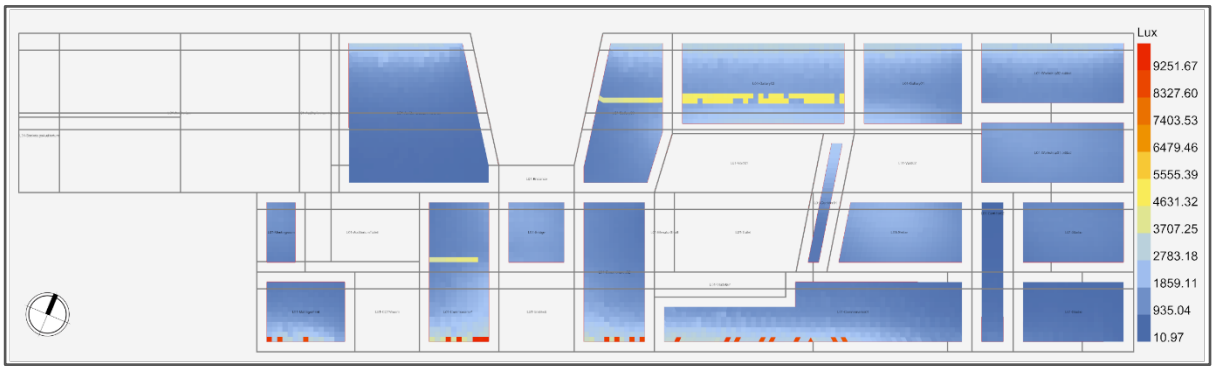

Figure 5-119 Point-In-Time Illuminance (First Floor, September 9 A.M)

September at 15:00

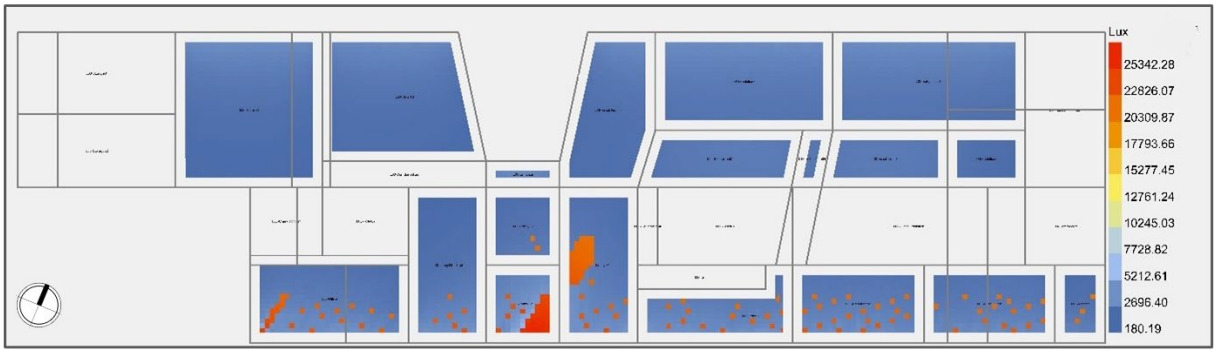

Figure 5-120 Point-In-Time Illuminance (Ground Floor, September 3 P.M)

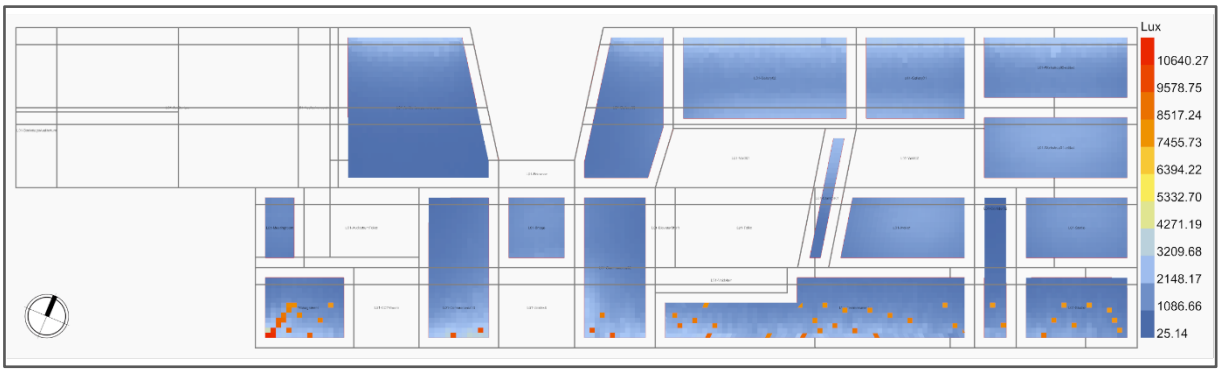

Figure 5-121 Point-In-Time Illuminance (First Floor, September 3 P.M).

March at 9:00

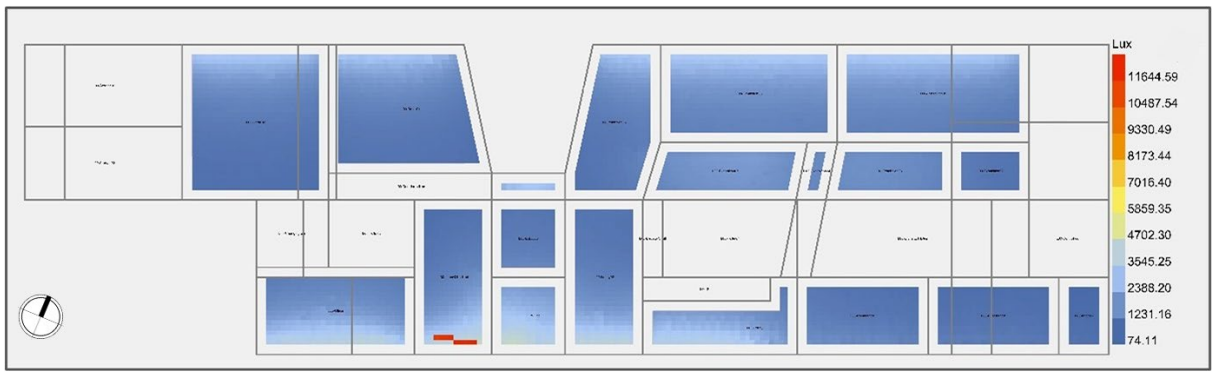

Figure 5-122 Point-In-Time Illuminance (First Floor, March 9 A.M).

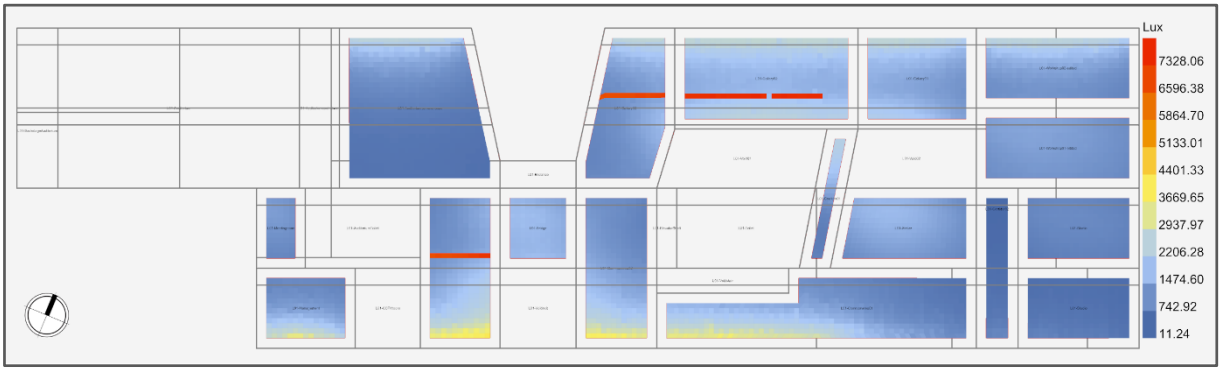

Figure 5-123 Point-In-Time Illuminance (First Floor, March 9 A.M).

March at 15:00

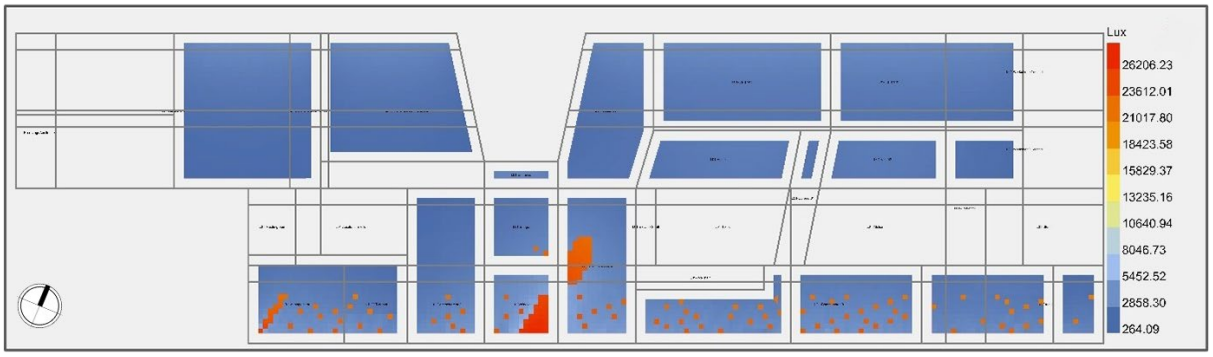

Figure 5-124 Point-In-Time Illuminance (Ground Floor, March 3 P.M).

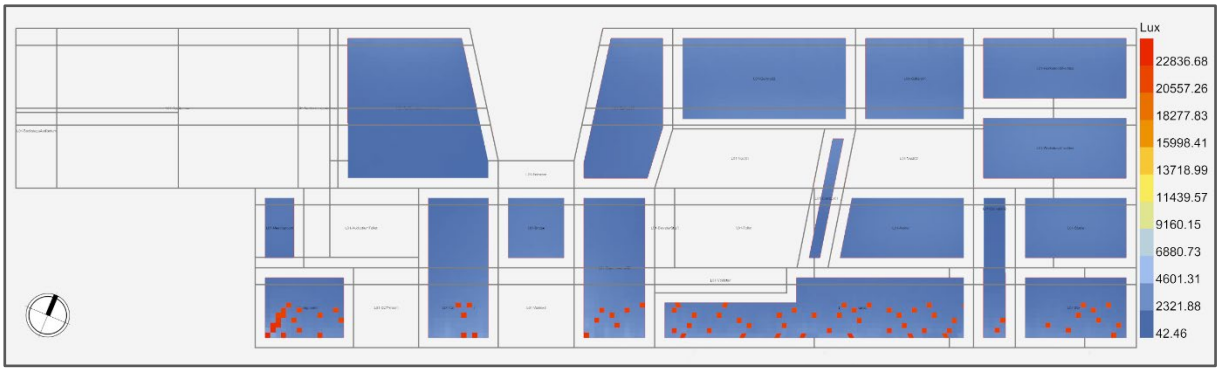

Figure 5-125 Point-In-Time Illuminance (First Floor, March 3 P.M).

B) Daylight Factor

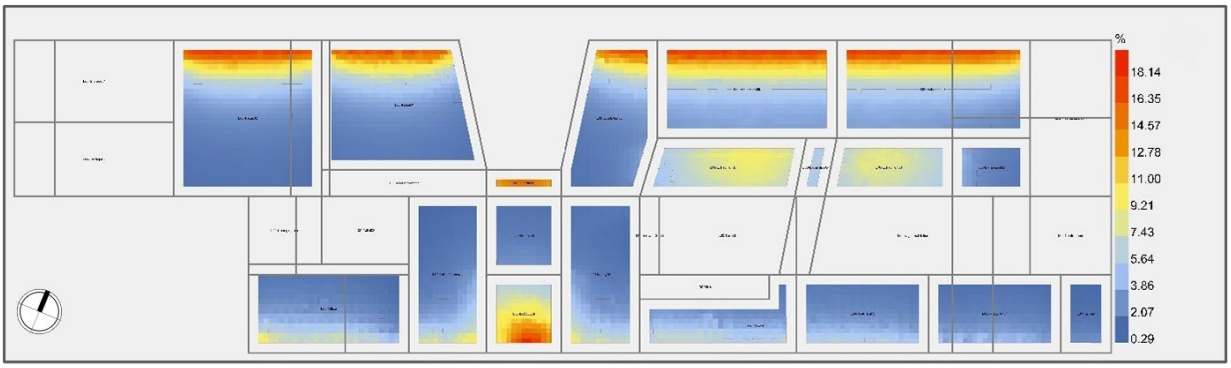

Figure 5-126 Daylight Factor between 2% and 5%, Ground floor.

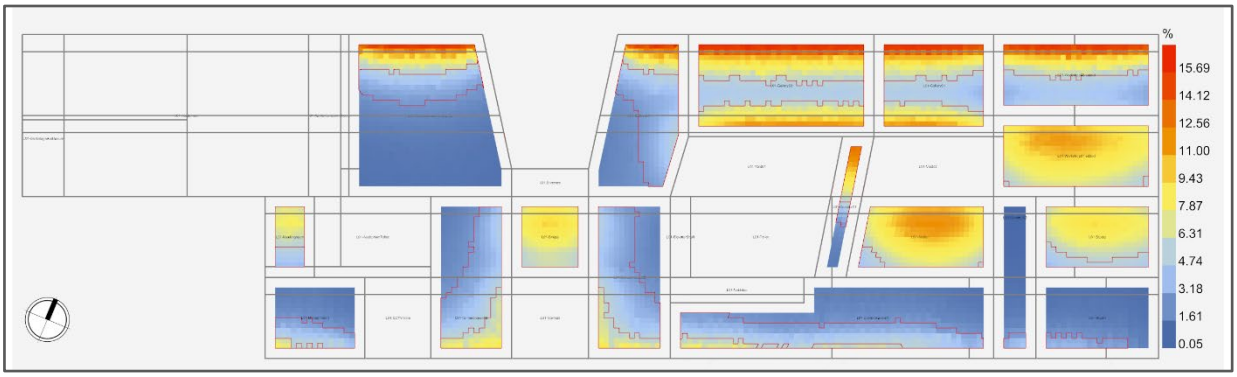

Figure 5-127 Daylight Factor between 2% and 5%, First floor.

C)Spatial Daylight Autonomy (sDA)

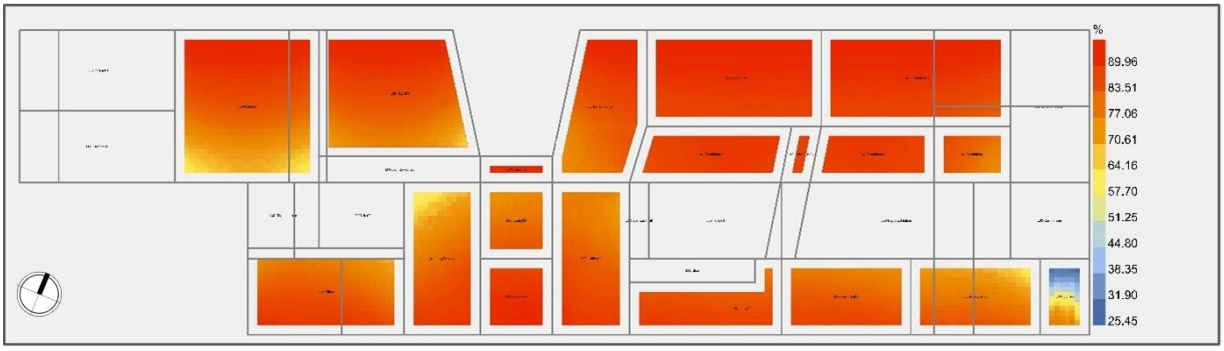

Figure 5-128 Daylight Autonomy (sDA300/50%): Percentage of regularly occupied floor area that achieves ≥300 lux for at least 50% of annual occupied hours. (Ground Floor)

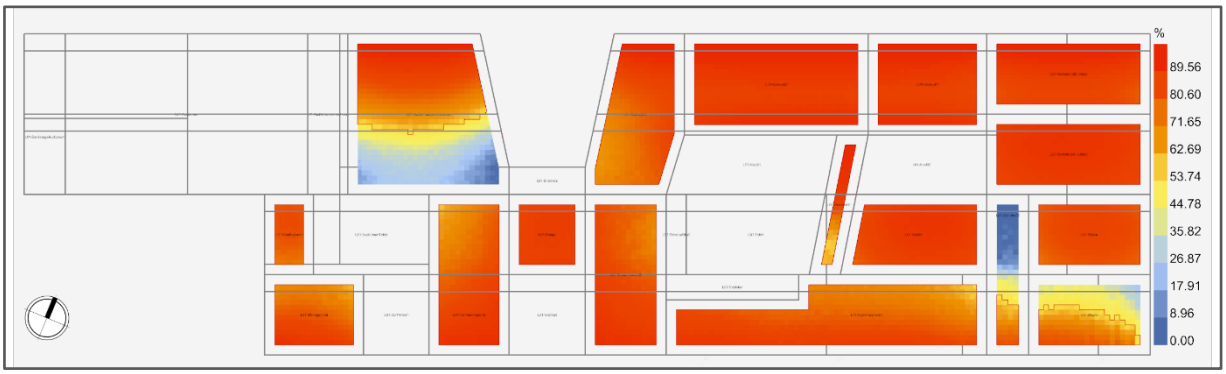

Figure 5-129 Daylight Autonomy (sDA300/50%), First Floor.

D)Useful Daylight Illuminance (UDI)

- **UDI (300–3000 lux)**

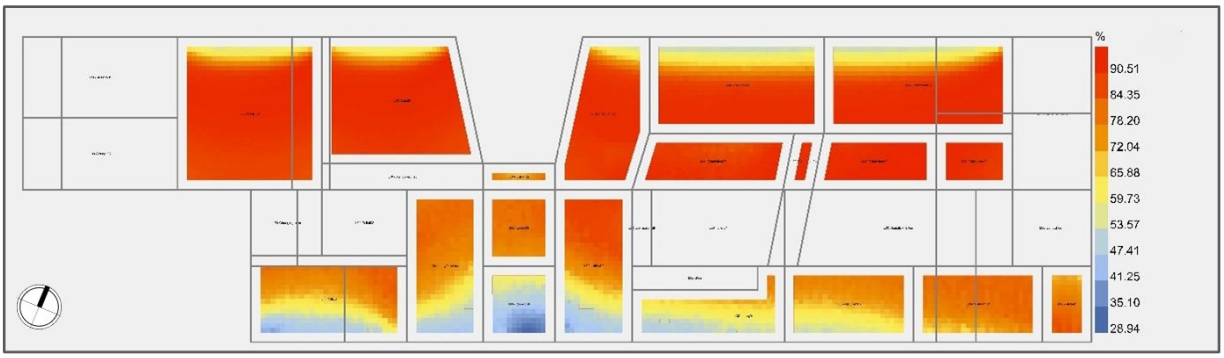

Figure 5-130 Percentage of UDI (300–3000 lux), Ground Floor

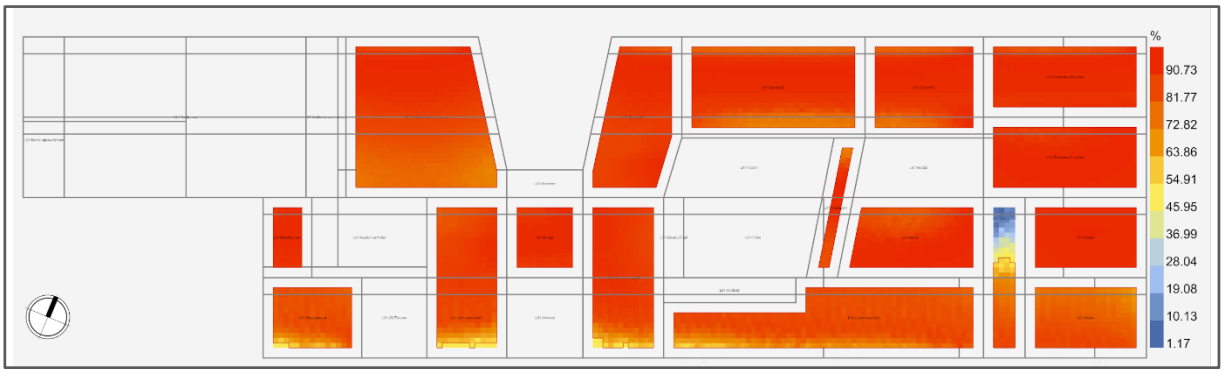

Figure 5-131 Percentage of UDI (300–3000 lux), First Floor

E) Annual Sunlight Exposure (ASE)

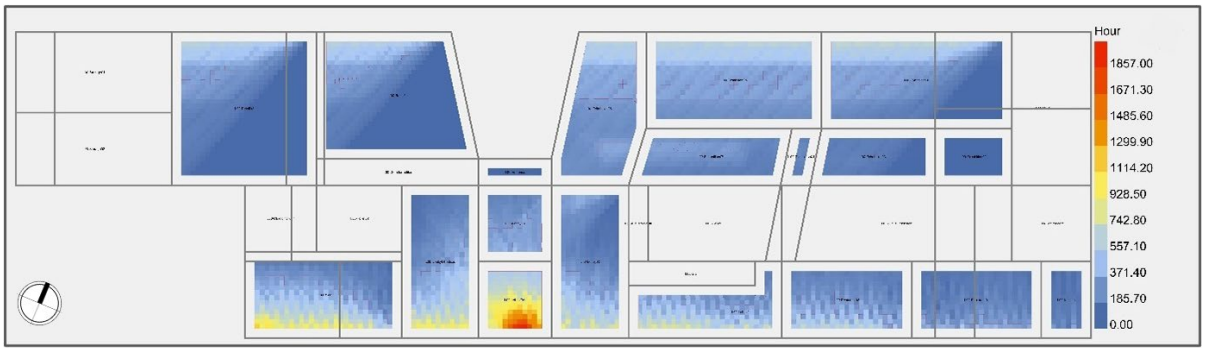

Figure 5-132 Spatial distribution of Annual Sunlight Exposure (ASE ≥ 250). Heatmap showing cumulative direct sunlight hours on the analysis grid, Ground Floor.

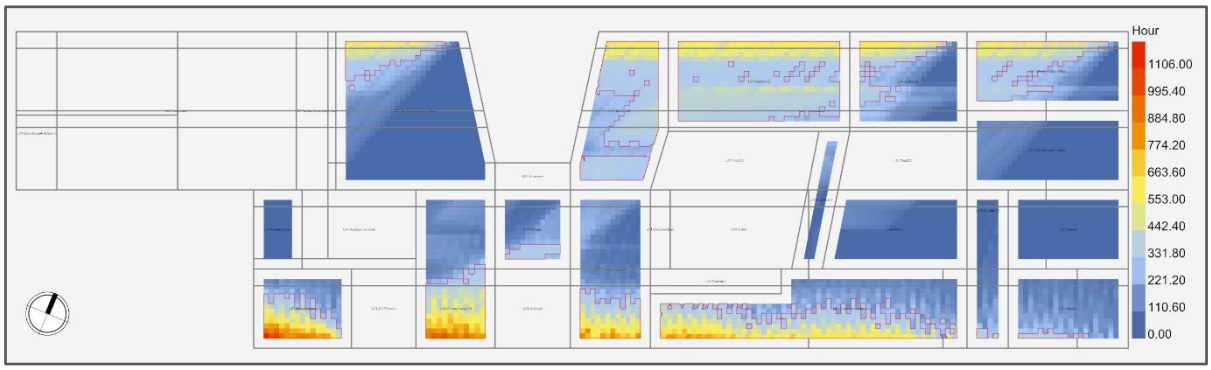

Figure 5-133 Spatial distribution of Annual Sunlight Exposure (ASE ≥ 250), First Floor.

F) Spatial Glare Autonomy (sGA)

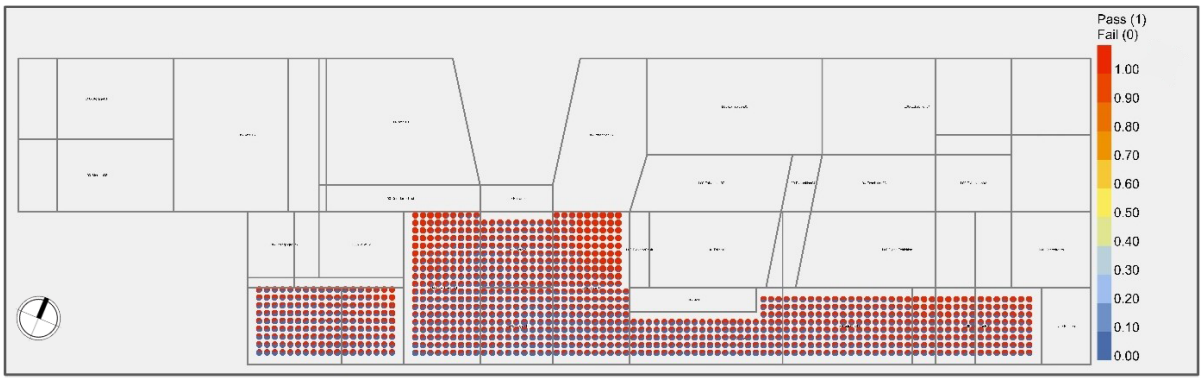

Figure 5-134 Spatial Glare Autonomy (sGA) pass/fail distribution across the analysis grids, showing the percentage of sensor points that remain below the glare threshold for the specified fraction of occupied hours (red = pass, blue = fail), Ground Floor.

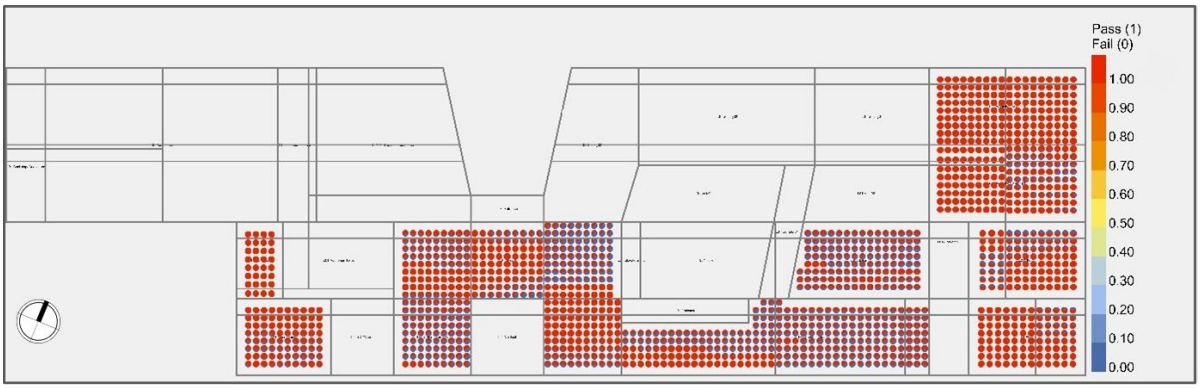

Figure 5-135 Spatial Glare Autonomy (sGA),First floor.

Results:

Energy Performance

- Total Energy Use Intensity (EUI) decreased from 181.41 to 176.56 kWh/m²·yr, corresponding to a −2.7% reduction, indicating a modest but consistent overall energy improvement.
- Heating demand increased from 56.12 to 64.78 kWh/m² (+15.4%), reflecting reduced passive solar gains due to shading.
- Cooling demand decreased from 53.84 to 40.34 kWh/m² (−25.1%), representing the most significant energy benefit of the optimized solution.
- Lighting, equipment, and water system loads remained effectively unchanged (<±0.1%), confirming that performance changes are driven primarily by façade and solar control strategies rather than operational assumptions.

Daylight Performance

- Spatial Daylight Autonomy (sDA) improved from 97.04% to 94.89%, remaining well above the 75% target and indicating sustained daylight sufficiency across occupied areas.
- Useful Daylight Illuminance (UDI ≥300–3000 lux) increased from 82.74% to 96.61%, corresponding to a +16.8% improvement, demonstrating a substantial shift toward visually comfortable daylight levels.

- Daylight Factor (2–5%) increased from 30.95% to 50.0%, a +61.6% improvement, indicating enhanced daylight penetration depth and distribution.
- Annual Sunlight Exposure (ASE) decreased from 51.42% to 12.47%, corresponding to a −75.8% reduction, moving the design significantly closer to recommended glare-control thresholds.
- Spatial Glare Autonomy (sGA) increased from 42.95% to 71.29%, representing a +66.0% improvement, confirming a substantial reduction in glare-prone conditions

Overall optimization feedback

The feedback obtained from the optimization process indicates that the proposed shading system demonstrates greater performance potential in terms of sDA and EUI, while its improvement range for sGA is limited. Beyond a certain threshold, further enhancement of glare performance could not be achieved through the current configuration.

Based on this feedback, it can be inferred that this limitation is primarily related to the two-dimensional and flat nature of the shading geometry. Consequently, designing a three-dimensional shading system with increased geometric complexity and additional input parameters, particularly incorporating horizontal surfaces, could enable the admission of more indirect daylight into the interior space. Such a strategy has the potential to reduce glare intensity and improve sGA performance, while maintaining the benefits observed for daylight availability and energy efficiency.

The final façade configuration is designed to operate through a seasonally scheduled adaptive approach. While the optimization process was carried out using a single global rotation parameter applied consistently across all south-facing zones, the operational behavior of the façade is structured around discrete seasonal adjustments based on solar position analysis for Milan (45.5°N).

The louver rotation is limited to the optimized range of 30° to 70° and is modified at predefined seasonal intervals rather than through continuous real-time movement. During winter, the louvers are kept in a relatively open position to allow greater daylight penetration and support passive solar gains. In the transitional seasons, the rotation increases to achieve a balance between glare control and sufficient daylight availability.

During summer, the louvers are rotated further to reduce oblique solar radiation and mitigate cooling demand.

This system does not depend on real-time sensor-based control. Instead, environmental responsiveness is achieved through scheduled seasonal adjustments derived from solar altitude and azimuth analysis. In this way, the façade maintains a level of climatic adaptability while preserving mechanical simplicity and operational reliability.

To conclude this chapter, one of the shading configurations applied to the complete building model. The following renderings illustrate how the optimized shading system affects the overall façade composition and spatial perception of the project.

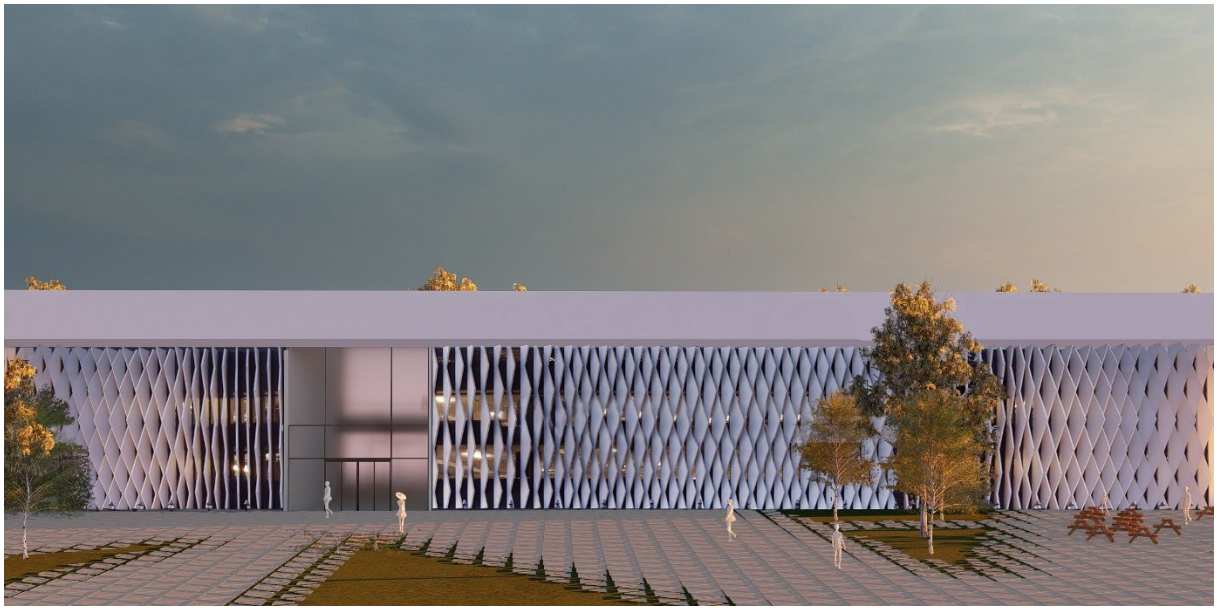

Figure 5-136 Rendered view of the south façade with the optimized louver-based shading system.

Figure 5-137 Rendered perspective view of the south façade with the optimized louver-based shading system.

06

CONCLUSION

This thesis has investigated the use of a performance-driven, multi-objective optimization procedure for façade design, with the aim of assisting architectural design choices in the presence of competing energy and daylight performance requirements. Rather than concentrating on the results, the study has endeavored to develop a systematic and repeatable approach able to identify performance compromises and inform design decisions in complex architectural design problems.

Traditional façade design procedures often involve iterative trial-and-error procedures guided by experience and intuition. Although these procedures might be adequate in simplified design problems, they become increasingly inaccurate as the complexity of the design problem and the number of interacting variables increase. When façade performance needs to be assessed in dynamic annual climatic conditions rather than in isolated static conditions, manual exploration becomes unfeasible. Moreover, the assessment of all possible design alternatives is computationally infeasible because of the exponential growth of the solution space with the number of variables.

To overcome this issue, an evolutionary multi-objective optimization approach using NSGA-II has been developed. Rather than exploring the entire solution space, the approach selectively samples representative areas and progressively evolves promising design alternatives over multiple generations. Non-dominated solutions comprising the Pareto front, which correspond to optimal trade-offs among competing objectives, are retained and propagated. By means of this evolutionary approach, the set of design alternatives progressively converges toward a systematic assembly of Pareto-optimal alternatives. Notably, the approach does not provide a definitive solution but instead informs architectural design choices by making performance compromises apparent.

A parametric and simulation-driven design process was established through the integration of façade modeling, climate-driven energy and daylight simulations, and evolutionary optimization. When tested on a commercial mixed-use building, the approach proved that façade performance is a complex and nonlinear interplay between energy demand, daylight availability, and glare mitigation. The outcome validated that multi-objective optimization is a systematic and reliable approach to investigate these interdependencies and find feasible performance trade-offs.

The optimized façade designs showed significant cooling demand reductions and improved daylight performance while reducing glare conditions prone to interior spaces. However, the outcome also showed inherent performance boundaries related to the chosen two-dimensional shading layout. After a certain point, further improvements in glare mitigation (sGA) were not possible without increasing geometric complexity. This suggests that façade geometry itself is a governing factor in daylight distribution and visual comfort. The research thus confirms the relevance of considering façade design as a multi-criteria problem where improvements in one performance aspect could limit another.

In addition to finding the best static rotation angles, the study used the optimization results to develop an operational façade strategy. While the optimization procedure used a single global rotation parameter to be applied everywhere in south-facing areas, the result interpretation allowed the development of a seasonally scheduled adaptive strategy. Based on solar position analysis for Milan (45.5° N latitude), the optimized rotation angles (30°-70°) were discretized into three operational states according to the season. During winter, louvers are kept relatively open to allow more daylight and passive solar gain. During transitional seasons, the rotation angle is increased to balance glare protection with sufficient daylighting. During summer, the louvers are set to a more closed position to prevent oblique solar radiation and reduce cooling loads.

This approach does not depend on real-time control based on sensor data. Instead, environmental responsiveness is achieved by means of pre-defined seasonal adjustments based on solar altitude and azimuth analysis. In this manner, the façade transforms from a static optimized shape to a seasonally climate-responsive adaptive system. In this manner, the research work proves that computational optimization can inform not only geometric arrangement but also operational logic, thus merging environmental simulation and architectural design.

The second aspect of the thesis's contribution is related to the interpretation and visualization of optimization results. Instead of considering optimization as a strictly computational process, the optimization process was defined as a decision-support system available to architectural designers. In this manner, the approach clarifies how input parameters affect energy and daylight performance criteria, thus improving transparency and informing design decisions based on performance knowledge.

The main contribution of this research work is methodological, rather than strictly numerical. Although the actual performance results are context-dependent, the optimization process structure, objective formulation, and post-optimization interpretation strategy are generally applicable to different building types and climatic conditions.

However, some limitations were found. In the NSGA-II algorithm used in the Grasshopper platform, the diversity of solutions in the Pareto front in later generations might decrease if many solutions are no longer dominated. This could lead to a failure of the crowding distance operator to preserve a uniform distribution, causing some areas of the objective space to be densely filled while others are sparsely filled. This could limit the ability to represent trade-offs in a comprehensive manner.

Other algorithms like NSGA-III, which use reference-point-based selection, could address this limitation by providing a more balanced distribution of elite solutions. Future studies could develop an NSGA-III-based plugin for Grasshopper to improve solution diversity and interpretability. Other potential extensions include the study of three-dimensional geometries of shading, dynamic sensor-based control schemes,

and the extension of comfort criteria to further analyze the performance of adaptive façades.

In conclusion, this thesis work has shown that the actual benefit of façade optimization does not reside in finding a single solution. Rather, it resides in organizing knowledge about performance in a manner that facilitates architectural reasoning. Through the integration of computational optimization, environmental simulation, and design interpretation, this work has contributed to the development of performance-based façade design methodologies.

07

REFERENCES

Alsukkar, M., Alwetaishi, M., Al-Saadi, S. and Alalouch, C. (2025)
Multi-objective *optimization of daylighting systems for energy efficiency and thermal–visual comfort in buildings: A review. Building and Environment, 248, 110946.*
https://doi.org/10.1016/j.buildenv.2024.110946

Attia, S., Gratia, E., De Herde, A. and Hensen, J.L.M. (2013)
Simulation-based decision support tools for early design stages: A review. Energy and Buildings, 49, pp.2–15.
https://doi.org/10.1016/j.enbuild.2012.12.033

Attia, S. (2018)
Evaluation of adaptive façade technologies for improving building performance. Energy and Buildings, 179, pp. 165–182.
https://doi.org/10.1016/j.enbuild.2018.09.015

Bäck, T.,Fogel, D., & Michalewicz, Z. (1997).
Handbook of Evolutionary Computation. OUP.
https://doi.org/10.1201/9781420050387

Boyd, S., & Vandenberghe, L. (2004).
Convex Optimization. Cambridge University Press.
https://web.stanford.edu/~boyd/cvxbook/

Carroll, W.L., Hitchcock, R.J. and Kutner, M.H. (2020)
A parametric study of façade design variables on building energy performance. Energy and Buildings, 210, 109728.
https://doi.org/10.1016/j.enbuild.2019.109728

Clarke, J.A. (2001)
Energy Simulation in Building Design.2nd edn.
Oxford: Butterworth-Heinemann.

Coello Coello, C. A. (2006).
Evolutionary multi-objective optimization.
https://doi.org/10.1109/MCI.2006.1597059

Coello Coello, C.A., Van Veldhuizen, D.A. and Lamont, G.B. (2007)
Evolutionary Algorithms for Solving Multi-Objective Problems. Springer.

Costa-Carrapiço, I. et al. (2020).
A systematic review of Genetic Algorithm-based multi-objective optimisation in building retrofit.
https://doi.org/10.1016/j.enbuild.2020.110322

Crawley, D.B., Lawrie, L.K.,
Winkelmann, F.C., Buhl, W.F., Huang, Y.J., Pedersen, C.O., Strand, R.K.,
Liesen, R.J., Fisher, D.E., Witte, M.J. and Glazer, J. (2001)
EnergyPlus: Creating a new generation building energy simulation program. Energy and Buildings, 33(4), pp.319–331.
https://doi.org/10.1016/S0378-7788(00)00114-6

Crawley, D.B., Hand, J.W., Kummert, M. and Griffith, B.T. (2008)
Contrasting the capabilities of building energy performance simulation programs. Building and Environment,
43(4), pp.661–673.
https://doi.org/10.1016/j.buildenv.2006.10.027

Deb, K. (2001).
Multi-Objective Optimization Using Evolutionary Algorithms. Wiley.
https://doi.org/10.1002/9780470316694

Deb, K., Pratap, A., Agarwal, S. and Meyarivan, T. (2002)
'A fast and elitist multiobjective genetic algorithm: NSGA-II', IEEE Transactions on Evolutionary Computation, 6(2), pp. 182–197, from
https://doi.org/10.1109/4235.996017

Delgarm, N. et al. (2016).
Multi-objective optimization of the building energy performance by means of PSO.
https://doi.org/10.1016/j.apenergy.2016.04.008

DesignBuilder Software Ltd. (2023)
DesignBuilder Software Documentation, from

https://designbuilder.co.uk

Dial GmbH (2023)
DIALux evo – Lighting Design Software, from
https://www.dialux.com

DOE (1980)
DOE-2 Engineers Manual.
Lawrence Berkeley National Laboratory.

Dorigo, M., & Stützle, T. (2004).
Ant Colony Optimization. MIT Press.
https://mitpress.mit.edu/9780262042192/ant-colony-optimization/

Equa Simulation AB (2023)
IDA ICE – Indoor Climate and Energy, from
https://www.equa.se/en/ida-ice

Fletcher, R. (2013).
Practical Methods of Optimization. Wiley.
https://doi.org/10.1002/9781118723203

Goharian, S., Mohammadi, M. and Banihashemi, S. (2025)
Designing adaptability strategy for a novel kinetic adaptive façade: Toward a pioneering method in dynamic-objects daylight simulation. Journal of Daylighting, 12(1), pp. 124–138.
https://doi.org/10.15627/jd.2025.9

Guglielmetti, R., Macumber, D. and Long, N. (2011)
OpenStudio: An open source integrated analysis platform.
Proceedings of the 12th International Building Performance Simulation Association Conference
(BS2011), Sydney, Australia.

Harshalatha, S. et al. (2024).

A review on simulation-based multi-objective optimization for building energy performance. https://doi.org/10.1007/s41024-024-00425-3

Hirsch, J.J. (2016)
eQUEST – The Quick Energy Simulation Tool, from
https://doe2.com/equest

IES Ltd. (2023) Integrated Environmental Solutions – Virtual
Environment (IES VE). , from
https://www.iesve.com

Illuminating Engineering Society (IES) (2012)
LM-83-12: Approved Method: IES Spatial Daylight Autonomy (sDA) and Annual Sunlight Exposure (ASE). New York: IES.

Izadi, A. et al. (2023).
A Systematic Review of Multi-Objective Optimization Methods of Building Energy Performance.
https://ijaup.iust.ac.ir/article-1-802-en.pdf

Jakubiec, J.A. and
Reinhart, C.F. (2011)
DIVA 2.0: Integrating daylight and thermal simulations using Rhinoceros 3D, Daysim and EnergyPlus. Proceedings of Building Simulation 2011, pp. 2202–2209.

Jones, T. (1995)
Evolutionary Algorithms, Fitness Landscapes and Search. PhD thesis, University of New Mexico.

Kauffman, S.A. (1993)
The Origins of Order: Self-Organization and Selection in Evolution.
Oxford University Press.

Kennedy, J., & Eberhart, R. (1995).
Particle Swarm Optimization (original PSO paper).
https://doi.org/10.1109/ICNN.1995.488968

Klein, S.A. et al. (2017)
TRNSYS 18 – A Transient System Simulation Program.
Solar Energy Laboratory, University of Wisconsin–Madison.

Ladybug Tools (2025)
Honeybee (Grasshopper) component documentation: “HB Model to OSM”. (Component description and license header as provided in the workflow documentation.)

Li, R. et al. (2025).
A review on multi-objective optimization of building performance.
https://pmc.ncbi.nlm.nih.gov/articles/PMC11870193/

Loonen, R.C.G.M., Trčka, M., Cóstola, D. and Hensen, J.L.M. (2013)
Climate adaptive building shells: State-of-the-art and future challenges. Renewable and Sustainable Energy Reviews, 25, pp. 483–493.
https://doi.org/10.1016/j.rser.2013.04.016

Loonen, R.C.G.M., Favoino, F., Hensen, J.L.M. and Goia, F. (2015)
Review of current status, requirements and opportunities for building performance simulation of adaptive façades. Building and Environment, 91, pp. 148–165.
https://doi.org/10.1016/j.buildenv.2015.02.017

Makki, M., Showkatbakhsh, M., Song, Y. and Kang, Z. (2019)
Multi-objective optimization of building design using Wallacei. Automation in Construction, 97, pp. 167–180.
https://doi.org/10.1016/j.autcon.2018.10.006

Nabil, A. and Mardaljevic, J.(2005)
Useful daylight illuminances: A replacement for daylight factors.
Lighting Research & Technology, 37(1), pp.41–57.
https://doi.org/10.1191/1365782805li128oa

National Renewable
Energy Laboratory (NREL) (n.d.) OpenStudio® Analysis Framework. , from
https://www.nrel.gov/buildings/openstudio-analysis-framework

Nguyen, A.-T.,Reiter, S. and Rigo, P. (2014)
A review on simulation-based optimization methods applied to building performance analysis. Applied Energy, 113, pp. 1043–1058.
https://doi.org/10.1016/j.apenergy.2013.08.061

Nguyen, A.-T., Reiter, S. and Rigo,P. (2014)
A review on simulation-based optimization methods applied to building performance analysis. Applied Energy, 113, pp.1043–1058.
https://doi.org/10.1016/j.apenergy.2013.08.061

Nocedal, J., & Wright, S. (2006).
Numerical Optimization. Springer.
https://doi.org/10.1007/978-0-387-40065-5

NREL (2023)
OpenStudio Documentation. National Renewable Energy Laboratory, from
https://openstudio.net

Ochoa, C.E., Aries, M.B.C. and Hensen, J.L.M. (2012)
State of the art in lighting simulation for building science: A literature review. Building and Environment, 50, pp.13–23.
https://doi.org/10.1016/j.buildenv.2011.10.007

Poli, R.,
Kennedy, J., & Blackwell, T. (2007). PSO overview.
https://doi.org/10.1007/s11721-007-0002-0

Pomponi, F., Piroozfar, P.A.E. and Southall, R. (2016)
Life cycle energy and carbon assessment of double skin façades. Energy and Buildings, 113, pp.152–162.
https://doi.org/10.1016/j.enbuild.2015.12.028

Reinhart, C.F. and Wienold, J. (2011)
The daylighting dashboard – A simulation-based design analysis for daylit spaces. Building and Environment,46(2), pp.386–396.
https://doi.org/10.1016/j.buildenv.2010.08.001

Reinhart, C.F., Mardaljevic, J. and Rogers, Z. (2006)
Dynamic daylight performance metrics for sustainable building design. LEUKOS, 3(1), pp.7–31.
https://doi.org/10.1582/LEUKOS.2006.03.01.001

Roudsari, M.S. and Pak, M. (2013)
Ladybug: A parametric environmental plugin for Grasshopper to help designers create an environmentally conscious design. Proceedings of BS2013, Chambéry, France, pp. 3128–3135.

Roudsari, M.S., Pak, M. and Smith, A. (2014)
Ladybug and Honeybee: A new generation of environmental plugins for Grasshopper. Proceedings of BS2014, Hyderabad, India.

Rutten, D. (2010)
Galapagos: On thelogic and limitations of generic solvers. Architectural Design, 80(2), pp. 132–135.

Sefaira Inc. (2023)
Sefaira Architecture Documentation, from
https://sefaira.com

Solemma LLC (2023)
ClimateStudio Documentation. , from
https://www.solemma.com/climatestudio

Tang, D., & Wang, Z. (2025).
An Enhanced NSGA-II Algorithm for Active Glass Curtain Wall Shading Systems.
https://doi.org/10.3390/en18071584

Tian, C., Li, X., Wu, Y. and Zhang, H. (2025)

*Parametric multi-objective optimization of building envelope retrofits using Honeybee–EnergyPlus and NSGA-II.*Case Studies in Thermal Engineering, 76,107297.
https://doi.org/10.1016/j.csite.2024.107297

Tzempelikos, A. and Athienitis, A.K. (2007)
The impact of shading design and control on building cooling and lighting demand. Solar Energy, 81(3), pp.369–382.
https://doi.org/10.1016/j.solener.2006.06.015

U.S. Department of Energy (DOE) (n.d.)
OpenStudio, from
https://www.energy.gov/eere/buildings/articles/openstudio

U.S. Green Building Council (USGBC) (2019)
LEED v4.1 Interior Lighting—Daylight Credit. Washington, DC.

Velux Group (2023)
VELUX Daylight Visualizer, from:
https://www.velux.com/daylight-visualizer

Vierlinger, R., Bollinger, K. and Leitner, J. (2017)
Octopus: A multi-objective optimization tool for architectural design. Proceedings of eCAADe 2017, pp. 451–460.

Ward, G.J. (1994)
The Radiance lighting simulation and rendering system. Proceedings of SIGGRAPH 1994, pp. 459–472.
https://doi.org/10.1145/192161.192286

Ward, G. and Shakespeare, R. (1998)
Rendering with Radiance: The Art and Science of Lighting Visualization. San Francisco: Morgan Kaufmann.

Wienold, J. and Christoffersen, J.(2006)

Evaluation methods and development of a new glare prediction model for daylight environments. Energy and Buildings, 38(7), pp.743–757. https://doi.org/10.1016/j.enbuild.2006.03.017

Wolpert, D.H. and Macready, W.G. (1997) *'No free lunch theorems for optimization'*, IEEE Transactions on Evolutionary Computation, 1(1), pp. 67–82.

Yao, J., Zhao, L., Li, B. and Wang,Z. (2024) *Multi-objective optimization of office egg-crate shadings to reduce energy use and improve thermal and visual comfort using NSGA-II.* Energy and Buildings, 294, 113219. https://doi.org/10.1016/j.enbuild.2023.113219

Zhang, Y., Liu, J., Chen, X. and Wang, Y. (2025) *Machine learning–assisted multi-objective optimization of integrated shading systems for daylight, glare and energy performance.* Building and Environment, 249, 111004. https://doi.org/10.1016/j.buildenv.2024.111004

Reference of figures:

Figure 1-1 Adaptive ETFE façade system of the Media-TIC Building. 2
Figure 1-2 Kinetic shading façade of the Kiefer Technic Showroom. 3
Figure 2-1 Diagram for a conventional (human-driven) design approach 10
Figure 2-2 Diagram for parametric design approach to optimization 10
Figure 2-3 Schematic diagram of a parametric algorithm;visual programming . Screenshot from Grasshopper optimization online workshop, Source: (HowToRhino, 2026) https://howtorhino.com/ 11
Figure 2-4 Example for design search space. Screenshot from Grasshopper optimization online workshop, Source: (HowToRhino, 2026) https://howtorhino.com/ 12

Figure 2-5 Optimization methods classification. Screenshot from Grasshopper optimization online workshop, Source: (HowToRhino, 2026) https://howtorhino.com/ 13
Figure 2-6 Example of a Pareto frontier for a multi-objective optimization problem with two objective functions. Source: (D. Somma, 2016). 22
Figure 2-7 Set of objective space solutions for objective functions $f1$, $f2$ along with A, B, and C solutions. Source: Kesireddy and Medrano (2024). 23
Figure 2-8 SD graph example. Source: Showkatbakhsh et al. (2018). 25
Figure 2-9 SD mean-value trendline chart example. Source: Showkatbakhsh et al. (2018). 27
Figure 2-10 Mean Fitness trendline chart example. Source: Showkatbakhsh et al. (2018). 29
Figure 2-11 Fitness Value chart example. Source: Showkatbakhsh et al. (2018). ... 30
Figure 2-12 Parallel coordinate plot example. Source: Showkatbakhsh et al. (2018). 31
Figure 2-13 The Diamond fitness Chart Example. Source: Showkatbakhsh et al. (2018). 31
Figure 2-14 example of demonstration of an objective space with 3 objectives. Source: Showkatbakhsh et al. (2018). 32
Figure 3-1 Workflow is used for optimization of dynamic shadings. Source: Chi et al. (2021) 40
Figure 3-2 Dynamic shadings: (a) dimensions of the shading structure, (b) dimensions of the component units, (c) genes: folding and rotational axes, and (d) perspective view. Source: Chi et al. (2021) 41
Figure 3-3 Example of shadings positions according to the sun trajectories in Cancun, Mexico, at 12 h Source: Chi et al. (2021) 42
Figure 3-4 Second exercise with a population of 500 genomes. UTCI optimization graphs for 21 June: (a) 8 h, (b) 12 h, and (c) 16 h. Source: Chi et al. (2021) 42
Figure 3-5 Pareto Front phenotypes: Solutions ranked as the best according to the two fitness..... 43
Figure 3-6 Comparison among the phenotypes during specific Source: Chi et al. (2021) 44

Figure 3-7 Comparative of the condition of a person throughout the year: (a) Shaded conditions vs. (b) unshaded conditions. Hourly data from the EPW file of Cancun, Mexico. Source: Chi et al. (2021) 44
Figure 3-8 Block diagram of the research. Source: Sorooshnia et al. (2023) 47
Figure 3-9 Parameters to calculate the configuration factor of a window. Sorooshnia et al. (2023) 49
Figure 3-10 Vertical eye luminance [lux] at a level of 1.7 m on January 1st for a north-facing room at Sydney Olympic Park under clear sky condition with the sun (left); DGP for three views at the same position, location and time to left graph. Sorooshnia et al. (2023) 50
Figure 3-11 Validating DGP simulation data by taking HDR images of HQ cameras and human subjects' assessment. Every virtual sensor in simulation is replaced with a camera and human subject to assess data Gathered from simulation. Sorooshnia et al. (2023) 52
Figure 3-12 To validate data, light-dependent resistor sensor (Low dark current and low working lux) and ambient light sensors (Near human eye spectral response and very low IR sensitivity) positioned at the points that virtual sensors. Figure 3 11 To validate dat 52
Figure 3-13 A single solution of shading system could be assumed to be installed on all layout north-facing windows in Sydney, alleviation DGP while keeping UDI at the highest possible level. Sorooshnia et al. (2023) 54
Figure 3-14 Changes optimum shading system brings to each case. Sorooshnia et al. (2023) 54
Figure 3-15 The algorithmic construction of the primitive geometry based on Al-Bahr towers geometry. 58
Figure 3-16 Illustration of (a) H-M-A process and effects (skin system); (b) algorithmic setup of the skin system. Source: Showkatbakhsh and Kaviani (2020) . 59
Figure 3-17 Illustration of mechanism B process and effects (protrusions). Source: Showkatbakhsh and Kaviani (2020) 60
Figure 3-18 The Al-Bahr towers and the selected number of Pareto fronts and their performance measurements. All of the selected candidates are performing better than the Al-Bahr towers. 61

Figure 4-1 Overview of the performance-driven façade optimization workflow from parametric modeling to Pareto-optimal solution selection and evaluation. 65
Figure 4-2 Ladybug features.Source: Ladybug..... 67
Figure 4-3 Ladybug Download weather component. 68
Figure 4-4 Honeybee Features. Source: Ladybug..... 69
Figure 4-5 Creating Zones Algorithm in 4 sections A/B/C/D. 70
Figure 4-6 Section A the process of internalizing Rhino Breps and intersecting them. 71
Figure 4-7 Zones classification and add air boundaries algorithm..... 71
Figure 4-8 Honeybee solve adjacency component algorithm. 72
Figure 4-9 Honeybee add subface algorithm..... 73
Figure 4-10 Program assignment workflow showing zone classification, ASHRAE based setpoint definition, and program type allocation using Honeybee in 3 steps(A,B,C). 73
Figure 4-11 Room categorization algorithm. 74
Figure 4-12 Definition of setpoint algorithm. 75
Figure 4-13 program Application algorithm. 75
Figure 4-14 People occupancy Program schedule visualized by Ladybug Hourly Plot. 76
Figure 4-15 Lighting Program schedule visualized by Ladybug Hourly Plot. 76
Figure 4-16 Honeybee material and construction set assignment algorithm. 77
Figure 4-17 Opaque wall construction workflow in Honeybee 78
Figure 4-18 Create a Construction Set object containing all energy constructions needed to create an..... 78
Figure 4-19 Energy simulation workflow using Honeybee–EnergyPlus integration. . 80
Figure 4-20 HB Annual Loads component, highlighted in Figure 4-19..... 81
Figure 4-21 Energy simulation workflow: (A) natural ventilation and idealized HVAC definition; (B) Honeybee model assembly with shading; (C) OpenStudio model translation and simulation execution; (D) SQL-based result extraction and visualization. 83
Figure 4-22 Zone-level definition of natural ventilation control and idealized HVAC operation using Honeybee components, including schedules, temperature-based ventilation logic, operable windows, and the HB Ideal Air system. 84

Figure 4-23 Assembly of Honeybee Rooms into a single building model with contextual shading geometry, showing the integration of thermal zones and external shading elements using the HB Model and HB Shade components prior to energy simulation. 85
Figure 4-24 Translation of the parametric Honeybee model into an OpenStudio model and execution of the annual energy simulation with defined parameters and outputs. 86
Figure 4-25 HB Model to OSM component, highlighted in Figure 4-24 87
Figure 4-26 Simulation results are read from the OpenStudio SQL file, processed into energy and comfort metrics, and visualized using Ladybug charts and surface-based color mapping. 88
Figure 4-27 HB End use intensity component, highlighted in Figure 4-26 89
Figure 4-28 Monthly energy balance showing the contribution of heating, cooling, lighting, equipment, ventilation, solar gains, and thermal storage, derived from HB Read Room Energy Result and processed using HB Thermal Load Balance. 90
Figure 4-29 Spatial distribution of exterior surface temperatures obtained using HB Read Face Result, ... 90
Figure 4-30 Thermal comfort performance evaluated using HB Read Room Comfort Result and LB PMV Comfort, showing operative temperature trends and the percentage of occupants dissatisfied (PPD) over the simulation period. 91
Figure 4-31 Honeybee-based daylight simulation setup integrating climate data, building geometry, shading, and sensor grids. 93
Figure 4-32 Point-in-time daylight simulation workflow for September at 15:00, evaluating indoor illuminance distribution against LEED thresholds. 95
Figure 4-33 Daylight Factor simulation workflow 96
Figure 4-34 Parametric Honeybee workflow for annual daylight simulation and evaluation of UDI and sDA metrics. 98
Figure 4-35 Workflow for annual daylight performance evaluation, illustrating UDI .. 99
Figure 4-36 Workflow for annual daylight performance evaluation, illustrating UDI Low 100
Figure 4-37 4 37 Workflow for annual daylight performance evaluation, illustrating UDI Up 100

Figure 4-38 Workflow for Annual Sunlight Exposure (ASE) assessment, showing calculation of direct sun hours on the sensor grid..... 101
Figure 4-39 Spatial Glare Autonomy (sGA) workflow illustrating image-based annual glare simulation, glare metric evaluation, and spatial mapping of glare-compliant sensor areas..... 102
Figure 4-40 Wallacei X component in Grasshopper. Source: Showkatbakhsh et al. (2018)..... 103
Figure 4-41 Wallacei X component, tabs general explanation..... 104
Figure 4-42 Wallacei X components, Tab 1 interface..... 105
Figure 4-43Wallacei X components, Tab 2 interface..... 107
Figure 4-44 Wallacei X components, Tab 3 interface..... 109
Figure 4-45 Overview of inputs in Fitness Value Component. 112
Figure 4-46 Overview of inputs in Mean Fitness Trendline Component. 113
Figure 4-47 Overview of inputs in Standard Deviation Component. 114
Figure 4-48 Overview of inputs in Standard Deviation Trendline Component. 115
Figure 4-49 Overview of inputs in Parallel Coordinate Plot Component. 116
Figure 4-50 PCP Analysis, Method 0. 117
Figure 4-51-51 PCP Analysis, Method 1. 118
Figure 4-52 PCP Analysis, Method 3. 119
Figure 4-53 Overview of inputs in Diamond Fitness Component. 119
Figure 4-54 Overview of inputs in Objective Space and Pareto Front Components. 121
Figure 4-55 Algorithm to demonstrate Objective Space by built-in Grasshopper components. 122
Figure 5-1 Overall computational workflow developed for the shading generating and energy simulation within an optimization algorithm to test on the case study. 124
Figure 5-2 First step of the framework: zone creation algorithm (refer toFigure 5-1) 125
Figure 5-3 Second step of the framework: Program assignment process algorithm126
Figure 5-4 Third step Material and construction set configuration in the framework.(refer to Figure 5-1)..... 127
Figure 5-5 step four: Energy analysis stage of the framework (refer to Figure 5-1)128
Figure 5-6 Step 5: Daylight analysis framework (refer to Figure 5 1..... 129

Figure 5-7 Shading setup stage of the framework, defining geometric parameters and controling variables for the external shading system (refer to Figure 5 1) 130
Figure 5-8 Optimization stage of the framework and related resulting charts production..... 131
Figure 5-9 Urban morphological map of Milan. The blue marker indicates the case study site location. 132
Figure 5-10 Zoomed-in view of the case study site, illustrating its constrained urban position between transport infrastructure and dense surrounding fabric 133
Figure 5-11 Three-dimensional massing representation of the case study building and its surrounding urban context. 133
Figure 5-12 Annual dry-bulb temperature heatmap for Milan (EPW data), illustrating hourly temperature variation across the year. 134
Figure 5-13 Annual thermal comfort distribution for Milan, indicating hourly periods classified as comfortable and uncomfortable based on the total comfort polygon. . 134
Figure 5-14 Solar radiation analysis of the case study building in Milan. (Left) Spatial distribution of annual incident radiation. (Right) Monthly radiation values (kWh/m²) for each façade and roof orientation. Solar radiation analysis of the case study building in..... 135
Figure 5-15 Annual hourly relative humidity (%) for Milan based on EPW weather data, demonstrating seasonal and daily variability in ambient moisture conditions.” 135
Figure 5-16 Annual wind rose for Milan (Linate EPW data), illustrating prevailing wind directions and corresponding wind speed distribution (m/s). 136
Figure 5-17 Summary of primary climatic parameters affecting the case study site in Milan. 137
Figure 5-18 Functional area distribution and vertical spatial organization of the case study building..... 138
Figure 5-19 Site plan of the case study building. 138
Figure 5-20 Ground floor plan of the case study building. 139
Figure 5-21 First floor plan of the case study building. 139
Figure 5-22 Rendered view of the south façade before the adoption of the optimized shader. 140

Figure 5-23 Rendered perspective view of the south façade before the adoption of the optimized shader. 140
Figure 5-24 Ground floor and First floor transition from architectural to thermal..... 143
Figure 5-25 Intersected Zones 3D Modeling..... 143
Figure 5-26 Boundary condition of case study. 144
Figure 5-27 Visualization of the parametric shading system..... 145
Figure 5-28 Existing and transformed mode of the case study. 145
Figure 5-29 Variable input of the parametric shading model..... 146
Figure 5-30 Variable input of the parametric shading model..... 146
Figure 5-31 Variable input of the parametric shading model..... 147
Figure 5-32 Variable input of the parametric shading model..... 147
Figure 5-33 Variable input of the parametric shading model..... 147
Figure 5-34 Variable input of the parametric shading model..... 148
Figure 5-35 algorithm of the shading system model 148
Figure 5-36 algorithm blow-up 1 149
Figure 5-37 algorithm blow-up 2 & 3..... 149
Figure 5-38 algorithm blow-up 4 150
Figure 5-39 blow-up 5..... 150
Figure 5-40 blow-up 6..... 151
Figure 5-41 Overview of available options in the Honeybee HB Search Programs component. 152
Figure 5-42 Assignment of heating and cooling setpoints and application of Honeybee program types. 154
Figure 5-43 Workflow for extracting and visualizing People occupancy schedules from assigned Honeybee Program Types, showing the deconstruction of program data and the resulting hourly schedule profile used in the energy simulations. 154
Figure 5-44 Workflow for extracting and visualizing Equipment schedules from assigned Honeybee Program Types, showing the deconstruction of program data and the resulting hourly schedule profile used in the energy simulations. 154
Figure 5-45 Workflow for extracting and visualizing lighting schedules from assigned Honeybee Program Types, showing the deconstruction of program data and the resulting hourly schedule profile used in the energy simulations. 155

Figure 5-46 Workflow for extracting and visualizing Hot water schedules from assigned Honeybee Program Types, showing the deconstruction of program data and the resulting hourly schedule profile used in the energy simulations. 155
Figure 5-47 Workflow for extracting and visualizing People occupancy schedules from assigned Honeybee Program Types, showing the deconstruction of program data and the resulting hourly schedule profile used in the energy simulations. 155
Figure 5-48 Workflow for extracting and visualizing Heating schedules from assigned Honeybee Program Types, showing the deconstruction of program data and the resulting hourly schedule profile used in the energy simulations. 155
Figure 5-49 Workflow for extracting and visualizing Cooling schedules from assigned Honeybee Program Types, showing the deconstruction of program data and the resulting hourly schedule profile used in the energy simulations. 156
Figure 5-50 Opaque wall construction workflow in Honeybee, showing (1) manual material definition using HB Opaque Material and (2) use of default materials via HB Search Material, assembled into an HB Opaque Construction for energy simulation. 156
Figure 5-51 Construction set workflow in Honeybee, organizing envelope, interior, and sub-surface constructions and assigning them to rooms. 158
Figure 5-52 Monthly thermal load balance illustrates the relative contributions of heat gains and losses by source across the year. 161
Figure 5-53 Monthly thermal load balance including balance_stor, illustrating the effect of thermal mass on heat storage and release alongside major heat gains and losses. 162
Figure 5-54 Monthly distribution of thermal comfort conditions based on PMV analysis, showing the fraction of occupied hours within comfort and discomfort ranges across the year. 163
Figure 5-55 Monthly variation of zone mean air temperature (°C) across the year, illustrating seasonal thermal trends and peak summer conditions. 164
Figure 5-56 The heat loss (negative) or heat gain (positive) through each building surfaces (kWh). 165
Figure 5-57 Total cooling energy intensity (kWh/m2), Ground Floor. 166
Figure 5-58 Total cooling energy intensity (kWh/m2), First Floor. 166
Figure 5-59 Total heating energy intensity (kWh/m2), Ground Floor. 167

Figure 5-60 Total heating energy intensity (kWh/m2), First Floor. 167
Figure 5-61 Total lights electricity energy intensity (kWh/m2), Ground Floor. 168
Figure 5-62 Total lights electricity energy intensity (kWh/m2), First Floor. 168
Figure 5-63 Total electric equipment energy intensity (kWh/m2), Ground Floor. 169
Figure 5-64 Total electric equipment energy intensity (kWh/m2), First Floor. 169
Figure 5-65 Total water uses equipment heating energy intensity (kWh/m2), Ground Floor. 170
Figure 5-66 Total water uses equipment heating energy intensity (kWh/m2), First Floor. 170
Figure 5-67 Total enclosure windows total transmitted solar radiation energy intensity (kWh/m2), Ground Floor. 171
Figure 5-68 Total enclosure windows total transmitted solar radiation energy intensity (kWh/m2), First Floor. 171
Figure 5-69 Point-In-Time Illuminance (Ground Floor, September 9 A.M). 172
Figure 5-70 Point-In-Time Illuminance (Fisrt Floor, September 9 A.M). 173
Figure 5-71 Point-In-Time Ilumminance (Ground Floor, September 3 P.M). 173
Figure 5-72 Point-In-Time Ilumminance (First Floor, September 3 P.M). 173
Figure 5-73 Point-In-Time Illuminance (Ground Floor, March 9 A.M)..... 174
Figure 5-74 Point-In-Time Illuminance (First Floor, March 9 A.M)..... 174
Figure 5-75 Point-In-Time Illuminance (Ground Floor, March 3 P.M). 175
Figure 5-76 Point-In-Time Illuminance (First Floor, March 3 P.M). 175
Figure 5-78 Daylight Factor between 2% and 5%, Ground floor. 176
Figure 5-78 Daylight Factor between 2% and 5%, First floor. 176
Figure 5-79 Daylight Autonomy (sDA300/50%): Percentage of regularly occupied floor area that achieves ≥300 lux for at least 50% of annual occupied hours. (Ground Floor) 177
Figure 5-80 Daylight Autonomy (sDA300/50%), First Floor. 178
Figure 5-81 Percentage of DI-Low (< 300 lux), Ground Floor. 179
Figure 5-82 Percentage of DI-Low (< 300 lux), First Floor. 179
Figure 5-83 Percentage of UDI (300–3000 lux), Ground Floor. 180
Figure 5-84 Percentage of UDI (300–3000 lux), First Floor. 180
Figure 5-85 Percentage of UDI-up (> 3000 lux), Ground Floor. 181
Figure 5-86 Percentage of UDI-up (> 3000 lux), First Floor. 181

Figure 5-87 Spatial distribution of Annual Sunlight Exposure (ASE ≥ 250). Heatmap showing cumulative direct sunlight hours on the analysis grid, Ground Floor..... 182
Figure 5-88 Spatial distribution of Annual Sunlight Exposure (ASE ≥ 250), First Floor. 182
Figure 5-89 Spatial Glare Autonomy (sGA) pass/fail distribution across the analysis grids, showing the percentage of sensor points that remain below the glare threshold for the specified fraction of occupied hours (red = pass, blue = fail), Ground Floor. 183
Figure 5-90 Spatial Glare Autonomy (sGA), First floor. 184
Figure 5-91 representative space for a faster optimization 185
Figure 5-92 SD graph for EUI,sDA and sGA criteria 187
Figure 5-93 Mean value trendline chart for all criteria 190
Figure 5-94 SD trendline chart for all criteria 192
Figure 5-95 Fitness value graph for all criteria 194
Figure 5-96 Parallel coordinate plot for all fitness objectives 197
Figure 5-97 Objective space visualization for all fitness criteria 198
Figure 5-98 PCP analysis 1 199
Figure 5-99 PCP analysis 2 199
Figure 5-100 Diamond chart for each objective 200
Figure 5-101 K-means clustering 201
Figure 5-102 Exported phenotypes 202
Figure 5-103 Exported phenotypes 203
Figure 5-104 Monthly thermal load balance illustrates the relative contributions of heat gains and losses by source across the year. 205
Figure 5-105 Monthly thermal load balance including balance_stor, illustrating the effect of thermal mass on heat storage and release alongside major heat gains and losses. 205
Figure 5-106 Monthly distribution of thermal comfort conditions based on PMV analysis, showing the fraction of occupied hours within comfort and discomfort ranges across the year. 205
Figure 5-107 The heat loss (negative) or heat gain (positive) through each building surfaces (kWh). 206
Figure 5-108 Total cooling energy intensity (kWh/m2), Ground Floor. 207
Figure 5-109 Total cooling energy intensity (kWh/m2),First Floor. 207

Figure 5-110 Total heating energy intensity (kWh/m2), Ground Floor. 207
Figure 5-111 Total heating energy intensity (kWh/m2), First Floor. 208
Figure 5-112 Total zone lights electricity energy intensity (kWh/m2), Ground Floor.208
Figure 5-113 Total zone lights electricity energy intensity (kWh/m2), First Floor..... 208
Figure 5-114 Total zone Electric Equipment energy intensity (kWh/m2), Ground Floor. 209
Figure 5-115 Total zone Electric Equipment energy intensity (kWh/m2), Ground Floor. 209
Figure 5-116 Window total transmitted solar radiation energy intensity (kWh/m2), Ground Floor..... 209
Figure 5-117 Window total transmitted solar radiation energy intensity (kWh/m2), First Floor. 210
Figure 5-118 Point-In-Time Illuminance (Ground Floor, September 9 A.M) 210
Figure 5-119 Point-In-Time Illuminance (First Floor, September 9 A.M) 210
Figure 5-120 Point-In-Time Illuminance (Ground Floor, September 3 P.M) 211
Figure 5-121 Point-In-Time Illuminance (First Floor, September 3 P.M). 211
Figure 5-122 Point-In-Time Illuminance (First Floor, March 9 A.M).....211
Figure 5-123 Point-In-Time Illuminance (First Floor, March 9 A.M)..... 212
Figure 5-124 Point-In-Time Illuminance (Ground Floor, March 3 P.M)..... 212
Figure 5-125 Point-In-Time Illuminance (First Floor, March 3 P.M)..... 212
Figure 5-126 Daylight Factor between 2% and 5%, Ground floor..... 213
Figure 5-127 Daylight Factor between 2% and 5%, First floor..... 213
Figure 5-128 Daylight Autonomy (sDA300/50%): Percentage of regularly occupied floor area that achieves ≥300 lux for at least 50% of annual occupied hours. (Ground Floor) 213
Figure 5-129 Daylight Autonomy (sDA300/50%), First Floor. 214
Figure 5-130 Percentage of UDI (300–3000 lux), Ground Floor 214
Figure 5-131 Percentage of UDI (300–3000 lux), First Floor 214
Figure 5-132 Spatial distribution of Annual Sunlight Exposure (ASE ≥ 250). Heatmap showing cumulative direct sunlight hours on the analysis grid, Ground Floor..... 215
Figure 5-133 Spatial distribution of Annual Sunlight Exposure (ASE ≥ 250), First Floor. 215

Figure 5-134 Spatial Glare Autonomy (sGA) pass/fail distribution across the analysis grids, showing the percentage of sensor points that remain below the glare threshold for the specified fraction of occupied hours (red = pass, blue = fail), Ground Floor. 215
Figure 5-135 Spatial Glare Autonomy (sGA),First floor. 216
Figure 5-136 Rendered view of the south façade with the optimized louver-based shading system. 219
Figure 5-137 Rendered perspective view of the south façade with the optimized louver-based shading system. 219

Reference of tables:

Table 2-1 Comparative overview of simulation and optimization tools used in building performance 38
Table 3-1 Independent parameters breakdown. 51
Table 3-2 Equipment used to measure metrics. Sorooshnia et al. (2023) 53
Table 3-3 Found near-optimum solution for each case using DIVA simulation. Sorooshnia et al. (2023) 55
Table 4-1 Summary of inputs, parameters, and outputs of the HB Annual Loads component used for annual thermal load and energy demand estimation. 81
Table 4-2 Inputs and Outputs of HB Model to OSM component 87
Table 4-3 Daylight Factors Considered in This Study 93
Table 4-4 Explanation of inputs in Fitness Value Component. 112
Table 4-5 Explanation of inputs in Mean Fitness Trendline Component. 113
Table 4-6 Explanation of inputs in Standard Deviation Component. 114
Table 4-7 Explanation of inputs in Standard Deviation Trendline Component. 115
Table 4-8 Explanation of inputs in Parallel Coordinate Plot Component. 117
Table 4-9 Explanation of inputs in Diamond Fitness Component. 120
Table 4-10 Explanation of inputs in Objective Space and Pareto Front Components. 121
Table 5-1 Initial setting of optimization 186
Table 5-2 Comparison of alternatives for the whole building 204